RADIOFREQUENCY ANALYSIS USING OPTICAL SIGNAL PROCESSING

W. N. Dawber

A Thesis Submitted for the Degree of PhD
at the
University of St Andrews

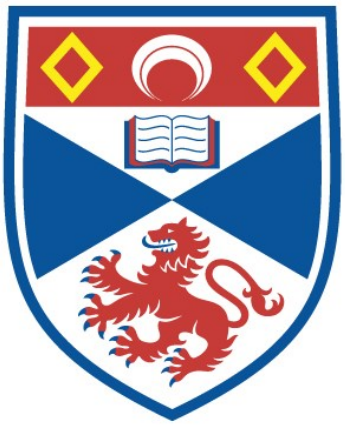

1991

Radiofrequency Analysis Using Optical Signal Processing

A thesis presented by

W. N. Dawber BA(Oxon), MSc

to the

University of St. Andrews

in application for the degree of

Doctor of Philosophy

April 1991

Declaration

I hereby certify that this thesis has been composed by me and is a record of work done by me and has not previously been presented for a higher degree.
This research was carried out in the Physical Sciences Laboratory of St. Salvator's College, in the University of St. Andrews, under the supervision of Dr. A Maitland.

I was admitted to the Faculty of Science of the University of St. Andrews under Ordinance general number 12 in October 1987 and as a candidate for the degree of PhD in October 1988.

W. N. Dawber

Certificate

I certify that W. N. Dawber has spent nine terms at research in the Physical Sciences Laboratory of St. Salvator's College, in the University of St. Andrew's, under my direction, that he has fulfilled the conditions of ordinance No. 16 (St. Andrews) and that he is qualified to submit the thesis in application for the degree of Doctor of Philosophy.

A. Maitland

Research Supervisor

Acknowledgements

I would like to thank Dr. Arthur Maitland for his guidance and encouragement throughout this work and to Peter Hirst and Brian Condon for many helpful discussions. I am particularly grateful to the Admiralty Research Establishment for financial support and to my industrial supervisor Dr. Phil Sutton for his enthusiasm, help and interest in the project.

Thanks must also go to all of the St. Andrew's students who have made life enjoyable inside and outside the department, above and below sea level.

Dedication

I dedicate this thesis to Charlotte, my fiancee, for all her help and encouragement.

Contents

Abstract

The basic form of conventional electronic and acoustooptic radiofrequency spectrum analysers is described. The advantages and disadvantages of the various systems are discussed with particular reference to radar signal processing in a hostile environment.

Acoustooptic interaction is described using electromagnetic wave theory and also in terms of particle dynamics. A discussion of the various factors which effect Bragg-cell performance is presented, together with experimental results from the characterisation of acoustooptic cells.

Coherent light detection is described when used in conjunction with a Bragg-cell spectrum analyser. Using this approach the dynamic range of the device may be dramatically increased. A novel approach is described which uses optical fibres in the Fourier transform plane and fusion spliced couplers to combine the signal and local oscillator beams. Experimental results are presented using single-mode fibres.

Improvements in diffraction efficiency, reduced material intermodulation and increased frequency resolution are possible in an acoustooptic spectrum analyser if a Bragg-cell with a long transducer is used. However this leads to reduced instantaneous bandwidth in a conventional configuration. Two new approaches are described which allow a long transducer to be used without loss of bandwidth.

An analysis of Bragg-cell diffraction within active and passive resonant optical cavities shows the diffraction efficiency per watt of a Bragg-cell may be increased by orders of

magnitude by placing it within a passive cavity. Various cavity configurations are analysed and experimental results are given.

A temporal analysis of light diffracted from radiofrequency pulses within an acoustooptic Bragg-cell is presented. Experimental evidence backs up the theory, which shows a possible means of eliminating the "Rabbit's Ears" phenomenon.

Conventional acoustooptic Bragg cells have bandwidths limited by the acoustic losses in the crystals used for the cells and impedance matching of the transducer to the driver and crystal. Commercial cells are available with bandwidths of several gigahertz.

Many applications require significantly larger bandwidths than are offered by conventional Bragg cells. We describe a new kind of diffraction cell with a potential bandwidth in excess of fifty gigahertz. The theory of operation and an example design are presented.

A novel ultra-high data rate optical communication link is described. This makes use of the temporal distribution produced by light diffracted from radiofrequency pulses within a Bragg-cell. Also a covert, free-space link is described. A two channel system is demonstrated using acoustooptic cells.

Glossary

$a(x)$	Optical cell aperture function
A_1	Amplitude of optical signal electric field strength
A_2	Amplitude of optical reference electric field strength
B	System bandwidth
B_{ij}	Relative dielectric impermeabilty of crystal
C	Capacitance per unit length of TWEOD crystal
c	Speed of light in vacuum
c_{33}	Elastic constant relating stress to strain
c_n	Fourier component
$CT_{f_1-f_2}$	Cross talk power between frequency channels f_1 and f_2
D	Length of TWEOD crystal in microwave propagation direction
D_S	System dynamic range
d	Grating spacing
$d_1(\rho,t)$	Fourier transform of phase modulated light entering cell
$d_1(\rho,\omega)$	Transform of phase modulated light entering cell
$d_2(\rho,t)$	Fourier transform of phase modulated light entirely within cell
$d_2(\rho,\omega)$	Transform of phase modulated light entirely within cell
$d_3(\rho,t)$	Fourier transform of phase modulated light leaving cell
$d_3(\rho,\omega)$	Transform of phase modulated light leaving cell
D_j	j-component of displacement current
D_{poly}	Polytone dynamic range with no Hecht intermodulation
e	Electronic charge
E_1	Amplitude of un-diffracted optical field

$E_1(0)$	Amplitude of un-diffracted field on entering crystal
E_2	Amplitude of electric field of diffracted optical wave
$E_2(0)$	Amplitude of diffracted field on entering crystal
E_b	Time varying electric field of diffracted optical wave
E_f	Time varying E-field of un-diffracted optical wave
F	Cavity finesse
f_1	Radiofrequency 1
f_2	Radiofrequency 2
f_L	Focal length of fibre-coupling lens
F_{l_c}	Focal length of collimating lens
$F_{l_{F.T.}}$	Focal length of transform lens
$F_{l_{in}}$	Focal length of input lens
f_s	Acoustic frequency
g	Single-pass cavity gain
g_2	Single-pass cavity gain for ray 2
H	Height of acoustic column (perpendicular to acoustooptic plane).
H_{fy}	y-component of time varying magnetic field strength of un-diffracted optical wave
H_{fz}	z-component of time varying magnetic field strength of un-diffracted optical wave
$i(t)$	Photocurrent
I_0	Average optical power of incident wave
I_d	Optical diffracted power from TWEOD
i_d	Detector dark current
I_i	Incident optical power
I_{in}	Optical cavity input power
I_n	Average optical power of n^{th} difraction order

Int_{1-2}	Relative Hecht intermodulation between f_1 and f_2
I_{out}	Optical cavity output power
i_{shot}	Shot-noise current
J_n	Bessel function of n^{th} order
k'_1	Un-diffracted optical wavevector
k*	Microwave wavevector in TWEOD
k_0	Un-perturbed optical wavevector
k_1	Un-diffracted optical wavevector
k_2	Diffracted optical wavevector
k_B	Wavevector of Bragg-diffracted light
k_s	Acoustic wavevector
L'	Acoustooptic interaction length in acoustic propagation direction
l	Inductance per unit length of TWEOD crystal
L	Length of cell in acoustic propagation direction
l_s	Illumination area of polychromatic source
N	Number of channels
DN	Dynamic range
n	Optical refractive index of crystal
n_p	Number of resolvable frequencies
P	Microwave power in TWEOD crystal
P_0	Un-diffracted optical power
P_1	Average un-diffracted optical power
$P_1(0)$	Average un-diffracted optical power on entering crystal
P_{1-2}	Hecht intermodulation power between f_1 and f_2
P_2	Average power density of diffracted optical wave
$P_2(0)$	Average diffracted optical power on entering crystal
P_d	Optical diffracted power

P_{max}	Maximum optical power before saturation of detector
P_{min}	Optical power for signal-to-noise ratio of unity
p_{mn}	Piezo-optic tensor
P_s	Average power density of acoustic wave
P_T	Average total acoustic power
P_{T_1}	Acoustic power 1
P_{T_2}	Acoustic power 2
$P_{T_{min}}$	Minimum detectable acoustic signal power
$P_{T_{ref}}$	Acoustic power in Bragg cell in reference arm
Q	Dimensionless parameter relating transducer size to optic and acoustic wavelengths
R	Detector load resistance
R_{best}	Optimum mirror reflectance
r_c	Observed linear electrooptic coefficient
S	Time varying acoustic strain
s(t)	Time-varying applied radiofrequency amplitude
S(x,t)	Phase modulation on incident plane optical wave passing through cell
S/N_{P_T}	Signal-to-noise ratio for acoustic power P_T
S_1	Amplitude of acoustic strain
S_d	Displacement of diffracted beam in polychromatic spectrum analyser
S_{fibre_x}	Horizontal displacement of input fibre
S_{fibre_y}	Vertical displacement of input fibre
S_{max}	Maximum electrical input signal power before detector saturation
S_{min}	Electrical signal power for signal-to-noise ratio of unity
SNR	Signal-to-noise ratio
S_x	Horizontal displacement of diffracted spot
S_y	Vertical displacement of diffracted spot

T	Cell transit time
T_s	Equivalent system temperature
T_m	Mirror transmission
t_h	Height of TWEOD crystal
t	Time
TWEOD	Travelling wave electrooptic diffractor
v	Acoustic velocity
V_3	Voltage across TWEOD crystal
v_s	Sound velocity in crystal
W	Acousic depth
w	Acoustic depth where $Q=\pi$
x,y,z	Cartesian coordinates
Z	Characteristic impedance of TWEOD crystal
α	Fraction of light directed into reference arm
δ	Round-trip cavity loss
Δ_B	Cavity loss at Bragg cell
Δ_{B2}	Cavity loss for ray 2 at Bragg cell
$\Delta\varepsilon$	$\varepsilon' - \varepsilon$
δF	Frequency off-set provided by mirror mis-alignment
Δf_s	Frequency resolution
$\Delta f_{s_{1/2}}$	Acoustic frequency bandwidth
$\Delta f_{s_{collimation}}$	Loss of frequency resolution due to collimation error
$\Delta f_{s_{grating}}$	Loss of frequency resolution due to spectrometer grating resolution
Δf_{s_T}	Total system frequency resolution
Δk_s	Change in acoustic wavevector
$\Delta k_{s_{1/2}}$	Spread of acoustic wavevectors
Δ_m	Cavity loss at a mirror

$\delta_{parasitic}$	Round-trip parasitic cavity loss
$\Delta\omega_{RF}$	Difference in angular frequency between signal and reference arms
$\Delta\emptyset$	Small angular change
$\delta\emptyset$	Angular mirror mis-alignment
$\Delta\emptyset_{1/2}$	Angular spread of acoustic propagation directions
$\Delta\emptyset_a$	Small change in propagation angle of acoustic wave
$\Delta\theta$	Bragg cell rotation angle
ε	Dielectric permitivity of crystal
ε'	Dielectric constant of perturbed crystal
ε_0	Dielectric permitivity of free-space
$\phi(y)$	Phase-front retardation at y
ϕ_0	Amplitude of phase-front retardation
ϕ_1	Phase delay for signal arm
$\phi_1,\ldots,\phi_8$	Unit amplitude phase terms
ϕ_2	Phase delay for reference arm
ϕ_f	Fibre core diameter
ϕ_s	Optical spot diameter
Γ_b	Rate of growth of diffracted optical wave in acoustic propagation direction
Γ_f	Rate of growth of un-diffracted optical wave in acoustic propagation direction
Γ_s	Rate of growth of acoustic field in acoustic propagation direction
η	Diffraction efficiency per watt of TWEOD
η_B	Diffraction efficiency per watt of cell
η_c	Optical fibre coupling efficiency
η_d	Detector efficiency
$\eta_{L_{ref}}$	Transmittance due to parasitic loss in reference arm
η_r	Reference arm transmittance
η_s	Signal arm transmittance

κ	Boltzmann's constant
Λ	Acoustic wavelength
λ	Free space optical wavelength
μ	Dielectric permeability of crystal
ρ	Spatial frequency
ρ_s	Spatial frequency corresponding to acoustic frequency ω_s
τ_a	Complex amplitude transmittance
τ	Pulse duration
τB	Time-bandwidth product
ω_1	Unperturbed optical frequency
ω_2	Optical angular frequency of diffracted wave
ω_ρ	Doppler shifted frequency corresponding to position ρ
ω_{RF}	Angular radiofrequency
ω_s	Acoustic angular frequency
$\emptyset$	Diffraction angle
$\emptyset'_d$	Diffraction angle outside TWEOD crystal
$\emptyset_1$	Angle of incidence in crystal
$\emptyset_2$	Angle of diffraction in crystal
$\emptyset_b$	Bragg angle in crystal
$\emptyset_d$	Angle of diffraction within crystal
$\emptyset_i$	Angle of incidence within crystal
$\emptyset_n$	Angle of diffraction of n^{th} order

1

Introduction to Acoustooptic Spectrum Analysers

1.1 ACOUSTOOPTIC SIGNAL PROCESSING

The applications for radiofrequency spectrum analysers, particularly Radar, [1.1, 1.2] often require monitoring a wide band of the electromagnetic spectrum with the ability to recognise desired characteristics of any signal which may appear in that band. By using this information the source and nature of the signal may then be obtained.

A high probability of intercept of transient signals over a broad frequency band, in a wide field of view, and with an environment crowded with many continuous-wave and pulsed signals is desired.

Severe problems arise when the band of interest contains a large number of signals of different frequencies, amplitudes and types of modulation. The signals may also have been modulated in such a way as to deliberately make identification as difficult as possible e.g. by using frequency hopping and spread-spectrum techniques.

Conventional receiver systems scan the band of interest, one frequency at a time. The probability of intercept for short duration signals is therefore reduced. A receiver system should simultaneously process the signals over the whole frequency range in order to satisfy the requirement for a high probability of intercept. A receiver system incorporating acoustooptic signal processing [1.3-1.7] can provide simultaneous

detection of radiofrequency over a wide dynamic range with 100% probability of intercept. The acoustooptic receiver produces the power spectrum of all the signals in its band simultaneously. The signals can be intermixed, pulsed or continuous-wave and may include broadband signals such as jammers or intrapulse modulated radars.

During the last decade the availability of the laser and of cheap and efficient charged coupled device (CCD) detector arrays [1.8] has led to the development of a wide range of special purpose systems capable of performing functions previously accomplished by microwave and lower frequency systems but with order of magnitudes greater speed and capacity. The emmergence of integrated optics and surface acoustic wave (S.A.W.) [1.9-1.13] devices has enabled miniature, robust, acoustooptic systems to be produced at relatively low cost.

As well as Fourier transformation, all types of multipoint mathematical multiplication of real and complex variables may be performed using acoustooptic signal processing techniques. These include correlations, convolutions and combinations of these with Fourier transforms[1.14-1.26]. One or more functions may be inputted, and the output(s) may be in one or two dimensions.

Digital computation has the advantage over optical in that it is easy to re-program, whereas the "program" of the optical computer is set when the optics are positioned. However the optical processor does what it is designed to do at an extremely high rate. The main feature of optical processors is that they process a large signal bandwidth in parallel. This is at the same time the biggest advantage and the biggest problem; an optical processor produces so much information that it is difficult to use it all !

1.2 THE ACOUSTOOPTIC SPECTRUM ANALYSER

The acoustooptic spectrum analyser is a deceptively simple optical processor. It performs a real time Fourier transform with only four active components; a light source, a Bragg-cell, a lens and a photodetector array.

The basic acoustooptic spectrum analyser is shown in figure 1.1

Light from the laser is expanded and collimated to pass through the acoustooptic cell aperture. The acoustooptic cell consists of a transducer bonded to a block of optically transparent material, as shown in figure 1.2. Radiofrequency signals to be analysed are applied to the transducer, which creates travelling acoustic waves in the block. The waves are absorbed at the other end of the block by sound absorbing putty or similar. The acoustic waves consist of periodic compressions and rarifactions, these create periodic changes in the optical refractive index of the material in the direction of acoustic propagation.

Light passing through the cell is phase modulated by the acoustic waves and a portion of the light is diffracted (This will be explained in more detail in section 1.3). The intensity and angle of diffraction is approximately proportional to the applied radiofrequency power and frequency, respectively. The Fourier transform lens creates the frequency transform in its focal plane. This is detected by the detector array placed in the focal plane of the lens.

1.3 THEORY OF ACOUSTOOPTIC DIFFRACTION

1.3.1 Qualitative treatment

There are many treatments for the solution of acoustooptic diffraction [1.27-1.37]. We will divide the problem into two regimes and solve each separately, with particular emphasis on deriving the characteristics relevant in acoustooptic spectrum analysis.

Consider the case of a uniform plane wave of monochromatic light (wavelength λ/n, where λ is the free space optical wavelength and n is the refractive index of the interaction medium) incident on a column of acoustic waves consisting of sinusoidal index variations (wavelength Λ) travelling at right angles to the optical beam.

Since the acoustic velocity is much less than the optical velocity we will first consider the acoustic wave to be stationary.

The light entering regions of compression experience a higher refractive index and have lower phase velocity than the light entering regions of rarefaction. As the light passes through the acoustic column the optical wavefront becomes distorted as shown in figure 1.3. Since the wave elements propagate essentially normal to the local phase front the distortion implies changes of direction for the wave elements. This leads to a redistribution of the light flux which must be considered when analysing deep (in the direction of optical propagation) acoustic columns. Significant simplification is possible by using approximations valid in various regions of operation.

1) Deep field (Bragg) regime. The amplitude re-distribution cannot be ignored, Bragg diffraction dominates.

2) Shallow field (Raman-Nath) case. When the acoustic wavelength is comparable in size to the optical wavelength and the amplitude re-distribution may be ignored.

For condition 2 to be valid the amplitude must remain uniform across the optical wavefront. Diffraction will tend to deviate the wavefront from this condition. We shall define an acoustic depth, w, where light diffraction from the front of the acoustic column spreads over one cycle of the acoustic wave at the back of the acoustic column. This is shown in figure 1.3.

If the depth of the acoustic column, W, is much greater than w then we will be in the deep field regime. If the width of the acoustic column is much less than w then we are in the shallow field regime.

We define the parameter

$$Q = \frac{2\pi W}{w} .$$

From figure 1.3 we see w is given by

$$w\varnothing = \frac{\Lambda}{2} \quad \text{and} \quad \varnothing = \frac{\lambda}{2n\Lambda} .$$

Hence, we have

$$Q = \frac{2\pi\lambda W}{n\Lambda^2} . \qquad 1.0$$

In practice the acoustooptic interaction is found to be predominantly Bragg-like for values of Q greater than about 10.

1.3.2 Bragg diffraction (high-Q case)

We first analyse the case where the interaction material is isotropic and the acoustic wavefronts are plane. Following the method of Quate et al. [1.30], we shall consider the case of light incident on a column of plane acoustic waves, travelling at angle $\emptyset_i$ with respect to the incident light, as shown in figure 1.4.

For the high - Q case, the acoustic waves behave very much like a crystal lattice. Light is diffracted from successive planes and diffraction takes place only at certain allowed angles of incidence ($\emptyset_i$) and diffraction ($\emptyset_d$), with just one diffracted beam angle giving constructive interference from successive planes.

It should be noted that the angles $\emptyset$ are the angles within the material with refractive index n. If the light enters the cell from free space then the angles $\emptyset$ outside the cell will be different due to refraction at the boundaries. For near normal incidence the angles will be approximately larger by a factor of n outside the cell.

Light scattered from a given acoustic wavefront must arrive at the new optical wavefront in phase. This condition requires the angle of incidence to be equal to the angle of diffraction.

$$\emptyset_i = \emptyset_d = \emptyset \ .$$

Light scattered from successive planes must arrive at the new wavefront in phase or with a path difference equal to an integral number of wavelengths. We see from figure 1.5 that the path difference for rays 1 and 2, scattered from successive planes is

$$AB + BC = 2\Lambda\sin\varnothing \ .$$

To satisfy the above conditions we require

$$m\lambda = 2n\Lambda\sin\varnothing,$$

where m is an integer. This is the "Bragg condition" for diffraction, when we have m=1.

In figure 1.6 the light is polarized with its E-vector in the plane of incidence. The figure also shows the addition of wavevectors k_1, k_2 and k_s which are the incident, scattered and acoustic wave vectors, respectively.

If the field is uniform and we neglect the coupling of the various waves, we can write for the E-field of the electromagnetic wave at angular frequency ω_1 and travelling in the positive z-direction as

$$E_f = \frac{E_1(z)}{2} \exp[\, i(\omega_1 t - k_1 z\sin\varnothing_1 - k_1 y\cos\varnothing_1)] + \text{complex conjugate} \ . \qquad 1.1$$

The average power density is

$$P_1 = \frac{1}{2}\sqrt{\frac{\varepsilon}{\mu}}\, E_1 E_1^* \qquad 1.2$$

and for the wave travelling in the negative z-direction (the reflected wave)

$$E_b = \frac{E_2(z)}{2} \exp[i(\omega_2 t + k_2 z \sin\varnothing_2 - k_2 y \cos\varnothing_2)] + \text{complex conjugate} \qquad 1.3$$

and the average power density is

$$P_2 = \frac{1}{2}\sqrt{\frac{\varepsilon}{\mu}}\, E_2 E_2^* \ . \qquad 1.4$$

The sound wave may be expressed in terms of the strain, S;

$$S = \frac{1}{2} S_1 \exp[i(\omega_s t - k_s z)] + \text{complex conjugate} \ . \qquad 1.5$$

The average power density in the sound wave is

$$P_s = \frac{1}{2} c_{33} v_s S_1 S_1^* \ , \qquad 1.6$$

where we have assumed longitudinal waves. The phase velocity of the sound wave is v_s and c_{33} is the elastic constant relating stress to strain along the z axis.

From the principles of conservation of energy and momentum we have

$$\omega_1 = \omega_2 + \omega_s \qquad 1.7$$

and

$$\mathbf{k_1} = \mathbf{k_2}+\mathbf{k_s}\ . \qquad 1.8$$

The vector components of the last equation are

$$k_1\sin\emptyset_1+k_2\sin\emptyset_2 = k_s \qquad 1.9$$

and

$$k_1\cos\emptyset_1 = k_2\cos\emptyset_2 \qquad 1.10$$

Since we have

$$\frac{\cos\emptyset_1}{\cos\emptyset_2} = \frac{k_2}{k_1} = 1 \text{ (approximately),} \qquad 1.11$$

the angle of incidence $\emptyset_1$ can be taken to be equal to the angle of reflection $\emptyset_2$ and we can write

$$(k_1+k_2)\sin\emptyset = k_s\ . \qquad 1.12$$

This is just the Bragg condition for diffraction described earlier.

Using Maxwell's equations we have

$$\frac{dE_f}{dz} = -\mu\frac{dH_{fy}}{dt}$$

$$\frac{dE_f}{dy} = \mu \frac{dH_{fz}}{dt} \qquad 1.13$$

and

$$\frac{dH_{fz}}{dy} - \frac{dH_{fy}}{dz} = \varepsilon \frac{d}{dt}\left[\frac{\varepsilon'}{\varepsilon}E_f + \frac{\varepsilon'}{\varepsilon}E_b\right], \qquad 1.14$$

where ε' is the dielectric constant of the perturbed crystal, proportional to the strain produced in the medium by the sound wave.

Using 1.1 and 1.3 in 1.13 and performing a time integration and a spatial differentiation, we have

$$\frac{d}{dz}\sqrt{\frac{\mu}{\varepsilon}}H_f = \left[\frac{1}{2}\, i\, \frac{1}{k_1 \sin\emptyset_1}\frac{d^2E_1}{dz^2} + \frac{dE_1}{dz} - \frac{1}{2} ik_1 E_1\right] \exp\{i(\omega_1 t - k_1 \sin\emptyset_1 z)\} + c.c. \qquad 1.15$$

where we have

$$\frac{\omega_1}{k_1} = \frac{1}{\sqrt{\mu\varepsilon}},$$

which is the velocity of the unperturbed electromagnetic wave.

If we write

$$\frac{\varepsilon'}{\varepsilon} = 1 + \frac{\Delta\varepsilon}{\varepsilon},$$

where we have assumed weak coupling,

$$\frac{\Delta\varepsilon}{\varepsilon} << 1 .$$

We may then neglect the first term in parenthesis in 1.15. This means that the change in amplitude of E_1 over a wavelength is small.

From equations 1.14 and 1.15 we have

$$\left[\sin\emptyset \frac{dE_1}{dz} - \frac{1}{2} ik_1 E_1\right] \exp[i(\omega_1 t + k_1 z\sin\emptyset - k_1 y\cos\emptyset)] + \text{complex conjugate}$$

$$= -\varepsilon\sqrt{\frac{\mu}{\varepsilon}}\frac{d}{dt}\{\frac{\varepsilon'}{\varepsilon}E_f + \frac{\varepsilon'}{\varepsilon}E_b\} . \qquad 1.16$$

In order to calculate the change in permitivity,

$$\frac{\varepsilon'}{\varepsilon} = 1 + \frac{\Delta\varepsilon}{\varepsilon},$$

we write the relative dielectric impermeability as

$$B_{ij} = k_0 \frac{dE_i}{dD_j} \qquad 1.17$$

where k_0 is the unperturbed optical wavevector in the medium and the changes in B due to strain are given by the piezo-optic tensor in the form

$$\Delta B_{ij} = p_{ijn} S_n \quad . \qquad 1.18$$

(We may also write the piezo-optic tensor as p_{mn} where m=ij).

It is necessary to work with the full photoelastic matrix when one studies the anisotropy of the diffracted light as a function of the polarisation of the incoming light. For polarisation with the E vector in the plane of incidence and for small Bragg angles we can assume that E is parallel to the optic axis. We designate the z direction (100) as 3, the direction normal to the (100) direction and parallel to the acoustic wavfronts (y) as 2. For cubic crystals we have the relations

$$\frac{\Delta\varepsilon_2}{\varepsilon} = -\frac{\varepsilon}{\varepsilon_0} p_{23} S_3 \qquad 1.19$$

and, for light polarised in the plane of incidence along the optic axis, we have

$$\frac{\Delta\varepsilon_1}{\varepsilon} = -\frac{\varepsilon}{\varepsilon_0} p_{23} S_3 \, . \qquad 1.20$$

Using equations 1.1, 1.3, 1.7, 1.9, 1.10, 1.19 and 1.20 in the right hand side of 1.16, we have

$$\frac{\varepsilon'}{\varepsilon}(E_f + E_b) =$$
$$\{ \frac{E_1}{2} - \frac{\varepsilon}{\varepsilon_0} p_{23} \frac{S_1}{2} \frac{E_2}{2} \} \exp[i(\omega_1 t - k_1 z \sin\Ø - k_1 y \cos\Ø)] + \text{c.c.} + \text{other terms.} \qquad 1.21$$

The terms written out are the only ones that can be used on the right of equation 1.16 in order to satisfy the equation for all z and t.

Equation 1.16 then becomes

$$\frac{dE_1}{dz} = i\frac{k_1}{\sin\Ø}\frac{\varepsilon}{\varepsilon_0}p_{23}\frac{S_1}{2}\frac{E_2}{2} \quad . \tag{1.22}$$

Similarly, we can arrive at the equation for E_2,

$$\frac{dE_2}{dz} = -i\frac{k_2}{\sin\Ø}\frac{\varepsilon}{\varepsilon_0}p_{23}\frac{S_1^*}{2}\frac{E_1}{2} \quad . \tag{1.23}$$

If we assume an exponential dependence for the fields on the z-direction of the form

$$\exp[\Gamma_s dz] \text{ and } \exp[-\Gamma_s dz] , \tag{1.24}$$

then we find

$$\Gamma_s = \frac{1}{2}\frac{k_1}{\sin\Ø}\sqrt{\frac{\omega_2}{\omega_1}\frac{\varepsilon}{\varepsilon_0}}p_{23}\sqrt{\frac{P_s}{2v_s c_{33}}} \quad . \tag{1.25}$$

Using equations 1.22, 1.23, 1.25 and the boundary condition that $E_2(L')=0$, we obtain

$$E_1 = E_1(0)\frac{\cosh\Gamma_s(z-L')}{\cosh\Gamma_s L'} \tag{1.26}$$

and

$$E_2 = -iE_1(0)\sqrt{\frac{\omega_2 S_1^*}{\omega_1 S_1}}\frac{\sinh\Gamma_s(z-L')}{\cosh\Gamma_s L'} \quad . \tag{1.27}$$

Therefore, at z=0 we have

$$\frac{E_2(0)}{E_1(0)} = i\sqrt{\frac{\omega_2}{\omega_1}}\tanh \Gamma_s L' \ . \qquad 1.28$$

For small values of $\Gamma_s L$ this becomes

$$\frac{P_2(0)}{P_1(0)} = \frac{|E_2(0)|^2}{|E_1(0)|^2} = [\Gamma_s L]^2 \ , \qquad 1.29$$

where we have approximated by setting

$\omega_1 = \omega_2$ and $\emptyset_1 = \emptyset_2 = \emptyset$.

If we further approximate, by setting $\sin\emptyset = \emptyset$, then we have for the ratio of the diffracted intensity to the incident intensity

$$\frac{P_2}{P_1} = \frac{k_1^2}{4}\left[\frac{\varepsilon}{\varepsilon_0} p_{23}\right]^2 \frac{1}{\emptyset^2}\frac{P_s L'^2}{2 v_s c_{33}} \ . \qquad 1.30$$

If the acoustic column has dimensions W and H, then, since the light impinges at angle $\emptyset$, the interaction length is given by

$L' = W\tan\emptyset = W\emptyset$, approximately.

If P_T is the total acoustic power in the column, then we have

$$P_S = \frac{P_T}{(WH)}$$

and

$$\frac{P_2}{P_1} = \frac{k_1^2}{8}\left[\frac{\varepsilon}{\varepsilon_0} p_{23}\right]^2 \frac{W}{H}\frac{P_T}{v_s c_{33}} \quad . \qquad 1.31$$

1.3.2 Effect of varying the acoustic frequency

If we vary the acoustic frequency w_S so that $\mathbf{k_S}$ changes to $\mathbf{k_S} + \Delta\mathbf{k_S}$, the diffracted intensity will change.

Equation 1.8 becomes

$$\mathbf{k_1}+\mathbf{k_2} = \mathbf{k_S}+\Delta\mathbf{k_S} \qquad 1.32$$

($\Delta\mathbf{k_S}$ is in the same direction as $\mathbf{k_S}$)

and in component form, equation 1.9 becomes

$$k_1 \sin\emptyset_1 + k_2 \sin\emptyset_2 = k_s + \Delta k_s \quad . \qquad 1.33$$

We replace equation 1.1 with

$$E_f = \frac{1}{2} E_1 \exp[i(\omega_1 t - k'_1 z \sin\emptyset)] + c.c. \qquad 1.34$$

where we have

$$k'_1 = k_1 - \frac{\Delta k_s}{2\sin\emptyset} \ , \qquad 1.35$$

with a similar expression for E_b. This then leads to a more general form for equations 1.22 and 1.23;

$$\frac{dE_1}{dz} + i\frac{\Delta k_s}{2}E_1 = i\frac{k_1}{\sin\emptyset}\frac{\varepsilon}{\varepsilon_0}p_{23}\frac{S_1}{2}\frac{E_2}{2} \qquad 1.36$$

$$\frac{dE_2}{dz} - i\frac{\Delta k_s}{2}E_2 = -i\frac{k_2}{\sin\emptyset}\frac{\varepsilon}{\varepsilon_0}p_{23}\frac{S_1^*}{2}\frac{E_1}{2} \ . \qquad 1.37$$

We assume solutions of the form

$$\exp[\Gamma_b z] \text{ and } \exp[-\Gamma_b z] \ , \qquad 1.38$$

then equation 1.25 becomes

$$\Gamma_b = \sqrt{\Gamma_s^2 - (\frac{\Delta k_s}{2})^2} \ . \qquad 1.39$$

The diffracted power may be obtained as before and equation 1.29 becomes

$$\frac{P_2(0)}{P_1(0)} = \frac{\omega_2}{\omega_1}\frac{\Gamma_s^2 \sinh^2\Gamma_b L'}{\Gamma_b^2 + \Gamma_s^2\sinh^2\Gamma_b L'} \ . \qquad 1.40$$

Using equation 1.39, 140 becomes

$$\frac{P_2(0)}{P_1(0)} = \frac{\omega_2}{\omega_1} \frac{\sinh^2\{\Gamma_s L[1 - \sqrt{\frac{\Delta k_s}{2\Gamma_s}}]\}}{1 - (\frac{\Delta k_s}{2\Gamma_s})^2 + \sinh^2\{\Gamma_s L' \sqrt{1 - (\frac{\Delta k_s}{2\Gamma_s})^2}\}} . \qquad 1.41$$

For small values of Γ_s (weak coupling), $\frac{\Delta k_s}{2\Gamma_s}$ can be much greater than unity and we can approximate equation 1.41 by the relation

$$\frac{P_2(0)}{P_1(0)} = \frac{\omega_2}{\omega_1} (\Gamma_s L')^2 \frac{\sin^2 \frac{\Delta k_s}{2} L'}{(\frac{\Delta k_s}{2} L')^2} . \qquad 1.42$$

1.3.3 Bandwidth for a fixed angle of incidence

From equation 1.42 we see that the FWHM of the diffraction pattern as the acoustic wavevector is changed is given by

$$\Delta k_{s_{1/2}} = \frac{2\pi}{L'} . \qquad 1.43$$

But we have

$$k_s = \frac{2\pi f_s}{v_s} \qquad 1.44$$

and hence we obtain

$$\Delta f_{s_{1/2}} = \frac{v_s}{L'} \quad . \qquad 1.45$$

Also we may write

$$L' = W\emptyset \qquad 1.46$$

and

$$(k_1+k_2)\sin\emptyset = k_s \quad . \qquad 1.47$$

Therefore, for small $\emptyset$ we may write

$$\emptyset = \frac{k_s}{2k_1} \qquad 1.48$$

and

$$\emptyset = \frac{\lambda}{2n\Lambda} \quad . \qquad 1.49$$

From equations 1.45, 1.46 and 1.49 we obtain the instantaneous radiofrequency bandwidth (FWHM)

$$\Delta f_{s1/2} = \frac{2nv_s^2}{f_s W\lambda} \quad . \qquad 1.50$$

1.3.4 Diffraction efficiency as a function of angle of incidence

We have found the variation of diffraction efficiency with frequency for a fixed angle of incidence. We now wish to find the variation of diffraction efficiency as the angle of incidence, $\emptyset_1$, changes.

As the RF frequency changes, the acoustic wavelength changes and the correct angle of incidence (equal to the Bragg angle) changes.

From equation 1.49, we obtain

$$\Delta\emptyset = \frac{\lambda}{2n\Lambda^2}\Delta\Lambda \qquad 1.51$$

and therefore we can write

$$\Delta k_s = \frac{4\pi n}{\lambda}\Delta\emptyset \ . \qquad 1.52$$

Equation 1.42 becomes

$$\frac{P_2(0)}{P_1(0)} = \frac{w_2}{w_1}(\Gamma_s L')^2 \operatorname{sinc}^2[\frac{\pi W}{\Lambda}\Delta\emptyset] \qquad 1.53$$

From equation 1.53 we see that the FWHM of the diffraction efficiency as a function of Bragg-cell rotation, $\Delta\emptyset$, is

$$\Delta\emptyset_{1/2} = \frac{\Lambda}{W} \ , \qquad 1.54$$

provided that we have $\Delta\emptyset_{1/2} << \emptyset$.

The FWHM is just the angular spread in acoustic propagation direction due to acoustic diffraction at the transducer. There is a set of acoustic waves over a range of angles $\Delta\emptyset_{1/2}$ available for diffraction of the optical beam. This is shown on the phase matching diagram, figure 1.7.

1.3.5 Phase matching diagrams

Phase matching diagrams are a graphical method of representing the Bragg condition (equation 1.32) in momentum space. We shall show that phase matching diagrams may be used to obtain the bandwidth of an acoustooptic spectrum analyser. This is particularly useful for diffraction in anisotropic media (see 1.3.6). Figure 1.7 shows the phase matching condition over the angular spread, $\Delta\emptyset_a$, of acoustic wave-vectors.

From figure 1.7, we see that

$$\emptyset_b = \frac{\Delta\emptyset_a k_s}{\Delta k_s} = \frac{k_s}{2k} \quad . \qquad 1.55$$

But from 1.54, we have

$$\Delta\emptyset_a = \Delta\emptyset_{1/2} = \frac{\Lambda}{W}$$

and, hence, we obtain

$$\Delta k_{s_{1/2}} = \frac{2k\Lambda}{W} \quad . \qquad 1.56$$

But we have

$$v_s = \frac{2\pi f_s}{k_s} \qquad 1.57$$

and

$$\Delta k_s = \frac{2\pi \Delta f_s}{v_s} \ . \qquad 1.58$$

From 1.56 and 1.59 we have

$$\Delta f_{s1/2} = \frac{2nv_s^2}{f_s W \lambda} \ , \qquad 1.59$$

as before.

1.3.6 Bragg diffraction in an anisotropic material

Figure 1.8 shows the phase matching condition for Bragg diffraction in an anisotropic material. The incident and diffracted wave vectors lie on different index ellipsoids and are of orthogonal polarisation states. The acoustic wavevector is k_s. The acoustic vector does not meet the index ellipsoid tangentially.

Figure 1.9 shows tangential phase matching in an anisotropic material. The crystal-cut is chosen for a given centre frequency such that the phase matching condition is satisfied

when the acoustic vector meets the index ellipsoid of the diffracted wave vector tangentially.

The phase matching criterion is then met, approximately, over a range of angles. In this way the usable bandwidth for a given angle of incidence is increased.

Figure 1.10 shows the tangential phase matching condition in an anisotropic material over the angular spread of acoustic wavevectors, $\Delta\emptyset_a$.

We will assume that the anisotropy is small so that we have $|\mathbf{k_1}| \approx |\mathbf{k_2}|$.

We then obtain

$$\Delta\emptyset_a = k_2 \, (1\text{-}\cos\Delta\emptyset_b) \quad \text{and} \quad \tan\Delta\emptyset_b = \frac{\Delta k_s}{k_2} \, . \qquad 1.60$$

For small we obtain

$$\Delta k_s = \sqrt{2k_s k_2 \Delta\emptyset_a} \, . \qquad 1.61$$

From 1.54 and 1.61 we have

$$\Delta k_{s_{1/2}} = \sqrt{\frac{4\pi k_2}{W}} \qquad 1.62$$

and from 1.58 and 1.62 the bandwidth is

$$\Delta f_{s1/2} = v_s \sqrt{\frac{2n}{k_2 W \lambda}} \quad . \qquad 1.63$$

Clearly, $\Delta f_{s1/2}$ can be much larger in this case than in the isotropic case (1.50), allowing the usable bandwidth to be limited by the transducer bandwidth rather than the phase matching criterion for a fixed light input angle.

1.3.7 Theoretical analysis of shallow field (Raman-Nath) acoustooptic diffraction

In the shallow field (Q << 1) approximation, the amplitude of the optical wavefront remains uniform and we may represent the acoustic field as a complex amplitude transmittance, given by

$$\tau_a = \sqrt{\tau_a}\, e^{i\phi(y)} \quad , \qquad 1.64$$

where $\phi(y)$ is given by

$$\phi(y) = \phi_0 \cos \frac{2\pi y}{\Lambda} \quad . \qquad 1.65$$

Δn is the amplitude of the index variation produced by the acoustic wave.

The diffraction pattern produced by the acoustic wave is given by the Fourier transform of the amplitude transmittance (1.65) with the variable $Y = \frac{y}{\lambda}$ replacing y. Since τ_a is periodic in y we obtain the Fourier series

$$A(\emptyset) = \sqrt{\tau_a} \sum_n c_n e^{i2\pi nY\lambda/\Lambda} \quad , \qquad 1.66$$

where c_n is given by

$$c_n = \int_{-\Lambda/2\lambda}^{\Lambda/2\lambda} \cos\frac{2\pi nY\lambda}{\Lambda} \exp\left\{ i\phi_0 \cos\frac{2\pi Y\lambda}{\Lambda} \right\} dY \quad . \qquad 1.67$$

By substituting

$$u = \frac{2\pi Y\lambda}{\Lambda} \qquad 1.68$$

in equation 1.67, we obtain

$$c_n = i^n \frac{\Lambda}{\lambda} J_n(\phi_0) \qquad n = ...-1,0,1,2,... \qquad 1.69$$

Equation 1.66 represents a series of diffracted waves travelling in the directions $\emptyset_n$ given by

$$\emptyset_n = \frac{n\lambda}{\Lambda} \quad . \qquad 1.70$$

This is shown schematically in figure 1.11.

The Fraunhofer diffraction pattern therefore consists of sharp lines in the directions $\emptyset_n$ with intensities given by

$$\frac{I_n}{I_0} = J_n^2(\phi_0) \ . \qquad 1.71$$

This calculation was carried out for an infinite length acoustic column. For finite apertures, the lines J_n will be angle-broadened by diffraction from the aperture.

1.4 EXPERIMENTAL VERIFICATION

1.4.1 Characterisation of a low-Q LiNOb3 Bragg-cell

1.4.1.1 Experimental layout

The apparatus is shown in figure 1.12. The ccd array is a Reticon 'K' series with 1024 elements on 25 μm centres. The Bragg-cell is a GEC Marconi Research centre Identity Y347251, SRC no.MRQ IS003, driven from a radiofrequency signal generator and amplifier, with a power monitor connected in parallel.

The Bragg-cell is fabricated from $LiNbO_3$ with a refractive index, n = 2.2, and acoustic velocity, v_s = 6600 m/s.

The Bragg-cell produces an acoustic column approximately 1mm * 20mm and about 10mm thick in the direction of optical propagation.

Light from a Helium-Neon laser is expanded, in the plane of the acoustic beam, using a 5 cm cylindrical lens, followed by a 1m spherical lens. In this way a beam is produced about 2cm by 1mm in the region of the Bragg-cell, which is collimated in the plane of the

acoustic beam. This provides good matching of the acoustic and optical beams. The beam is then passed through the Bragg-cell. The diffracted light is re-collimated and focused onto the ccd array. The Bragg-cell is mounted on a rotation stage which allowed movement in the 2 axes perpendicular to the optic axis, as well as rotation in the plane of the acoustic beam.

Rotation of the Bragg-cell is measured by reflecting light from a Gre-Ne laser using a mirror mounted on the cell. The reflected light falls on to a distant graduated scale.

1.4.1.2 Diffraction efficiency as a function of radiofrequency power

The radiofrequency power applied to the cell is varied, having optimised the diffracted beam intensity (first order), at 118 MHz. The output is monitored on the oscilloscope, being careful not to saturate the ccd array, by using graded neutral density filters.

The results are shown in figure 1.13.

1.4.1.3 Diffraction efficiency as a function of cell misalignment

The experiment is repeated with the radiofrequency power set at 200mW. The cell is rotated in the plane of the acoustic beam and the relative diffracted power, in the first order, measured as before. The results are shown in figures 1.14 and 1.15.

1.4.1.4 Variation in diffraction efficiency with frequency

The radio frequency was varied, whilst holding the radiofrequency power constant at 400mW. The Bragg-cell was first realigned for optimum efficiency with each change in

frequency, and then the experiment was repeated holding the Bragg-cell fixed. The results are shown in figure 1.16.

The open squares are the points taken with re-alignment between each reading. The closed squares were taken with the cell optimally aligned at 120 MHz.

1.4.1.5 Variation of resolution with aperture illumination

The output from the ccd array was photographed, with a 'scope camera, with an adjustable stop in front of the Bragg-cell, so that the cell was illuminated by a truncated Gaussian profile. The results are shown in figure 1.17.

Figures 1.17a to 1.17d show the increase in full width at half maximum (FWHM) as the aperture is closed down at 120MHz. The side lobe structure also becomes more pronounced as the aperture is closed. The FWHM with the aperture fully open is approximately 125μm. Figure 1.17e shows the side lobe structure in more detail, with the central maximum off-scale. Figure 1.17f is taken at 70MHz with the aperture open and has an FWHM of approximately 75μm.

1.4.1.5 Comparison of results with theory

The diffraction efficiency of the cell is approximately linear with the applied radiofrequency power, for low diffraction efficiencies, as predicted by equation 1.31

$$\frac{P_2}{P_1} = \frac{k_1^2}{8}\left(\frac{\varepsilon}{\varepsilon_0} p_{23}\right)^2 \left(\frac{W}{H}\right) \frac{P_T}{2 v_s c_{33}}$$

The diffraction efficiency as a function of angular misalignment is given theoretically by equation 1.53, for small $\Delta\emptyset$.

$$\frac{P_2(0)}{P_1(0)} = \frac{w_2}{w_1} (\Gamma_s L)^2 \, \mathrm{sinc}^2[\frac{\pi W}{\Lambda}\Delta\emptyset] \qquad 1.53$$

This clearly doesn't fit the data in figures 1.14 and 1.15 very well. The central maximum is about the same width as the side lobes, rather than being twice as wide, as implied by the above formula. Equation 1.53 assumes operation in the Bragg regime. We show below that this is not entirely valid for this cell.

If we just take account of the position of the first minimum in the angular distribution then we obtain a value for the length of the transducer. From equation 1.53 the first minimum occurs at an angular misalignment given by

$$\Delta\theta_{min} = \frac{\Lambda}{W} . \qquad 1.72$$

We see from figure 1.14 that the first minimum occurs at an angular misalignment of 0.01 rad. Inside the cell the angle $\Delta\theta_{min}$ will be n - times smaller. We have

$$\Delta\theta_{min} = \frac{0.01}{n} , \qquad 1.73$$

and hence we obtain

$$W = 12 \text{ mm} .$$

From equation 1.0 we obtain

$Q = 7.2$.

The value for the cell is therefore operating in a regime which is between the Bragg and Raman-Nath regimes.

There is little difference between the two sets of results for alignment at the centre frequency and alignment at the operating frequency (figure 1.15). If this cell were used in a conventional acoustooptic radiofrequency spectrum analyser, then the usable bandwidth would be limited by the piezo-electric coupling efficiency, rather than a lack of tracking of the Bragg angle.

The frequency resolution in figures 1.15 is consistent with diffraction at the aperture, the width of the central maximum being of the order, $\Delta\emptyset = \lambda/D$, where D is the illuminated aperture.

1.4.2 Characterisation of a high-Q Bragg-cell

The experimental characterisation procedure has been repeated using a high-Q Bragg-cell.

The Bragg-cell is a "Automates et Automatismes" A.A. DTX100, fabricated in TeO_2 with refractive index $n = 2.26$ and acoustic velocity v_s (slow shear wave) = 800m/s.

The acoustooptic interaction is anisotropic in this cell. The cell may be operated with the input laser beam in either of two orthogonal polarisation states. With the light polarised in one state the phase matching is tangential, as described in section 1.3.6. With the light

polarised in the orthogonal state the phase matching is "normal", as described in section 1.3.5. The phase diagram for the "normal" coupling is shown in figures 1.18 and 1.19.

1.4.2.2 Diffraction efficiency as a function of radiofrequency power

Figure 1.20 shows the variation of diffraction efficiency with radiofrequency power.

1.4.2.3 Diffraction efficiency as a function of cell misalignment

Figure 1.21 shows the variation of diffraction efficiency with cell misalignment at 134 MHz.

The angular separation of the maximum and first minimum is 0.005 rad. The FWHM is 3.5 mrad.

1.4.2.4 Variation in diffraction efficiency with frequency

Figures 1.22 and 1.23 show the variation of diffraction efficiency as the radio frequency is changed, with the laser light polarised for "normal" and "tangential" type phase matching, respectively. The Bragg-cell is aligned for optimum diffraction efficiency at 126 MHz.

The Bandwidth (FWHM) of the cell for "normal" phase matching is 6.4 MHz

The Bandwidth of the cell for "tangential" phase matching is at least 50 MHz

1.4.2.5 Comparison of results with theory

The position of the first minima of diffraction as a function of cell angular misalignment implies a transducer length of (from 1.70)

$$W = \frac{n\Lambda}{\Delta\theta_{min}} \qquad 1.74$$

$W = 2.6$ mm

and from equation 1.0 we have

$Q = 128$

From figure 1.19 we calculate the bandwidth for the "normal" phase matching.

Equation 1.55 becomes

$$2\emptyset_b = \frac{\Delta\emptyset_a k_s}{\Delta k_s} = \frac{k_s}{k} \qquad 1.75$$

and we obtain

$$\Delta f_{s1/2} = \frac{nv_s^2}{f_s W\lambda} \qquad 1.76$$

$\Delta f_{s1/2} = 6.5$ MHz

The measured value for the bandwidth is 6.4 MHz in good agreement. It should be noted that this is half the bandwidth that would have been obtained for an isotropic interaction of the same Q.

1.5 CONCLUSION

The basic form of conventional acoustooptic radiofrequency spectrum analysers has been described.

The acoustooptic interaction has been described using electromagnetic wave theory and also in terms of particle dynamics (phase diagrams in momentum space), together with experimental results from the characterisation of the acoustooptic cells used in the following chapters.

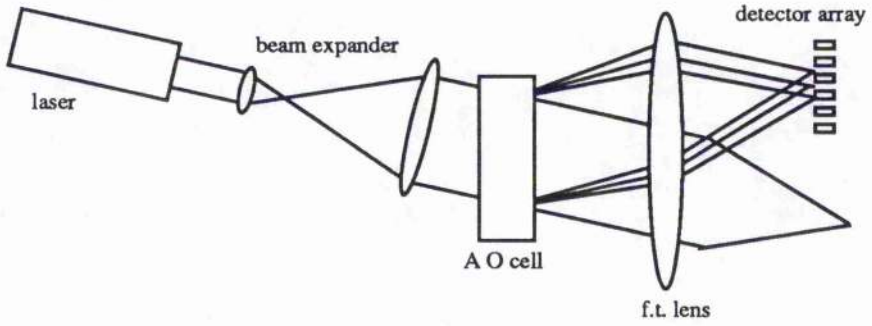

Figure 1.1

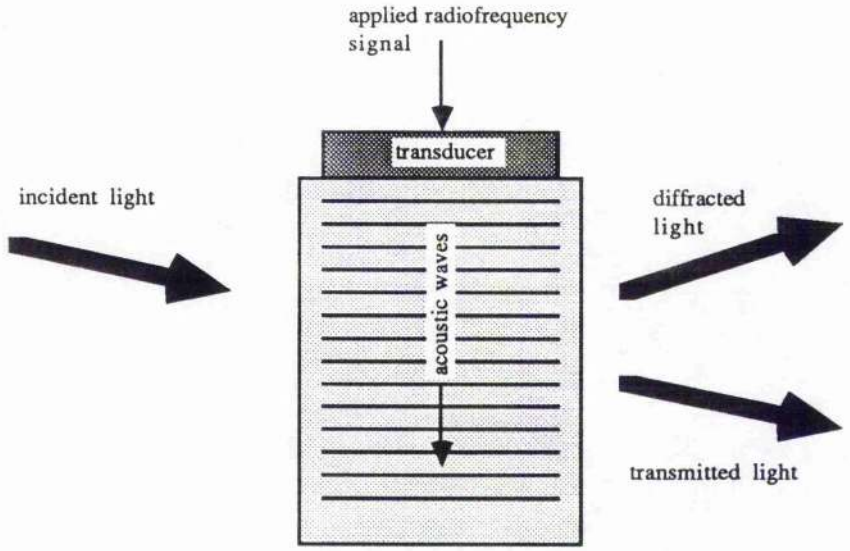

Figure 1.2

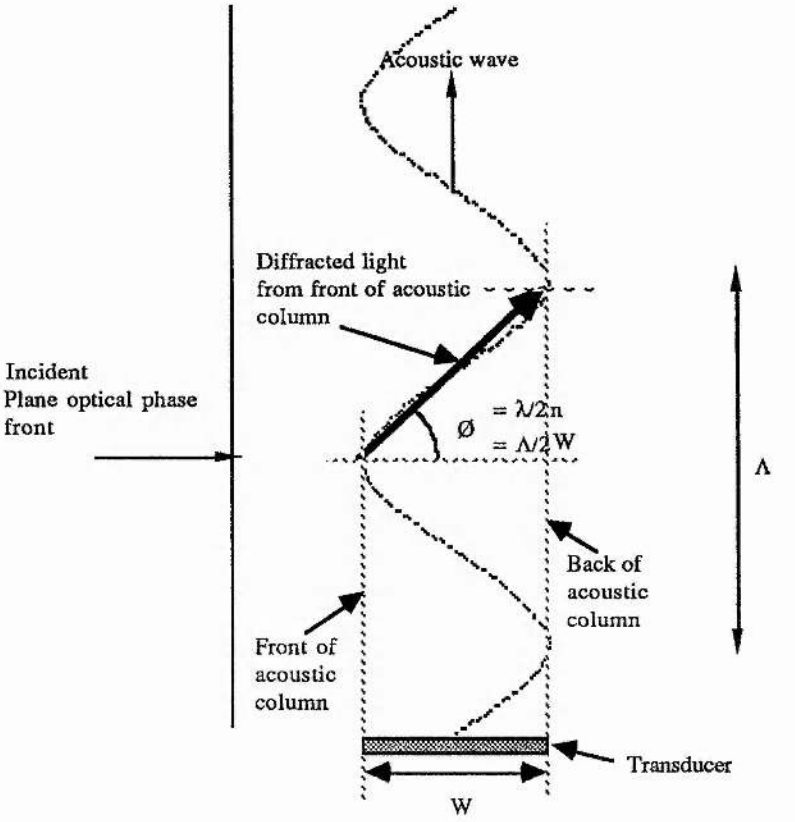

Figure 1.3

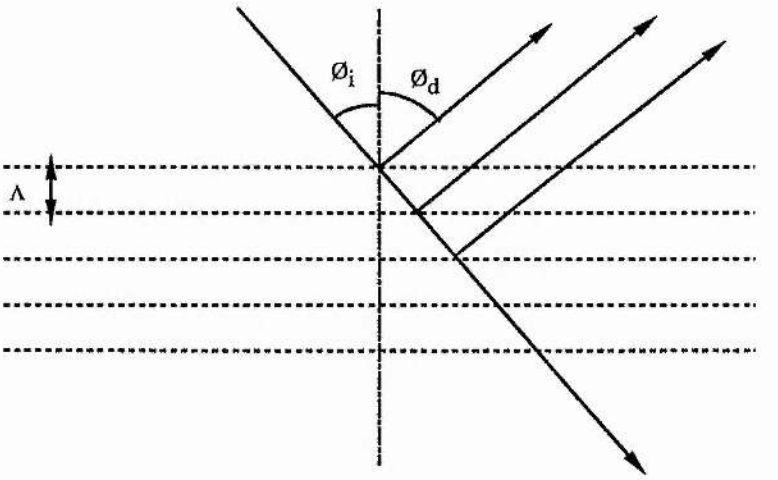

Figure 1.4

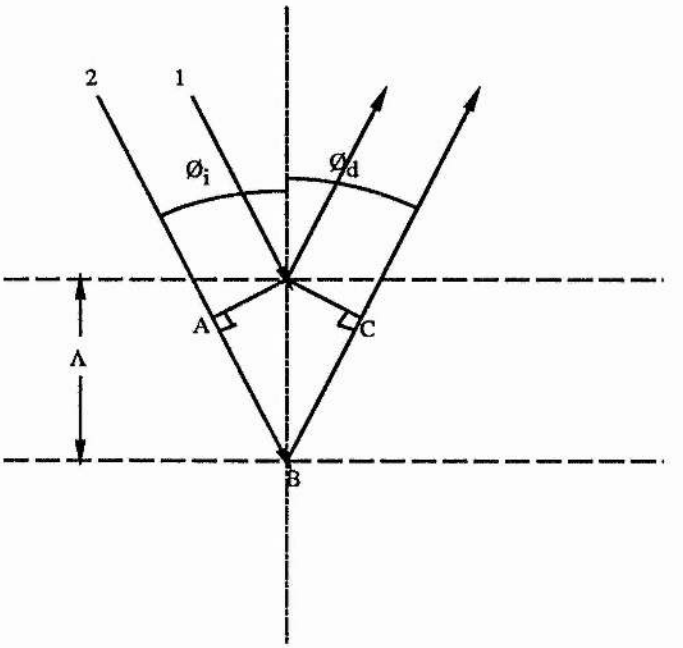

Figure 1.5

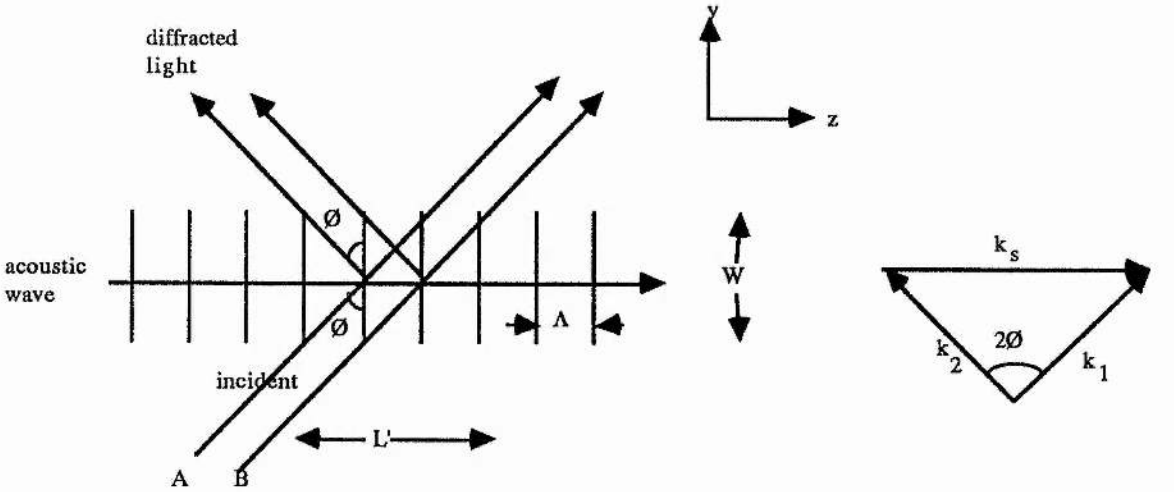

Figure 1.6

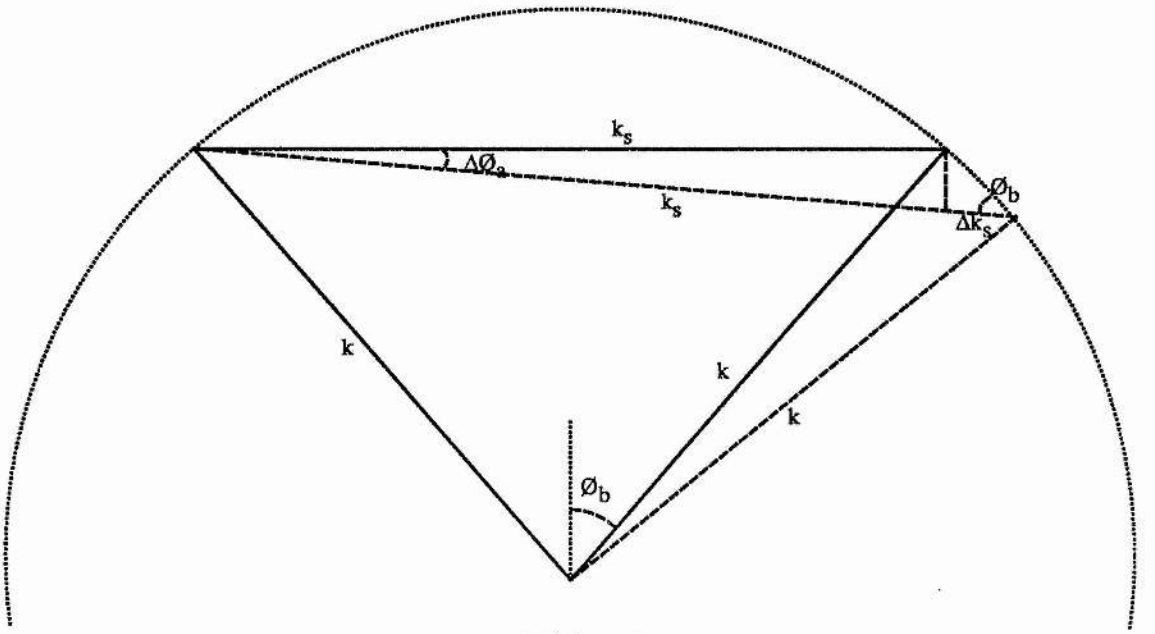

$$\emptyset_b = \frac{\Delta\emptyset_a k_s}{\Delta k_s} = \frac{k_s}{2k}$$

Figure 1.7

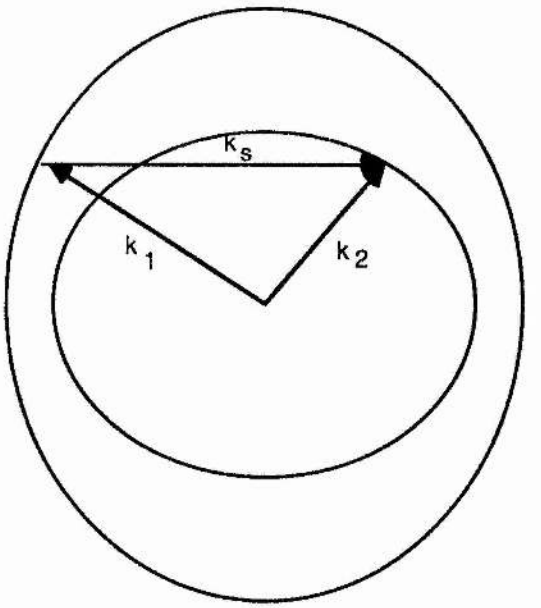

Figure 1.8

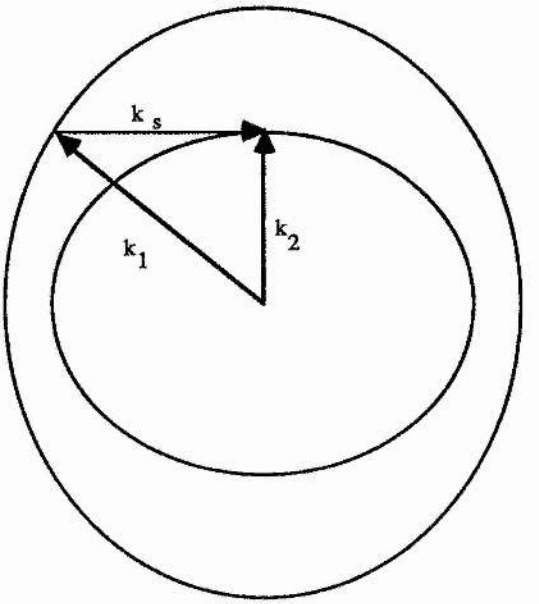

Figure 1.9

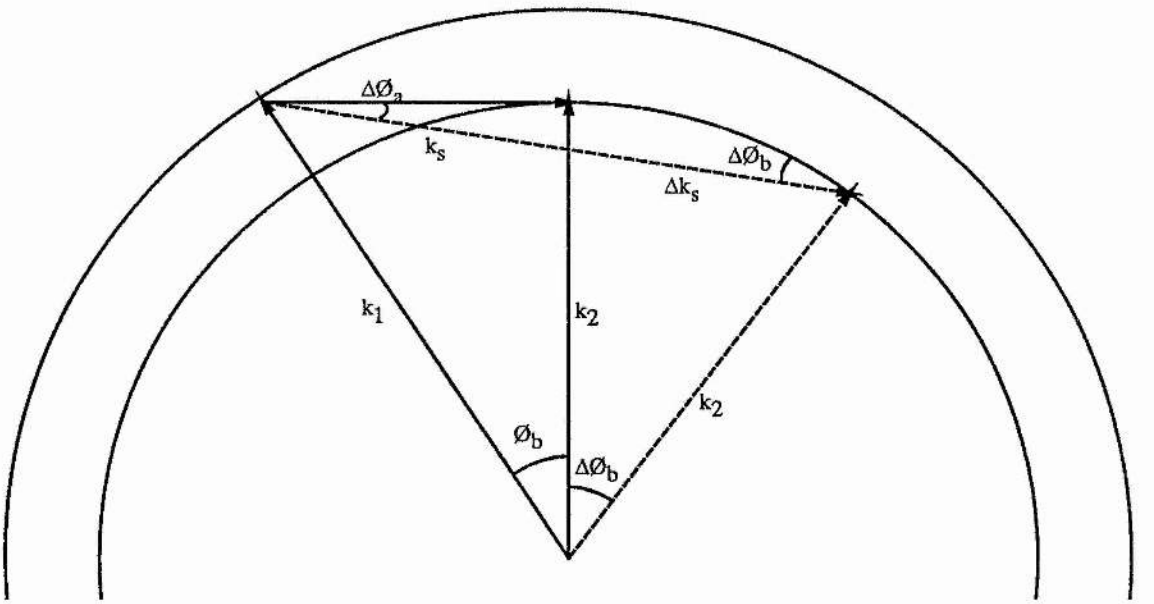

$$\Delta\varnothing_a = k_2 (1-\cos\Delta\varnothing_b) \qquad \tan\Delta\varnothing_b = \frac{\Delta k_s}{k_2}$$

Figure 1.10

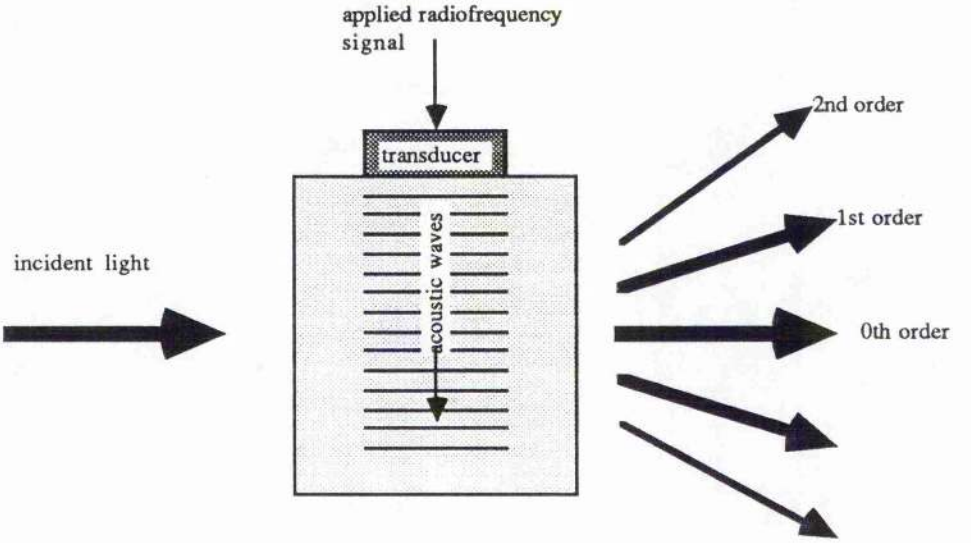
applied radiofrequency
signal
transducer
acoustic waves
incident light
2nd order
1st order
0th order

Figure 1.11

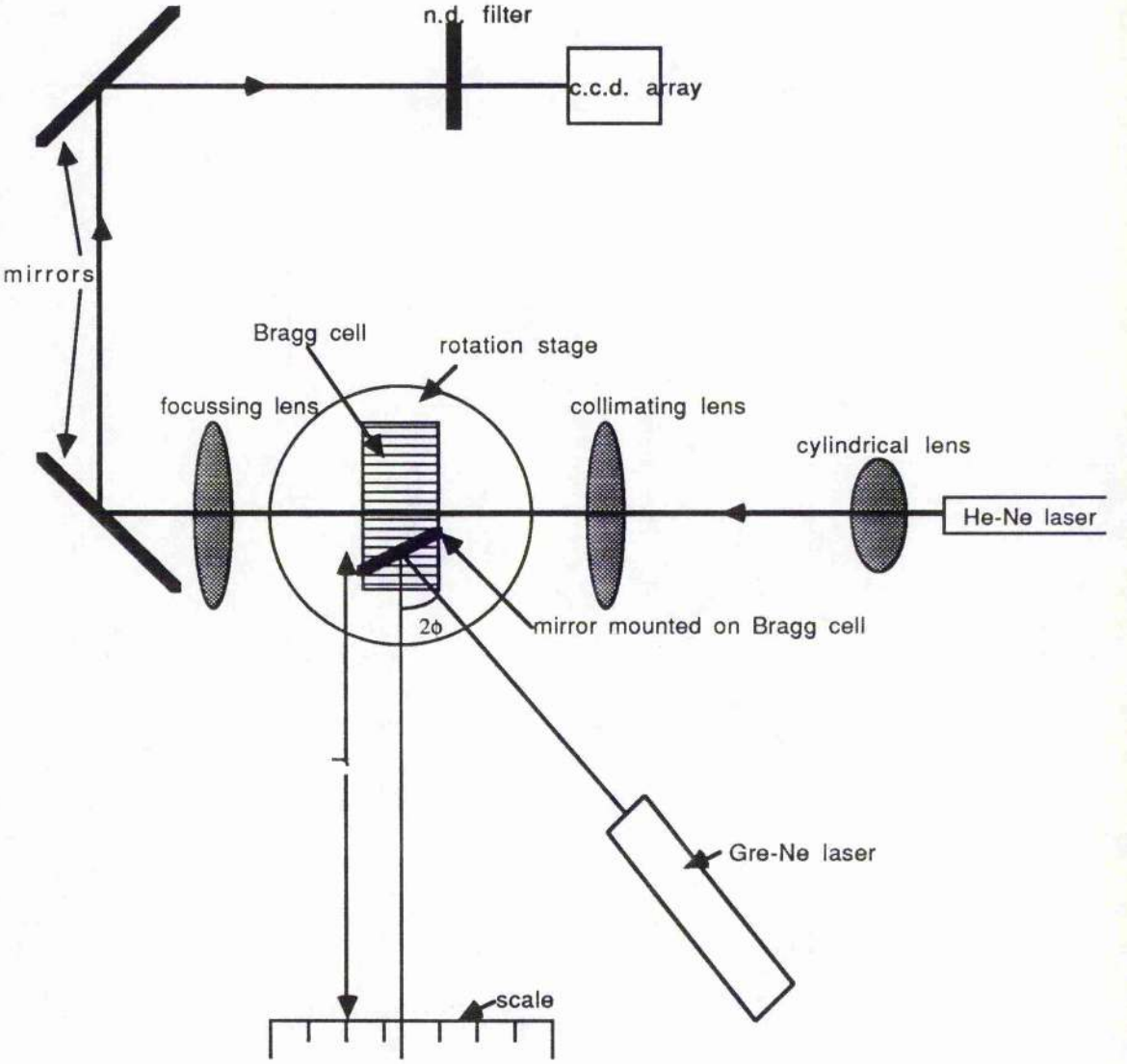
n.d. filter
c.c.d. array
mirrors
Bragg cell
rotation stage
focussing lens
collimating lens
cylindrical lens
He-Ne laser
2ϕ
mirror mounted on Bragg cell
Gre-Ne laser
scale

Figure 1.12

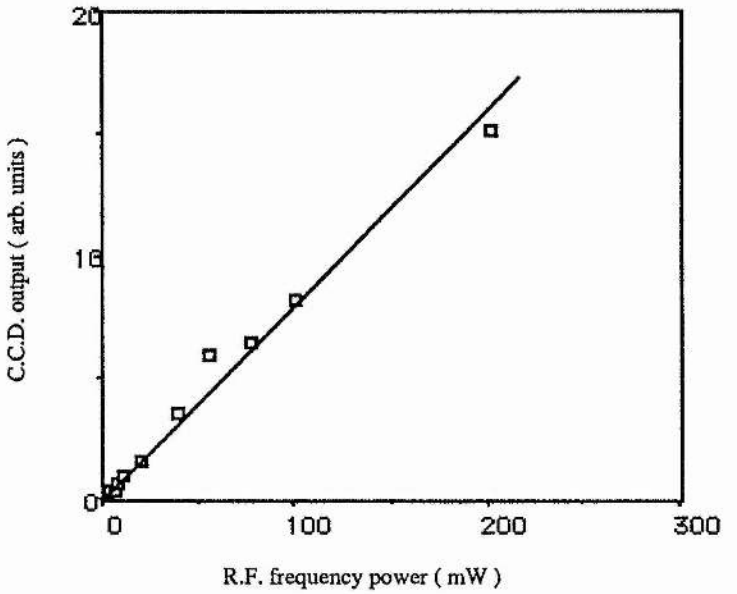

Figure 1.13

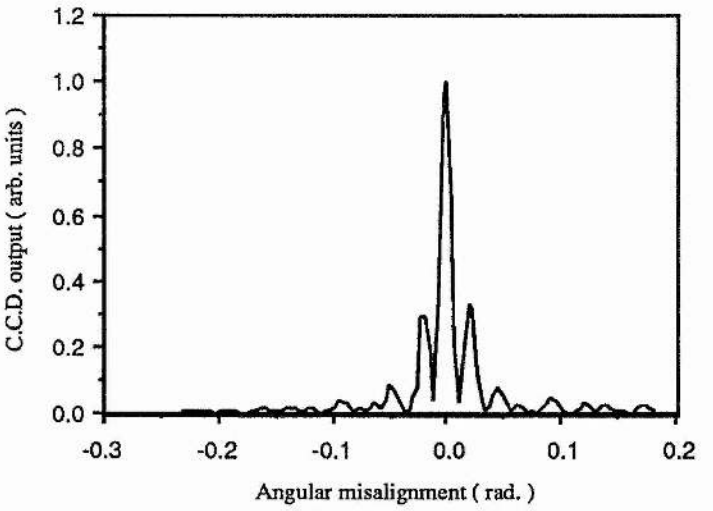

Figure 1.14

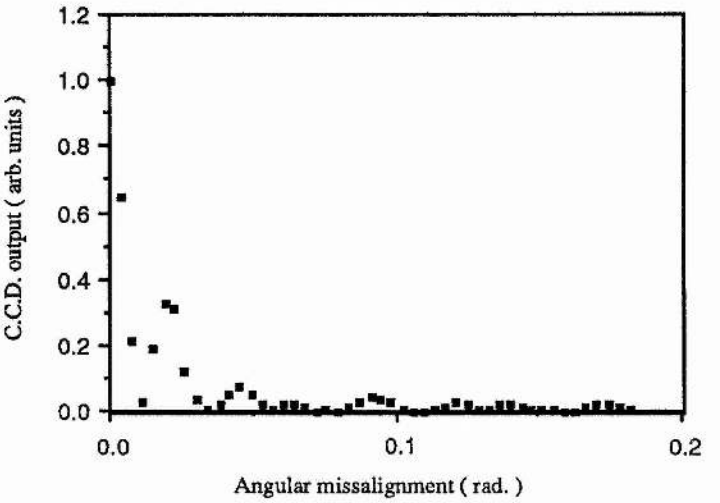

Figure 1.15

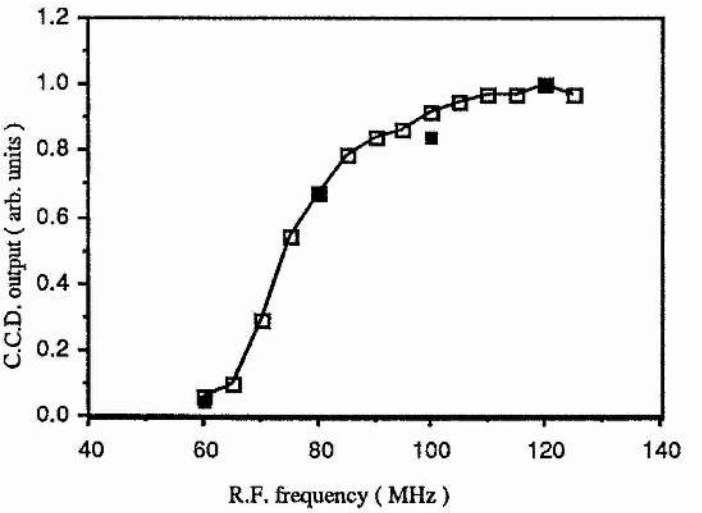

Figure 1.16

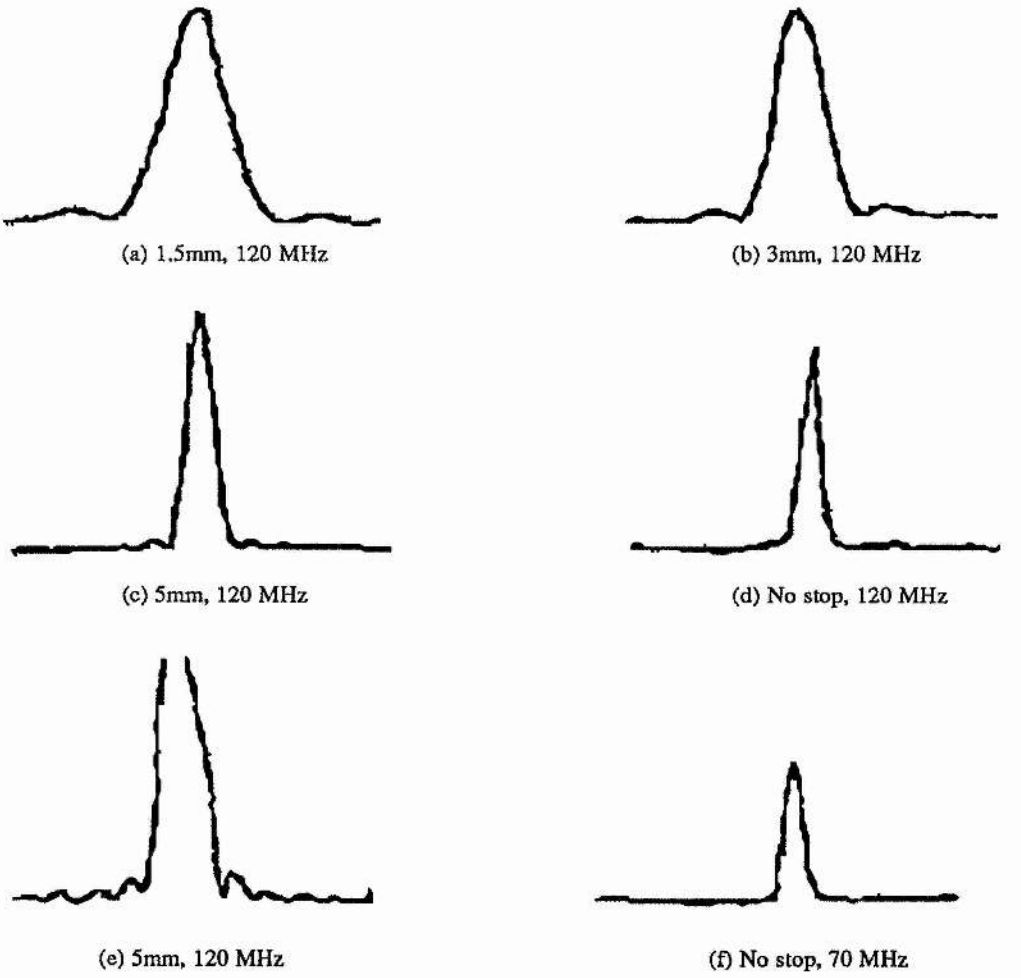
(a) 1.5mm, 120 MHz
(b) 3mm, 120 MHz
(c) 5mm, 120 MHz
(d) No stop, 120 MHz
(e) 5mm, 120 MHz
(f) No stop, 70 MHz
20um

Figure 1.17

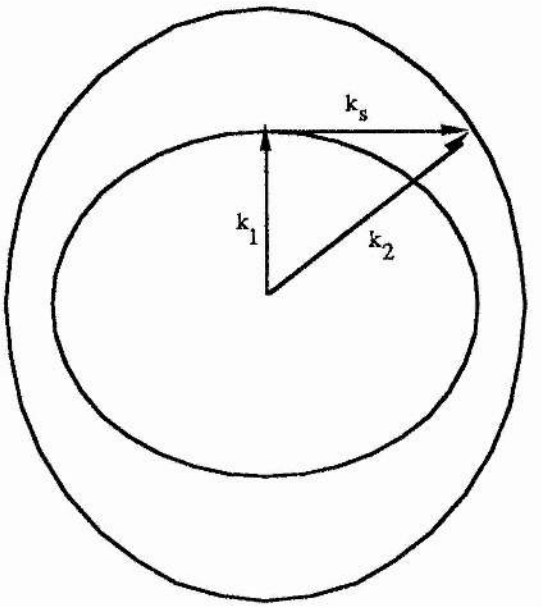

Figure 1.18

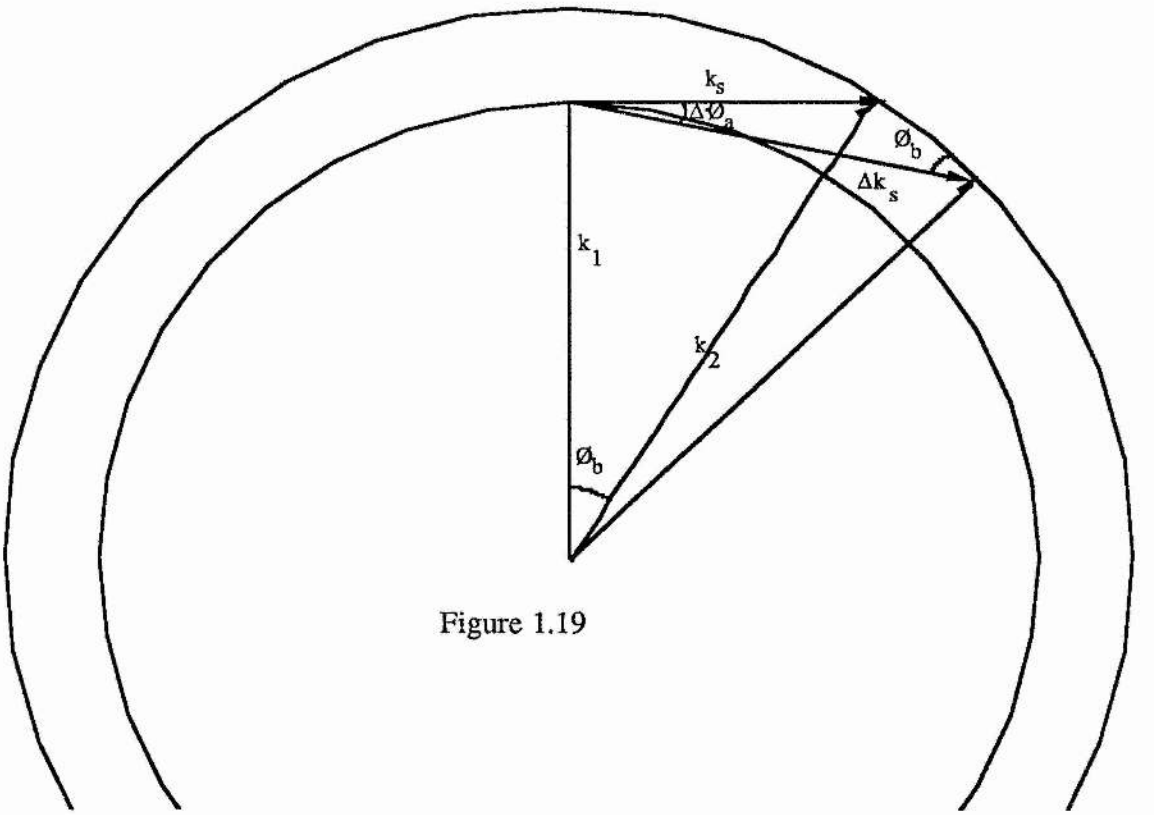

Figure 1.19

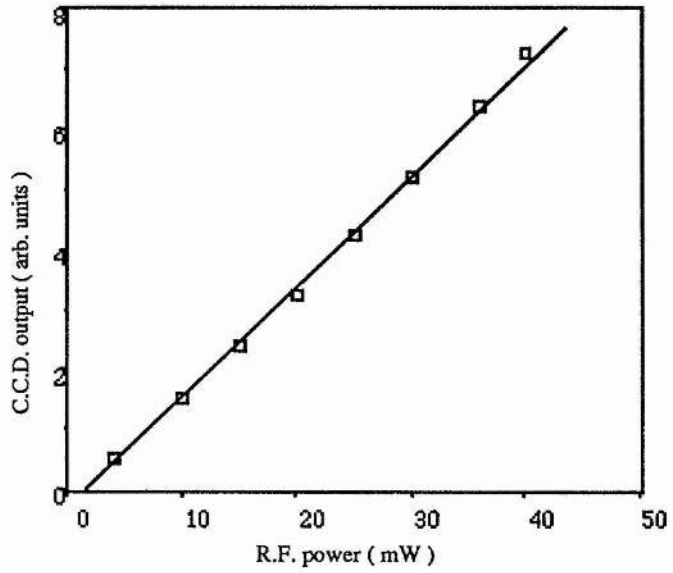

Figure 1.20

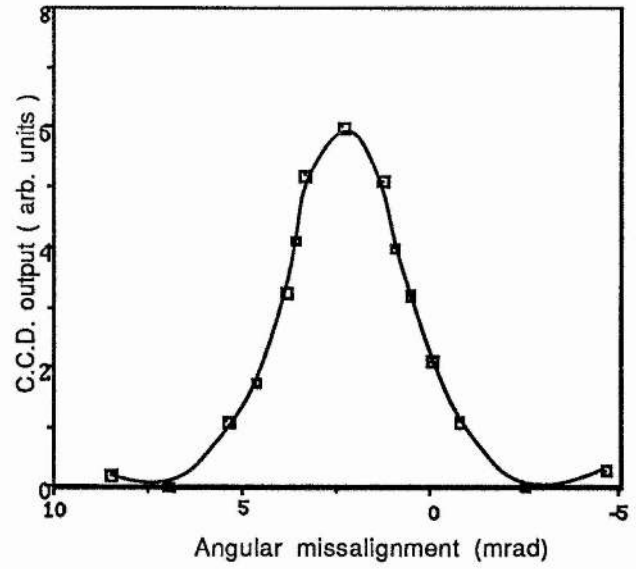

Figure 1.21

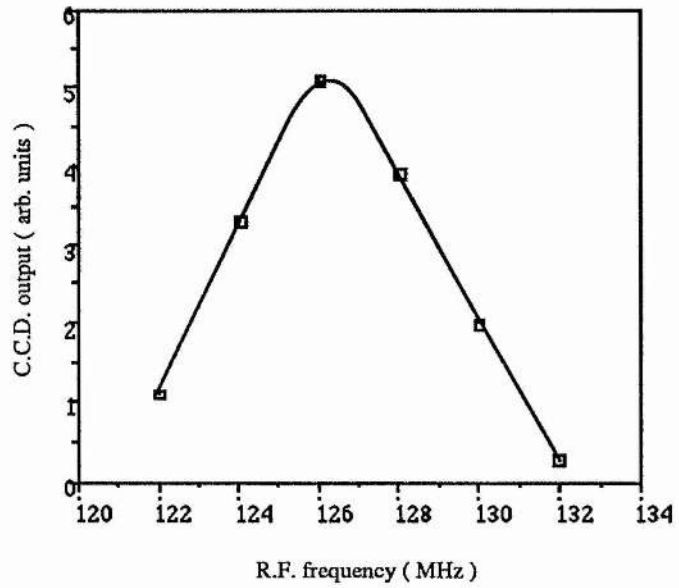

Figure 1.22

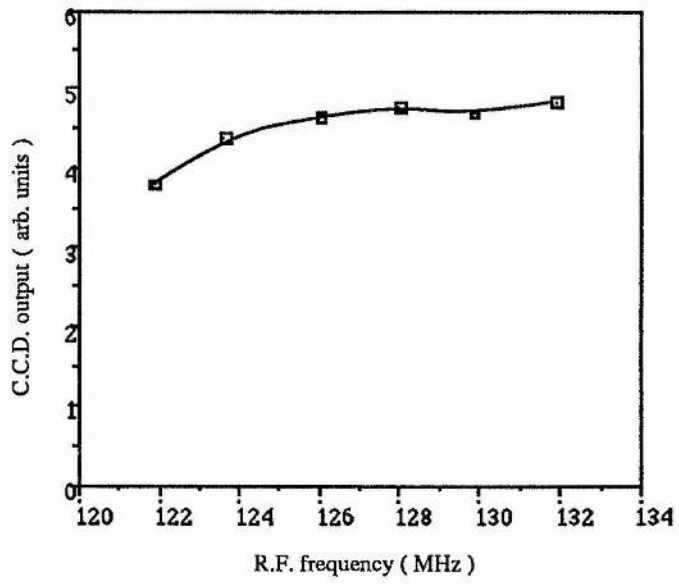

Figure 1.23

1.5 REFERENCES

[1.1] "Antennas and receivers for EW systems"

R. Kyle

Conf. proc. Miltary Electronics Defence Expo, 408-13, 1978

[1.2] "Acoustooptic spectrum analyser for laser radar applications"

C. Williams, M. Jennings

Proc. SPIE Int. Soc. Opt. Eng. (USA) vol. 663, 159-65, 1986

[1.3] "E.W. receivers using acoustooptic and ultrasonic components"

J. Tsui, W.Brumfield

IEEE Ultrasonics Symposium Proc. vol. 1, 345-50, 1984

[1.4] "Acoustooptic techniques for real time SAR imaging"

M.Honey, D.Psaltis

Proc. SPIE Int. Soc. Opt. Eng. (USA) vol. 545, 108-17, 1985

[1.5] "Channelised integrating ESM receivers using a Bragg-cell"

R. Bowman

IEE Proc. F (GB) vol.132, no.4 , 275-9 July 85

[1.6] "Optical processing of pulsed Doppler and FM stepped radar signals"

D. Casasent, F. Casasayas

AO Vol. 14, No. 6, 1364, Jun 75

[1.7] "Optical Processing of Radar Signals with Fresnel Diffraction Masks"

H. Stark, F. Tutteur, M. Sayar

AO Vol. 10, No. 12,2728, Dec 71

[1.8] "Acoustooptc spectrum analysis of radar signals using an integrating photodetector array"

J. Lee

A.O. vol. 20, No. 4 , 595-600, 15 Feb 81

[1.9] "Acoustooptic interaction for most effective deflection of unguided light via acoustic surface waves"

A. Alippi, A.Palma, L.Palmieri, G.Socino

AO Vol. 15, No. 10, 2400-2404, Oct 76

[1.10] "Surface wave acoustooptic signal processors"

N. Berg, J.Lee, B.Udelson

Optical Engineering Vol.19, No.3, 359-369, May 80

[1.11] "Integrated optics: a tutorial review"

P. Laybourn, J. Lamb

The radio and electronic engineer, Vol. 51, No. 717, 397-413, Jul 81

[1.12] "Thin film travelling wave light modulator

A. Attard

AO Vol. 21, No. 13 2348-2355, Jul 82

[1.13] "Time integrating acoustooptic correlator"

R. Sprague, C. Koliopoulos

A.O. Vol. 15, No. 1, 89-92, Jan 76

[1.14] "Multi channel optical correlator for radar signal processing"

D. Casasent, E. Klimas

A.O. vol. 17, No. 13, 2058-2062, July 78

[1.15] "Acoustooptic implementation of real and near real time signal processing"

N.Beag, J.Lee, W,Cassaday

Optical Engineering Vol.18, No. 4, 420-428, Jul 79

[1.16] "Squared signal correlation and a possible acoustoptic implementation"

A. Goutzoulis and V. Vijaya Kumar

AO Vol. 23, No. 6, 798-802, Mar 84

[1.17] "Optical correlation of Fresnel images"

G. Meltz, W.Maloney

AO Vol. 7, No. 10, 2091-2099, Oct. 68

[1.18] "Optical image correlation using acoustooptic and charge coupled devices"

D.Psaltis

AO Vol. 21, No. 3, 491-495, Feb. 82

[1.19] "Fresnel diffraction by a semitransparent straight edge object with acoustically coherence controllable illumination"

Y.Ohtsutka, Y.Mei Cheah

AO Vol. 23, No. 2, 300-306, Jan 84

[1.20] "Frequency multiplexed and pipelined iterative optical systolic array processors"

D. Cassasent, J.Jackson,C.Neuman

AO Vol. 22, No. 1, 115-124, Jan 83

[1.21] "Correlator based on an integrated optical spatial light modulator"

C.Verber, R.Kenan,J.Busch

AO Vol. 20, No. 9, 1626-1629, May 81

[1.22] "Hybrid time and space integrating processors for spread spectrum applications"

G.Silbershatz, D.Cassasent

AO Vol. 22, No. 14, 2095-2103, Jul 83

[1.23] "Adaptive optical processor"

A.VanderLugt

AO Vol. 21, No. 22, 4005-4011, Nov. 82

[1.24] "Systolic time integrating acoustooptic binary processor"

A.Goutzoulis

AO Vol.23, No. 22, 4095-4099, Nov 84

[1.25] "Incoherent spatial filtering with a scanning heterodyne system"

G.Inbetouw and Ting-Chung Poon

AO Vol. 23, No. 224, 4571-4574, Dec 84

[1.26] "Characteristics of acoustooptic devices for signal processors"

I. Chang, D. Hecht

Optical Eng. Vol. 21, No. 1, 076-081 Jan 82

[1.27] "Acoustooptic signal processing"

Berg, Lee

Marcel Dekker inc ISBN 0-8247-1667-12

[1.28] "Acoustooptics"

J. Sapriel

John Wiley and sons ISBN 0-471-99700-5

[1.29] "Ultrasonic signal processing"

A. Alipi

World Scientific ISBN 9971-50-864-8

[1.30] "Interaction of light and microwave sound"

C.F. Quate, C.D. Wilkinson and D.K. Winslow

AO vol. 53 No. 10, Oct 65.

[1.31] "Electromagnetic propagation in periodic stratified media. I. General theory"

P. Yeh, A. Yariv and C. Hong

JOMA Vol. 67, No. 4, April 77

[1.32] "Optical spectrum analysis of large space bandwidth signals"

C. Thomas

AO Vol. 5, No. 11, 1782-1790, Nov 66

[1.33] "Optical considerations for an acoustooptic deflector"

L.Dickson

AO Vol.11, No. 10, 2196-2203, Oct 72

[1.34] "Performance and optical characterisation of efficient wideband gallium phosphide Bragg cells"

R.Bonney, O.Zehl, J.Rosenbaum, M.Price

AO Vol. 23, No. 16, 2778-2783, Aug 84

[1.35] "Matrix formalism for the analysis of acoustooptic beam steering"

R.Pieper, A.Korpel

AO Vol. 22, no. 24, 4073-4081, Dec 83

[1.36] "Bragg-cell diffraction patterns"

A. Vander Lugt

AO Vol. 21, No.6, 1092-1100, 15 Mar 82

[1.37] "Simple acoustic modulators"

J.Hamer, D.Channin

AO Vol. 11, No. 10, 2203- ,Oct 72

2

Coherent Detection in an Acoustooptic Spectrum Analyser using Optical Fibres

2.1 INTRODUCTION - COHERENT DETECTION

In order to increase the dynamic range of an optical detector, the optical signal to be measured may be heterodyned with a second, reference, signal at a slightly different frequency before falling on to the detector (see figure 2.1). The resultant signal from a power (square law) detector will contain a component at the difference frequency. We have for the power at the detector

$$P = (E_1 + E_2)(E_1 + E_2)^* \qquad 2.1$$

where E_1, E_2 are the electric fields of the signal and reference beams, given by

$$E_1 = A_1 \exp[i(\omega_0 t + \phi_1)] \qquad 2.2$$

and

$$E_2 = A_2 \exp[i(\omega_0 t + \omega_{RF} t + \phi_2)] \qquad 2.3$$

and where

A_1, A_2 = amplitude of electric fields.

ω_0, $\omega_0 + \omega_{RF}$ = frequency of signal and reference fields.

ϕ_1, ϕ_2 = phase delay for signal and reference beams.

Then we have for the light power falling on the detector

$$P = \{ A_1 \exp[i(\omega_0 t + \phi_1)] + A_2 \exp[i(\omega_0 t + \omega_{RF} t + \phi_2)] \} \{ A_1 \exp[-i(\omega_0 t + \phi_1)] + A_2 \exp[-i(\omega_0 t + \omega_{RF} t + \phi_2)] \} \quad 2.4$$

Which we write as

$$P = A_1^2 + A_2^2 + 2A_1 A_2 \cos(\omega_{RF} t + \phi_2 - \phi_1) \quad 2.5$$

The first two terms are the normal "incoherent" terms, proportional to the square of the incident E-fields. The third term is a component at the difference frequency whose magnitude is proportional to the *amplitude* of the signal E-field.

This has important consequences for pre-detector signal processing in that it allows the dynamic range of a system to be greatly improved. Consider a system using (square law) detectors with a dynamic range of DN dB. We have

$$DN = 10 \log_{10}\left(\frac{P_{max}}{P_{min}}\right) \quad 2.6$$

where P_{max} and P_{min} are the maximum and minimum powers measurable by the detectors.

For a complete system, the dynamic range is defined in terms of maximum and minimum input signal powers, S_{max} and S_{min}, that may be measured.

We have

$$D_S = 10 \log_{10} \left(\frac{S_{max}}{S_{min}} \right) \qquad 2.7$$

In a system using non-coherent detection, the signal power, S, is proportional to the light power, P, arriving at the detectors ($P \alpha S$). If there is enough light to saturate the detectors at large signal powers then we see from 2.6 and 2.7 that the system dynamic range will be equal to the detector dynamic range,

$$D_S = DN .$$

For a system using coherent detection the signal is proportional to the amplitude of the incident light, $P \alpha S^2$, and equation 2.7 for the system dynamic range becomes

$$D_s = 10 \log_{10} \left(\frac{P^2_{max}}{P^2_{min}} \right) \qquad 2.8$$

or

$$D_S = 20 \log_{10} \left(\frac{P_{max}}{P_{min}} \right) \qquad 2.9$$

If there is sufficient light reaching the detectors to saturate them at large signal powers then the system dynamic range becomes (from 2.6 and 2.9),

$$D_S = 2DN .$$

We see in the case where the detectors saturate at large signal powers then the system dynamic range is doubled (on a logarithmic scale) by using coherent detection. For example in a conventional, incoherent, system using detectors with 30dB dynamic range, the maximum achievable system dynamic range is 30dB. The coherent system could have a 60dB dynamic range - an improvement by a factor of one thousand.

We have assumed that the ratios of the minimum to maximum detected signals are the same for the coherent and power detector systems and that there is sufficient light to saturate the detectors at S_{max}. In practice this is not always the case and we must look at particular systems to evaluate the improvement in dynamic range brought about by using coherent detection.

2.2 DYNAMIC RANGE IN SPECTRUM ANALYSER SYSTEMS USING COHERENT DETECTION

We shall now look at the case where the system using coherent detection does not have enough light to saturate the detectors (it is found that in practice this is usually the case). In this situation the dynamic range is not necessarily doubled by incorporating coherent detection.

2.2.1 Free space reference beam

In order to improve the dynamic range of a signal processor using a Bragg-cell as a spectrum analyser, coherent detection may be used by combining un-diffracted light from the laser source with the diffracted light which has passed through the Bragg-cell [2.1]. This is shown in figure 2.2. The light passing through the Bragg-cell is frequency shifted by the applied radiofrequency input to the Bragg-cell. The two beams arriving at

the detector therefore differ in frequency by the applied radiofrequency. There will be a component in the output from the detector at the radiofrequency, proportional to the amplitude of the field from the diffracted beam.

From chapter 1 we have, for the diffraction efficiency of a Bragg-cell

$$\frac{P_2}{P_1} = \frac{k_1^2}{8}\left[\frac{\varepsilon}{\varepsilon_0} p_{23}\right]^2 \frac{W}{H}\frac{P_T}{v_s c_{33}} \quad . \qquad 1.31$$

We write this as

$$P_2 = \eta_B P_T P_1 \, . \qquad 2.10$$

The interferometric spectrum analyser is shown in figure 2.3. The signal and reference arm transmittances are η_s and η_r, taking into account all losses, and the fraction of light transmitted to the reference arm is α. Then we have, from equation 2.5, for the power reaching the detectors

$$\frac{P_d}{P_0} = \alpha\eta_r + (1-\alpha)\eta_s + 2\left[\alpha\eta_r(1-\alpha)\eta_s\right]^{1/2}\cos(\Delta\omega_{RF}t + \Delta\phi) \, , \qquad 2.11$$

where $\Delta\omega_{RF}$ is the difference in frequency between signal and reference beams, $\Delta\phi$ is the phase difference and P_0 is the laser power. The signal strength is given by

$$\langle i(t)^2\rangle R = R P_0^2 \eta_d^2 \left[\alpha\eta_r(1-\alpha)\eta_s\right], \qquad 2.12$$

where i(t) is the time varying component of the photocurrent, R is the detector load resistance and η_d is the detector efficiency.

The output current from the photodetectors may be written in the form

$$i = \eta_d P_d + i_d \qquad 2.13$$

where i_d is the dark current. We have assumed the detectors do not saturate for the light power levels involved.

The signal-to-noise ratio is then given by [2.2]

$$SNR = \frac{R< i^2_{signal} >}{R< i^2_{shot} > + \text{Thermal noise} + R<\text{Dark current}^2>},$$

where i_{shot} is the shot noise, $i_{shot} = \sqrt{2eiB}$, and the thermal noise is $4\kappa T_s B$, B is the detector bandwidth, κ is the Boltzmann constant, e is the electron charge, i is the photocurrent and T_s the equivalent system temperature. Then from 2.12 we obtain

$$SNR = \frac{RP_0^2\eta_d^2\left[\alpha\eta_r(1-\alpha)\eta_s\right]\cos^2(\Delta\phi)}{2eBR\left\{P_0\eta_d\{\alpha\eta_r+(1-\alpha)\eta_s\} + i_d\right\} + 4\kappa T_s B}. \qquad 2.14$$

Where we have assumed the d.c. dark current noise has been filtered-off.

In order to calculate the dynamic range we need to evaluate the maximum and minimum detectable signals. We will define the minimum detectable signal as that which produces

a signal-to-noise ratio of unity when the system integrates the signal for a time 1/B. Equation 2.14 gives the minimum detectable signal arm transmittance, $\eta_{s_{min}}$.

We have

$$\eta_{s_{min}} = \frac{2eBR\left\{P_0\eta_d\alpha\eta_r + i_d\right\} + 4\kappa T_s B}{RP_0^2\eta_d^2\left[\alpha\eta_r(1-\alpha)\right] - 2eBRP_0\eta_d(1-\alpha)} \qquad 2.15$$

and hence we obtain the minimum detectable signal power

$$P_{T_{min}} = \frac{2eBR\left\{P_0\eta_d\alpha\eta_r + i_d\right\} + 4\kappa T_s B}{\left\{RP_0^2\eta_d^2\left[\alpha\eta_r(1-\alpha)\right] - 2eBRP_0\eta_d(1-\alpha)\right\}\eta_B\eta_L} \qquad 2.16$$

where η_L is the transmittance in the signal arm due to parasitic losses only.

If dark current and thermal noise are the dominant sources of noise then equation 2.16 becomes

$$P_{T_{min}} = \frac{2eBRi_d + 4\kappa T_s B}{RP_0^2\eta_d^2\alpha\eta_r(1-\alpha)\eta_B\eta_L} \qquad 2.16a$$

2.2.1.1 Effect of intermodulation

If there is sufficient light to saturate the detectors at high signal levels then the maximum detectable signal strength will be governed by detector saturation. The dynamic range will be detector limited as described in section 2.1.

If detector saturation does not occur then the maximum signal will be limited by third-order two-tone intermodulation. This effect occurs when two or more signals (a polytone signal) are present and produces spurious diffracted beams.

Consider the case where we have two signals present at frequencies f_1 and f_2. The light may first be diffracted by f_1. This diffracted beam may then be diffracted back in to the direction of the incident beam by f_2. This corresponds to a frequency $f_1 - f_2$. This doubly diffracted beam is not usually in the frequency region of interest, it may however be diffracted again by f_1 giving a beam of light corresponding to a frequency $2f_1 - f_2$. This is the third-order two-tone intermodulation. It usually *is* in the region of interest and is of magnitude

$$P_{1-2} = P_0 \left(\frac{\eta_B}{3}\right)^3 P_{T_1}^2 P_{T_2} . \qquad 2.17$$

This assumes all of the multiple diffraction processes occur at the correct Bragg angle for diffraction and that each takes place over one third of the interaction length, W (from equation 1.31 we see that the diffraction efficiency is proportional to W). In a high "Q" cell the intermodulation term will be smaller due to Bragg angle mis-matches.

The relative intermodulation is given in dB by

$$Int_{1-2} = 10 \log_{10}\left[\frac{P_{1-2}}{P_1}\right] \qquad 2.18$$

where P_1 is the diffraction due to f_1 alone.

From 2.17 and 2.18, we have

$$Int_{1-2} = 10 \log_{10}\left[\frac{\eta_B^2 P_{T_1} P_{T_2}}{27}\right] \qquad 2.19$$

This is the level in dB of the spurious intermodulation below the real signal. For example, if we have the diffraction efficiency at P_{max} limited to less than 1 %, equation 2.19 gives the spurious intermodulation at 54 dB below the true signal level.

The monotone dynamic range increases with increasing maximum diffraction power,

$$D = 10 \log_{10}\left[\frac{P_{T_{max}}}{P_{T_{min}}}\right],$$

however the polytone intermodulation increases with increasing maximum diffraction efficiency.

We must choose the maximum signal strength to give the largest intermodulation-free polytone dynamic range. This will occur when the monotone dynamic range at maximum signal power is equal to the intermodulation level at that power. i.e. when we have

$$D_S = - Int_{1-2} \text{ at } P_{T_{max}} . \qquad 2.20$$

From equations 2.6, 2.19 and 2.20 we obtain

$$10 \log_{10}\left[\frac{P_{T_{max}}}{P_{T_{min}}}\right] = -10 \log_{10}\left[\frac{\eta_B^2 P_{T_{max}}^2}{27}\right], \qquad 2.21$$

and hence the maximum signal strength which gives the largest polytone dynamic range is given by,

$$P_{T_{max}} = \left[\frac{27\, P_{T_{min}}}{\eta_B^2}\right]^{1/3}. \qquad 2.22$$

The polytone dynamic range, D_{poly}, is then given by equations 2.6 and 2.22,

$$D_{poly} = 10 \log_{10}\left[\frac{27}{\eta_B^2 P_{T_{min}}^2}\right]^{1/3} \qquad 2.23$$

Equation 2.16 gives $P_{T_{min}}$ and equation 1.31 and 2.10 give η_B. Given the detector dark current and the other values in equation 2.16 we may predict the system polytone dynamic range.

2.2.2 Power spectrum analyser

In the conventional power spectrum analyser equation 2.11 becomes

$$\frac{P_d}{P_0} = \eta_s \qquad 2.24$$

and equation 2.14 becomes

$$SNR = \frac{RP_0^2\eta_s^2\eta_d^2}{2eBR\left\{i_d + P_0\eta_d\eta_s\right\} + 4\kappa T_s B} \qquad 2.25$$

and we have

$$\eta_{s_{min}} = \frac{-2eBRP_0\eta_d + \sqrt{\left[2eBRP_0\eta_d\right]^2 + 4RP_0^2\eta_d^2\{4\kappa T_s B + 2eBRi_d\}}}{2RP_0^2\eta_d^2} \qquad 2.26$$

and

$$P_{T_{min}} = \frac{-2eBRP_0\eta_d + \sqrt{\left[2eBRP_0\eta_d\right]^2 + 4RP_0^2\eta_d^2\{4\kappa T_s B + 2eBRi_d\}}}{\left[2RP_0^2\eta_d^2\right]\eta_B\eta_L} \qquad 2.27$$

The maximum signal strength will be limited by third-order two-tone intermodulation and we obtain the polytone dynamic range as described in section 2.2.1.1.

$$D_{poly} = 10\log_{10}\left[\frac{27}{\eta_B^2 P_{T_{min}}^2}\right]^{1/3} \qquad 2.23$$

2.2.2.1 Experimental results for power acoustooptic spectrum analyser

The power acoustooptic spectrum analyser configuration was described in chapter 1, section 1.4.2. The maximum signal strength is limited by saturation of the the ccd

detector array, and the minimum by noise in the detectors. The monotone dynamic range is therefore equal to the detector dynamic range.

The measured monotone dynamic range is 24 dB.

Third-order two-tone intermodulation is measured by simultaneously applying radiofrequency signals at 131MHz and 142MHz , 130mW in each signal. The spurious signal levels are initially below the noise level of the ccd array. However by removing neutral density filters placed in front of the array, the spurious signals caused by intermodulation are raised above the noise floor. This causes the true signals to saturate the detector elements at their respective positions. By noting the density of the filters removed and the levels of real and spurious signals, the relative intermodulation level is measured.

With the Bragg-cell aligned for tangential phase matching (broad instantaneous bandwidth) the intermodultion is measured at 30dB below the "real" signal level.

With the Bragg-cell aligned for "normal" phase matching (narrow instantaneous bandwidth) the intermodulation level is below the noise level of the detectors.

The intermodulation level predicted by equation 2.19 is

$$Int_{1\text{-}2} = 10 \log_{10}\left[\frac{\eta_B^2 P_{T_1} P_{T_2}}{27}\right]$$

For the tangential phase matching the diffraction efficiency per watt, η_B, is known to be approximately one hundred percent per Watt for both frequencies and we obtain the relative intermodulation level,

$Int_{1-2} = -32$ dB .

This is in good agreement with the observed -30dB intermodulation level.

Where "normal" phase matching is used, the phase matching condition cannot be simultaneously satisfied for the two frequencies. The diffraction efficiency per watt, η_B, is not one hundred percent per watt for both frequencies. The intermodulation would therefore be expected to be reduced from the theoretical value in equation 2.19.

Intermodulation of the input signal caused by the amplifiers was at least 40dB below signal level and is therefore assumed negligible. (This was measured by applying the radiofrequency signals from the amplifier directly to an electronic spectrum analyser).

2.2.3 Bragg-cell in reference arm

The coherent system described above has a free space reference arm. The frequency of the combined signal arriving at the detectors has the same frequency as the applied radiofrequency signal. The detector bandwidth must therefore be as large as the applied signal bandwidth.

From equation 2.16 we see that the minimum detectable signal increases with detector bandwidth. The dynamic range therefore decreases with increased detector bandwidth.

The system shown in figure 2.4 has a Bragg-cell placed in the reference arm with a broadband signal applied to it [2.3 - 2.4]. The cell in the reference arm has the same acoustic velocity and is placed with the same optical path distance to the Fourier transform (detector) plane as the cell in the signal arm. This means that similar displacements in the Fourier plane correspond to similar differences in radiofrequency for both cells. For any position in the Fourier plane there will be a radiofrequency difference for the Doppler shifted light diffracted from the two cells, which is independent of the position in the plane. The value of this difference depends on the angular offset, $\delta\emptyset$, provided by the mirrors and is given by

$$\delta F = \frac{2v_s}{\lambda}\delta\emptyset \qquad 2.28$$

(At each point there is also a small spread of frequencies equal to the resolution of the two cells.)

The detectors are only required to have a bandwidth given by δF. Since this may be much smaller than the signal bandwidth, a larger dynamic range is implied. However, less light will reach the detectors than in a conventional power spectrum analyser. This is because the reference arm will have a lower transmittance due to the (less than one hundred percent) diffraction efficiency of the extra cell in the reference arm. We may express this loss of light by writing

$$\eta_r = \eta_{L_{ref}}\eta_B{}^P T_{ref}, \qquad 2.29$$

where $\eta_B{}^P T_{ref}$ is the diffraction efficiency of the cell in the reference arm.

The decrease in η_r will tend to decrease the dynamic range by increasing the minimum detectable signal, $P_{T_{min}}$, as shown by equations 2.16 and 2.23, assuming the dark current and thermal noise are the dominant sources of noise. However, large reference signal powers,$P_{T_{ref}}$, and hence large diffraction efficiencies, $\eta_B P_{T_{ref}}$, may be used for the reference cell, minimising the loss of light (the spurious signals from two-tone third-order intermodulation will appear at the correct point in space in the Fourier plane and do not adversely effect the output). The gain in dynamic range brought about by using smaller bandwidth detectors may then outweigh the loss due to reduced reference light powers.

2.3 USE OF OPTICAL FIBRES

2.3.1 Introduction

In conventional acoustooptic spectrum analyser systems the detector size limits the frequency resolution attainable. For high resolution, small detectors must be used. These give poor dynamic range due to low efficiencies, η_d, and large dark currents, i_d, as shown in equation 2.16

The detectors are usually individually wired because sequentially scanned arrays cannot operate fast enough to cope with the short pulses used in many radar systems. If the detectors are small, then the wires leading to them will be close together and this leads to cross-talk between adjacent frequency channels.

The problems of low dynamic range and cross-talk due to small detectors can be avoided by using optical fibres. By placing a fibre array in the Fourier plane and then fanning the fibres out, large detectors may be used, plus large separations between adjacent wires,

without sacrificing resolution. This is shown in figure 2.5. Coupling of the reference and signal beams may then be achieved by guiding the reference beam in an optical fibre and then combining it with the signal beams, also in fibres, using fibreoptic couplers, as shown figure 2.6.

2.3.2 Experimental use of singlemode optical fibres in an interferometric spectrum analyser

To explore the feasibility of the use of optical fibres a single channel device was constructed as shown in figure 2.7.

The laser source is a "Uniphase" 20mW Helium Neon. The cable splitter is an Anzac DS409-4 50/50 power splitter and the power meter is a Hewlett Packard 438A. The Bragg-cell is a "Automates et Automatismes" A.A.DTX100., as described in section 1.4.2.

The fibre optic cable is single mode at 633nm, with a 125μm cladding, and the fibre coupler is an Aster SM 633 50/50 125c. The receiving photodiode circuit and following amplifiers are "home constructed" using the BPX 65 photodiode and OM335 hybrid amplifiers. These are described in the appendix 1. The spectrum analyser is a Hewlett Packard 855B . The signal-to-noise ratios are taken using a bandwidth, B, of 3 MHz, this being the largest available on the spectrum analyser.

2.3.2.1 Experimental results

The output from the spectrum analyser is shown schematically in figure 2.8, which shows the output with 120MHz input to the Bragg-cell, with the fibre picking up light from the first order diffraction spot.

The peak at 120 MHz is the required output. The peak at 409MHz is due to the laser running in two modes, separated by 409MHz. The peaks at 289MHz and 529Mhz are sidebands on the 409MHz, introduced by the 120Mhz signal. This can be demonstrated by blocking one of the arms - the 120, 289 and 529MHz signals are extinguished, leaving just the 409MHz, at a reduced level. This two mode operation of the laser has also been observed in visibility measurements.

Figure 2.9 shows the variation in signal-to-noise ratio with input radiofrequency power. These results were obtained using a 3.5 mm focal length coupling lens in the far field of the Bragg-cell.

Figure 2.10 shows the variation in signal-to-noise ratio as the focal length of the transform lens is varied, with 290mW radiofrequency power applied to the cell.

2.3.2.2 Analysis of results

Coherent, heterodyne, detection of the diffracted orders from a Bragg-cell have been observed using single-mode optical fibres to guide and combine the light in reference and signal arms.

The output power increases linearly with applied radiofrequency power, as predicted by equation 2.12.

The signal-to-noise ratio increases as $[1/f_l]^2$. This can be explained by considering the coupling efficiency in to the signal fibre.

Optimum (aligned and normal) coupling efficiency, η_c, is given by

$$\eta_c = \left[\frac{\phi_f}{\phi_s}\right]^2 \left[1-\left\{\frac{n-1}{n+1}\right\}^2\right], \qquad 2.30$$

for light spot diameters greater than the fibre core diameter and where the incident light has a divergence less than the acceptance angle of the fibre (~ 20 degrees).

The refractive index of the fibre is n, ϕ_f is fibre core diameter and ϕ_s is the light spot diameter incident on the fibre.

The diffraction limited spot size is given by

$$\phi_s = \frac{\lambda}{L} f_l \,. \qquad 2.31$$

Hence, we obtain the coupling efficiency

$$\eta_c = \left[\frac{\phi_f L}{\lambda f_l}\right]^2 \left[1-\left\{\frac{n-1}{n+1}\right\}^2\right]. \qquad 2.32$$

We see the coupling efficiency, η_c, and hence the signal-to-noise ratio increase as $[1/f_l]^2$.

The monotone dynamic range is not purely detector limited (there is not enough light to saturate the detectors). The received signal power is proportional to the applied

radiofrequency power and therefore the monotone dynamic range is equal to the maximum signal-to-noise ratio. This occurs at the maximum signal power obtainable from the amplifiers, which is 290mW.

Third-order two-tone intermodulation limits the usable polytone dynamic range as described in section 2.2.1. We have from equation 2.23 the polytone dynamic range

$$D_{poly} = 10 \log_{10}\left[\frac{27}{\eta_B^2 P_{T_{min}}^2}\right]^{1/3} \qquad 2.33$$

Knowledge of the signal-to-noise ratio at P_T, S/N_{P_T}, allows us to calculate $P_{T_{min}}$ and hence the dynamic range. Assuming the noise is predominatly due to dark current and thermal noise in the detector, we have approximately

$$S/N_{P_T} = 10 \log_{10}\left[\frac{P_T}{P_{T_{min}}}\right], \qquad 2.34$$

and therefore

$$P_{T_{min}} = P_T \exp - \left\{\frac{S/N_{P_T}}{10}\right\}. \qquad 2.35$$

Using equations 2.33 and 2.35 we obtain the polytone dynamic range

$$D_{poly} = \frac{2}{3} S/N_{P_T} + \frac{10}{3} \log_{10}\left\{\frac{27}{\eta_B^2 P_T^2}\right\} \qquad 2.36$$

We see from figure 2.11 that the signal-to-noise ratio at 290mW, $S/N_{0.29}$, is given approximately by

$$S/N_{0.29} = 10 \log_{10}\left(\frac{1300}{f_l^2}\right) \qquad 2.37$$

Using equation 2.36 we obtain the polytone dynamic range in terms of the focal length of the coulping lens

$$D_{poly} = 29.1 - 13.3 \log_{10}[\, f_l \,] \qquad 2.38$$

For optimum coupling the diffraction spot size is equal to the fibre core diameter. This occurs at f_l = 1cm, approximately, giving the optimum polytone dynamic range

$$D_{poly} = 55.7 \text{ dB}$$

In this experiment there is only one channel. In a real spectrum analyser with N channels, the reference arm must be split in to N fibres. If these reference channels are all created from one laser source the amount of light in each reference fibre will be reduced by a factor of 1/N. We may represent this in our model for dynamic range by reducing the reference arm transmittance by a factor of 1/N. We see from equation 2.16a that the minimum detectable signal, $P_{T_{min}}$, is inversely proportional to the reference arm transmittance, η_r, if dark current and thermal noise are the dominant sources of noise. The dynamic range will therefore be reduced by adding more channels. Equation 2.23 for the polytone dynamic range becomes

$$D_{poly} = 10 \log_{10}\left[\frac{27}{\eta_B^2 N^2 P_{T_{min\ 1}}^2}\right]^{1/3}, \qquad 2.23$$

where $P_{T_{min\ 1}}$ is the minimum detectable signal for a one channel system.

Equation 2.38 then becomes,

$$D_{poly\cdot} = 29.1 - 13.3 \log_{10}[\, f_1 \,] - 6.7 \log_{10} [N] \,. \qquad 2.39$$

We see that as the focal length of the transform lens increases the usable dynamic range decreases. However in a real spectrum analyser we will have an array of fibres in the focal plane of the lens. The fibres will have "dead spaces" between them caused by the cladding. If one hundred percent probability of intercept is required, then the diffraction spot diameter must be greater than or equal to the core-to-core spacing in the detector array.

The conventional single mode fibres used in this experiment have a core diameter of 6μm. The cladding diameter is 127μm. The minimum diffraction spot size is therefore 127μm for 100% probability of intercept. From equation 2.31 this implies a transform lens with focal length f_1 = 0.2m. This gives a usable dynamic range (from equation 2.39) .

$$D_{poly\cdot} = 38.4 - 6.7 \log_{10} [N] \qquad 2.40$$

This equation shows that with a system with 100 channels then the polytone dynamic range will be 25dB. In order to improve on this figure an array of micro-lenses might be

placed directly in front of the fibre ends. If these each gave optimum coupling equivalent to a 1cm focal length lens then the polytone dynamic range would be 42 dB.

2.3.4 Conclusion

We have derived equations to explain the dynamic range performance of acoustooptic spectrum analyser systems, including the effects of intermodulation.

A simple power acoustooptic spectrum analyser configuration has been tested. The dynamic range was limited by the detector array to 24 dB. Intermodulation effects were observed with the Bragg-cell in a "low-Q configuration". When the Bragg-cell is used in a "high-Q configuration" the intermodulation fell below measurable levels. The intermodulation levels agreed well with theory.

A single channel coherent spectrum analyser has been constructed using optical fibres to couple the signal and reference beams. The monotone dynamic range of this device was 83 dB with optimum coupling. (Calculated from the polytone dynamic range with f_1=1cm). The polytone dynamic range is reduced by third-order two-tone intermodulation to 55.7dB. The polytone dynamic range for a real multi-channel system will be further reduced from this value (D_{poly} = 42 dB for a 100-channel device).

In order to achieve one hundred percent probability of intercept an array of micro lenses will be required unless further loss (D_{poly} = 25 dB) in dynamic range can be tolerated.

Note that these results were achieved using low-grade optics and detectors. These figures should be improvable with higher quality components.

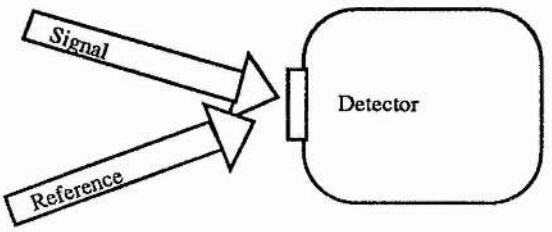

Figure 2.1

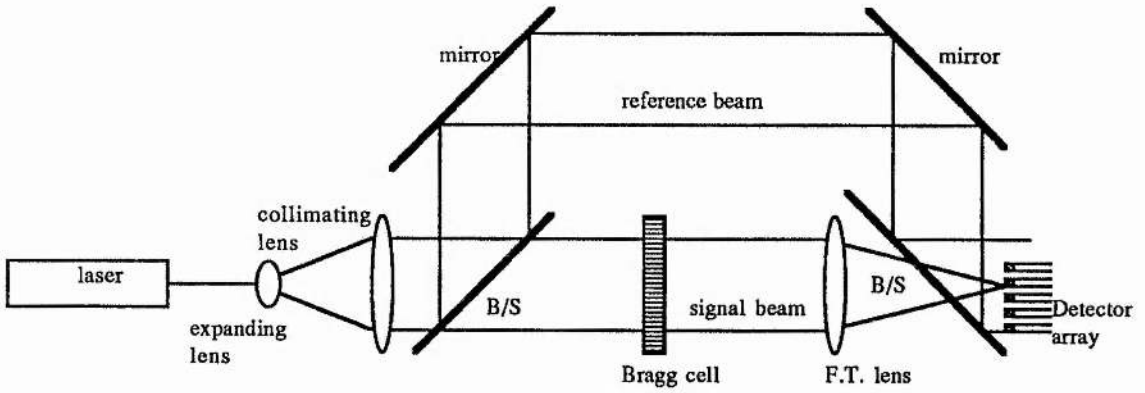

Figure 2.2

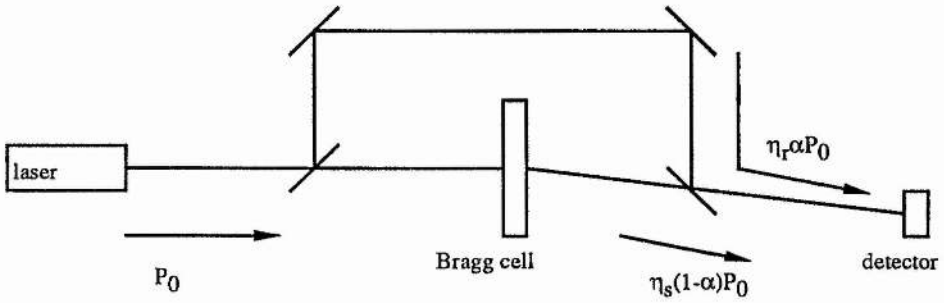

Figure 2.3

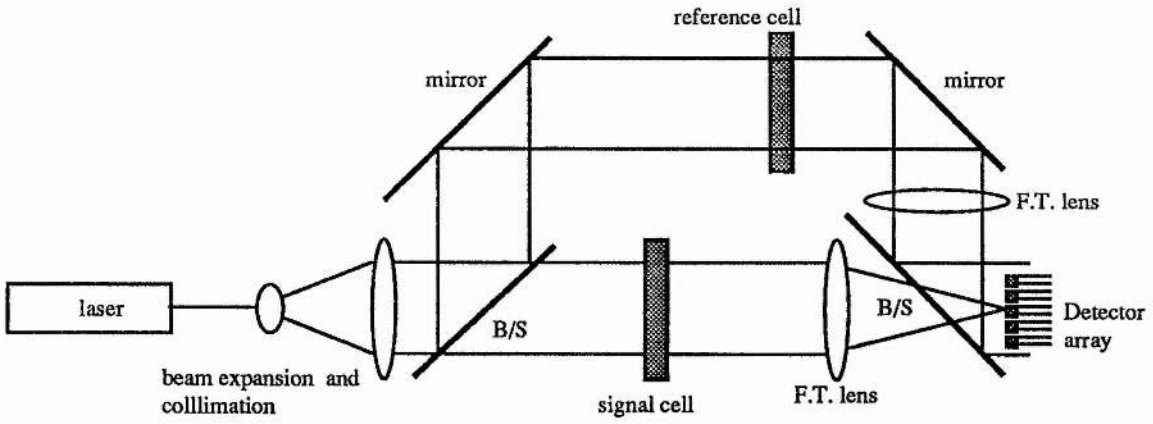

Figure 2.4

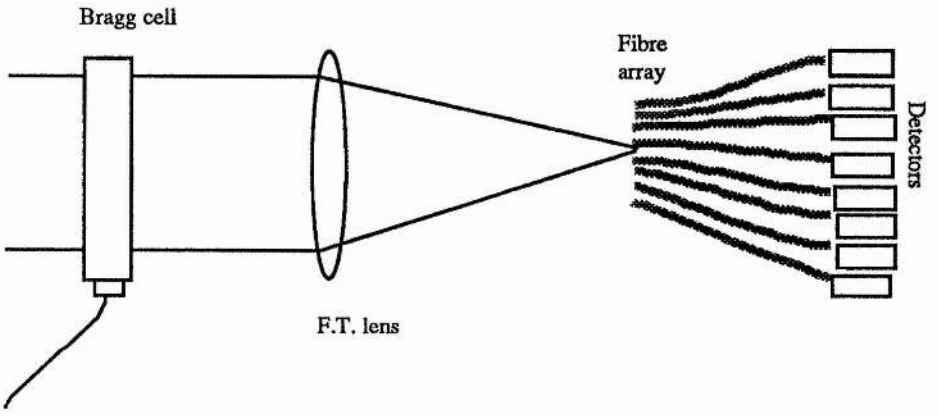
Bragg cell
Fibre
array
Detectors
F.T. lens

Figure 2.5

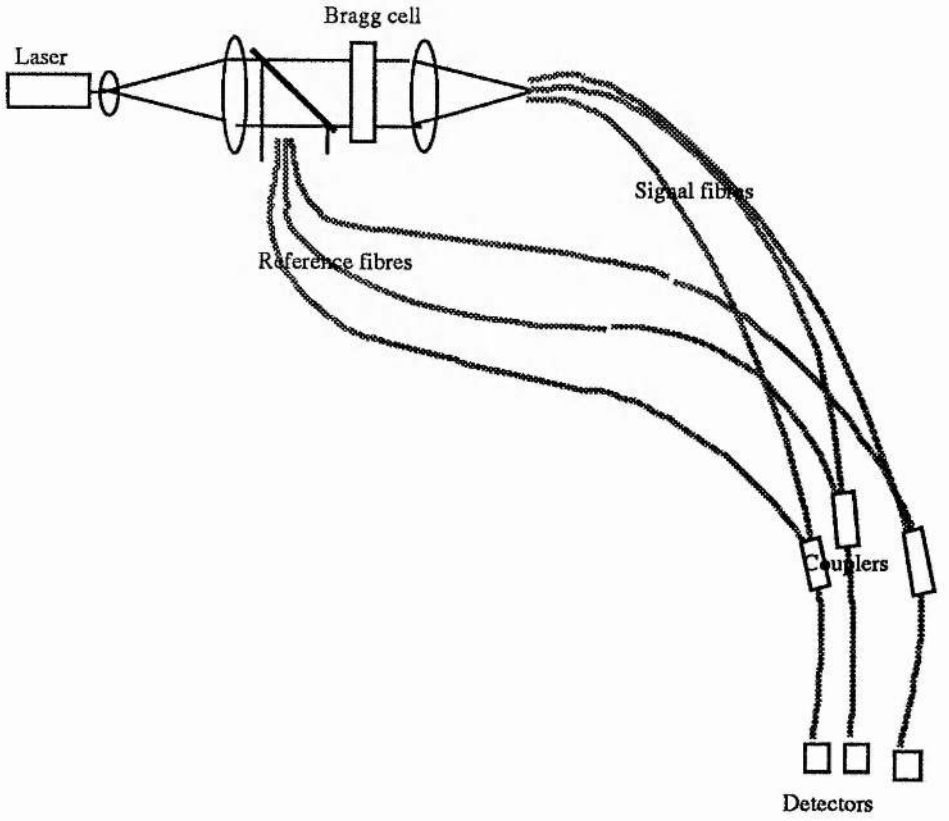
Bragg cell
Laser
Signal fibres
Reference fibres
Couplers
Detectors

Figure 2.6

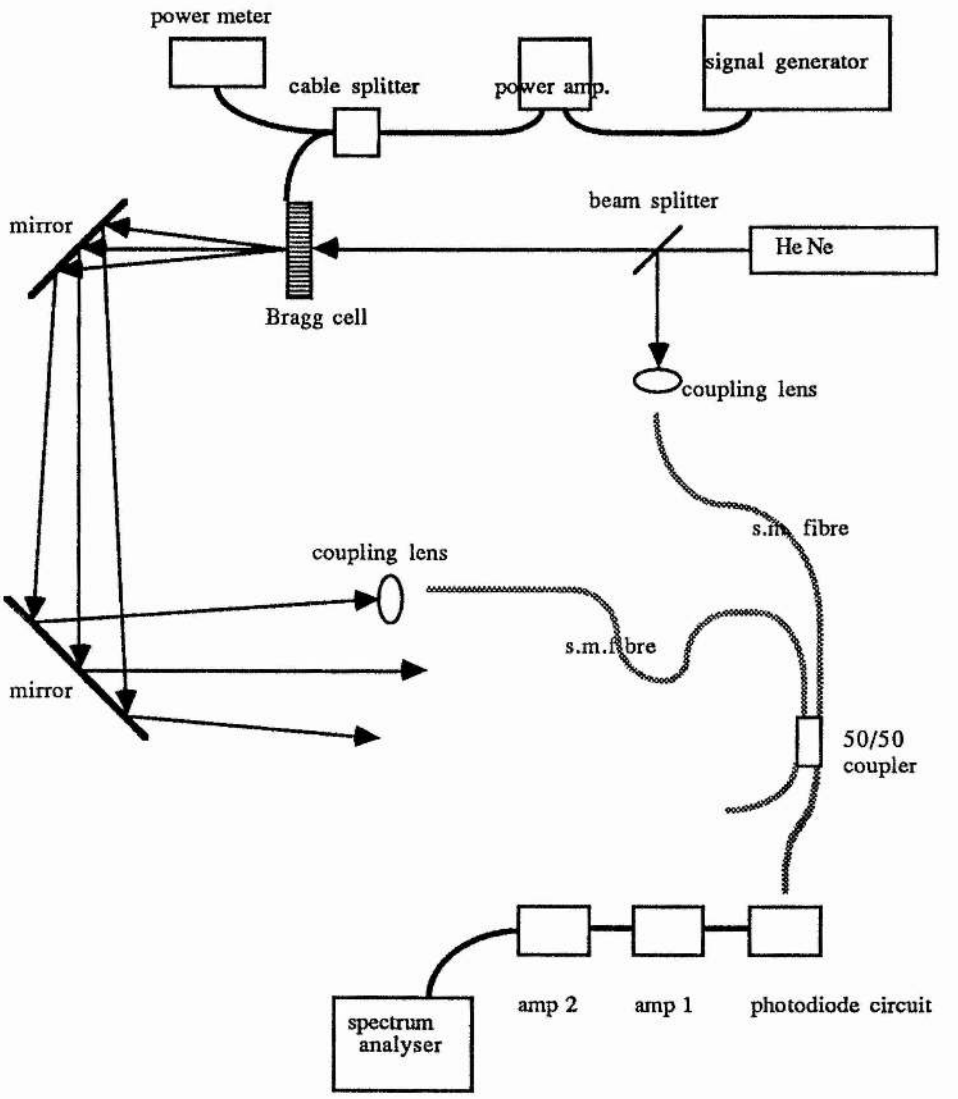

Figure 2.7

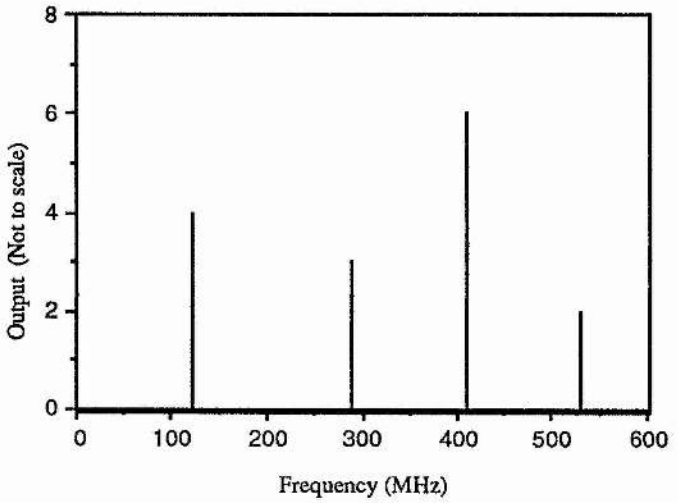

Figure 2.8

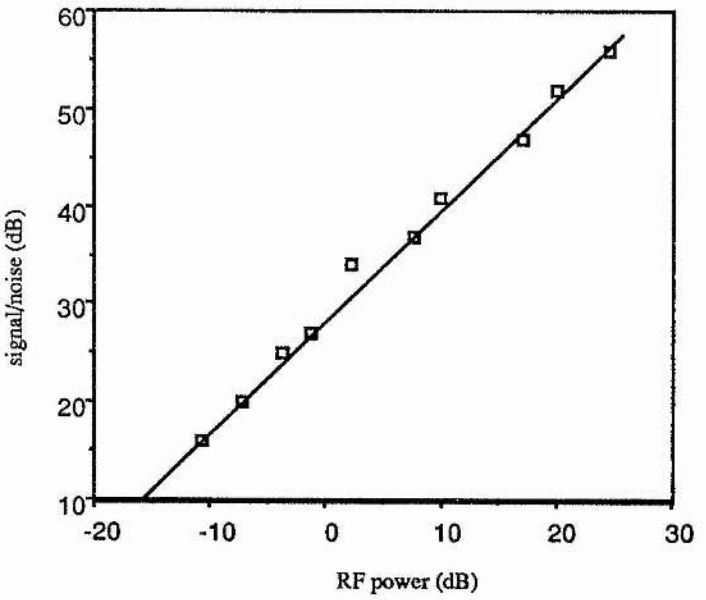

Figure 2.9

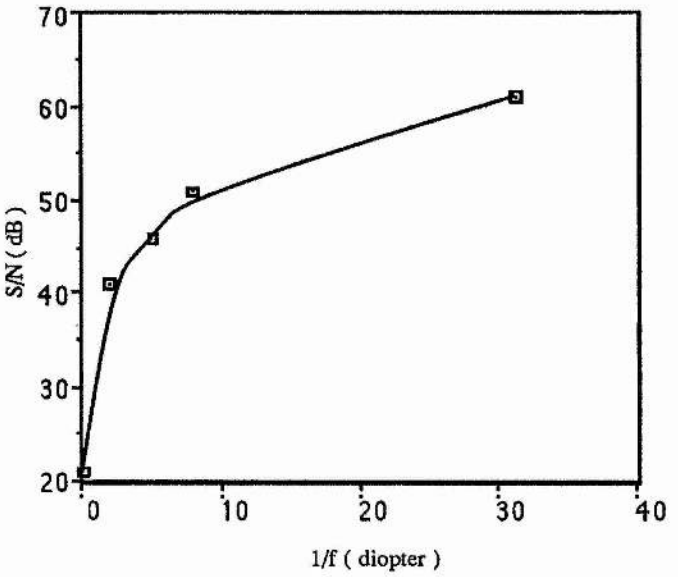

Figure 2.10

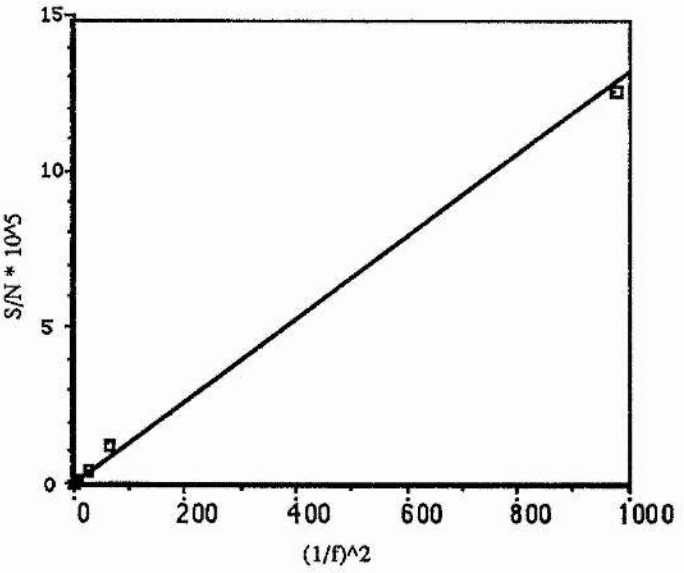

Figure 2.11

2.8 REFERENCES

[2.1] "Real time electrooptical signal processors with coherent detection"

M. King, W. Bennet, L.Lambert, M.Arm

AO Vol. 6, No. 8, 1367-1375, Aug. 67

[2.2] "Noise"

F .R. Conner

Edward Arnold ISBN 07131 34593

[2.3] "Interferometric spectrum analyser"

A.Vander Lugt

AO Vol. 20, No.16, 2770-2779, Aug. 81

[2.4] "Spatial and temporal spectra of periodic functions for spectrum analysis"

A.Vander Lugt, A. Bardos

AO Vol.23, No.23, 4269-4278, Dec 84

3

Wide Bandwidth Acoustooptic Spectrum Analyser using a High-Q cell and Monochromatic Light

3.1 INTRODUCTION

A standard acoustooptic, power, spectrum analyser system, as described in chapter 1, is shown in figure 3.1. A collimated beam of monochromatic light is incident on the acoustooptic cell at the Bragg angle for diffraction at the desired centre radiofrequency. As the radiofrequency in the cell changes the Bragg angle for diffraction changes. The light incident on the cell is no longer at the correct angle for Bragg diffraction and the diffraction efficiency decreases. This reduction in diffraction efficiency as the radiofrequency is tuned away from the centre frequency leads to a finite instantaneous bandwidth.

The instantaneous bandwidth increases with decreasing "Q". For many systems a large bandwidth is required and hence a low-Q cell is used. This has several undesirable effects on the system parameters.

Efforts have been made to increase the available bandwidth of a high-Q cell using phased array transducer techniques [3.1, 3.2].

We describe here a new system architecture which allows the use of a high-Q cell whilst maintaining a large fractional bandwidth.

3.2 EFFECT OF "Q" ON ACOUSTOOPTIC SPECTRUM ANALYSER PERFORMANCE

3.2.1 Bandwidth

The instantaneous bandwidth for a fixed angle of incidence was calculated in chapter 1. We have

$$\Delta f_{s1/2} = \frac{2nv_s^2}{f_s W\lambda} \qquad 1.58$$

and we have

$$Q = \frac{2\pi\lambda W}{n\Lambda^2}. \qquad 1.0$$

Hence from equations 1.0 and 1.58 we have

$$\frac{\Delta f_{s1/2}}{f_s} = \frac{4\pi}{Q}. \qquad 3.1$$

We see that the fractional bandwidth is inversely proportional to the Q of the acoustooptic cell for the standard set-up of figure 3.1.

3.2.2 Diffraction efficiency

The diffraction efficiency is given by

$$\frac{P_2}{P_1} = \frac{k_1^2}{8}\left[\frac{\varepsilon}{\varepsilon_0} p_{23}\right]^2 \frac{W}{H}\frac{P_T}{v_s c_{33}} \quad . \qquad 1.31$$

From equations 1.0, 1.47 and 1.31 we obtain

$$\frac{P_2}{P_1} = \frac{k_1}{32 \sin\emptyset_B}\left[\frac{\varepsilon}{\varepsilon_0} P_{23}\right]^2 \frac{P_T}{v_s c_{33}}\frac{Q}{H} \qquad 3.2$$

We see that the diffraction efficiency per watt is proportional to the Q of the cell.

3.2.3 Intermodulation

In the derivation of equation 1.31 we have assumed that the perturbation in the dielectric impermeability brought about by the acoustic wave is linear with acoustic power density. That is, we have

$$\Delta B_{ij} = p_{ijn} S_n \quad . \qquad 1.18$$

For high power densities this relation breaks down and the acoustoptic interaction becomes non-linear. This effect produces "Material" intermodulation.

In deriving equation 1.16 from 1.15 and 1.14 we assumed $\Delta\varepsilon/\varepsilon << 1$. For large coupling this is not true and the acoustooptic interaction becomes non-linear.

The above non - linearities increase with increasing power density. We may re-write equation 3.2 in terms of acoustic power density. We have for the acoustic power density,

$$P_S=P_T/(WH) \qquad 3.3$$

and from 3.2, 3.3 and 1.0 we obtain for the diffraction efficiency

$$\frac{P_2}{P_1}=\frac{1}{128\sin^2\varnothing_B}\left[\frac{\varepsilon}{\varepsilon_0}P_{23}\right]^2\frac{P_S Q^2}{v_s c_{33}} \; . \qquad 3.4$$

We see that for a given diffraction efficiency the acoustic power density, P_S, increases quadratically with decreasing Q.

Third order two tone (Hecht) intermodulation was described in section 2.2.1. This type of intermodulation is caused by multiple diffraction by two different radiofrequencies within the cell. The acoustooptic interaction bandwidth increases with decreasing Q (equation 3.1). Since Hecht intermodulation requires the simultaneous diffraction of two different radiofrequencies, the effect of this intermodulation will be increased as the Q of the cell is decreased. This was shown experimentally in section 2.2.2.1.

We conclude that the various forms of intermodulation described all increase as the Q of the acoustooptic cell is reduced.

3.2.4 Resolution

The frequency resolution of an acoustooptic spectrum analyser is fundamentally limited by the finite aperture of the cell, L. We have

$$\Delta f_s = \frac{L}{v_s} \qquad 3.5$$

The resolution is further reduced by the spread of acoustic propagation directions within the cell. The effective acoustic wavelength for diffraction of the optical beam changes as the angle of incidence changes over the spread of wavevectors. This is shown in figure 3.2.

The spread in effective acoustic wavelengths brought about by the angular spread of acoustic waves is given by

$$\Delta\Lambda = \frac{\Lambda(1-\cos\Delta\phi_a)}{2} \qquad 3.6$$

For small $\Delta\phi_a$ equation 3.6 becomes

$$\Delta\Lambda = \Lambda\frac{\left[\Delta\phi_a\right]^2}{4} \qquad 3.7$$

But from equation 1.54 we have,

$$\Delta\phi_a = \Delta\phi_{1/2} = \frac{\Lambda}{W}.$$

Using 1.54 and 3.7 we obtain,

$$\frac{\Delta\Lambda}{\Lambda} = \frac{\Lambda^2}{4W^2} . \qquad 3.8$$

We also have, approximately,

$$\lambda = 2\Lambda\emptyset_B \qquad 3.9$$

and

$$V_s = f_s\Lambda . \qquad 3.10$$

Therefore, from equations 3.9 and 3.10, we have

$$\frac{\Delta\Lambda}{\Lambda} = \frac{\Delta\emptyset_B}{\emptyset_B} = \frac{\Delta f_s}{f_s} \qquad 3.11$$

where Δf_s is the radiofrequency spread due to the range of acoustic wave directions in the cell.

From equations 3.8, 3.10 and 3.11, we obtain

$$\frac{\Delta f_s}{f_s} = \frac{\Lambda^2}{4W^2} \qquad 3.12$$

and, from equations 3.1 and 3.12, we obtain for the fractional resolution due to acoustic diffraction,

$$\frac{\Delta f_s}{f_s} = \left[\frac{\lambda \Delta f_{s_{1/2}}}{4nv_s}\right]^2 . \qquad 3.13$$

In terms of Q, equation 3.13 becomes, for the resolution due to acoustic diffraction

$$\Delta f_s = f_s{}^3 \left[\frac{\lambda \pi}{Qnv_s}\right]^2 . \qquad 3.14$$

The resolution therefore decreases as the Q of the cell decreases. The loss in resolution due to low-Q is unlikely to be significant compared with the aperture resolution limit, 3.5, except in systems with a very large bandwidth and centre frequency.

3.2.5 Cross-talk

In a conventional system using a low-Q cell there is cross-talk between different radiofrequencies. If two radiofrequencies are present in the cell simultaneously, then light diffracted away from the incident light beam by one radiofrequency leaves less light available for diffraction by the other. The fractional degree of cross-talk in dB is $CT_{f_1\text{-}f_2}$ and is defined by

$$CT_{f_1\text{-}f_2} = 10 \log_{10}\left[\frac{P_{1\text{-}2}}{P_1}\right], \qquad 3.15$$

where P_1 is the diffraction due to f_1 alone and $P_{1\text{-}2}$ is the cross-talk from f_2 while monitoring f_1.

We obtain

$$CT_{f_1-f_2} = 10 \log_{10}\left[(P_{T_2}\eta_B)\right] \qquad 3.16$$

We have assumed that the diffraction efficiencies for f_1 and f_2 are the same (a low-Q cell is being used). For a high-Q cell this will not be the case and the cross-talk will be less than predicted by equation 3.16.

3.3 SINGLE CHANNEL SPECTRUM ANALYSER CONFIGURATION USING A HIGH-Q CELL

3.3.1 Introduction

In an effort to exploit the advantages of a high-Q cell whilst maintaining a large bandwidth the architecture shown in figure 3.3 was devised.

Light from the Helium-Neon laser is input to the high Q acoustooptic cell over a range of angles. This is accomplished using the cylindrical lenses L_1 and L_2 Cylindrical lens L_3 recollimates the light after diffraction by the cell. Spherical lens L_4 focuses the diffracted light on to the ccd array. The acoustooptic cell is the same as that described in section 1.4.2.

Light which is incident on the cell over a small range of angles, $\Delta\emptyset$, centred around the Bragg angle is diffracted. As the radiofrequency in the cell changes, the Bragg angle for diffraction changes and the light being diffracted arrives at a new angle of incidence.

The resolution is limited by the Q of the cell. Equation 3.1 gives the bandwidth, $\Delta f_{s_{1/2}}$, for a fixed angle of incidence. With a spread of angles of incidence angles, the instantaneous bandwidth becomes the frequency resolution,

$$\Delta f_s = \frac{4\pi}{Q} f_s \,.$$

The dynamic range will be less than the dynamic range for a similar, power, spectrum analyser, because only a fraction $4\pi/Q$ of the incident light is diffracted.

3.3.2 Experimental results

The experiment is set-up as shown in figure 3.3.

The ccd output is shown in figure 3.4 for radio frequencies applied to the Bragg-cell at 170, 150, 130, 110 MHz at 9.7 mW per channel.

The instantaneous bandwidth is limited by the amplifier bandwidth of 60 MHz.

The measured frequency resolution is 11 MHz. (This is the FWHM of the spots on the ccd output). The theoretical resolution, calculated from the Q (from section 1.4.2.4) of the cell, is 12.8 MHz.

The dynamic range is limited to 24 dB. This is the ccd detector dynamic range, as described in chapter 2, section 2.2.2.1.

3.3.3. Conclusion

The limited frequency resolution makes this architecture unsuitable for most applications unless an extremely large transducer is used in the cell. In this case the dynamic range may become limited due to the small proportion of light diffracted.

3.4 THE MULTI-SOURCE ACOUSTOPTIC SPECTRUM ANALYSER

3.4.1 Description

The architecture described in the preceeding section allowed a high-Q cell to be used in a widebandwidth application at the expense of poor resolution and reduced light levels. An alternative system-architecture is described here which maintains a high resolution at large bandwidths whilst using a high-Q cell.

Monochromatic light is input to the cell in a range of discrete angles both in and out of the plane of the acoustic beam. This is achieved by illuminating several optical fibres with a laser. The ends of the fibres are placed in a linear array. The array is orientated at an angle with respect to the acoustic axis of a Bragg-cell as shown in figure 3.5. A lens is placed one focal length distant from the array. Light leaving the array is collimated by the input lens and passes through the Bragg-cell at an angle dependent on the position of the fibre from which it emerged.

Light which is diffracted by the acoustic wave in the cell passes through the transform lens and arrives at the focal plane where it is detected. The vertical and horizontal displacements of the diffracted spot in the transform plane are given by

$$S_x = -\left\{ S_{fibre_x} \frac{f_{l_{F.T}}}{f_{l_{in}}} \right\} + \varnothing_B f_{l_{F.T.}} \qquad 3.17$$

and

$$S_y = -\left\{ S_{fibre_y} \frac{f_{l_{F.T}}}{f_{l_{in}}} \right\} \qquad 3.18$$

where S_{fibre_x} and S_{fibre_y} are the horizontal and vertical displacements of the fibre which emitted the light, $f_{l_{F.T}}$ and $f_{l_{in}}$ are the respective focal lengths of the transform and input lenses.

We may write equations 3.17 and 3.18 as

$$S_x = \left[\emptyset_B - \emptyset_{fibre_x} \right] f_{l_{F.T.}} \qquad 3.19$$

and

$$S_y = - \emptyset_{fibre_y} f_{l_{F.T.}} \qquad 3.20$$

where we have defined $\emptyset_{fibre_x}$ and $\emptyset_{fibre_y}$ to be

$$\emptyset_{fibre_x} = \frac{S_{fibre_x}}{f_{l_{in}}} \qquad 3.21$$

and

$$\emptyset_{fibre_y} = \frac{S_{fibre_y}}{f_{l_{in}}} \qquad 3.22$$

We see that each fibre has a unique diffraction spot position in the vertical (y) direction.

The horizontal position of the diffracted spot depends on the diffraction angle, $\emptyset_B$, (and hence the radiofrequency) and the horizontal position of the fibre.

Each fibre acts as the light source for a separate narrow bandwidth spectrum analyser . The input angle to the cell in the horizontal plane, $\emptyset_{fibre_x}$, determines the centre radiofrequency around which light from a fibre will be diffracted by the Bragg-cell. Each fibre has a number of detectors associated with it at a vertical displacement S_y in the Fourier plane. The bandwidth for each fibre is just the bandwidth for a fixed angle of incidence calculated in section 3.1,

$$\frac{\Delta f_{s1/2}}{f_s} = \frac{4\pi}{Q} \qquad 3.1$$

In order to cover a given total bandwidth, B, the number of fibres required is

$$N = \frac{B}{\Delta f_{s1/2}} \qquad 3.23$$

From equations 3.1 and 3.23, we have

$$N = \frac{BQ}{4\pi f_s} \qquad 3.24$$

The angular separation of the fibres is given by

$$\Delta\emptyset_{fibre_x} = \frac{\Delta f_{s1/2}}{f_s}\emptyset_B \cdot \qquad 3.25$$

Hence from equations 3.1 and 3.25, we obtain

$$\Delta\emptyset_{fibre_x} = \frac{4\pi\emptyset_B}{Q} \qquad 3.26$$

Each fibre covers a bandwidth, $\Delta f_{s1/2}$, and the number of resolvable points in that bandwidth is

$$n_p = \frac{\Delta f_{s1/2}}{\text{resolution}} \qquad 3.27$$

If we ignore loss of resolution due to low Q, we have, from equations 3.1, 3.5 and 3.27,

$$n_p = \frac{4\pi f_s L}{Qv_s} \qquad 3.28$$

This is the number of detectors per input fibre.

As the value of Q increases more input fibres are needed to cover the full bandwidth and the number of resolvable points per fibre decreases until there is just one resolvable point per input fibre. When this condition is met, there is one detector for each input fibre. Each fibre matches the Bragg angle for diffraction at a particular frequency and there is a matching detector for that frequency in the transform plane. This is the arrangement shown in figure 3.6.

The dynamic range may be increased by using coherent, heterodyne, detection (as described in chapter 2). Optical fibres may guide the reference beams and are coupled with the received signal using fibre couplers. This is shown in figure 3.7 which also shows pig-tailed laser diodes which might be used to provide a compact, robust system. Since the number of reference arms per source is n_p the dynamic range will be increased by a factor of approximately N/n_p, where N is the number of output channels.

3.4.2 Experimental verification

3.4.2.1 Experimental arrangement

The experimental arrangement is shown in figure 3.8. A linear array of 50/125 μm multi-mode fibres is placed at the focus of a 5cm lens, inclined at about 30 degrees to the vertical. Three of the fibres are illuminated with a 10mW Helium Neon laser and the collimated beams are passed through the Bragg-cell. The diffracted light is passed through a 100cm lens and focused on to a 1000μm multi-mode fibre, leading to a photomultiplier.

The transducer response is first measured by measuring the optimally aligned diffraction efficiency as a function of frequency. The Bragg-cell is aligned for optimum diffraction efficiency for a set of radiofrequencies whilst monitoring the diffracted light intensity from one input fibre. (Trace 0 in figure 3.9).

The Bragg-cell is then lined up at 160MHz for fibre 1 and the output from the three fibres is measured, without altering the alignment of the cell. The radiofrequency is then varied and the output from the three fibres is measured without altering the alignment of the cell.

3.4.2.2 Results

The results are shown in figures 3.9 and 3.10

Trace 0 in figure 3.9 shows the transducer response (re-aligning the Bragg-cell for each change of radiofrequency). The other three traces are the diffracted outputs from the three fibres, the Bragg-cell is aligned for optimum diffraction of the light from fibre 1 at 160 MHz. The results are normalised as a fraction of the un-diffracted light from each respective input fibre.

Figure 3.10 shows the diffraction efficiency of fibres 1, 2 and 3 normalised to the transducer response.

3.4.2.3 Discussion and comparison with theory

Figure 3.11 shows a theoretical plot for the three channels, obtained by measuring the horizontal displacement of the zero orders of the three channels in the transform plane to obtain the angular range of the input fibres. The value of W for the Bragg-cell was obtained by noting that the variation of diffraction efficiency with input angle reaches a first minimum at 0.011 radians (see chapter 1.).

The results for the relative diffraction efficiency show fairly good agreement with the simple theory, especially considering that a square "top hat" type of acoustic distribution was assumed, in order to produce the theoretical curves. This is known to be a fairly inaccurate assumption, based on the results of chapter 1, which showed significant

deviations from a true $sinc^2$ variation of diffraction efficiency with input angle, for large angles.

The experiment used a low-Q cell, the bandwidth being largely limited by the transducer bandwidth, as opposed to the acoustooptic bandwidth. However it can be seen from figure 3.10 that the acoustooptic bandwidth of the combined three input fibres is greater than that for a single input.

3.5 CONCLUSION

We have shown that the use of a high-Q cell in an acoustooptic spectrum analyser offers a number of advantages;

1) High diffraction efficiency per watt,
2) Low intermodulation,
3) High resolution,
4) Low cross-talk.

A system architecture has been described which incorporates multiple input light beams, allowing a high-Q cell to be used without loss of Bandwidth. This architecture has the additional benefit that as the number of channels increases, the dynamic range remains constant. In the coherent detection architectures described in chapter 2 the dynamic range decreased with increasing number of channels.

A proof-of-principal experiment has been performed with three separate input beams.

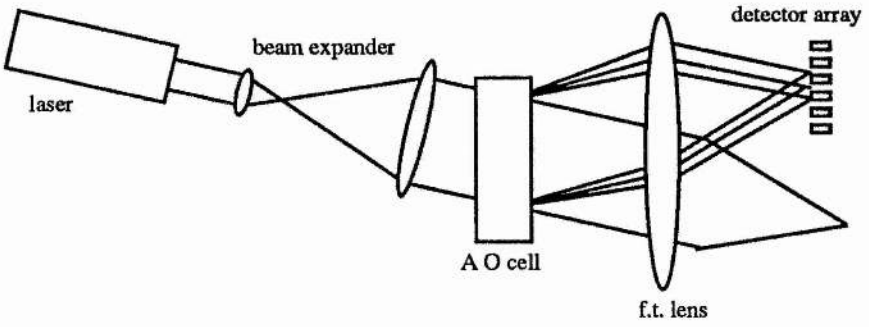

Figure 3.1

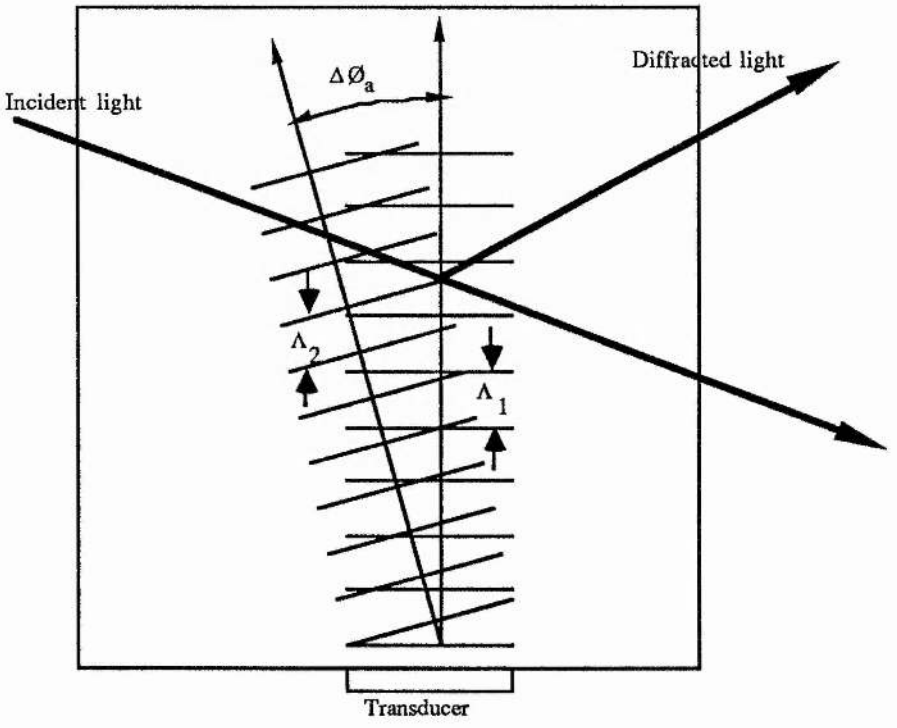

Figure 3.2

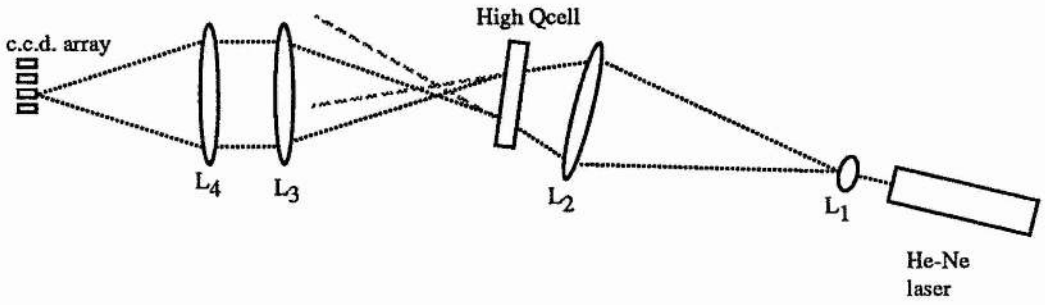

Figure 3.3

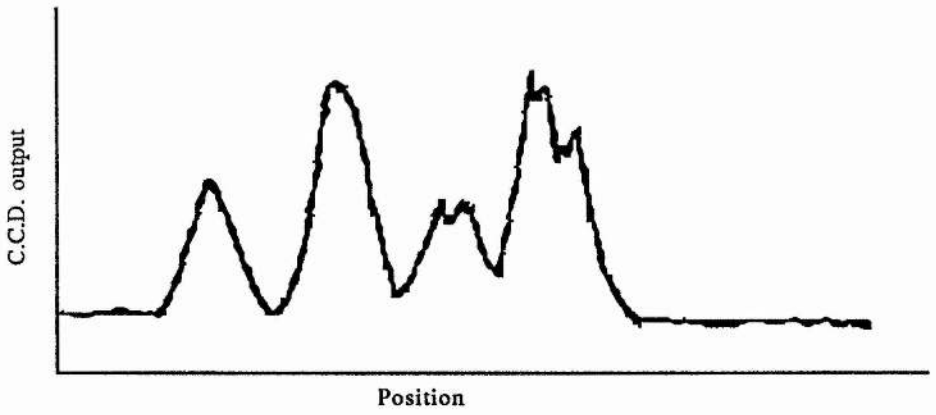

Figure 3.4

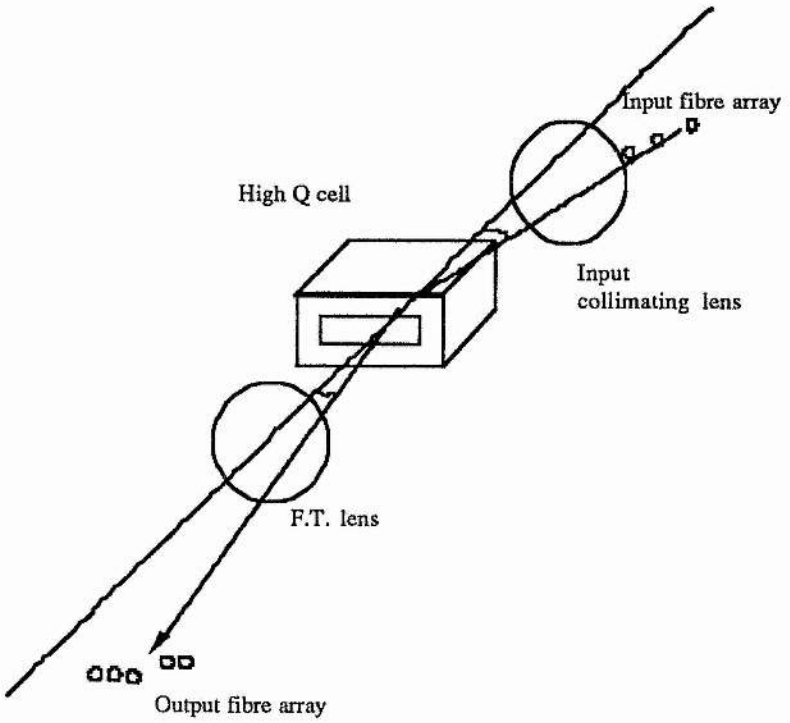
Input fibre array
High Q cell
Input
collimating lens
F.T. lens
Output fibre array

Figure 3.5

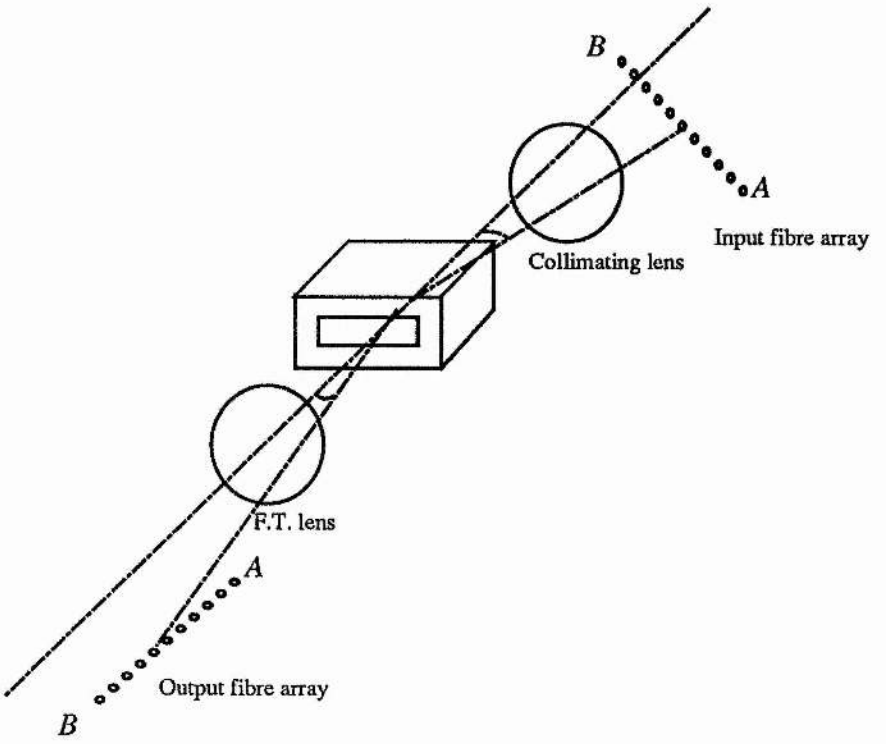

Figure 3.6

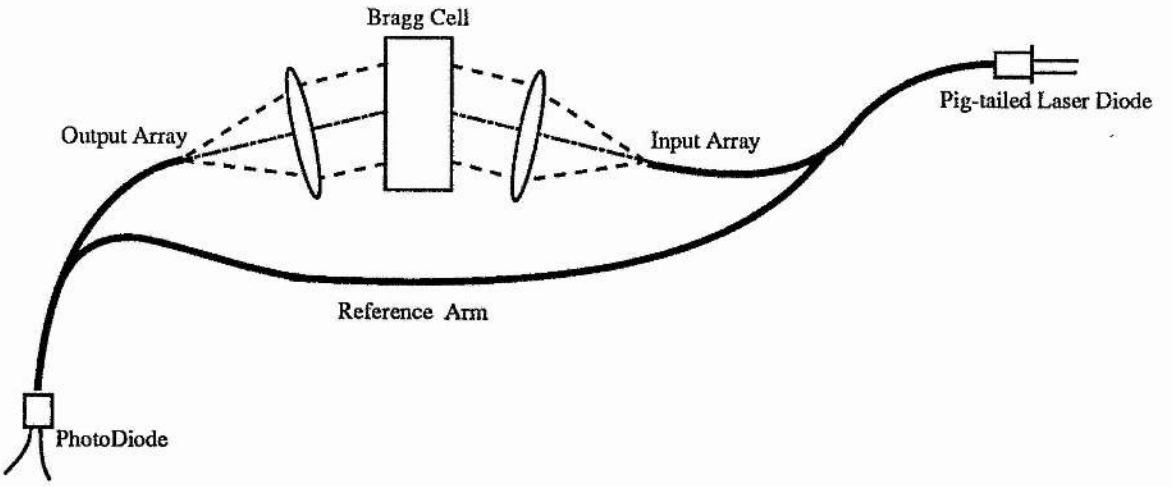

Figure 3.7

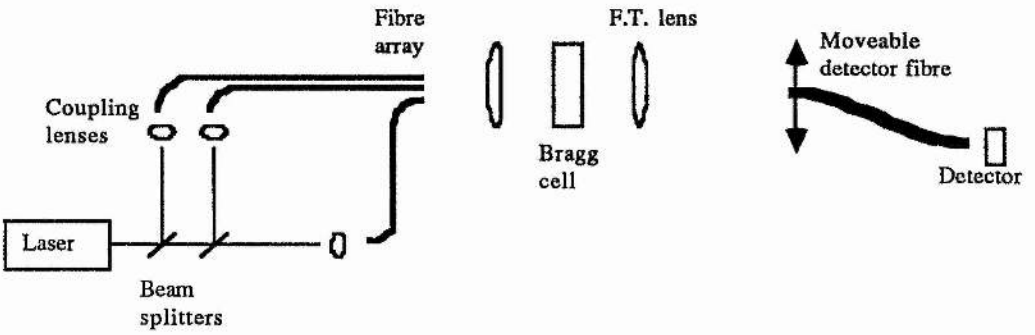

Figure 3.8

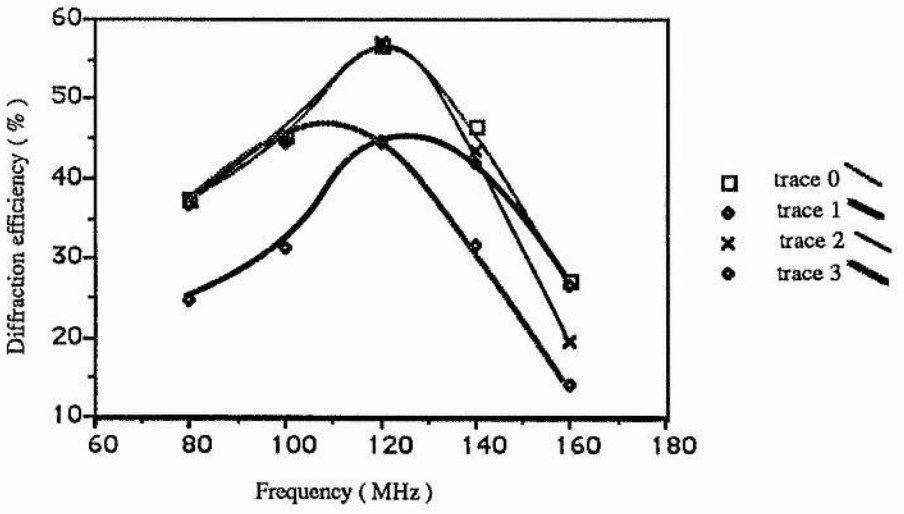

Figure 3.9

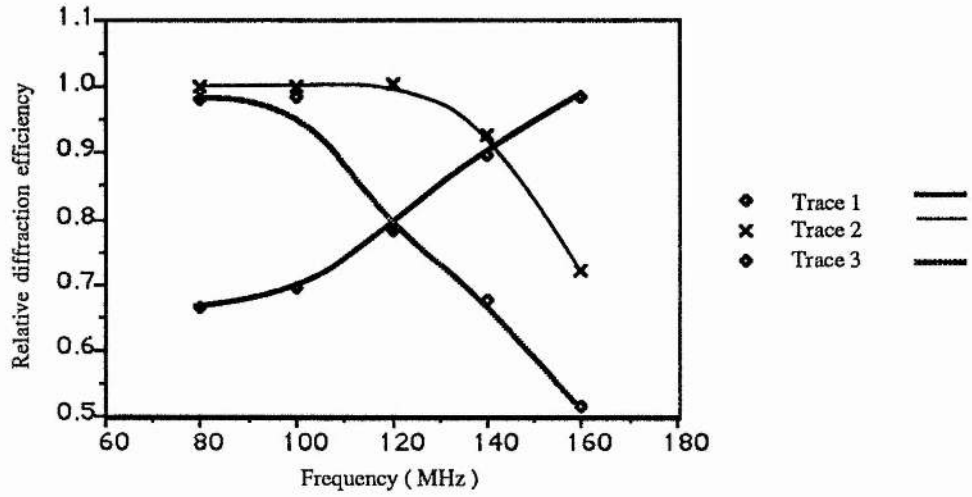

Figure 3.10

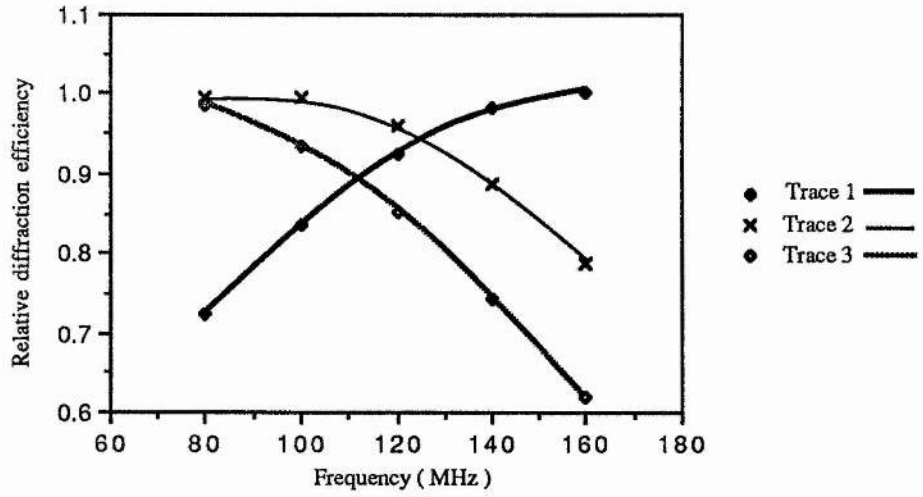

Figure 3.11

3.5 REFERENCES

[3.1] "Broadband Acoustooptic Deflectors: New Results"

G. ALphonse

AO Vol. 14, No. 1, 201-207, Jan 75

[3.2] "Wideband acoustooptic Bragg cells using phased array techniques: design and modeling"

K. Mai, D. Penunuri

Proc. SPIE - Int Soc. Opt. Eng. (USA) vol. 753, 2-9, 87

[3.3] "Acoustooptic Bragg cells: - A Heuristic analysis of the effects of 'Q' upon performance"

A. Shaw

Memorandum ARE TM AW(R)F 87009

4

Polychromatic Radiofrequency Spectrum Analysers

4.1 INTRODUCTION

The conventional acoustooptic spectrum analyser achieves a wide bandwidth by using a low-Q cell, as described in the preceding chapter. In order to obtain a wide bandwidth for diffraction with a high-Q cell it is necessary to provide a range of input angles for the monochromatic light.

Acoustooptic tuneable chromatic filters (AOTF) have been constructed for optical spectral analysis [4.1-4.4]. Polychromatic light has also been used in combination with acoustooptic cells for colour scanning displays [4.5].

An alternative method of increasing the bandwidth whilst using a high-Q cell in an radiofrequency spectrum analyser is to use polychromatic light. The Bragg condition for diffraction may be written as

$$\lambda = 2 \frac{v_s}{f_s} \sin\emptyset_B \, . \qquad 4.1$$

We see that for a given Bragg angle, $\emptyset_B$, and radiofrequency, f_s, there is an optical wavelength which satisfies the condition for Bragg diffraction. As the radiofrequency

changes, the optical wavelength for diffraction at that angle changes. An acoustooptic spectrum analyser can therefore be constructed as shown in figure 4.1.

A plane beam of polychromatic light is incident on the high-Q Bragg-cell at an angle $\emptyset_{in}$. Light diffracted from the cell at an angle $\emptyset_{out} = \emptyset_{in}$ falls on the input slit of an optical spectrum analyser. The wavelength of the light is inversely proportional to the radiofrequency in the Bragg-cell. The spectrum analyser consists of a diffraction grating and detector array.

Light is diffracted from the grating at an angle, $\emptyset_d$, given by

$$\sin\{\emptyset_d + \emptyset_i\} = \frac{m\lambda}{d}, \qquad 4.2$$

where $\emptyset_i$ is the angle of incidence on the grating, m is the diffraction order and d is the grating spacing. If we consider the first order diffraction only then, for small $\emptyset_d$, $\emptyset_i$, we have

$$\emptyset_d = \frac{\lambda}{d} - \emptyset_i . \qquad 4.3$$

The displacement of the diffracted beam in the detector plane is

$$S_d = F_l\left[\frac{\lambda}{d} - \emptyset_i\right], \qquad 4.4$$

where F_l is the focal length of the transform lens in the spectrum analyser. From equation 4.1 we obtain the position of light reaching the detectors which has been diffracted by the Bragg-cell

$$S_d = F_l\left[\frac{2V_s \sin\emptyset_B}{f_s d} - \emptyset_i\right]. \qquad 4.5$$

We see that the displacement of the light reaching the detectors is inversely proportional to the radiofrequency applied to the Bragg-cell and, for small changes in the radiofrequency, the displacement of light falling on the detector array of the spectrum analyser is approximately linear with radiofrequency. The system may therefore be used as a radiofrequency acoustooptic spectrum analyser.

4.2 SYSTEM PARAMETERS

4.2.1 Bandwidth

If a high-Q cell is used then the bandwidth will be chiefly limited by the optical bandwidth of the source. From equation 4.1 we have

$$\frac{\Delta\lambda}{\lambda} = -\frac{\Delta f_{s\,1/2}}{f_s}. \qquad 4.6$$

Therefore the fractional optical bandwidth is equal to the fractional radiofrequency bandwidth.

4.2.2 Resolution

The fundamental limit of resolution is restricted by the aperture of the Bragg-cell and is given by equation 3.5,

$$\Delta f_s = \frac{L}{v_s} .$$

However, it is often difficult to collimate a polychromatic source to a divergence less than the diffraction limit of the Bragg-cell aperture. Un-collimated light decreases the resolution.

Equation 4.1 is, for small $\emptyset_B$,

$$f_s = 2\frac{v_s}{\lambda}\emptyset_B \qquad 4.7$$

and hence we obtain the fractional resolution due to angular spreading of the input beam

$$\frac{\Delta f_s}{f_s} = \frac{\Delta\emptyset_B}{\emptyset_B} . \qquad 4.8$$

In practice, the source is usually collimated using a slit, as shown in figure 4.2. The divergence angle, not including diffraction, is then

$$\Delta\emptyset = \frac{l_s}{f_{l_c}} , \qquad 4.9$$

where l_s is the size of the illumination area and f_{l_c} is the focal length of the collimating lens. From equations 4.7, 4.8 and 4.9 we obtain the resolution due to collimation

$$\Delta f_{s_{collimation}} = \frac{2v_s l_s}{\lambda f_{l_c}} . \qquad 4.10$$

We see that, as the acoustic velocity increases, the resolution becomes poorer, for a given geometric collimation.

Another source of decrease of system resolution is due to the limitation of size of the diffraction grating in the optical spectrum analyser. The fractional resolution of the grating is given by

$$\frac{\Delta\lambda}{\lambda} = \frac{D}{d}, \qquad 4.11$$

where D is the length of the grating and d is the line spacing. From equations 4.6 and 4.11 we obtain the frequency resolution of the grating,

$$\Delta f_{s\ grating} = \frac{f_s D}{d}. \qquad 4.12$$

The overall system resolution, Δf_{s_T}, is therefore the sum of the contributions from Bragg-cell aperture, lack of collimation of the source and resolution of the spectrum analyser (equations 3.5, 4.10 and 4.12 respectively).

4.2.3 Dynamic range

The dynamic range will be the same as that given in chapter 2 for the power spectrum analyser but with the laser power replaced by the light power reaching the detectors. This is given by the spectral intensity of the source integrated over the solid angle accepted by the system and the bandwidth of each detector. The minimum detectable signal is (from equation 2.23)

$$P_{T_{min}} = \frac{-2eBR\eta_d + \sqrt{\left[2eBR\eta_d\right]^2 + 4R\eta_d^2\{4\kappa TB+2eBRi_d\}}}{[P_a]^2 R\eta_B\eta_d^2\eta_L}, \qquad 4.13$$

where P_a is given by

$$P_a = P_0 l_s^2 \Omega\Delta\lambda \qquad 4.14$$

and where P_0 is the source intensity per unit area per unit solid angle per unit optical frequency. The solid angle accepted by the spectrum analyser is Ω and $\Delta\lambda$ is the optical bandwidth accepted by each detector.

The optical bandwidth accepted by each detector is given by

$$\Delta\lambda = \lambda\frac{\Delta f_{s_T}}{f_s}. \qquad 4.15$$

We see from equation 4.13 that the minimum detectable signal is inversely proportional to P_a. From equations 4.14 and 4.15 we see that P_a is proportional to the resolution, Δf_{s_T}. Therefore, the minimum detectable signal is proportional to the resolution. The dynamic range is given by

$$D = 10\log_{10}\left\{\frac{P_{T_{max}}}{P_{T_{min}}}\right\}. \qquad 2.29$$

The maximum signal, $P_{T_{max}}$, is limited by third-order two-tone modulation as for the monochromatic case. The dynamic range is therefore limited by the source intensity and decreases as the resolution improves.

4.3 POLYCHROMATIC LIGHT SOURCES

4.3.1 Introduction

The requirements for a light source for a polychromatic acoustooptic spectrum analyser are

1) Large fractional spectral bandwidth. This is necessary for a large radiofrequency bandwidth.

2) High spectral intensity (Watts / metre^2 / Ω / Hz). Required for a large dynamic range.

3) Spectral profile must be reasonably constant over region of interest. This is necessary to give a linear frequency response.

4) Stability. A stable source is required for consistent results.

4.3.2 Xenon arc-lamp

4.3.2.1 Experimental configuration

The experimental layout is shown in figure 4.3

The " Cermax " LX75F Xenon arc-lamp (75 Watts) has the spectral profile shown in figure 4.4. The profile is reasonably constant from 350 to 720 nm and therefore satisfies conditions (1) and (3). The arc lamp features a short length arc and parabolic mirror to collimate the light to a divergence angle of 7 degrees. Light leaving the lamp is further collimated using a pair of lenses and a variable slit as shown in figure 4.3.

The optical spectrum analyser incorporates a ccd array similar to the one described in chapter 1 for the characterisation of the monochromatic spectrum analyser. It is therefore possible to compare signal-to-noise ratio and dynamic range for the polychromatic and monochromatic spectrum analysers.

4.3.2.2 Experimental results

Figure 4.5 shows the output from the ccd array in the optical spectrum analyser for a set of radiofrequencies (144.9, 146.7, 150, 152.4, 154.7 MHz) applied to the Bragg-cell. The collimation slits are adjusted to give a resolution of 0.5 MHz. The entrance slit to the spectrum analyser is matched to the collimation slit by observing the output as the slit is closed. - The resolution ceases to improve when the entrance slit is smaller than optimum.

Figure 4.6 shows the variation of signal-to-noise ratio with resolution with RF drive power of 300mW. The maximum achievable resolution (S/N = 1) is 0.3 MHz. This is approximately equal to the diffraction limit of the Bragg-cell aperture.

The output varies with time due to movements of gas within the lamp. The amplitude of these fluctuations is at approximately 3 dB below the signal level.

4.3.2.3 Use of fibre optics for collimation

The problems associated with spatial variations in intensity emitted by the arc lamp can be reduced by using a multi-mode optical fibre in place of the pin-hole in the collimating optics. This is shown in figure 4.7. Spatial variations in intensity across the fibre input are averaged out after a few meters propagation within the fibre. However, a reduction

of at least 1 dB in signal strength is experienced due to coupling losses into the fibre, as described in section 2.3.2.2.

4.3.2.4 Conclusion and comparison with monochromatic system

A Xenon arc lamp has been demonstrated as a source in a polychromatic radiofrequency spectrum analyser. The bandwidth is comparable with the monochromatic architecture using the same Bragg-cell, being limited by the piezo-electric coupling bandwidth.

The maximum achievable resolution, and hence time-bandwidth product, is similar to that obtained in the monochromatic system, the resolution being limited by the Bragg-cell aperture.

The signal-to-noise ratio achieved is limited by the resolution of the system. As the resolution improves the signal level decreases. At diffraction limited resolution (0.2 MHz) the signal-to-noise ratio is approximately unity for the highest acceptable radio frequency power levels within the Bragg-cell. Since the dynamic range cannot exceed the maximum signal-to-noise ratio, a small dynamic range results (0 dB at maximum resolution). However, for a resolution of 3 MHz the maximum signal-to-noise ratio is 130. This is equivalent to a 21dB monotone dynamic range.

We conclude that for systems not requiring large dynamic range or high resolution a Xenon arc lamp provides a suitable source. However the purpose for using polychromatic sources is to allow high-Q cells to be used. The advantages of a high-Q cell would not be realised in a system having a low resolution and small dynamic range.

We therefore conclude that Xenon arc lamps are not an ideal source for polychromatic radiofrequency spectrum analysers.

4.3.3 Ultra-high luminescance light emitting diodes

Light-emitting-diodes (LEDs) typically have bandwidths of tens of nanometers with total light output powers of milli-watts. Two main types of LED are available, the side and the edge-emitting diode. These are shown in figures 4.8 and 4.9.

The emission area of the side emitting diode is usually around 200 μm diameter. Edge-emitting light emitting diodes (ELEDS) are designed for coupling high powers into single-mode optical fibres. They incorporate index and electrical guiding to confine the emission area. The refractive index of the active region of the PN junction is slightly higher than that of the surrounding material, providing guiding perpendicular to the junction plane. A stripe contact is used to produce carrier confinement and hence gain guiding within the plane of the junction.

A further refinement to the ELED is the truncated-ridge edge-emitting light-emitting-diode (TRELED), as shown in figure 4.10. This type of diode features index guiding in the plane of the junction provided by the narrow ridge structure. The ridge is terminated before the end facet of the diode to provide a lossy region which prevents lasing. The emission area is 4.4 μm perpendicular to the junction and 8 μm in the plane of the junction.

The diode operates at around 850 nm, with a bandwidth (FWHM) of 40nm.

4.3.3.2 Experimental configuration

The experimental set-up is shown in figure 4.11. Light from a TRELED is collimated by the 10 cm collimating lens before being input to a Bragg-cell and spectrum analyser, as before.

4.3.3.3 Experimental results

The frequency resolution (FWHM) is 0.3 MHz.

The 3dB bandwidth is 6 MHz.

The dynamic range is 24 dB.

4.3.3.4 Comparison with theory

The resolution of the system due to collimation errors is given by equation 4.10 as

$$\Delta f_{s_{collimation}} = \frac{2v_s l_s}{\lambda f_{l_c}} \qquad 4.10$$

and we have,

$$\Delta f_{s_{collimation}} = 160\text{kHz} .$$

Since the resolution limit due to diffraction is about 200 kHz, we would expect a system resolution of around 0.36 MHz. The measured value of 160 KHz is compatible with this.

The bandwidth of the system given by equation 4.6 is

$$\Delta f_s = f_s \frac{\Delta\lambda}{\lambda}$$

and this gives $\Delta f_s = 7$ MHz, in good agreement with the experimental value of 6 MHz.

The dynamic range was limited by the dynamic range of the detector , which was restricted by saturation at 100mW radiofrequency drive power.

4.3.3.5 Conclusion

The TRELED provides a possible source for a polychromatic radiofrequency spectrum analyser. The relatively high spectral intensity allows good dynamic range and frequency resolution. Its compactness and ruggedness make it an attractive proposition in many applications. However the small fractional bandwidth will prove to be a limitation for many applications, but it should be possible to design a TRELED with a larger spectral width than the one tested here.

4.3.4 Ultra-short pulse Laser

Optical pulses of less than 20 femtoseconds duration have been produced by passively mode-locked CW ring dye lasers with a pulse repetition rate of 100 MHz and a mean power of 100mW.

Extra-cavity pulse shortening, employing self phase modulation from a fibre-grating pair, allows the pulse length to be reduced to less than 10 femtoseconds.

Light from this laser has a spectral bandwidth of 100 nm centred around 500nm. The light is highly collimated and very intense and would be ideal for use in a polychromatic radiofrequency spectrum analyser, giving good resolution, large dynamic range and wide fractional bandwidth. However at present these lasers are large, expensive and difficult to maintain at optimum performance. Versions based on optical-fibre cavities are being developed and should be available in the future as compact units with stable outputs.

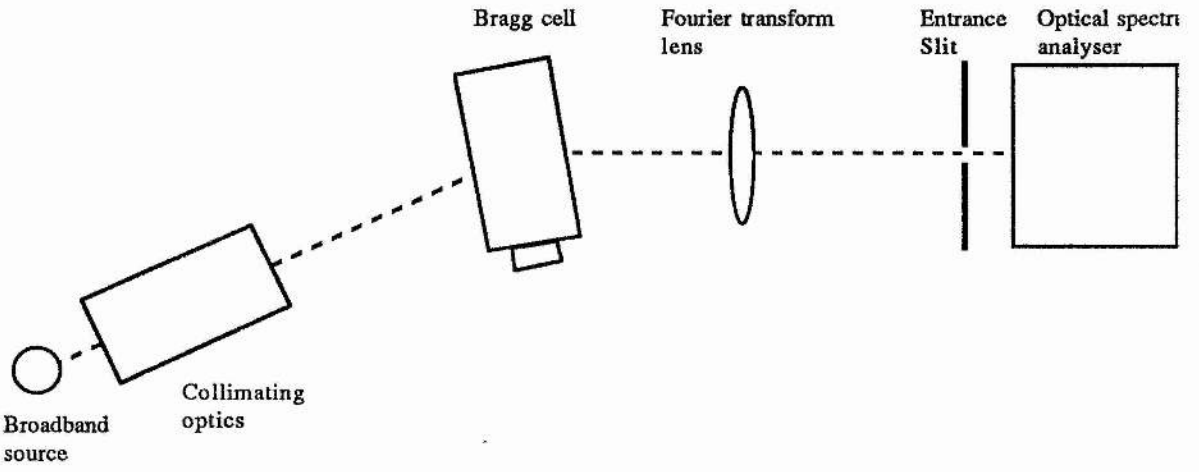

Figure 4.1

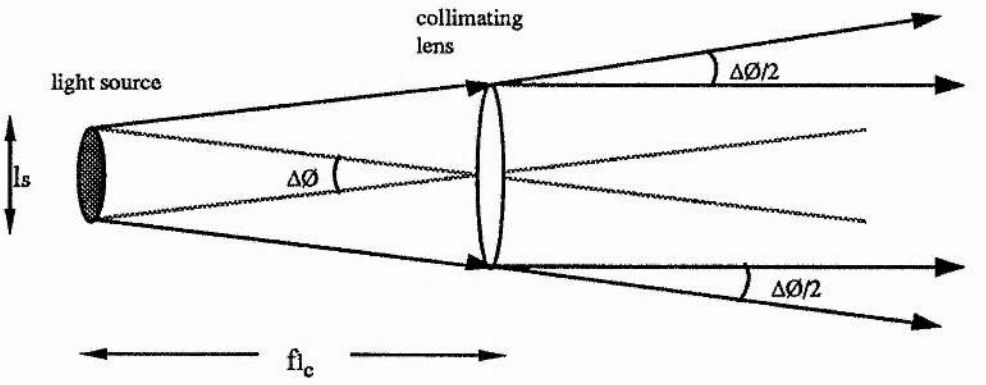

Figure 4.2

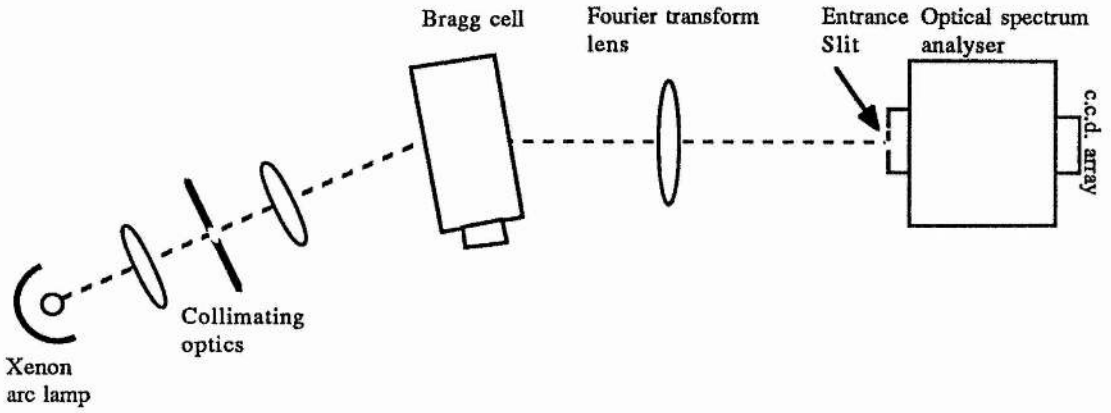

Figure 4.3

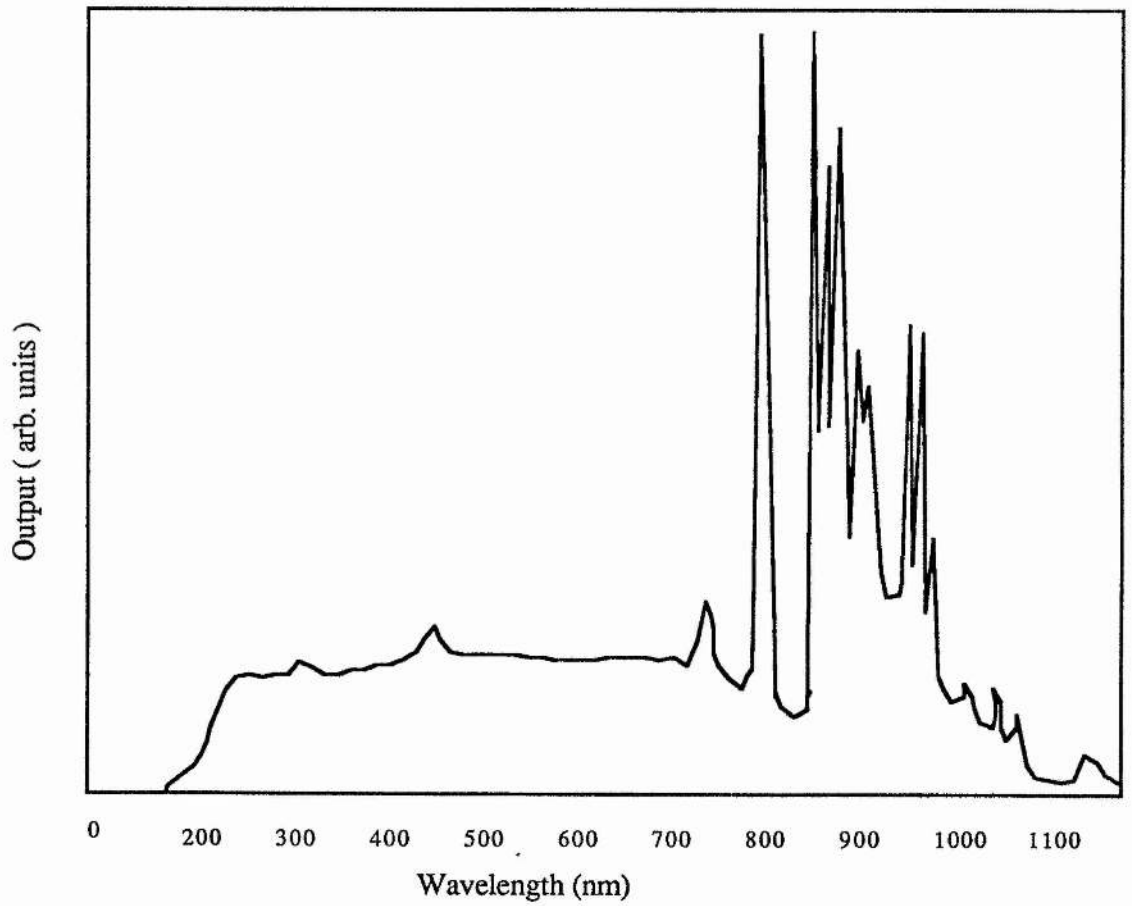

Figure 4.4

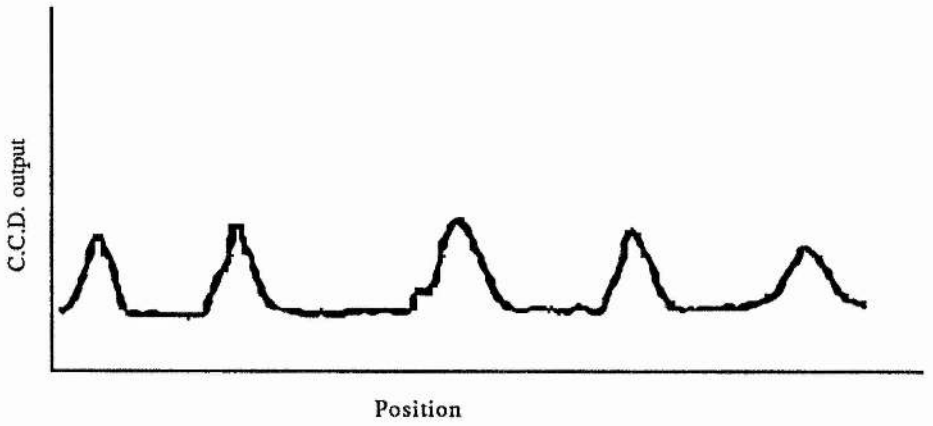

Figure 4.5

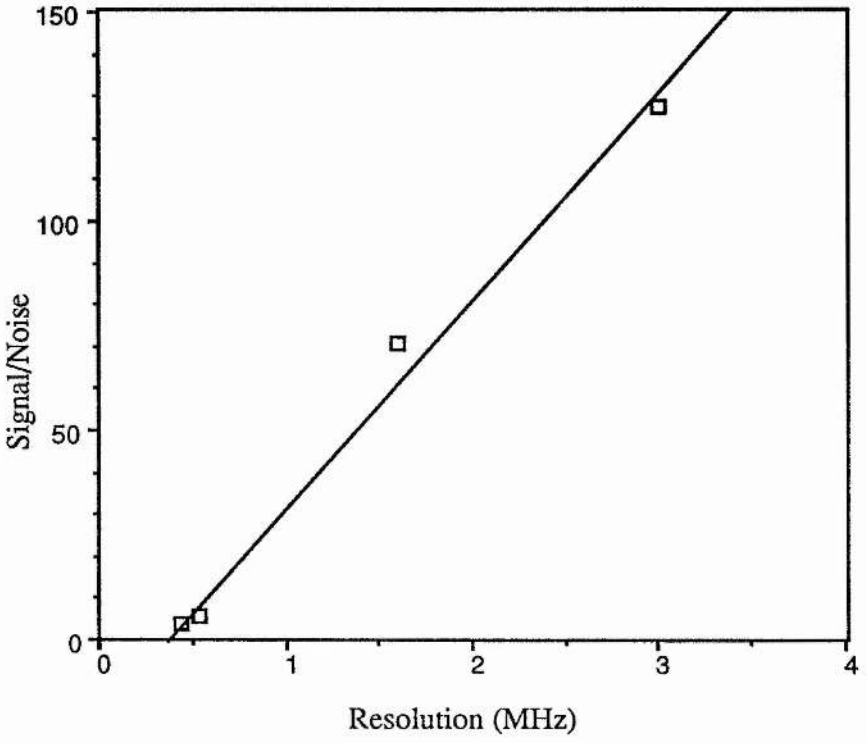

Figure 4.6

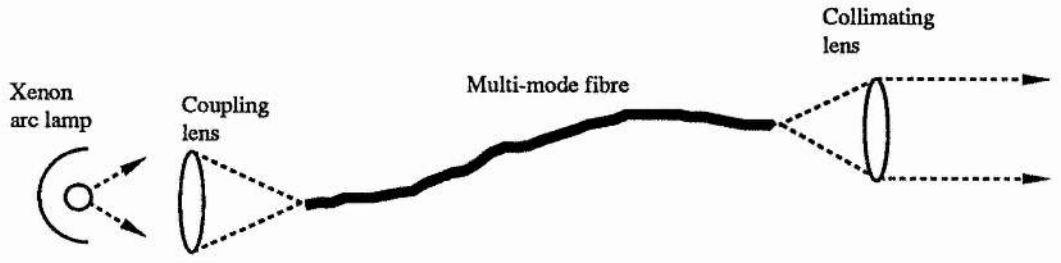

Figure 4.7

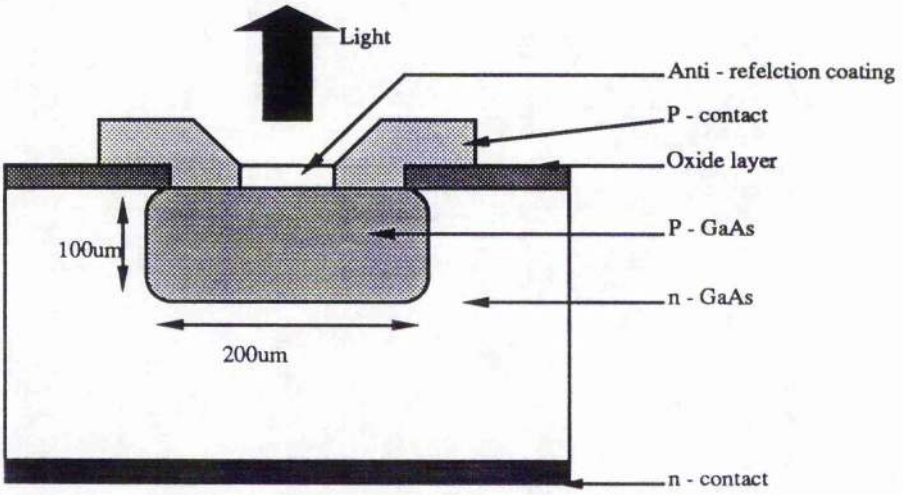

Figure 4.8

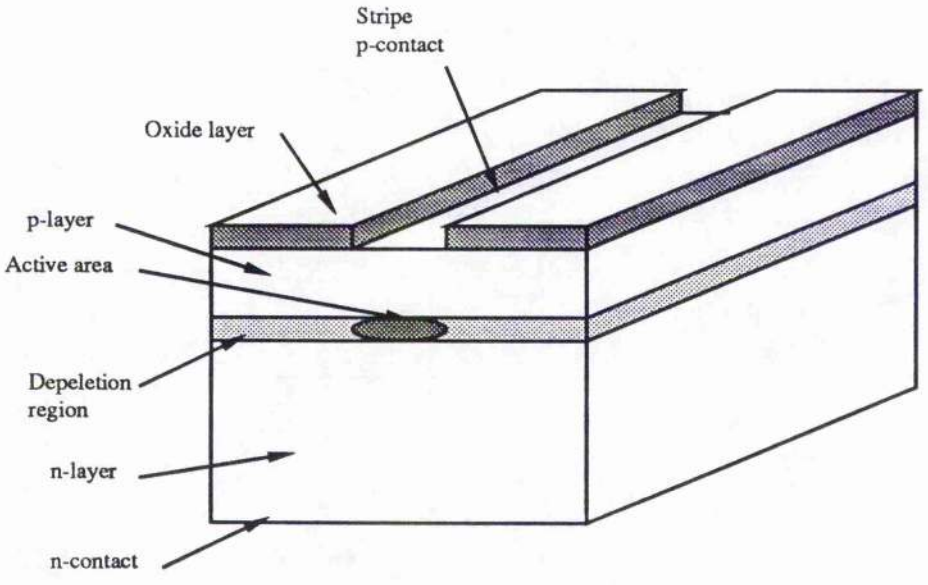

Figure 4.9

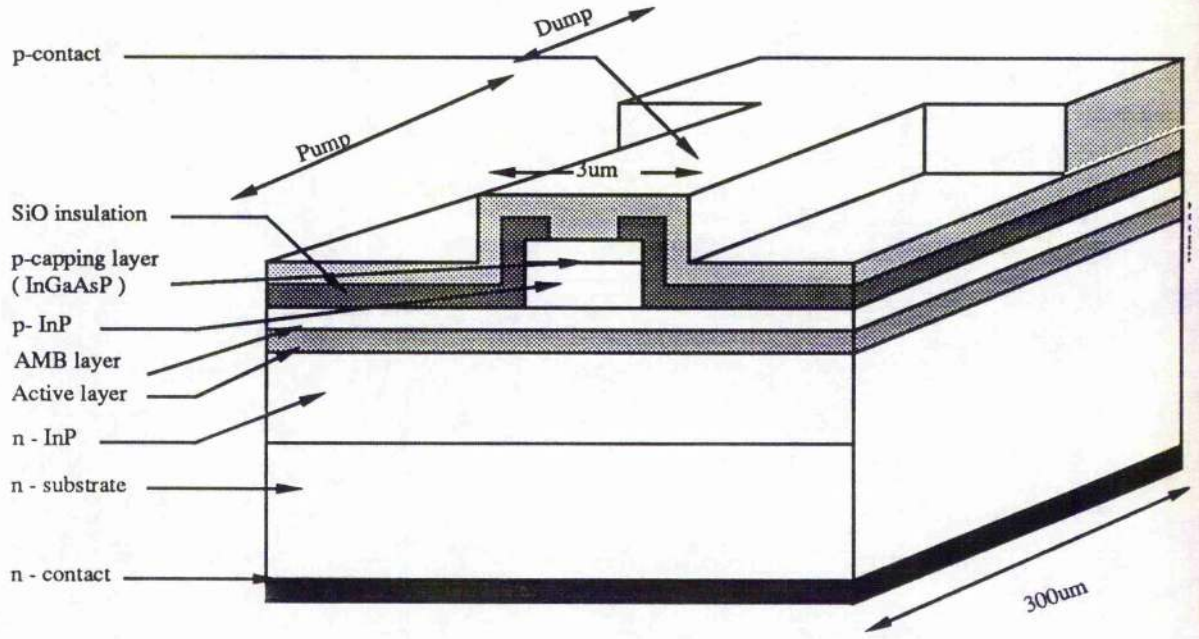

Figure 4.10

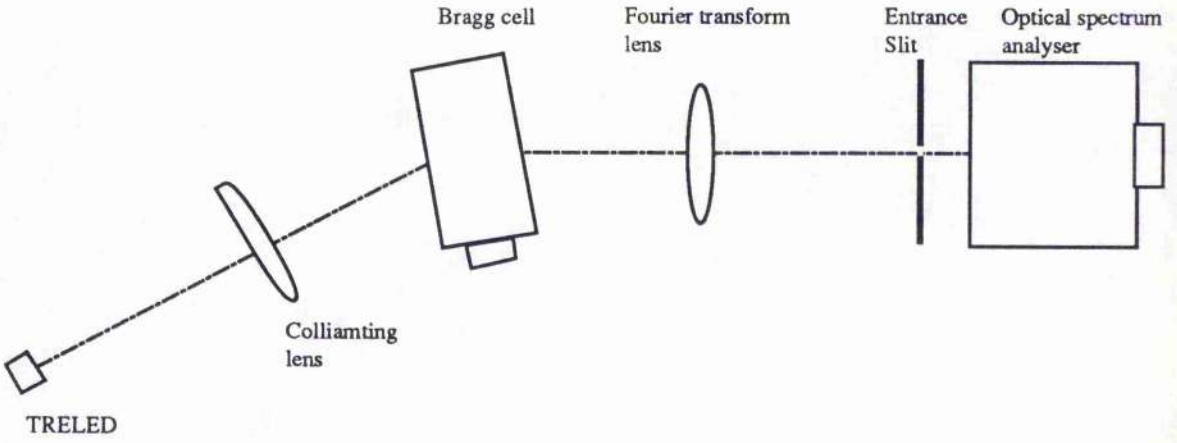

Figure 4.11

4.4 REFERENCES

[4.1] "Independent acoustooptic modulation of the two wavelengths of a bichromatic light beam"

M. Gazalet, G. Waxin, J. Rouvaen, R. Torguet, E. Bridoux

A.O. Vol. 23, Non. 5, 674-681, Mar 84

[4.2] "Temporal response of high-reolution acoustoopic tunable filters"

M. Gottlieb, Z. Kun

A.O. Vol. 22, No. 14, 2104-2108, Jul 83

[4.3] "High resolution noncollinear acoustooptic filters with variable passband characteristics: design"

A. Sivanayagm, D. Findlay

A.O. Vol. 23, No. 24, 4601-4608, Dec 84

[4.4] "Astronomical spectrophotometry with an acoustooptic filter photometer"

B. Bates, D. Halliwell, D. Findlay

A.O. Vol.23, No. 2, 257-260, Jan 84

[4.5] "Bichromatic nondispersive acoustooptic deflector"

M. Gazalet, C. Bruneel, R. Torguet, G. Thomin, B. Nongaillard

A.O., Vol.23, No. 13, 2192-2197, Jul 84

5

Bragg-cell Diffraction in Resonant Cavities

5.1 INTRODUCTION

Existing acoustooptic spectrum analysers have dynamic range limited by intermodulation. We have shown in chapters 2 and 3 that, by using a high-Q cell, intermodulation may be greatly reduced. In a conventional architecture a high-Q cell results in small bandwidth.

We have shown in chapter 4 that the bandwidth may be maintained in a system incorporating a high-Q cell by using a polychromatic light source (see figure 5.1). However the light powers reaching the detectors when using polychromatic sources are usually small. In order to achieve a large signal-to-noise ratio it is necessary to use large radiofrequency powers. Unfortunately, high acoustic powers cause high intermodulation and hence low polytone dynamic range, as described insection 2.2.1.1.

If the diffraction efficiency per watt of the Bragg-cell could be increased then the radiofrequency power required for a given light level reaching the detectors would be reduced. The material intermodulation would be decreased and the dynamic range increased.

It has been shown [5.1] that the diffraction efficiency of a stationary grating may be improved by placing the grating in a resonant cavity. We show that this also applies to light diffracted from an acousto-optic Bragg-cell, so that the diffraction efficiency per watt

may be increased. Following the method of Steier, Kavounas, Sahara and Kumar [5.1] we use a plane wave analysis, equating the fields before and after one round trip (this is valid if the cavity is at resonance).

5.2 TWO MIRROR CAVITY

Figure 5.2 shows a Bragg-cell in a resonant two-mirror cavity with one mirror 100% reflecting and the other with reflectance R. The electric field of the input beam E_{IN} is fed into the Bragg-cell at the Bragg angle and a fraction f of the light is diffracted to E_4. The fraction f is a function of the angle of diffraction, θ, at the Bragg-cell. The remainder passes through the cell to E_T. The diffracted output from the cavity is E_{OUT}.

Then we have

$$E_1 = E_6 \exp(ik_B l_1) , \qquad 5.1$$

$$E_2 = - R^{1/2} M E_1 , \qquad 5.2$$

$$E_3 = E_2 \exp(k_B l_1) , \qquad 5.2$$

$$E_4 = FBE_3 + Bf^{1/2} E_{in} \exp(i\omega_s t) , \qquad 5.4$$

$$E_5 = - ME_4 \exp(ik_B 2l_2) , \qquad 5.5$$

$$E_6 = FBE_5 ,$$

and 5.6

$$E_{out} = MPE_1 , \qquad 5.7$$

where we have defined

$$M = (1- \Delta_m)^{1/2} , \qquad 5.8$$

$$F = (1- f)^{1/2} , \qquad 5.9$$

$$B = (1- \Delta_B)^{1/2} , \qquad 5.10$$

$$P = (1-R)^{1/2} , \qquad 5.11$$

k_B is the propagation constant of the Bragg-diffracted light,

ω_s is the frequency of the acoustic wave,

and the round trip cavity losses are assumed to take place at the mirrors (Δ_m at each mirror) and the Bragg-cell (Δ_B for each pass through the cell). This excludes mirror coupling and Bragg diffraction.

Equating the fields after one round trip we obtain,

$$\frac{E_{out}}{E_{in}} = - \frac{FB^2M^2Pf^{1/2}\exp[i\{k_B(l_1 +2l_2) + \omega_s t\}]}{1-F^2B^2M^2R^{1/2}\exp[ik_B2(l_1 + l_2)]} , \qquad 5.12$$

which shows that the output E-field is frequency-shifted by the acoustic frequency with respect to the input E-field. In terms of intensity, we have

$$\frac{I_{out}}{I_{in}} = \frac{E_{out}E_{out}^{*}}{E_{in}E_{in}^{*}} = \frac{TE_1E_1^{*}}{E_{in}E_{in}^{*}} \qquad 5.13$$

with transmission, T_m, given by

$$T_m = 1-R \,. \qquad 5.14$$

At cavity resonance we have

$$l_1 + l_2 = \frac{m\pi}{k_B} \,, \qquad 5.15$$

where m is an integer. Then we obtain

$$\frac{I_{out}}{I_{in}} = \frac{B^4M^4F^2P^2f}{\{1-F^2B^2M^2R^{1/2}\}2} \,. \qquad 5.16$$

This ratio is a maximum for a mirror reflectivity, R_{best}, given by

$$R_{best} = B^4M^4F^4 \,. \qquad 5.17$$

Then we get

$$\frac{I_{out}}{I_{in}} = \frac{B^4M^4F^2f}{1-F^4B^4M^4} \,. \qquad 5.18$$

This equation shows that a Bragg-cell within a cavity can have a much larger efficiency than that of a Bragg-cell alone (=f), provided scattering losses are kept small.

Figure 5.3 shows the ratio of diffracted light intensity from the cavity as compared with a Bragg-cell alone as a function of round-trip parasitic loss. The cavity has been given an optimum mirror reflectivity, as in equation 5.17, for each value of round-trip loss, optimised at 1% cell efficiency. The parasitic loss from the cavity is the round-trip loss, excluding that diffracted from the cell and transmitted by the mirror. We have

$$\delta=\delta_{transmitted}+\delta_{diffracted}+\delta_{parasitic}, \qquad 5.19$$

$$\delta_{parasitic}= 2\Delta_m+2\Delta_B. \qquad 5.20$$

For round-trip parasitic losses less than about 10% , the improvement in diffracted power is greater than an order of magnitude.

Figures 5.4, 5.5 and 5.6 show the ratio of the cavity output to the cell output as a function of cell efficiency. The round-trip parasitic losses are 22%, 10% and 4% respectively. The cavities have mirror reflectances optimised for a cell efficiency of 1%.

Figures 7 and 8 show the cavity output as a function of cell efficiency for 10% and 4% parasitic losses.

These figures show that the cavities have a linear response for cell efficiencies less than about 5%. As the cavities become more efficient (smaller parasitic losses) the non-linearities become more pronounced and start to become significant at lower cell efficiencies.

If we introduce gain, g, into the cavity at the position of the Bragg-cell, then, for small intensities well below saturation, we have

$$E_4 = BFg^{1/2}E_3 + Bf^{1/2}g^{1/2}E_{in}\exp[i\omega_s t] \qquad 5.21$$

and

$$E_6 = BFg^{1/2}E_5 . \qquad 5.22$$

Combining 5.1, 5.2, 5.3, 5.5, 5.7, 5.21 and 5.22, we obtain

$$\frac{I_{out}}{I_{in}} = \frac{B^4M^4F^2fPg^2}{\{1-F^2B^2M^2gR^{1/2}\}^2} . \qquad 5.23$$

If the round-trip gain is equal to the cavity loss, then lasing occurs and we have

$$g = \frac{1}{F^2B^2M^2R^{1/2}} \qquad 5.24$$

5.2.1 White light radiofrequency spectrum analyser using the two mirror cavity configuration

Figure 5.9 shows an arrangement for using the linear-cavity enhanced Bragg-cell diffraction in a white-light radiofrequency spectrum analyser. The wavelength of the diffracted light reaching the spectrometer slit is inversely proportional to the radiofrequency applied to the Bragg-cell.

If the mirrors are held fixed, then the bandwidth of the system is limited to the bandwidth of the cavity. We have

$$d\nu = \frac{c\delta}{l_1 + l_2} \qquad 5.25$$

and

$$\delta = 2\Delta_m + 2\Delta_B + 2f + 1 - R \; . \qquad 5.26$$

Then we have the fractional bandwidth, given by

$$\frac{d\omega}{\omega} = \frac{d\lambda}{\lambda} = \frac{\lambda[2\Delta_B + 2\Delta_m + 2f + 1\text{-}R]}{l_1 + l_2} \; . \qquad 5.27$$

This ratio is of the order of 10^{-6}, so that a practical radiofrequency spectrum analyser could not be based on a fixed cavity using this configuration. However, if one of the mirrors is repeatedly cycled through one free spectral range, then the wavelength which is diffracted to the slit will be on resonance in the cavity twice during each cycle. The light reaching the spectrometer will consist of a series of pulses, whose amplitude is proportional to the amplitude of the radiofrequency applied to the cell. (The system remains linear, as shown in figures 5.4 to 5.8, for low diffraction efficiencies but starts to saturate for cell efficiencies above 5%. The usable dynamic range will therefore be limited to input radiofrequency powers less than those which give greater than 5% cell efficiencies). The ratio of the time between pulses, τ_l, to the pulse width, τ_p, is of the order of the finnesse, F, of the cavity. We have

$$\frac{\tau_l}{\tau_p} \cong F$$

$$F = 2\pi/\delta \qquad 5.28$$

and

$$F = 2\pi/(2\Delta_B+2\Delta_m+2f+1-R)\ . \qquad 5.29$$

F is of the order of 10. The signal pulses will therefore have duration of around 1/10th of the scan period.

5.3 FOUR MIRROR CONFOCAL CAVITY CONFIGURATION

5.3.1 Introduction

The four mirror confocal cavity configuration is shown in figure 5.10. Figures 5.11 and 5.12 show that the round-trip path-length remains constant for small changes in Bragg angle.

The decreases in length of the horizontal parts of the round-trip path-length are approximately compensated for by the increases in length of the inclined parts as the angle θ changes to $\theta+d\theta$. The 4-mirror configuration can be used as a radiofrequency sprectrum analyser with monochromatic light by measuring the Bragg output angle as the radiofrequency changes.

Using a scalar plane wave analysis, as above, we have

$$E_1 = Bf^{1/2}E_{in}\exp(i\omega_s t) + BFE_6 \quad 5.30$$

$$E_2 = E_1\exp(ik_B l_1) \quad 5.31$$

$$E_3 = -MR^{1/2}E_2 \quad 5.32$$

$$E_4 = -ME_3\exp(ik_B l_2) \quad 5.33$$

$$E_5 = B_2E_4 \quad 5.34$$

$$E_6 = M^2E_5\exp(ik_B l_3) \quad 5.35$$

$$E_{out} = MPE_2 \quad 5.36$$

where we have written

$$B_2 = (1 - \Delta_{B2})^{1/2} \quad 5.37$$

and

$$B = (1 - \Delta_B)^{1/2} \quad 5.38$$

and

Δ_B is the scattering loss on passing through the cell for the Bragg-angle rays, E_{in} and E_6, Δ_{B2} is the scattering loss for the ray E_4 on passing through the cell,

l_1 is the optical path length for the rays from E_6 to E_2,

l_2 is the optical path length for the rays from E_3 to E_4,

l_3 is the optical path length for the rays from E_4 to E_6

At cavity resonance, we have

$$l_1 + l_2 + l_3 = \frac{2m\pi}{k_B} \qquad 5.39$$

Equating the fields after one round -trip, we obtain

$$\frac{E_{out}}{E_{in}} = \frac{MPBf^{1/2}\exp[i(k_B l_1 + \omega_s t)]}{1 - R^{1/2}BB_2FM^4} \qquad 5.40$$

and we have

$$\frac{I_{out}}{I_{in}} = \frac{B^2M^2P^2f}{\{1 - R^{1/2}BB_2FM^4\}^2} \qquad 5.41$$

Introducing gain into the cavity at the Bragg-cell, we have

$$E_1 = Bf^{1/2}g^{1/2}E_{in}\exp(i\omega_s t) + BFg^{1/2}E_6 \qquad 5.42$$

and

$$E_5 = B_2 g_2^{1/2} E_4 \qquad 5.43$$

where g is the gain for the Bragg-angled rays, E_{in} and E_6, and g_2 is the gain for the ray E_4

Finally, we obtain

$$\frac{I_{out}}{I_{in}} = \frac{BMPfg}{\{1 - R^{1/2}BB_2FM^4(gg_2)^{1/2}\}^2} \qquad 5.44$$

Once again lasing occurs when the round trip gain equals the round trip loss. This occurs when the gain is given by,

$$gg_2 = \frac{1}{RB^2B_2^2F^2M^8} \qquad 5.45$$

5.3.2 Bandwidth, resolution and dynamic range

The usable bandwidth of the combined cavity and Bragg-cell is limited, for monochromatic systems, by the bandwidth of the cavity with the cell in it. This is given, approximately, by

$$d\nu = c\delta / L \qquad 5.46$$

where c is the speed of light in the cavity, δ is the round-trip cavity-loss, and L is the optical path length for the round-trip.

For the confocal cavity configuration, δ is given by

$$\delta = \Delta_B + \Delta_{B2} + \nu + 4\Delta_m + 1 - R \qquad 5.47$$

and L is given by

$$L = l_1 + l_2 + l_2 \qquad 5.48$$

Therefore, from equations 5.46, 5.47 and 5.48, we obtain

$$d\nu = \frac{c[\Delta_B + \Delta_{B2} + \nu + 4\Delta_m + 1 - R]}{l_1 + l_2 + l_2} \qquad 5.49$$

Alternatively, we may express dν in terms of the cavity finesse, for small cavity losses, δ is given, approximately, by

$$\delta = 2\pi / F \qquad 5.50$$

where F is the finesse of the cavity. Hence, we have

$$d\nu = \frac{2\pi c}{LF} \qquad 5.51$$

The dynamic range of the combined grating and cavity is approximately that of the cell alone, provided diffraction efficiencies, f, are held small .

For the combination, we have

$$\frac{I_{out}}{I_{in}} = \frac{B^2M^2P^2f}{\{1 - R^{1/2}BB_2FM^4\}^2} \qquad 5.52$$

For small diffraction efficiencies ($f << 1$), this expression is approximately proportional to f, and hence the output, I_{out}, varies linearly with the diffraction from the cell. The dynamic range of the cavity combination will, therefore, be similar to that of the cell alone. The resolution of the combined cavity and Bragg-cell is approximately the same as that of a cell with the same illumination area of incident light. The output is approximately proportional to the diffraction efficiency, f, of the Bragg-cell alone. This has a variation with output angle for a given input angle which defines the resolution of the Bragg-cell. Therefore, the variation of the combined cavity and Bragg-cell with output angle must be the same as for that of a cell alone. Hence, the angular resolution of the combined cavity and cell is the same as that of a cell alone. However, this may be quite poor due to the narrow beam waist required to satisfy the condition of constant round trip path length within the range of output angles q produced by the radiofrequency bandwidth.

5.4 MULTI CHANNEL FIBRE OPTIC CAVITIES

To avoid the problems of limited bandwidth and resolution imposed by the above monochromatic systems, a multiple cavity system could be utilised. For each frequency channel, a different cavity is used, tuned to its respective wavelength. See figures 5.13 and 5.14. Figure 5.13 shows the system with an input beam, E_{in}, and the Bragg diffracted light passing round one fibre ring cavity. Figure 5.14 shows just one channel. The piezo-electric cylinder is used to keep the cavity on resonance for its given frequency. The light coupled out of the cavity is E_{out}.

Using an analysis similar to that above, we obtain

$$\frac{I_{out}}{I_{in}} = \frac{(BL^2PC_1)^2 f}{\{1 - BFL^2C_2C_3R^{1/2}\}^2} \qquad 5.53$$

where we have

$$C_1 = (1 - \Delta_{c1})^{1/2} \qquad 5.54$$

$$C_2 = (1 - \Delta_{c2})^{1/2} \qquad 5.55$$

$$C_3 = (1 - \Delta_{c3})^{1/2} \qquad 5.56$$

Δ_{c1} is the coupling loss into the fibre at E_4 for the Bragg diffracted light from the cell,

Δ_{c2} is the coupling loss into the fibre at E_4 for the light which has passed around the loop,

Δ_{c3} is the coupling loss from E_1 to E_2,

Δ_L is the scattering loss at the lenses,

and R is the transmission at the coupler, so that a fraction 1-R of the light in the fibre is transmitted to E_{out}.

The coupling loss Δ_{c1} varies as the Bragg-angle changes and will be different for each channel. (Normally it would be unity unless the frequency of the radiofrequency signal is such as to couple light into that channel). The full width of the cell may be illuminated, so that with this system the resolution and the bandwidth are maintained whilst still retaining the diffraction efficiency enhancement of the cavity.

5.5 CONCLUSION

The use of cavity enhanced Bragg-cell diffraction within acoustooptic radiofrequency spectrum analysers should allows reductions in intermodulation by reducing the acoustic

power densities in the Bragg-cell required for a given received optical power at the detectors.

A practical polychromatic system with a high dynamic range, low intermodulation and large bandwidth could be realised without the usual problems associated with extremely low light levels at the detectors.

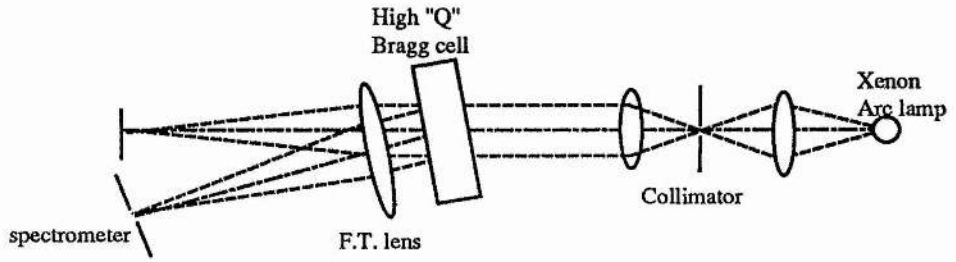

Figure 5.1

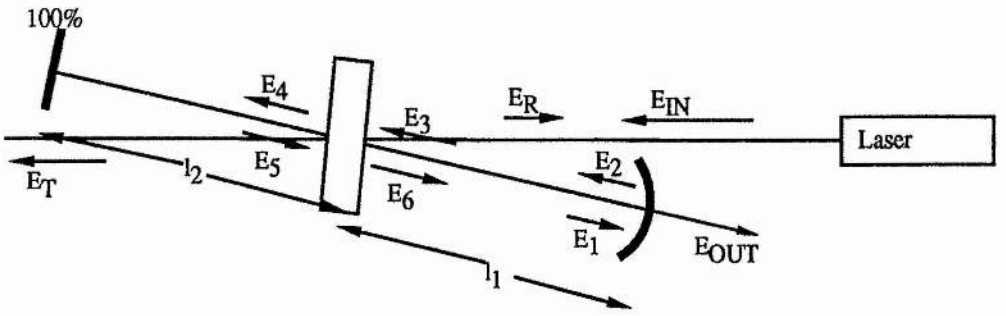

Figure 5.2

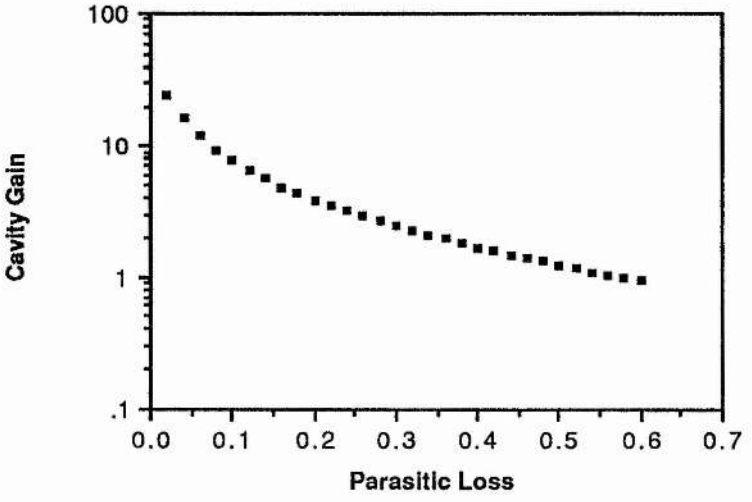

Figure 5.3

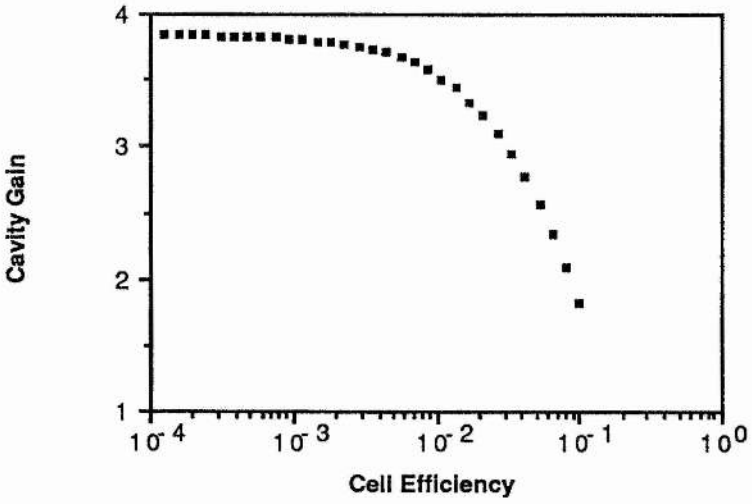

Figure 5.4

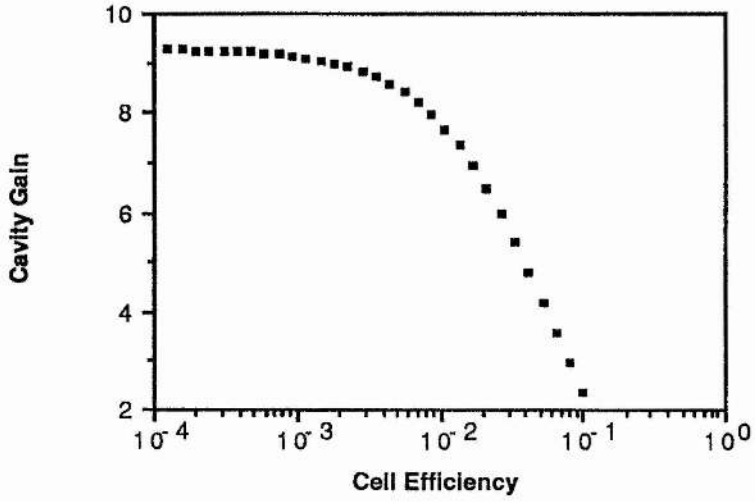

Figure 5.5

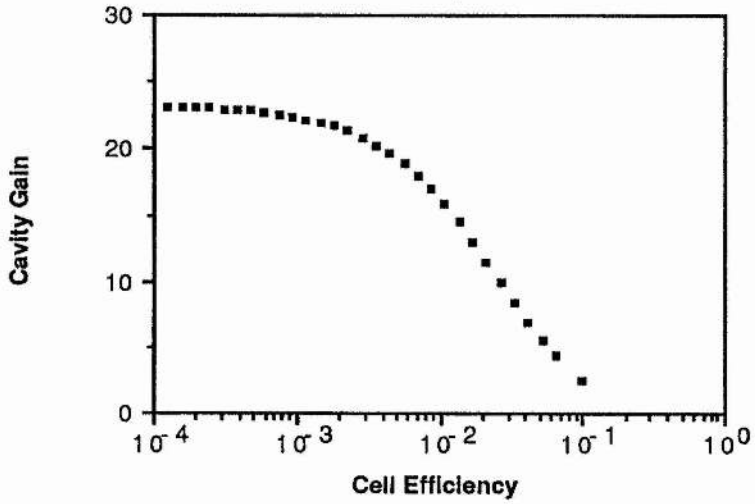

Figure 5.6

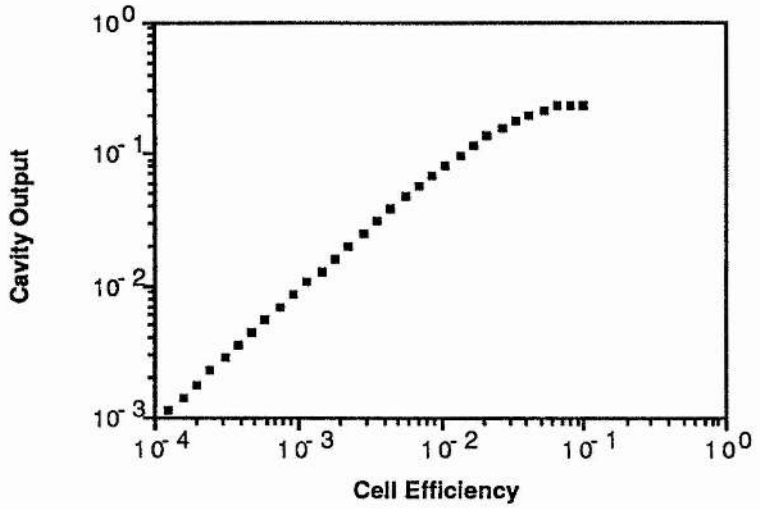

Figure 5.7

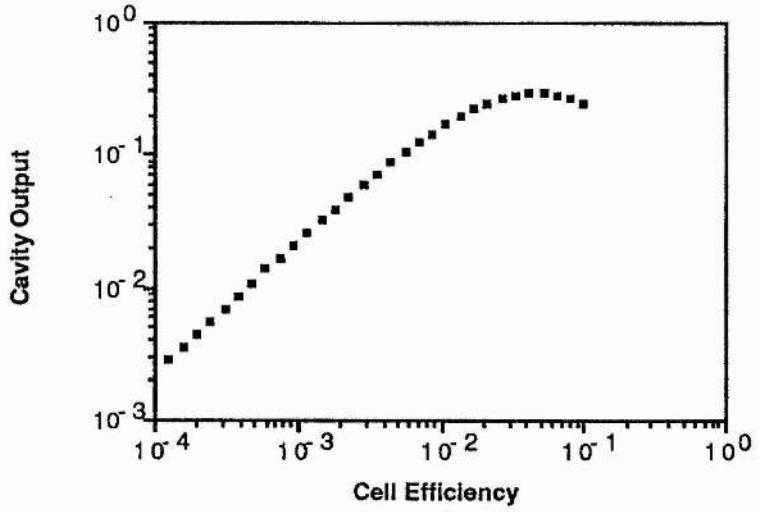

Figure 5.8

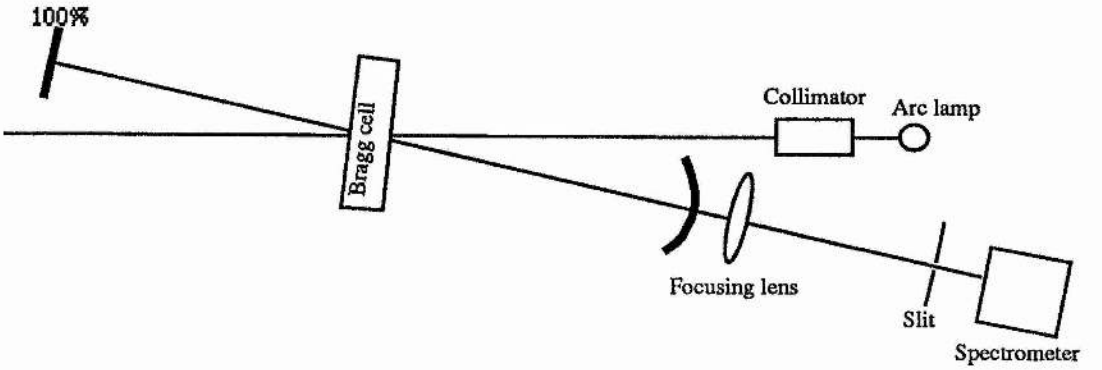

Figure 5.9

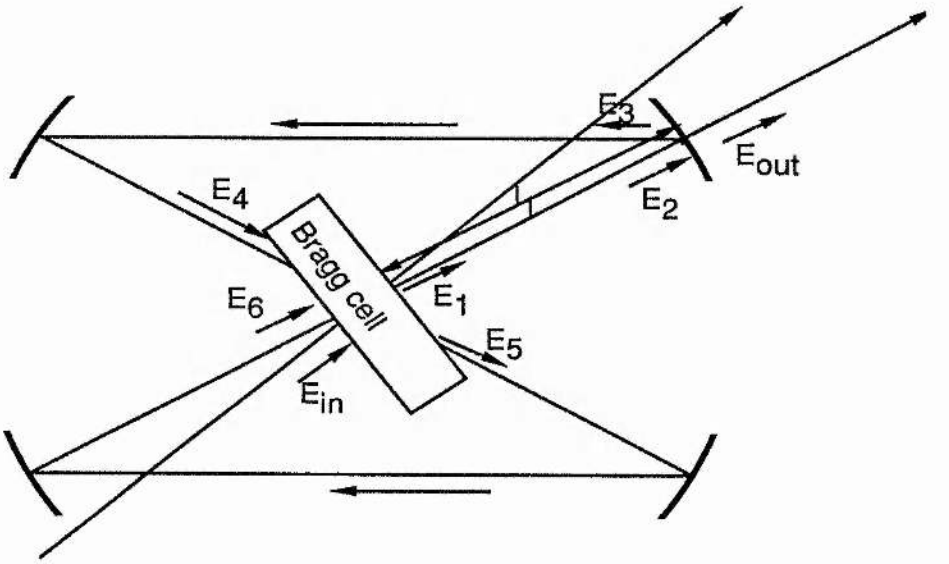

Figure 5.10

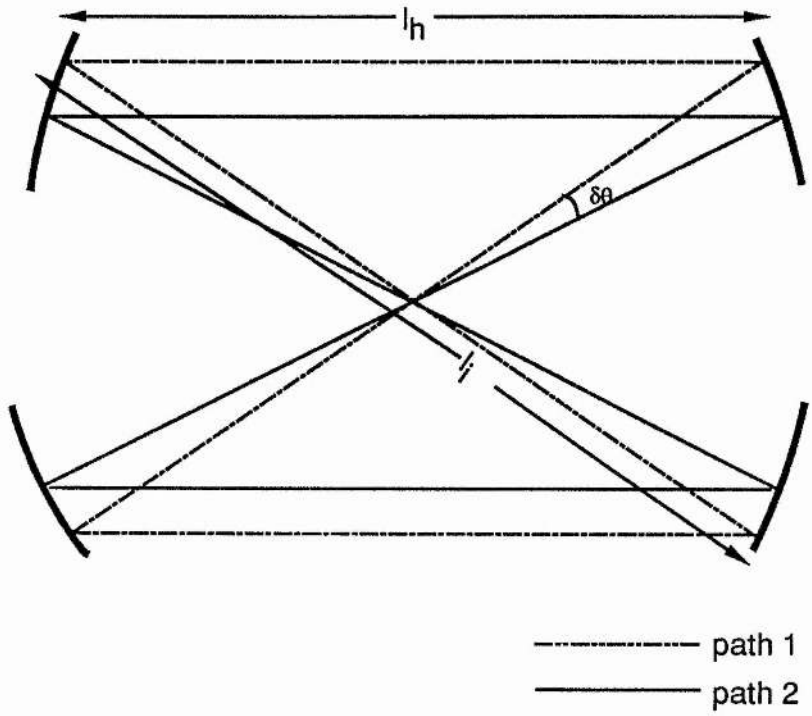

Figure 5.11

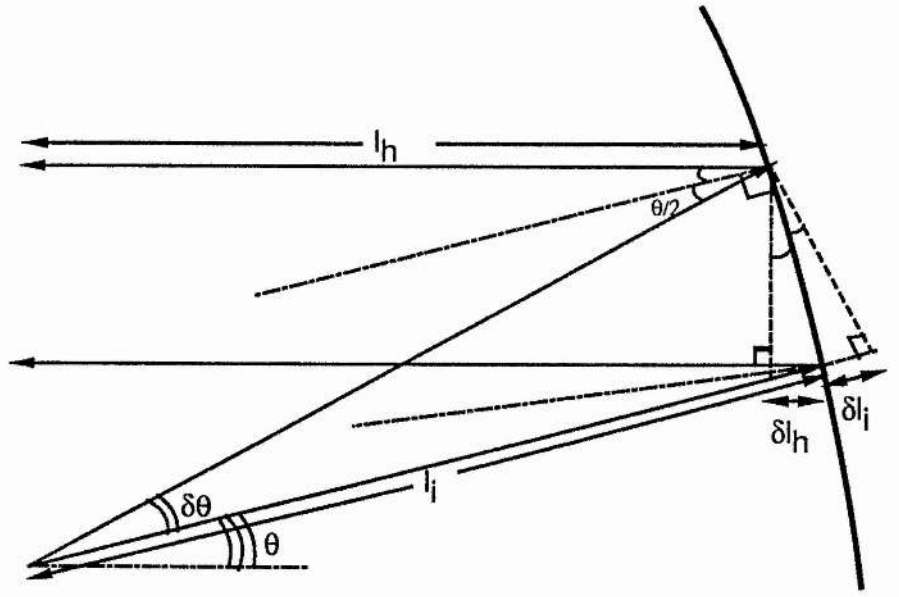

$$\delta l_h = \delta l_i = l_i \sin(\theta/2)\delta\theta$$

Figure 5.12

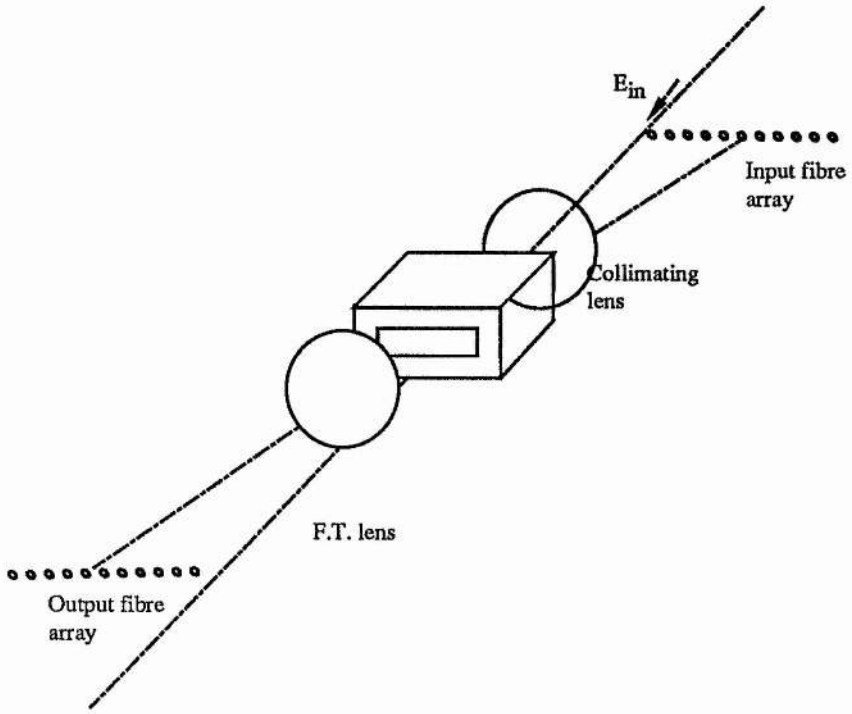

Figure 5.13

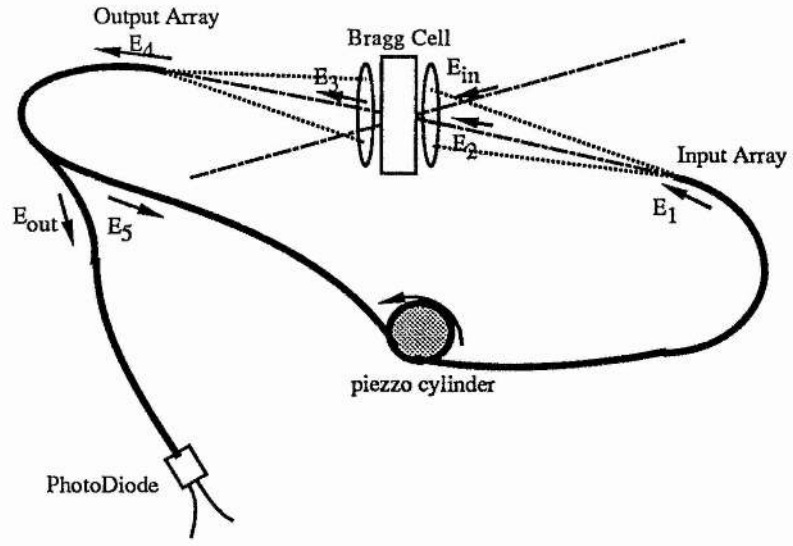

Figure 5.14

5.8 REFERENCES

[5.1]. "Enhanced optooptical light deflection using cavity resonance"

Steier, Kavounas, Sahara and Kumar.

A.O. Vol. 27, No.8, 1603-1606, April 88

6

Temporal Analysis of Light Diffracted from Radiofrequency Pulses within an Acoustooptic Bragg-Cell

6.1 INTRODUCTION

The study of radio-frequency pulses within acoustooptic spectrum analysers has been receiving much attention [6.1-6.5] with work being aimed at eliminating false alarms ("Rabbit's Ears") caused by the clipping effect of the finite temporal window of the system.

Previous work has involved eliminating the false alarms by means of complex post-detection electronics using pattern recognition to distinguish "real" signals from those created by the aperturing effects of the spectrum analyser.

In this chapter we analyse the temporal and spatial variation of light diffracted by radio-frequency pulses within a Bragg-cell. We show that a simple post-detection filter may be employed to remove false alarms.

6.2 THEORETICAL ANALYSIS

In order to determine the temporal profile we shall assume that the diffraction pattern is described wholly by the Fourier transform of the aperture function with only the positive

components being produced. This is valid for a high-Q cell, operated in the linear, weak-signal, Bragg regime.

The radiofrequency signal, s(t), is applied to the cell and creates a phase modulation on the incident plane laser beam given by

$$S(x,t) = s(t-x/v)\exp[i\omega_s(t-x/v)] , \qquad 6.1$$

where v is the acoustic velocity in the cell, x is the direction of propagation of the acoustic wave and ω_s is the radiofrequency.

The spatial distribution of the diffraction pattern is given by the Fourier transform,

$$d(\rho,t) = \int_{-\infty}^{\infty} S(x,t)a(x)\exp(i\rho x)dx , \qquad 6.2$$

where ρ is the spatial frequency given by

$$\rho = \frac{2\pi}{\lambda}\sin\theta \qquad 6.3$$

and λ is the optical wavelength and θ is the angle of diffraction.The optical aperture in the cell is described by a(x). We shall assume even illumination and no attenuation of the acoustic beam so that we have

$a(x) = 0$ for $x<-L/2$

$a(x) = 1$ for $-L/2<x<L/2$

$a(x) = 0$ for $x>L/2$

where L is the length of the optical aperture.
Here we are interested in the temporal angular frequencies, ω, present at a particular spatial frequency, ρ.

For a detector monitoring the diffraction pattern at a spatial position corresponding to the spatial frequency, ρ, the angular frequencies present are given by

$$d(\rho,\omega) = \int_{-\infty}^{\infty} d(\rho,t)\exp(-i\omega t)dt\,, \qquad 6.4$$

where we have assumed that the detector monitors the entire period during which the pulse exists within the cell.

There are three stages in the evolution of the pulse as it passes through the cell. First it enters the cell, increasing in length. In the second phase the pulse passes through the cell either filling it ($\tau > T$), or passing through with constant length, $v\tau$ ($\tau < T$). In the third phase the pulse leaves the cell, decreasing in length as it does so.

First we first calculate the spatial distribution due to diffraction by the pulse as a function of time, t. Then the temporal distribution is derived for the three stages of evolution of the pulse. The complete temporal distribution is the sum of the three contributions.

A more complete derivation of the following equations is given in appendix 2.

6.2.1 Short pulse case

We shall first consider the case of a pulse with duration, τ, less than the time window, T, of the cell. The pulse first enters the cell with its tail clipped by the window, then passes through the window until its leading edge reaches the end of the window when it begins to leave the cell.

For $t<\tau$ the pulse is entering the system and the diffraction pattern is given by equation 6.2 where we have

$$d_1(\rho,t) = \int_{-L/2}^{-L/2+vt} A\exp[i\omega_s(t-x/v)]\exp(i\rho x)dx \qquad 6.5$$

$$= Avt\exp[i(\rho+\rho_s)vt/2]\mathrm{sinc}[(\rho-\rho_s)vt/2]\exp[i(\rho_s-\rho)L/2] \qquad 6.6$$

and so we may write

$$d_1(\rho,t) = A\phi_1 vt\exp[i(\rho+\rho_s)vt/2]\mathrm{sinc}[(\rho-\rho_s)vt/2]\ , \qquad 6.7$$

where ϕ_1 is a phase factor.

For $t<\tau$ the diffraction pattern is a sinc function with angular half width λ/vt.

For $\tau<t<T$ the pulse is entirely within the cell and we have

$$d_2(\rho,t) = \int_{-L/2+vt}^{-L/2+vt+v\tau} A\exp[i\omega_s(t-x/v)]\exp(i\rho x)dx \qquad 6.8$$

$$=A\nu\tau\exp[i\{(\nu\tau-L)(\rho-\rho_s)/2+\nu t\rho\}]\mathrm{sinc}[(\rho-\rho_s)\nu\tau/2]\ . \qquad 6.9$$

But we may write

$$\rho v = \omega_\rho\ , \qquad 6.10$$

where ω_ρ is the Doppler shifted centre-frequency corresponding to the spatial frequency ρ.

Then we have

$$d_2(\rho,t) = A\nu\tau\exp[i(\nu\tau-L)(\rho-\rho_s)/2]\exp(i\omega_\rho t)\mathrm{sinc}[(\rho-\rho_s)\nu\tau/2] \qquad 6.11$$

and we obtain

$$d_2(\rho,t) = A\nu\tau\exp(i\omega_\rho t)\mathrm{sinc}[(\rho-\rho_s)\nu\tau/2]\phi_2\ , \qquad 6.12$$

where ϕ_2 is a phase term.

For $\tau<t<T$ the spatial distribution is a sinc function with angular half width $\lambda/\nu\tau$.

For $T<t<T+\tau$ the pulse is leaving the cell. By symmetry we see that the diffraction pattern must be the same as that for the pulse entering the system, but with a different phase term, ϕ_3.

$$d_3(\rho,t) = \phi_3 d_1(\rho,t)\ , \qquad 6.13$$

$$d_3(\rho,t) = A\phi_4\nu t\exp[i(\rho+\rho_s)\nu t/2]\mathrm{sinc}[(\rho-\rho_s)\nu t/2]\ . \qquad 6.14$$

The temporal distribution is given by equation 6.4 where we have

$$d(\rho,\omega) = \int_0^{\tau} d_1(\rho,t)\exp(-i\omega t)dt + \int_{\tau}^{T} d_2(\rho,t)\exp(-i\omega t)dt + \int_{T}^{T+\tau} d_3(\rho,t)\exp(-i\omega t)dt . \quad 6.15$$

We write equation 6.15 as

$$d(\rho,\omega) = d_1(\rho,\omega) + d_2(\rho,\omega) + d_3(\rho,\omega) , \quad 6.16$$

where we have

$$d_1(\rho,\omega) = \int_0^{\tau} d_1(\rho,t)\exp(-i\omega t)dt \quad 6.17$$

$$d_1(\rho,\omega) = \frac{A\tau\phi_1}{\rho-\rho_s}\{\phi_6 \mathrm{sinc}[(\omega_s-\omega)\tau/2] - \phi_5 \mathrm{sinc}[(\omega_\rho-\omega)\tau/2]\} , \quad 6.18$$

where ϕ_5 and ϕ_6 are phase terms .

The contribution to the temporal profile for $t < \tau$ consists of two sinc functions, in frequency space, centred around ω_ρ and ω_s with FWHM of $2\pi/\tau$.

$$d_2(\rho,\omega) = \int_{\tau}^{T} d_2(\rho,t)\exp(-i\omega t)dt \quad 6.19$$

$$d_2(\rho,\omega) = A\phi_2\phi_7 v\tau(T-\tau)\mathrm{sinc}[(\rho-\rho_s)\tau/2]\mathrm{sinc}[(\omega_\rho-\omega)(T-\tau)/2] , \quad 6.20$$

where ϕ_7 is a phase term.

The contribution to the temporal profile for $\tau<\tau<T$ consists of a sinc function, in frequency space, centred around ω_ρ with a FWHM of $2\pi/(T-\tau)$.

For $t > T$ we have

$$d_3(\rho,\omega) = \int_T^{T+\tau} d_3(\rho,t)\exp(-i\omega t)dt \qquad 6.21$$

$$= \int_T^{T+\tau} \phi_3 d_2(\rho,t)\exp(-i\omega t)dt \qquad 6.22$$

and we see

$$d_3(\rho,\omega) = \phi_3\, d_1(\rho,\omega)\ . \qquad 6.23$$

The contribution to the temporal profile for $t > T$ is the same as that for $t<\tau$ but with a different phase, ϕ_3.

The total temporal distribution of the pulse travelling through the whole cell is given by

$$d(\rho,\omega) = d_1(\rho,\omega) + d_2(\rho,\omega) + d_3(\rho,\omega) \qquad 6.24$$

$$d(\rho,\omega) = \phi_1(1+\phi_3)\frac{A\tau}{\rho-\rho_s}\{\phi_6 \mathrm{sinc}[(\omega_s-\omega)\tau/2] - \phi_5\,\mathrm{sinc}[(\omega_\rho-\omega)\tau/2]\}$$
$$+ 2\phi_2\phi_7\frac{A(T-\tau)}{\rho-\rho_s}\mathrm{sinc}[(\rho-\rho_s)v\tau/2]\mathrm{sinc}[(\omega_\rho-\omega)(T-\tau)/2]\,. \qquad 6.25$$

The distribution contains terms centred around ω_ρ with FWHM of $2\pi/\tau$ and $2\pi/(T-\tau)$, the relative magnitudes dependent on the pulse length, τ, compared with the Bragg-cell aperture T. There is also a term centred around ω_s with FWHM $2\pi/\tau$, proportional to the pulse length, τ.

The distribution centred around ω_s comes from the stage where the pulse is clipped by the aperture, entering and leaving the cell. It is produced by the fixed, clipped, edge of the pulse.

The distribution centred around ω_ρ is produced by the moving edges of the pulses and there are contributions from all stages in the evolution of the pulse.

6.2.2 Long-pulse case

For a pulse with duration greater than the Bragg-cell aperture, i.e. $\tau > T$, the contributions from the pulse entering and leaving the cell are similar to those produced by the short pulse.

For $t < T$ (pulse entering the cell) the spatial distribution is given by

$$d_1(\rho,t) = A\phi_1 vt\exp[i(\rho+\rho_s)vt/2]\mathrm{sinc}[(\rho-\rho_s)vt/2]\,. \qquad 6.26$$

The contribution to the temporal distribution is

$$d_1(\rho,\omega) = \frac{AT\phi_1}{\rho-\rho_s}\{\phi_6 \mathrm{sinc}[(\omega_s-\omega)T/2] - \phi_5\, \mathrm{sinc}[(\omega_\rho-\omega)T/2]\}\,. \qquad 6.27$$

There are similar terms for $\tau < t < T+\tau$ (pulse leaving the cell).

For the time the pulse fills the cell, $T<t<\tau$, we have a new term given by

$$d_2(\rho,t) = \int_{-L/2}^{L/2} A\exp[i\omega_s(t-x/v)]\exp(i\rho x)dx \qquad 6.28$$

$$d_2(\rho,t) = A\exp(i\omega_s t)L\,\mathrm{sinc}[(\rho-\rho_s)L/2]\,. \qquad 6.29$$

The spatial distribution is a sinc function with angular half width λ/L.

The contribution to the temporal distribution is then given by equation 6.4 where we have

$$d_2(\rho,\omega) = \int_{T}^{\tau} A\exp(i\omega_s t)L\,\mathrm{sinc}[(\rho-\rho_s)L/2]\exp(-i\omega t)dt \qquad 6.30$$

$$d_2(\rho,\omega) = AL(\tau-T)\mathrm{sinc}[(\rho-\rho_s)L/2]\mathrm{sinc}[(\omega_s-\omega)(\tau-T)/2]\phi_1\,, \qquad 6.31$$

where ϕ_1 is a phase term.

The contribution to the temporal profile for $T<t<\tau$ is a sinc function centred at ω_s with half-width, $\frac{2\pi}{\tau-T}$.

The full temporal distribution for the long pulse is then

$$d(\rho,\omega) = (1+\phi_3)\frac{AT\phi_4}{\rho-\rho_s}\{\phi_6 \mathrm{sinc}[(\omega_s-\omega)T/2] - \phi_5\,\mathrm{sinc}[(\omega_\rho-\omega)T/2]\}$$
$$+ 2\phi_8\frac{A(\tau-T)}{\rho-\rho_s}\sin[(\rho-\rho_s)L/2]\,\mathrm{sinc}[(\omega_s-\omega)(\tau-T)/2]\,. \qquad 6.32$$

The full temporal distribution contains two terms centred around ω_s with FWHM of $2\pi/T$ and $2\pi/(\tau-T)$. There is a term centred around ω_ρ proportional to T with FWHM of $2\pi/T$.

The distribution centred around ω_s has contributions from all stages in the evolution of the pulse. The pulse is always being clipped by the aperture so there is always a fixed edge.

The distribution centred around ω_ρ is created when the pulse is entering and leaving the cell, when there is a moving edge to the pulse.

6.3 EXPERIMENTAL VERIFICATION

6.3.1 Experimental arrangement

The apparatus shown in figure 6.1 was used to investigate the temporal variation of the diffracted light from the the Bragg-cell, 4.

Light from the laser, 1, is expanded and collimated before passing through the beam splitter, 5. This separates the light in two, half being used as a reference, and the other half passing through the Bragg-cell, having been clipped by the slit, 3.

The diffracted beam is then deflected off the rotateable mirror, 6, before being amplitude divided again at beam splitter 5 . One half is passed through a lens and falls on a ccd array, 8, at the focal plane of the lens. The other half joins the un-diffracted reference beam at the beam splitter, 5. The reference beam has the same polarisation as the diffracted beam, the reference beam having passed through a quarter wave plate, 10.

The combined beams are then passed though a lens and fall on to the high speed photo-diode (BPX 65), 9, in the focal plane of the lens.

The output from the photodiode is amplified and monitored on a spectrum analyser. The temporal evolution of a given frequency band can then be observed by taking the spectrum analyser output, on manual sweep, with the bandwidth set to 3 MHz.
By rotating the mirror, 6, the spatial frequency, ρ, under observation can be changed.

6.3.2 Experimental results

Figures 6.3 - 6.11 show the frequency components present at a spatial position, ρ, corresponding to a centre frequency, $\omega_\rho/2\pi$, equal to 133.7 MHz for various pulse durations. The output is integrated over a period of about 10 seconds

The carrier frequency, $\omega_s/2\pi$, is 130.8 MHz with a pulse-to-pulse spacing of 1μs.

The slit width, L, is 1.25 mm The acoustic velocity, v, is 800 m/s corresponding to an optical window, T, of 2 μs.

Figures 6.12 - 6.19 show the output from the spectrum analyser centred on one radiofrequency, $\omega_\rho/2\pi$=133.7 MHz and figs 18-26 are centred at $\omega_\rho/2\pi$=130.8 MHz. The spectrum analyser bandwidth is 3MHz. The pulse durations are the same as for figures 6.3 - 6.11.

The results confirm the theoretical treatment showing that while the pulses are entering or leaving the cell then there are two frequency bands present, sinc functions centred at ω_ρ and ω_s. For a short pulse, τ<<T, the band at ω_ρ dominates. For longer pulses, τ >>T, the band centred at ω_s is dominant.

The bandwidth of the distribution around ω_s decreases with increasing pulse duration. The bandwidth at ω_ρ is inversely proportional to slit width. This is shown in figures 6.28 - 6.33 which show the frequency components for various slit widths for a pulse duration, τ, of 100 ns.

Figures 6.36 and 6.35 show the envelope traced out by rotating the mirror, 6, to adjust ρ for pulse durations, τ , of 100ns and 1.1 μs, respectively. Figure 6.34 shows the distribution at the position corresponding to $\omega_\rho/2\pi$=135MHz for the same slit width, 1.25mm.

The envelope follows the Fourier transform of the applied signal.

Figure 6.37 shows the temporal profile at $\omega_\rho/2\pi$=133.7 MHz,

$\omega_s/2\pi$=130.8 MHz,

$\omega=\omega_\rho$,

τ=700ns,

and T=2.5μs

The cell is illuminated unevenly. The light distribution is intense near the transducer, tailing away gradually with increasing distance from the transducer. The temporal profile now closely matches the input profile, despite the optical window being much longer than the pulse duration.

We have shown that the carrier frequency, ω_s, is only produced when the pulse is clipped by an edge. Since there is only one sharp edge we obtain the temporal profile of the pulse by monitoring ω_s.

The rise time is limited by the bandwidth of the spectrum analyser (3 MHz for this measurement). If a larger bandwidth, BW, had been used then the position, ρ, would need to be changed to ensure $(\omega_\rho-\omega_s)>BW$ If this condition is not fulfilled then frequency components at ω_ρ start to reach the output.

6.4 APPLICATIONS AND CONCLUSIONS

We have shown that the diffraction pattern produced by radiofrequency pulses within a Bragg-cell contain two Doppler shifted frequency components. When the pulse is clipped by the aperture there are frequency components at the carrier frequency of the pulses, ω_s.

When there is a moving edge in the cell, the diffraction pattern contains frequency components corresponding to the spatial position being monitored, ω_ρ.

By monitoring the frequency components, ω_s, away from the expected frequencies, ω_ρ, at the spatial position, ρ, it is possible to determine whether a pulse is evolving within the cell. The presence of frequency components at ω_s indicate that the pulse is clipped by the aperture.

In existing spectrum analysers when a pulse first enters the optical window its Fourier transform, $d(\rho,t)$, is spread over a large range of spatial frequencies, ρ. Detectors looking at spatial frequencies away from the centre frequency, ω_s, then detect a signal as pulses enter or leave the cell. These are spurious frequency signals in the sense that they are created by the finite temporal aperture of the system and are not present in the original signal. They are known as "Rabbits Ears" due to the two blips seen on an oscilloscope monitoring a detector as a pulse travels through the cell.

In the two cell interferometric architecture [6.6] shown in figure 6.2, the reference cell is driven by a chirp signal so that it creates a spatial and temporal distribution which matches that from the signal cell, for cw signals.

The beat-frequency between reference and signal arms is constant for all spatial frequencies, ρ, to within the resolution limit of the Bragg-cell apertures, for cw signals. The beat-frequency, ω_B, depends on the angular misalignment of the reference and signal beams, given by

$$\omega_B = v(\rho_{rs} - \rho_s)$$

where ρ_{rs} is the spatial frequency of the reference cell at the position in space corresponding to the centre frequency of the signal cell.

When a pulse enters the signal cell then two frequencies will be produced by the signal cell at spatial positions, ρ, away from the centre frequency position, ρ_s. The beat-frequencies will then be centred on ω_B and $\omega_B+(\omega_\rho-\omega_s)$. Therefore, if a band-stop filter is attached to the outputs from each of the detectors with its stop band centred at ω_B then any output from this filter will indicate that the signal from that detector is not at the centre-frequency. This may then be used to discriminate the "Rabbit Ears" from the true Fourier components.

The bandwidth of the stop-band filter should be chosen to match the resolution of the cells.

By employing non-uniform illumination it is possible to obtain temporal information to better resolution than that of the aperturing window, by observing the temporal evolution of the carrier frequency, ω_s, at a spatial position, ρ, well away from the carrier frequency position in space.

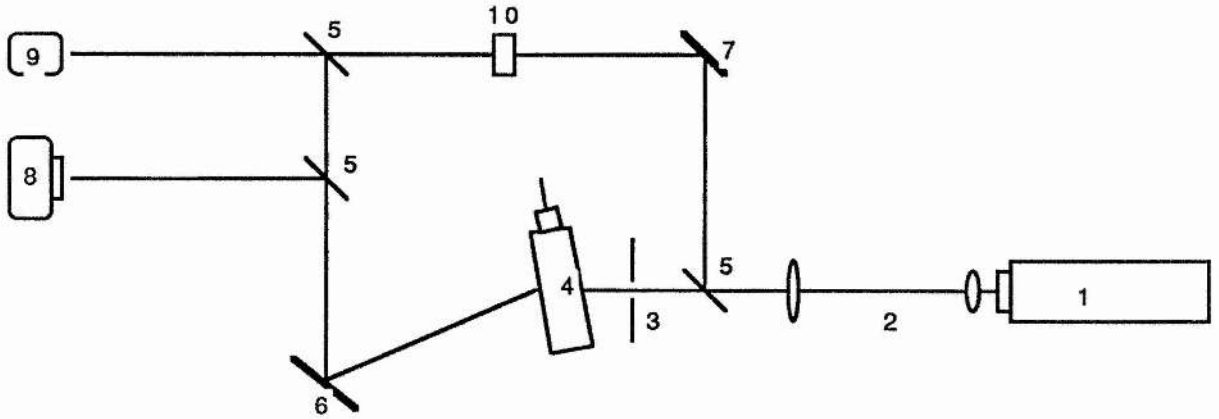

1 HeNe laser

2 Beam expansion and collimating optics

3 Adjustable slit

4 Bragg-cell

5 Pellicle beam splitter

6 Rotateable mirror

7 Fixed mirror

8 ccd array

9 High speed photodiode

10 Quarter wave plate

11 Fourier transform lens

12 Fourier transform lens

Figure 6.1

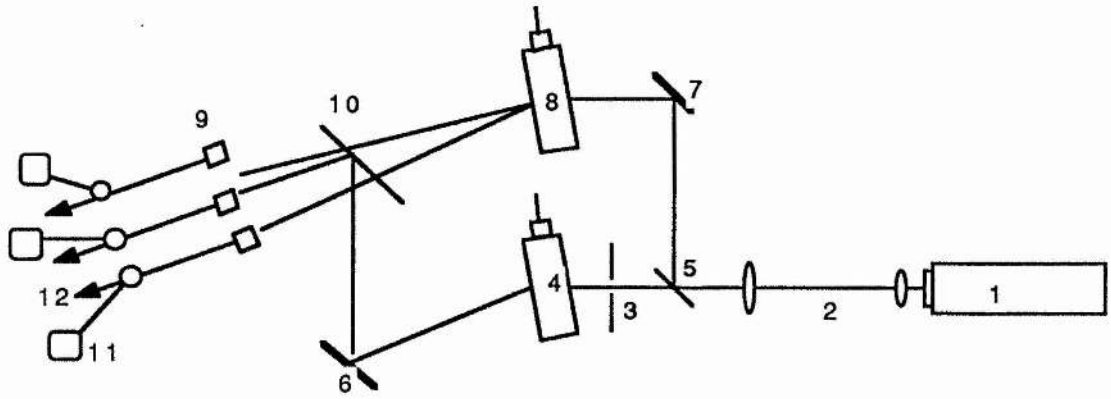

1 Laser

2 Beam expansion/spatial filter

3 Slit

4 Signal Bragg-cell

5 Beam splitter

6 Mirror

7 Mirror

8 Reference cell

9 Detector array

10 Beam splitter

11 Stop-band filter

12 Signal from detector

Figure 6.2

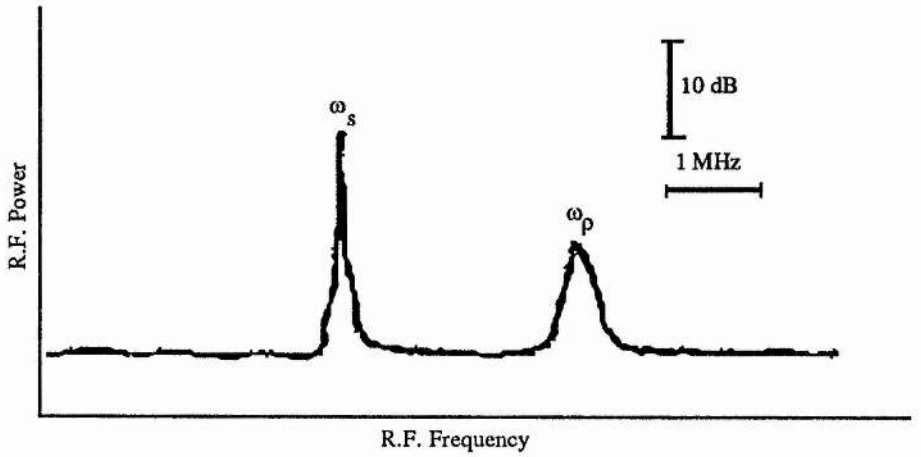

$\tau = 25\ \mu s$

Figure 6.3

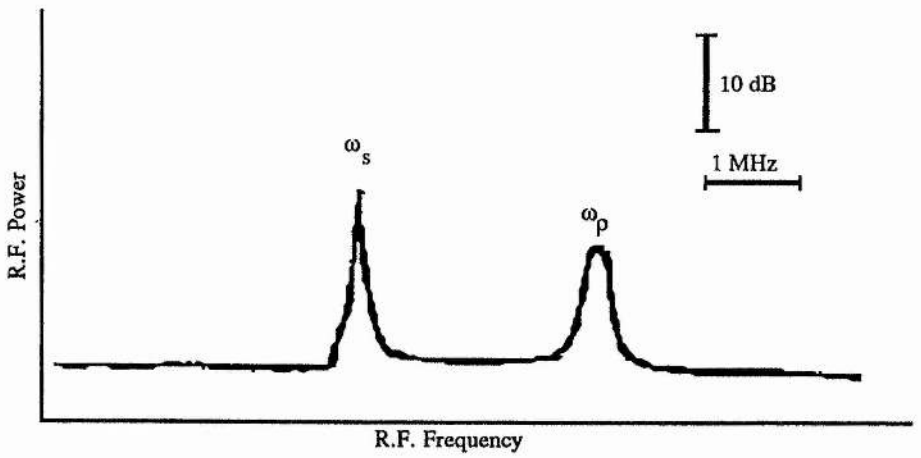

$\tau = 8\mu s$

Figure 6.4

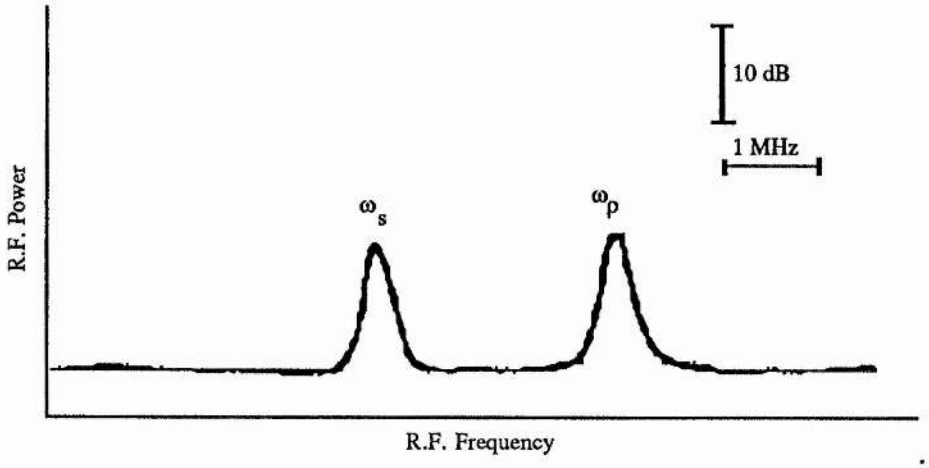

$\tau = 4\mu s$

Figure 6.5

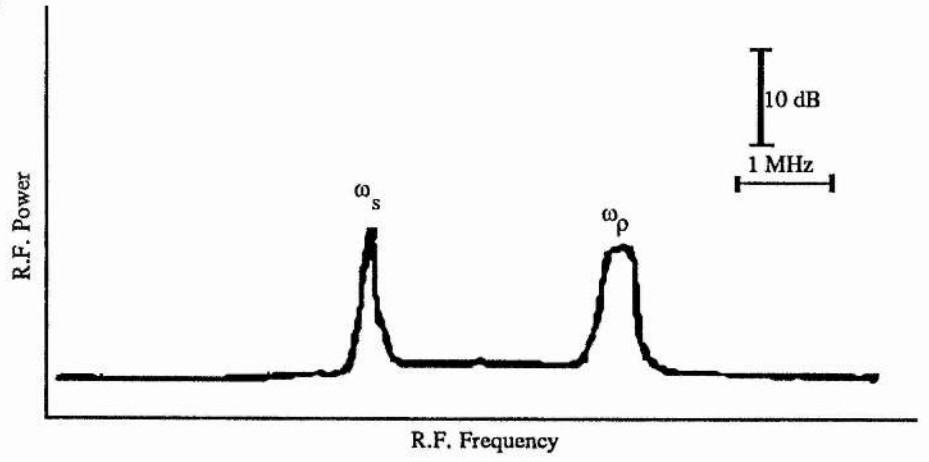

$\tau = 2\mu s$

Figure 6.6

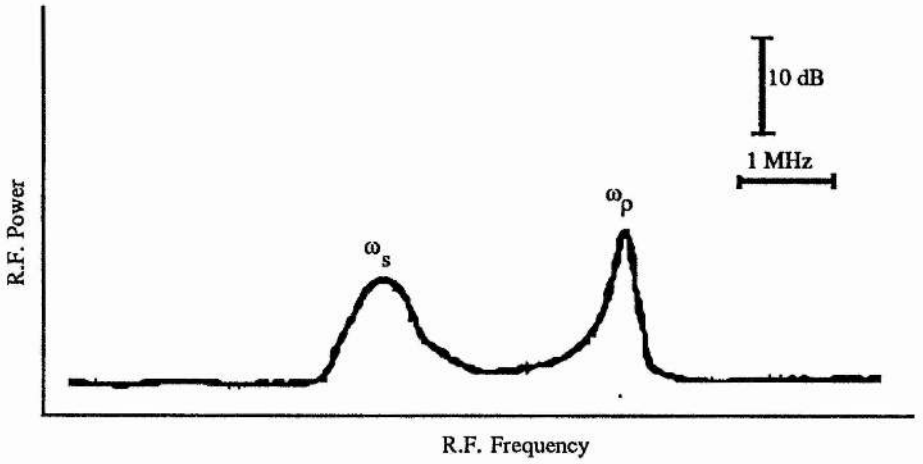

$\tau = 1.2\mu s$

Figure 6.7

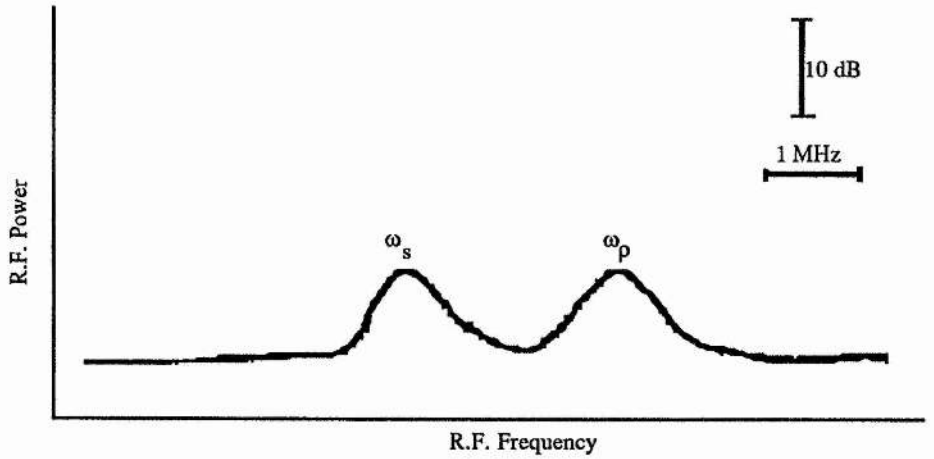

$\tau = 0.8\mu s$

Figure 6.8

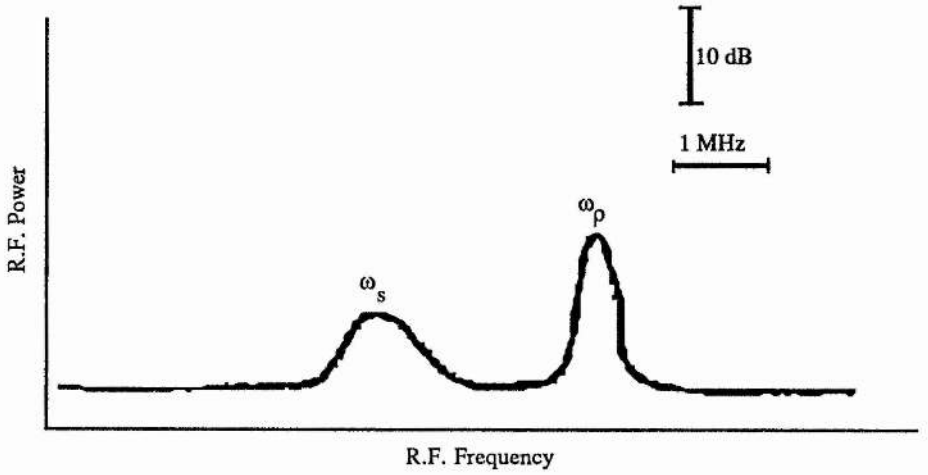

$\tau = 0.4\mu s$

Figure 6.9

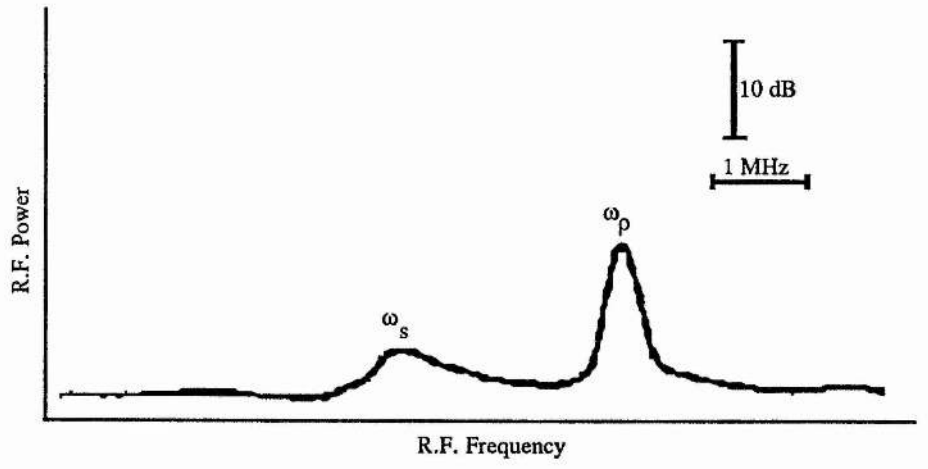

$\tau = 0.2\mu s$

Figure 6.10

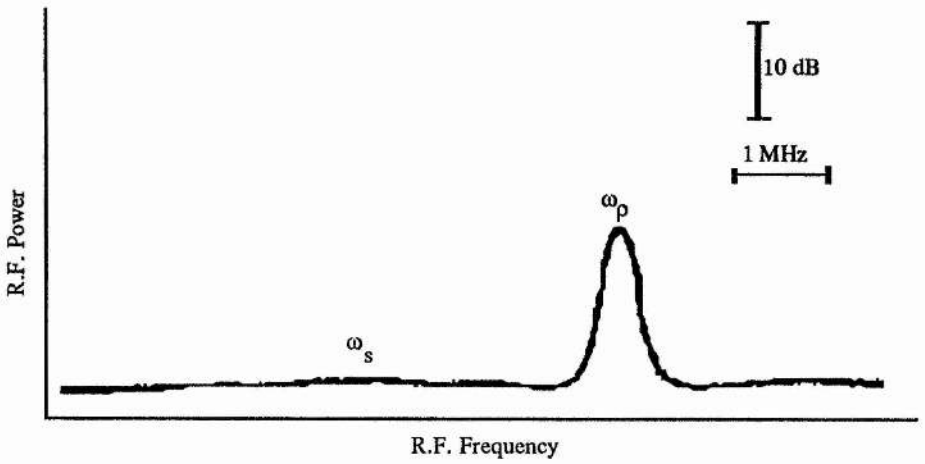

$\tau = 0.1\mu s$

Figure 6.11

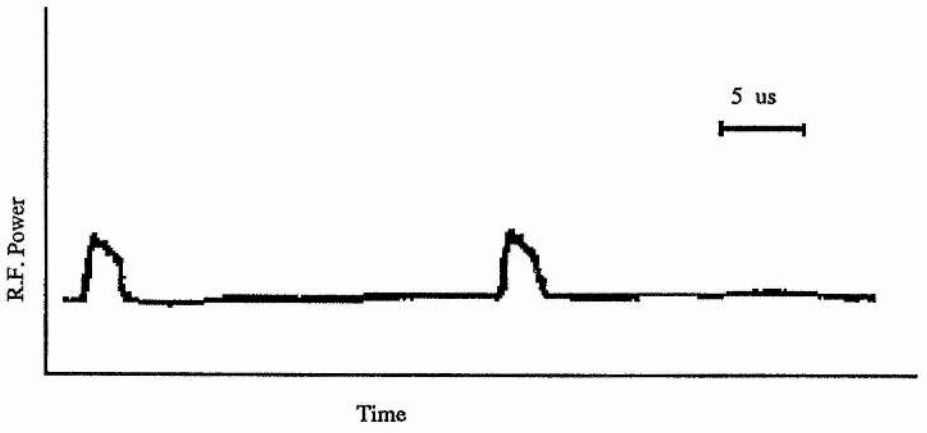

$\tau = 25\mu s$

Figure 6.12

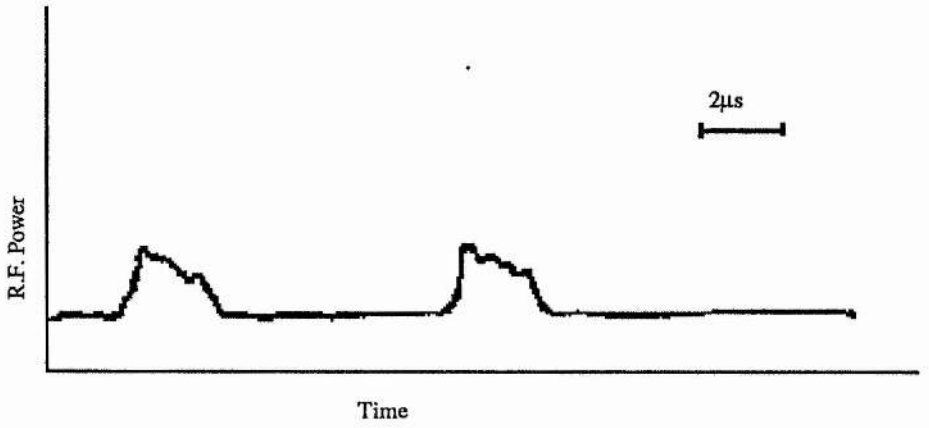

$\tau = 8\mu s$

Figure 6.13

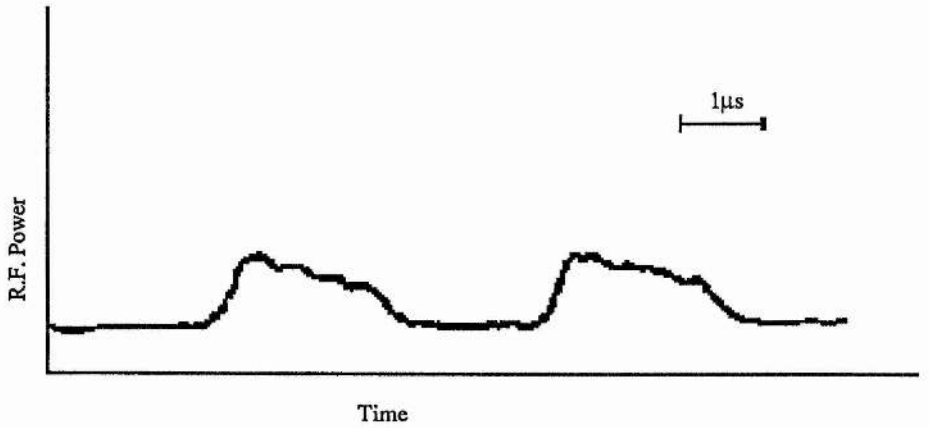

$\tau = 4\mu s$

Figure 6.14

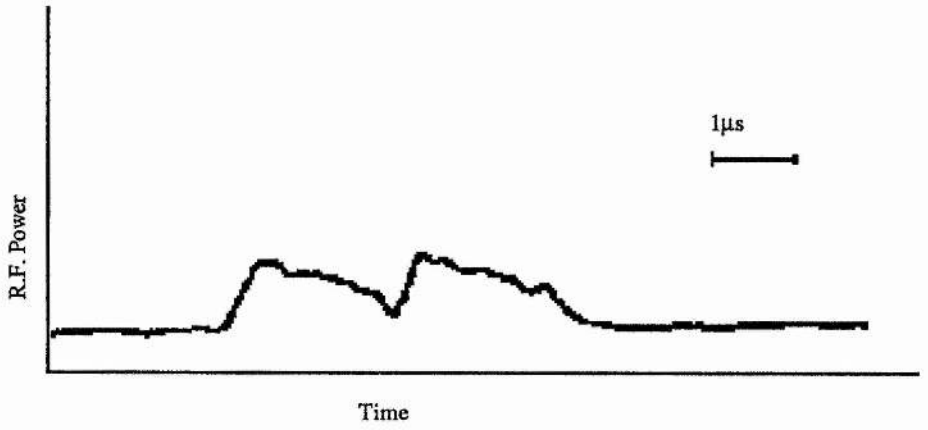

$\tau = 2\mu s$

Figure 6.15

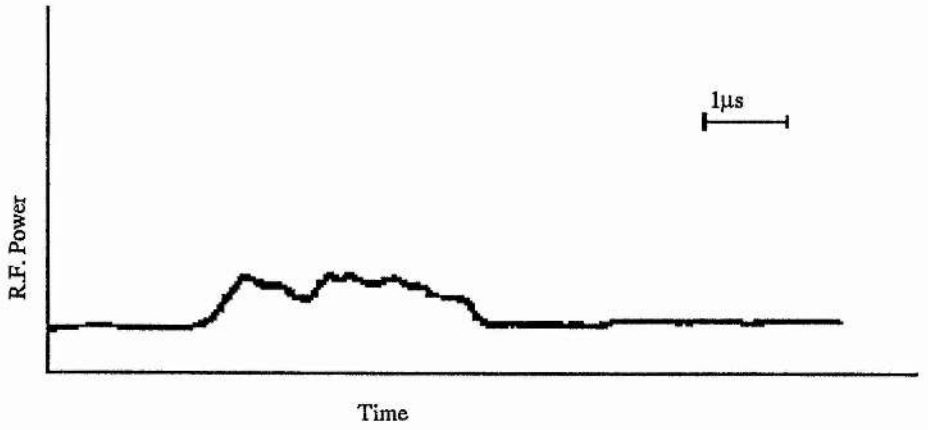

$\tau = 1.2\mu s$

Figure 6.16

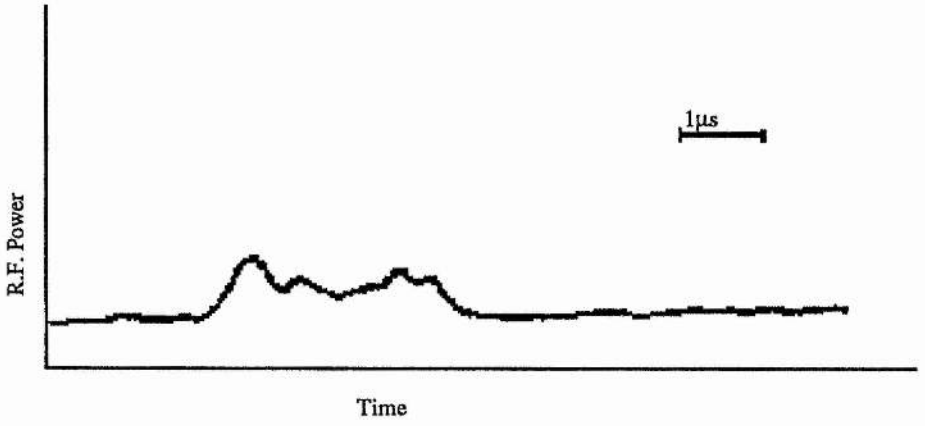

$\tau = 0.8\mu s$

Figure 6.17

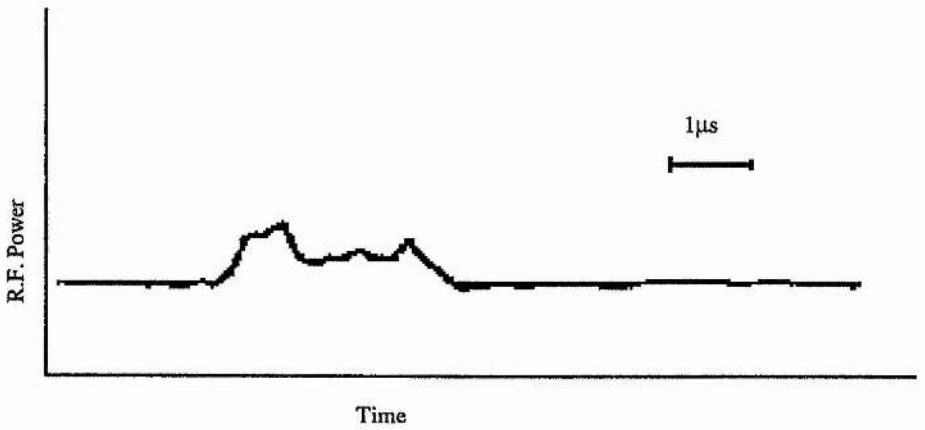

$\tau = 0.4\mu s$

Figure 6.18

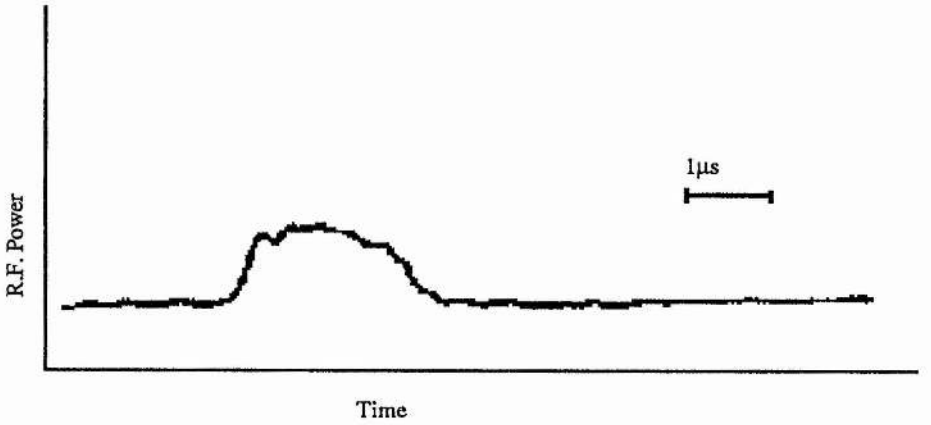

$\tau = 0.2\mu s$

Figure 6.19

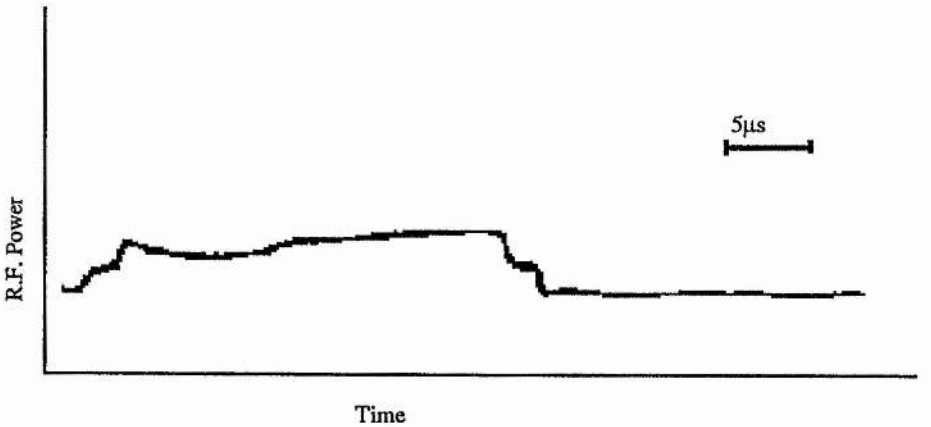

$\tau = 25\mu s$

Figure 6.20

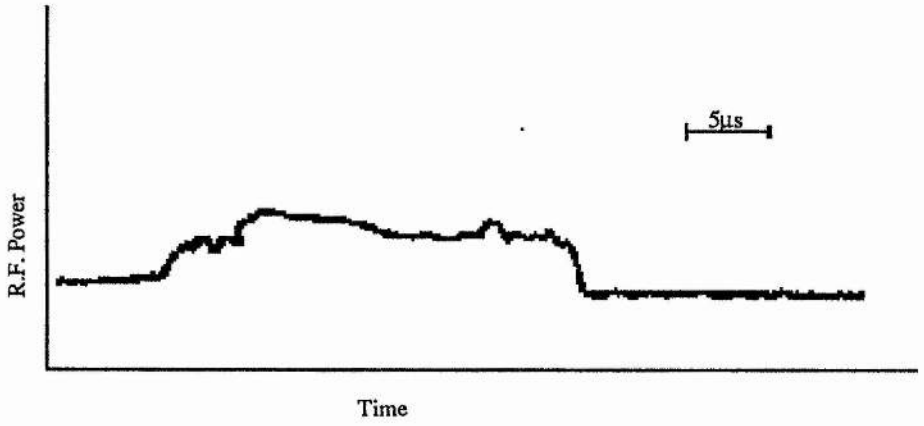

$\tau = 8\mu s$

Figure 6.21

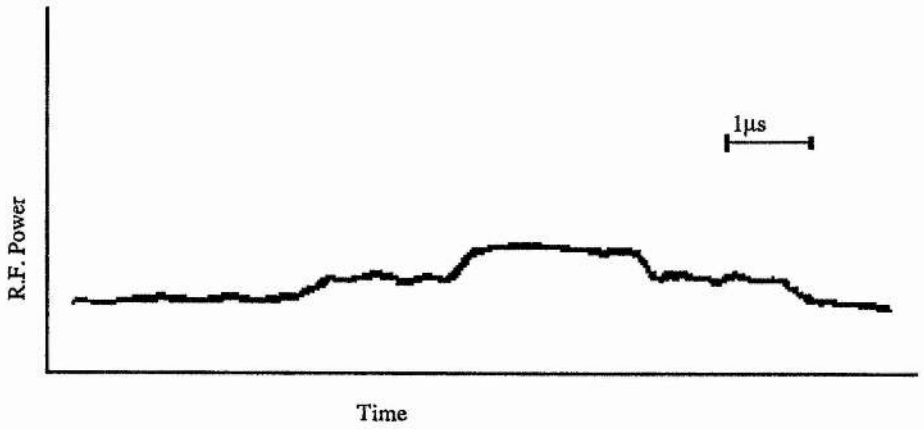

$\tau = 4\mu s$

Figure 6.22

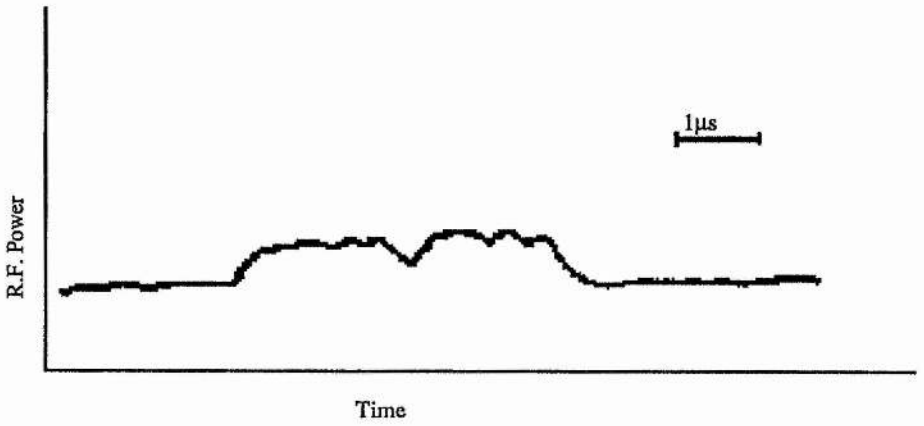

$\tau = 2\mu s$

Figure 6.23

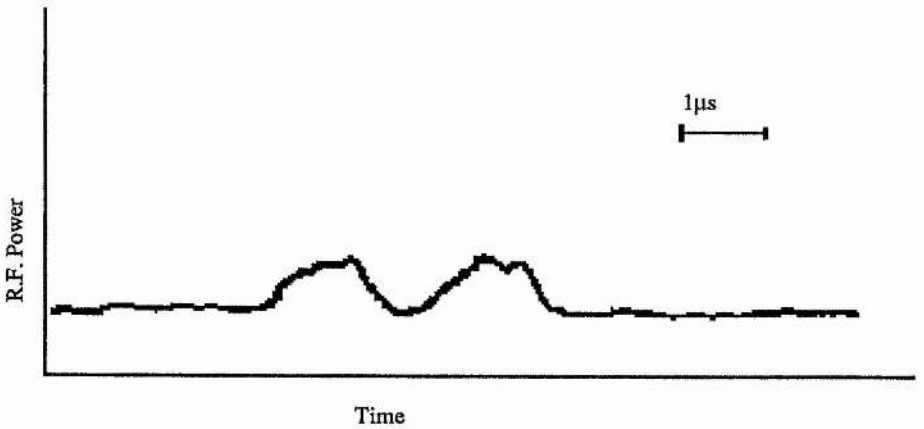

$\tau = 1.2\mu s$

Figure 6.24

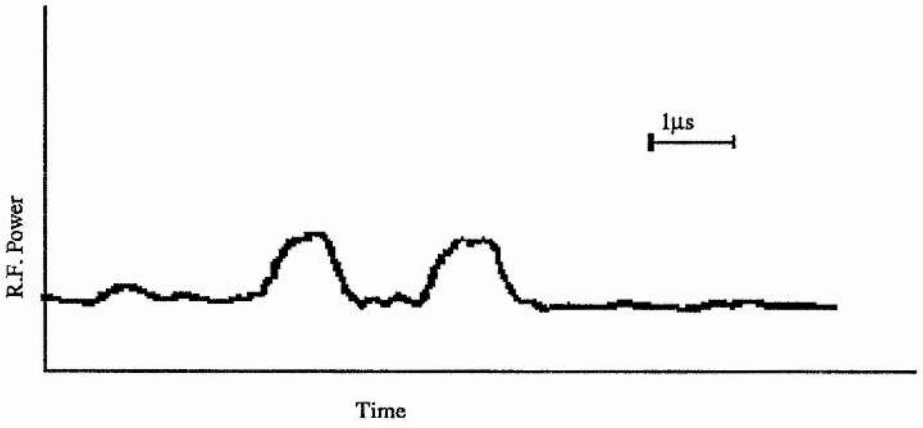

$\tau = 0.8\mu s$

Figure 6.25

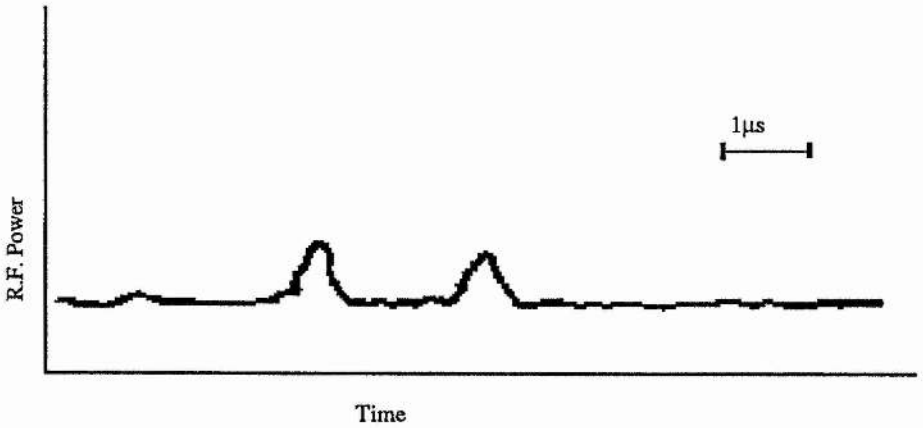

$\tau = 0.4\mu s$

Figure 6.26

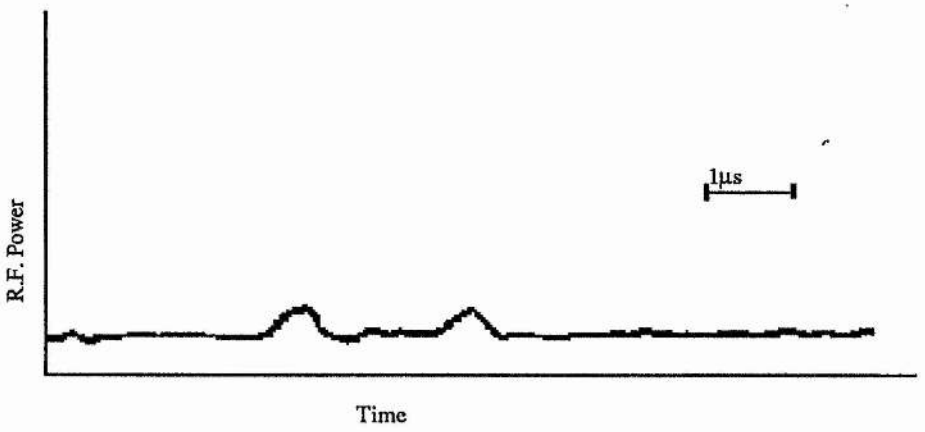

$\tau = 0.2\mu s$

Figure 6.27

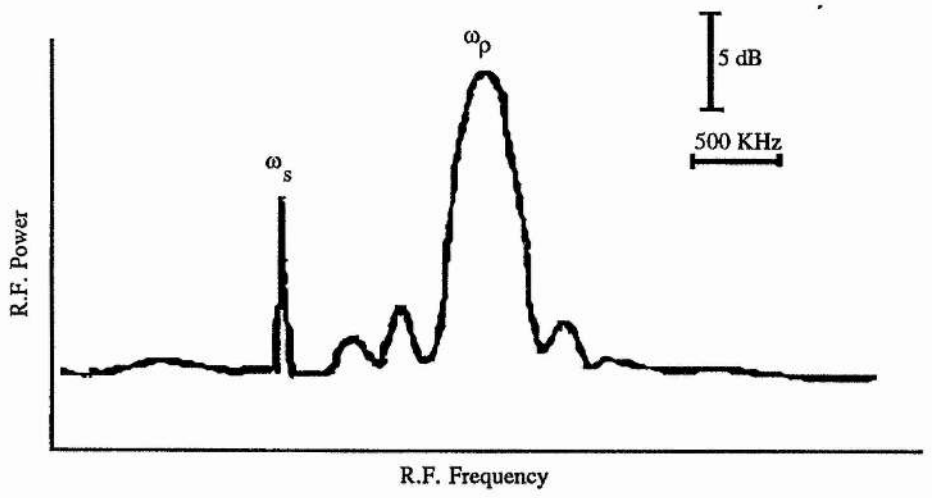

L = 1.5 mm

Figure 6.28

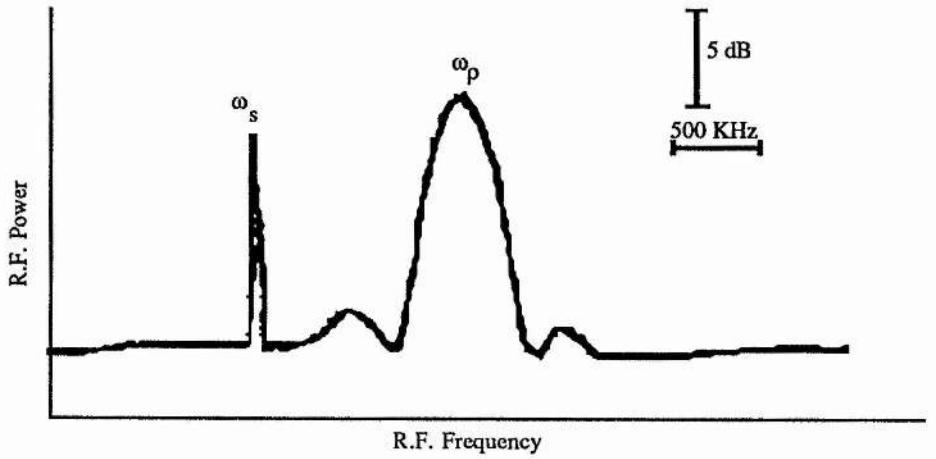

L = 1.25mm

Figure 6.29

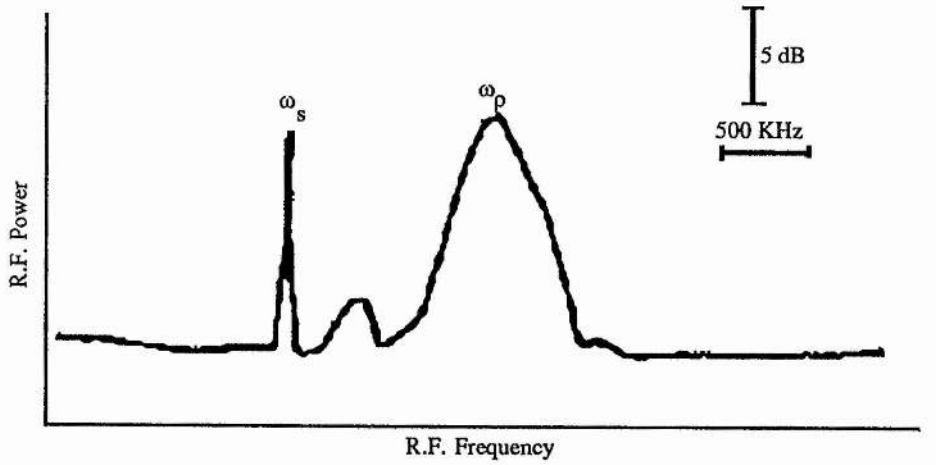

L = 1mm

Figure 6.30

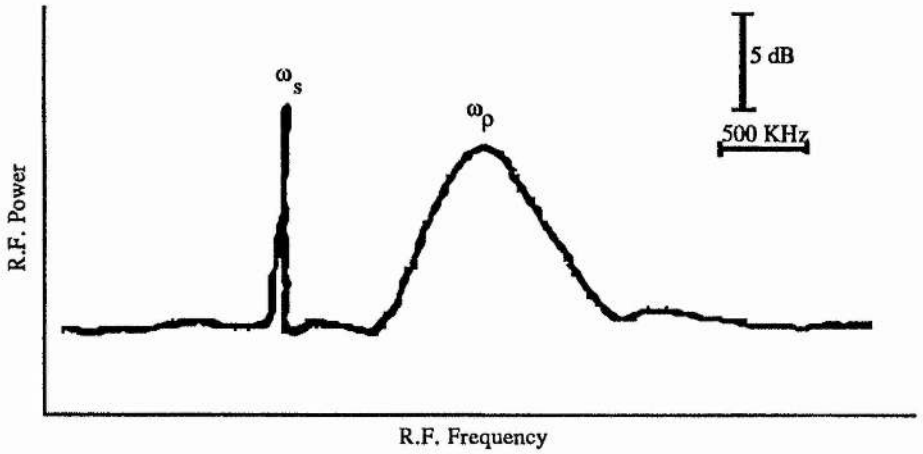

L = 0.75mm

Figure 6.31

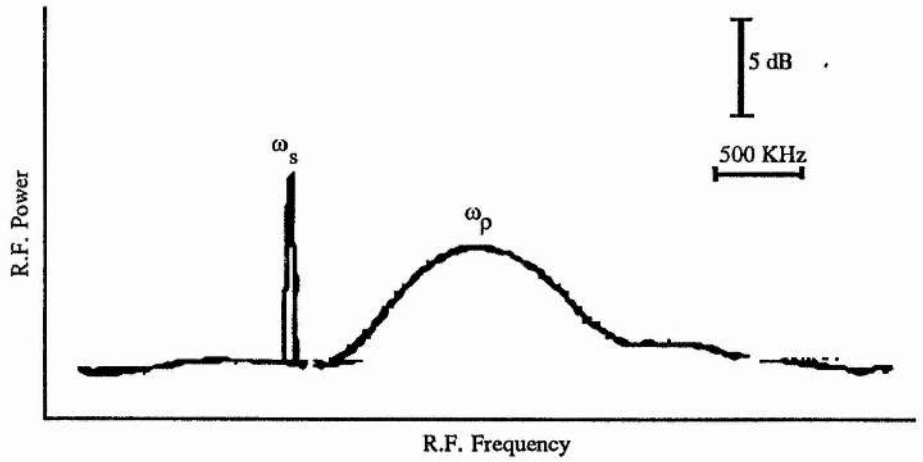

L = 0.5mm

Figure 6.32

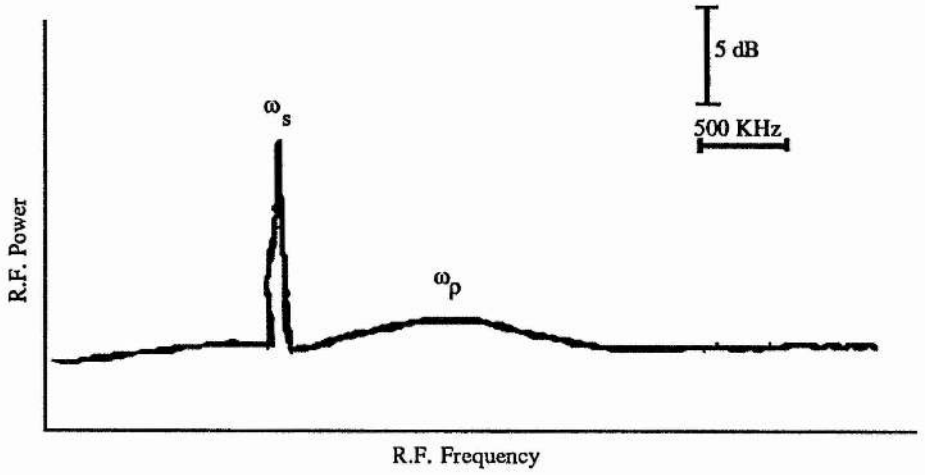

L = 0.25mm

Figure 6.33

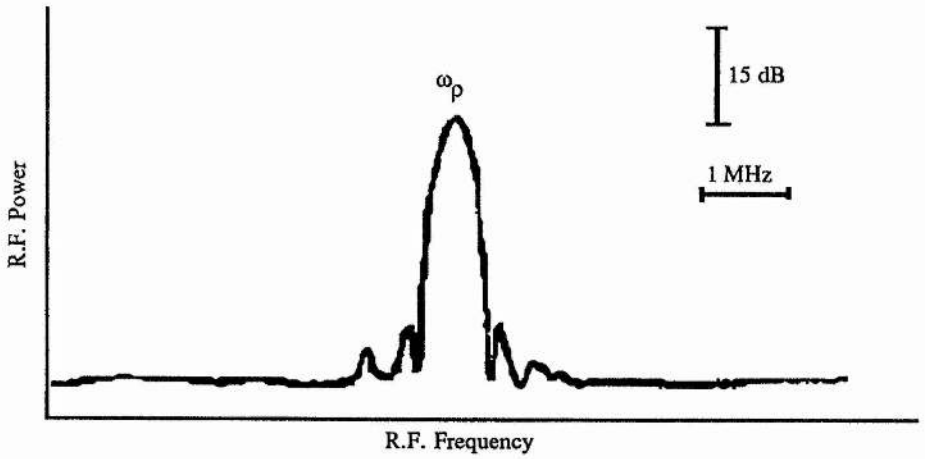

$\tau = 1.1\mu s$

Figure 6.34

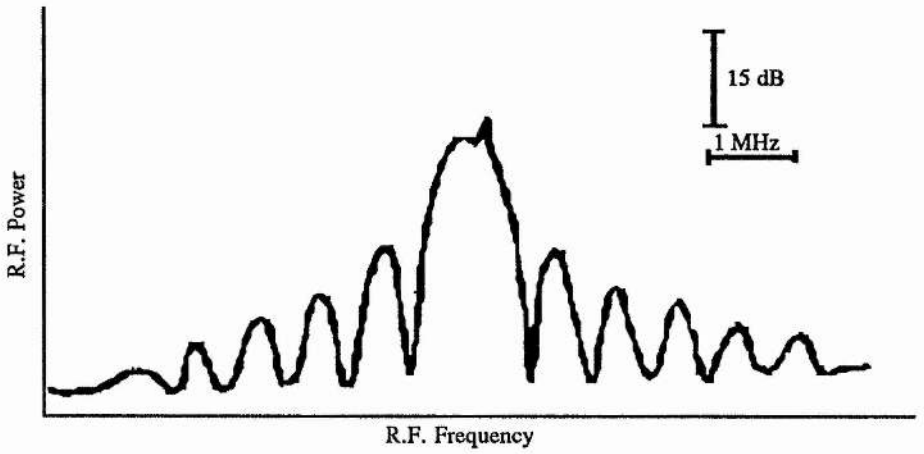

$\tau = 1.1\mu s$

Figure 6.35

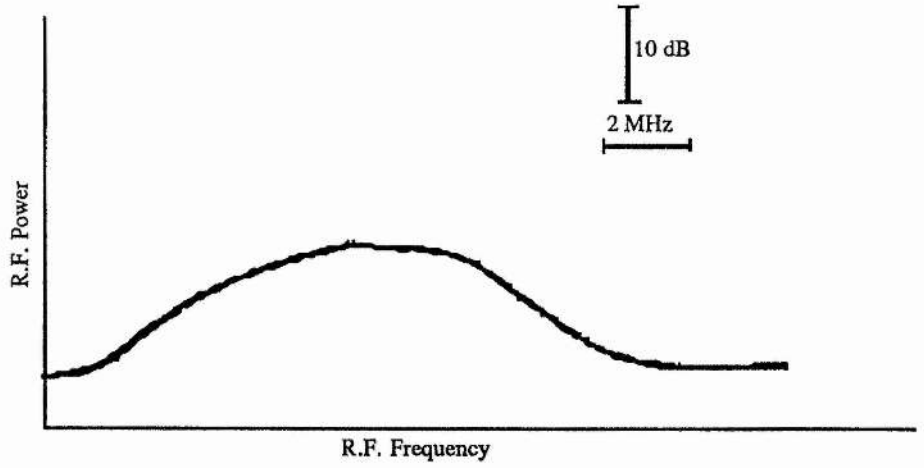

$\tau = 0.1\mu s$

Figure 6.36

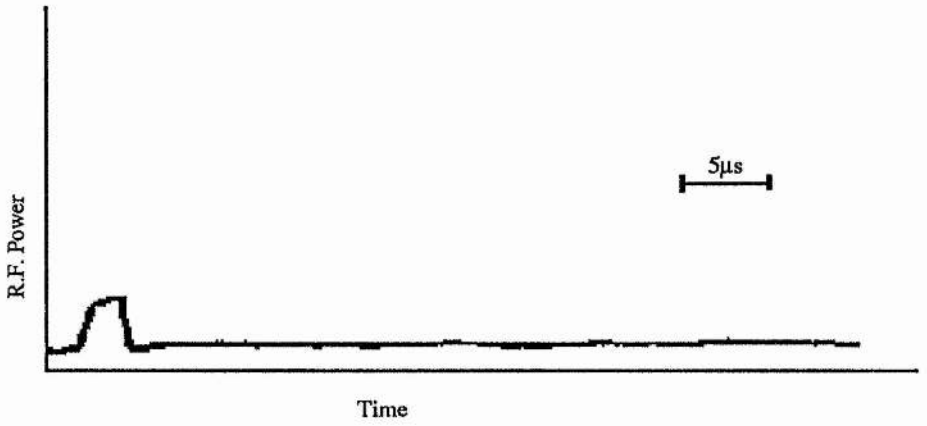

$\tau = 0.15\mu s$

Figure 6.37

6.5 REFERENCES

[6.1] "Spatial and Temporal response of an acoustooptic Bragg-cell"

A Vander Lugt

A.O. 15 Sep '89 Vol 28 No. 23

[6.2] "Temporal frequencies of short and evolving pulses in interferometric spectrum analysers"

P. Wisseman and A. VanderLugt

A.O. Vol. 28, No. 18, 3800-3809, Sep 89

[6.3] "Acoustooptic Spectrum Analyser: Detection of Pulsed Signals"

J. Lee, J. Wight

A.O. Vol. 25, 193-198, 86

[6.4] "The temporal response of an acoustooptic Bragg-cell"

A.P.Shaw

ARE Funtingdon, Private communication

[6.5] "Temporal response of the Acoustooptic modulator: Geometrical optics model in the low scattering efficiency limit"

R. Johnson

A.O. (USA) Vol. 16, No.2, 507-14, Feb 77

[6.6] "Interferometric Spectrum Analyser"

A. Vander Lugt

A.O. Vol. 20, No. 16, Aug 81

7

Travelling-wave Electrooptic Diffraction

7.1 INTRODUCTION

Conventional acoustooptic Bragg-cells have bandwidths limited by the acoustic losses in the crystals used for the cells and impedance matching of the transducer to the driver and crystal. Commercial cells are available with bandwidths of several Gigahertz.

Many applications require significantly larger bandwidths than are offered by conventional Bragg-cells. In this chapter we describe a new kind of diffraction cell with a potential bandwidth in excess of 50 Gigahertz. The theory of operation and an example design are presented.

7.2 DESCRIPTION

The fundamental requirement for a diffraction cell for spectrum analysis is the generation of a moving phase grating controlled by the spectral characteristics of an applied signal. We propose that such a grating could be created by a travelling electric or magnetic wave in an electro or magnetooptically active medium.

With reference to figure 7.1, a travelling electric field could, for instance, be derived by guiding an electrical signal along a transmission line, where an electrooptically active material forms part of the line.

The geometry of the device is to be arranged such that the phase grating may be interrogated by an optical beam.

Work has been published [7.1-7.6] showing static electrooptic Bragg diffraction, using an electrode array to create the phase grating, at switching rates up to 1 GHz. Further work on travelling wave electrooptic interference modulators [7.7-7.12] has shown modulation rates in excess of 30 GHz, with a theoretical limit in excess of 100 GHz. The Travelling-wave electrooptic diffraction (TWEOD) cell is a combination of these two proven technologies.

7.3 THEORY OF OPERATION

The electrooptic effect may be written as

$$\frac{1}{n^2} = \frac{1}{n_0^2} + rE + RE^2 + \text{higher terms}, \qquad 7.1$$

where n is the refractive index of a material within an electric field E, and n_0 is the unperturbed refractive index.

For a birefringent crystal the Indicatrix is given by

$$\sum_{ij} \frac{1}{n^2} + r_{ijk}E_k + R_{ijkl}E_kE_l + \ldots = 1 \quad . \qquad 7.2$$

For a crystal with a predominantly linear electrooptic effect, the induced change in refractive index, Δn, is given by

$$\Delta n = n_0^3 r_c E_3 , \qquad 7.3$$

where r_c is the observed linear electrooptic coefficient. The diffraction intensity ratio of the resulting phase grating is given by equation 1.71

$$\frac{I_d}{I_i} = J_n^2(k\Delta nL) , \qquad 7.4$$

where n is the diffraction order and k is the optical wavenumber in the crystal. We have assumed that we are operating in the Raman-Nath regime, i.e. Q<1, where Q is the parameter,

$$Q = \frac{k^{*2}L}{n_0 k_0} , \qquad 7.5$$

where k_0 and k^* are the free-space optical and microwave wavenumbers in the crystal, respectively.

Then for the first diffraction order, operating at low diffraction efficiencies, we have

$$\frac{I_d}{I_i} = \left(\frac{k\Delta nL}{2}\right)^2 . \qquad 7.6$$

From 7.3 we have

$$\frac{I_d}{I_i} = \left\{\frac{kr_c E_3 L}{2}\right\}^2 \qquad 7.7$$

and

$$\frac{I_d}{I_i} = \left\{\frac{\pi n_0^4 r_c L E_3}{\lambda_0}\right\}^2 . \qquad 7.8$$

For the parallel plate transmission line shown in figure 2, the power, P, transmitted along the line is given by,

$$P = \frac{V_3^2}{Z}, \qquad 7.9$$

where Z is the characteristic impedance. Hence, we have

$$P = V_3^2 \sqrt{\frac{C}{l}}, \qquad 7.10$$

where the capacitance per unit length, C, is given by

$$C = \frac{\varepsilon_3 L}{t} \qquad 7.11$$

and the inductance per unit length, l, is given by

$$l = \frac{\mu t_h}{L} \qquad 7.12$$

From 7.9, 7.11 and 7.12, we have

$$P = V_3^2 \frac{L}{t_h} \sqrt{\frac{\varepsilon_3}{\mu}}. \qquad 7.13$$

But the *applied* field is

$$E_3 = \frac{V_3}{t_h} \qquad 7.14$$

and so we get

$$P = E_3^2 L t_h \sqrt{\frac{\varepsilon_3}{\mu}}. \qquad 7.15$$

From 7.8 and 7.15, we obtain the diffraction intensity ratio for the grating

$$\frac{I_d}{I_i} = \left\{ \frac{\pi n_0^4 r_c}{\lambda_0} \right\}^2 \frac{L}{t_h} \sqrt{\frac{\mu}{\varepsilon_3}} P. \qquad 7.16$$

The diffraction efficiency per watt, η, is given by

$$\eta = \frac{I_d}{I_i} \frac{1}{P}, \qquad 7.17$$

or

$$\eta = \left\{ \frac{\pi n_0^4 r_c}{\lambda_0} \right\}^2 \frac{L}{t_h} \sqrt{\frac{\mu}{\varepsilon_3}} . \qquad 7.18$$

The maximum interaction length, L, is limited by the requirement that the phase of the applied radiofrequency wave must not change significantly (i.e. by not more than a quarter wavelength) as the optical wavefronts pass through the interaction region.

We may write

$$\frac{n_0 L}{c} < \frac{1}{4f} , \qquad 7.19$$

where f is the radio frequency.

The maximum value of L is then given by

$$L_{max} = \frac{c}{4fn_0} . \qquad 7.20$$

The time-bandwidth product of the grating, τB, is

$$\tau B = \frac{D\sqrt{\varepsilon_3}}{c} B , \qquad 7.21$$

where B is the bandwidth. (The time-bandwidth product may be shown to be equal to the number of resolvable frequency ranges.)

The frequency resolution, Δf, is given by

$$\Delta f = \frac{1}{\tau} , \qquad 7.22$$

where τ is the transit time of the radiofrequency wave in the interaction region.

Thus, we get

$$\Delta f = \frac{c}{D\sqrt{\varepsilon_3}} . \qquad 7.23$$

The diffraction angle inside the crystal, θ_d, is

$$\theta_d = \frac{\lambda_0 f \sqrt{\varepsilon_3}}{n_0 c} \qquad 7.24$$

and the diffraction angle in free space is

$$\theta_d' = n_0 \theta_d \qquad 7.25$$

7.4 DESIGN EXAMPLE USING $BaTiO_3$

The above equations have been used to design a 50 GHz diffraction cell fabricated in bulk $BaTiO_3$ using the parallel plate transmission line geometry shown in figure 7.2.

It can be seen from equation 7.21 that, in order to obtain a large time-bandwidth product for the cell, the radiofrequency dielectric constant, ε_3, must be large and the propagation

distance, D, should be long. Furthermore, from equation 7.18, we see that for a high diffraction efficiency we also require that the product $r_c n_0^4$ is large.

A number of candidate materials were considered, including KDP, ADP, AlGaAs, GaAs, $LiTiNbO_3$ and $LiNbO_3$. Eventually ferroelectric $BaTiO_3$ was selected, the relevant values being :-

$r_c = 108 \times 10^{-12}\ mV^{-1}$ $\quad n_0 = 2.44$

$\varepsilon_1 = \varepsilon_2 = 3000$ $\quad \varepsilon_3 = 170$

The dimensions of the device were derived to be

$L = .6$ mm $\quad t_h = .9$ mm $\quad D = 100$ mm

The value of L is maximised as in equation 7.20. The size of t_h is chosen to give a 50Ω impedance and the length, D, will be limited by crystal growth techniques.

The theoretical characterisation of the TWEOD gives the following parameters:-

Bandwidth = 50 GHz

Centre frequency = 50 GHz

Impedance = 50 Ω

$\eta = 0.5$ % per watt

$\lambda_0 = 633$ nm

$\tau B = 217$

$\Delta f = 231$ MHz

$\theta_d' = 1.4$ mrad

7.5 ALTERNATIVE IMPLEMENTATIONS

There are a number of alternative implementations of the TWEOD. These may exploit some of the following :-

1) Use of slow wave structure. (See appendix).

2) Electrooptic effect in a pin-diode.

3) Electrooptic effect in a laser diode.

4) Electrooptic effect in a heterostructure.

5) Electrooptic effect in epitaxial layers.

6) Use of a microstrip transmission line.

7) Electrooptic effect across a pn-junction.

8) Magnetooptic devices.

9) Use of waveguide instead of transmission line.

10) Quantum well structures.

11) Electro and magnetooptic absorption and polarisation effects.

7.6 A HIGH TIME-BANDWIDTH DESIGN

In order to increase the time-bandwidth product a material with a higher dielectric constant than the electrooptic material may be encorprated on either side of the active region. This is shown in figure 7.3. The "high dielectric" material has dielectric constant ε_1. The active layer contains the electrooptic material with dielectric constant ε_3. This will produce an effective dielectric constant for the transmission line given by

$$\varepsilon_{eff} = \frac{\varepsilon_1 \varepsilon_3 (2t_1 + t_2)}{\varepsilon_1 t_2 + 2\varepsilon_3 t_1} \qquad 7.26$$

where we have assumed $t_1 = t_3$ and

$$t_h = 2t_1 + t_2 \qquad 7.27$$

Equation 7.14 for the *applied* field across the middle layer becomes

$$V_3 = \frac{2\varepsilon_3 t_1 + \varepsilon_1 t_2}{\varepsilon_1} E_3 \qquad 7.28$$

From 7.9, 7.10, 7.11, 7.12, 7.26, 7.27 and 7.28, we have

$$P = \left\{ \frac{2\varepsilon_3 t_1 + \varepsilon_1 t_2}{\varepsilon_1} E_3 \right\}^2 \frac{L}{2t_1 + t_2} \sqrt{\frac{\varepsilon_{eff}}{\mu}} \qquad 7.29$$

The diffraction intensity ratio for the grating is, from 7.8 and 7.29,

$$\frac{I_d}{I_i} = \left\{ \frac{\pi n_0^4 r_c L}{\lambda_0} \right\}^2 \left\{ \frac{\varepsilon_1}{2\varepsilon_3 t_1 + \varepsilon_1 t_2} \right\}^2 \frac{2t_1 + t_2}{L} \sqrt{\frac{\mu}{\varepsilon_{eff}}}\, P \qquad 7.30$$

From 7.17 and 7.30, the diffraction efficiency per watt is

$$\eta = \left\{ \frac{\pi n_0^4 r_c L}{\lambda_0} \right\}^2 \left\{ \frac{\varepsilon_1}{2\varepsilon_3 t_1 + \varepsilon_1 t_2} \right\}^2 \frac{2t_1 + t_2}{L} \sqrt{\frac{\mu}{\varepsilon_{eff}}} \qquad 7.31$$

The high dielectric constant could be doped ceramic Barium Titanate, which may have an extremely large dielctric constant and a low loss tangent.

7.7 CONCLUSION

We have shown the possibility of a diffraction cell (TWEOD) with a bandwidth in excess of 50GHz. A TWEOD could be used in a conventional acoustooptic type of spectrum analyser configuration, to produce a radiofrequency spectrum analyser with extremely large bandwidth.

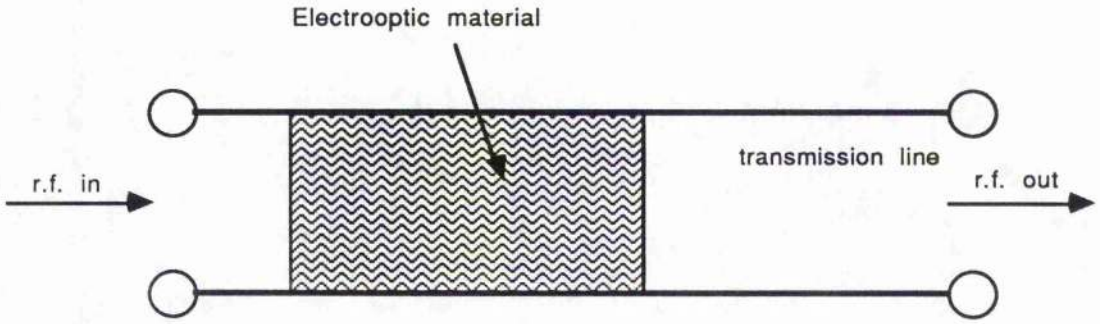

Figure 7.1

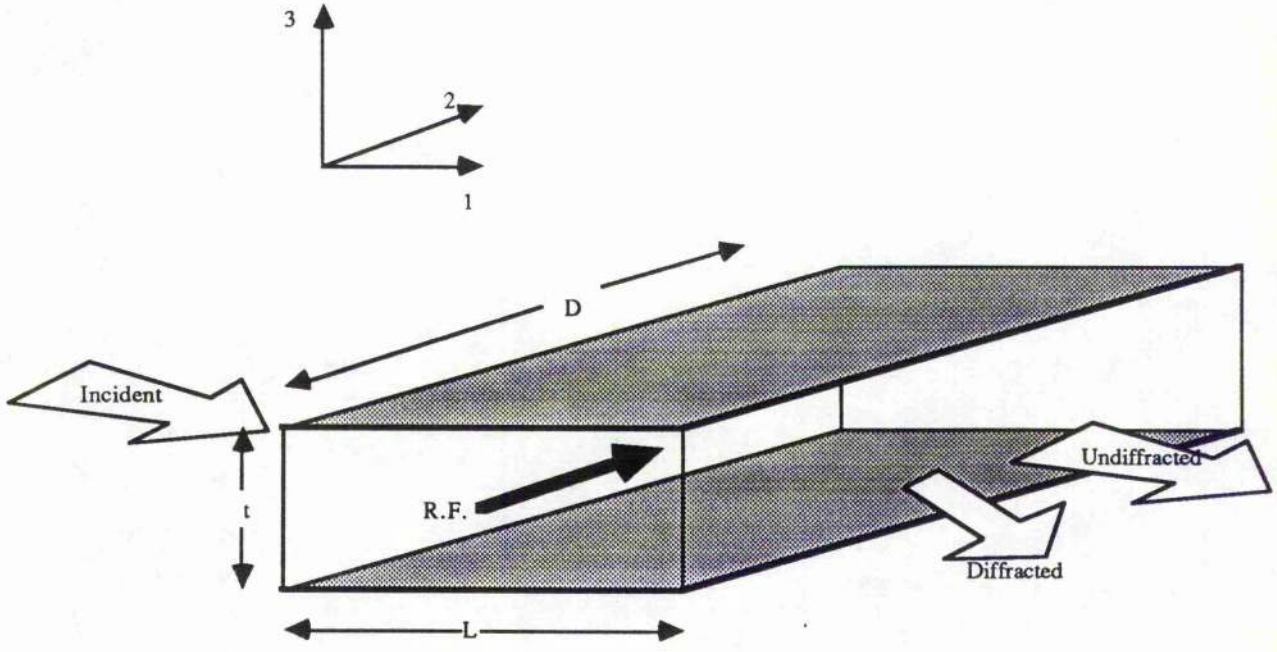

Figure 7.2

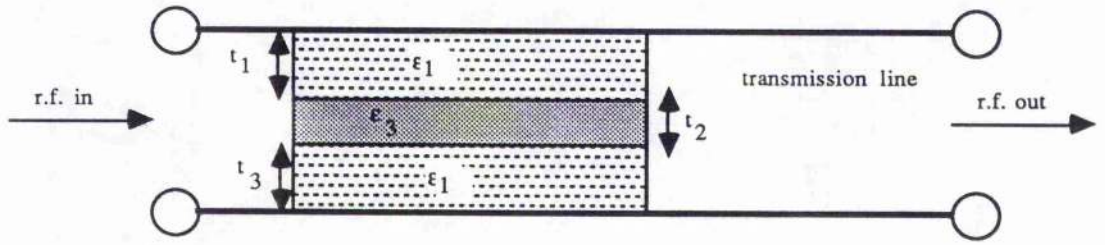
r.f. in
t_1
ε_1
ε_3
t_2
t_3
ε_1
transmission line
r.f. out

Figure 7.3

7.7 REFERENCES

[7.1] Electrooptic Light Modulators.

I.P.Kaminov and E.H.Turner

AO 5,10 (Oct 66), p 1612

[7.2] Electrooptic Bragg diffraction switches in low cross talk integrated optics switching matrix.

E.M. Philipp-Ritz,R. Linares,M. Fakuda.

AO 21, 12 (Jun 82), p 2189

[7.3] Four wave theory of electrooptic gratings with a simple expansion for use in design.

Yim-Kul Lee and R.P. Kenan

AO 28, 1 (Jan 89), p 74

[7.4] Electrooptic Bragg deflection modulators: Theoretical and experimental studies.

Yong-Kyung Lee and Shyh Wand

AO 15, 6 (Jun 76), p 1565

[7.5] Travelling wave amplitude modulator with 1 GHz bandwidth for coherent light optical communication.

S.R. Adhav, R.S. Adhav and H. Van de Vaart

AO 20, 5 (March 81), p 867

[7.6] Electrooptic diffraction modulation in Ti - diffused $LiTaO_3$.

G.L. Tangonan, D.L. Pepsechini, J.F. Lotspeich and M.K. Barnoski

AO 17, 20 (Oct 78), p 3259

[7.7] A high frequency Ga As optical guided-wave electrooptic interferometric modulator

J.P. Donnelly, N.L. DeMeo, G.A. Ferrante and K.B. Nichols.

IEEE J. Quantum Electron., QE-21, 1, (Jan 85) p 18-21

[7.8] GaAs PIN electrooptic travelling wave modulator at 1.3 μm

S.H. Lin, S.Y. Wang and Y.M. Houng.

Elec. Letts., 22, 8 (Aug 86) p 934-5

[7.9] Optical guided-wave GaAS monolithic interferometer

J.P. Donnelly, N.L. DeMeo, G.A. Ferrante, K.B. Nichols and F.J. O'Dnnell.

Appl. Phys. Lett 45, 4, (Aug 84) p462-4.

[7.10] Waveguide electrooptic modulators

R.C. Alferness.

IEEE Trans. Microwave Theory Tech. MTT-30,8 (Aug 82) p1121-37

[7.11] Broadband Y-branch electrooptic GaAs waveguide interferometer for 1.3 μm.

P. Buchmann, H. Kaufman

Appl. Phys. Lett. 46, 5 (Mar 85) p462-4, March 85

[7.12] A high frequency GaAs optical guided-wave electrooptic interferometric modulator

J. P. Donnelly et al.

IEEE J. Quantum Electron. QE-21, 1 (Jan 85) p18-21

[7.13] Design of an GaAlAs travelling wave Mach-Zehnder electrooptic modulator.

Optoelectronic materials, devices, packaging and interconnects, D.M. Materna, A.M. Ferendeci and K.B. Bhasin.

Proc. SPIE 836, T.E. Batchman, et al., eds, SPIE, 1987, p195-8.

[7.14] Lightwave technology for microwave systems: principles and applications.

Kul B. Bhasin and Afshin S. Daryoush

Short course sc40 given at SPIE's OE Lase 1990, 15th January SPIE 1990, sc 40

8

An Optical Frequency Division Multiplexer

8.1 INTRODUCTION

Modern computing and communication systems require ever higher data transmission rates. The speed of transmission is limited by the usable bandwidth of the transmission medium. In the case of transmission along coaxial cables, for example, data rates are limited to around a few hundred megahertz over large distances.

Optical transmission systems offer theoretical bandwidths of Peta-hertz (10^{15} Hz). If the transmission is in a dispersive medium, then this data-rate is significantly reduced. In commercially available single mode optical fibres, for instance, the theoretical limit is greater than a few hundred gigahertz. However, current state-of-the-art technology limits maximum data rates to around one gigahertz. This limitation arises from the maximum speeds at which the driving electronics can operate. Attempts have been made [8.1-8.2] to achieve time division multiplexing optically but these still require high speed electronics.

Parallel processing techniques may be employed to exploit the available bandwidth in optical transmission links. The data is transmitted simultaneously along a number of orthogonal channels. The total data-rate is the sum of the data-rates of the individual channels. Each channel may then operate at a data-rate which is small compared with the total bandwidth. The system is not limited by the speed of the driving electronics.

This chapter describes an invention which uses frequency division multiplexing to create orthogonal channels, together with a means of modulating and demodulating each channel. The invention permits very high data transmission rates to be achieved multi-synchronously. In addition, the data transmission format offers a high level of security against illicit surveillance.

8.2 PRINCIPLE OF OPERATION

The light from a laser is passed through an acoustooptic device which creates a spatial distribution of Doppler shifted optical frequencies in the focal plane of a lens. A spatial light modulator (SLM) selects and modulates this distribution, thus creating discrete data channels (frequency division multiplexed). Heterodyne techniques are employed to produce modulation at the Doppler frequency for each channel. The received signal is demultiplexed using an acoustooptic radio frequency spectrum analyser [8.3 - 8.5].

The basic multiplexer is shown in Figure 8.1. Light from the laser, 1, is expanded and collimated, 2. A beam-splitter, 3, is used to create a reference beam, 8. The signal beam is passed through an acoustooptic Bragg-cell, 4. A frequency chirp or polychromatic radiofrequency signal is applied to the transducer of a Bragg-cell. An acoustic wave is then created within the cell. Laser light passing through the cell is diffracted by the acoustic wave. The angles of diffraction of the laser light are proportional to the frequency components of the applied signal. This produces a spatial distribution in the focal plane of the lens, 5. The transverse displacement from the optic axis is proportional to the radiofrequency signal applied to the Bragg-cell .

It is important to note that the diffracted light is Doppler-shifted by the frequency of the applied radiofrequency signal [8.8-8.11]. If a broadband signal is present then the Doppler shift varies across the spatial distribution by an amount proportional to the transverse displacement from the optic axis. This means that, for any transverse position there will be an associated Doppler frequency. Data channels are then defined by allocating a transverse region to each channel.

The SLM, 6, is placed at the focal plane of the lens, 5. Each element of the SLM defines and modulates an independent data channel, 7. The maximum modulation rate (bandwidth) of each channel is proportional to the separation of the channels. The total capacity of the system is the sum of the channel bandwidths and this is determined by the Bragg-cell's bandwidth.

8.2.1 Temporal analysis of light diffracted by a Bragg-cell

The analysis in chaper 6 gives the spatial and temporal variation of light diffracted by radiofrequency pulses within a Bragg-cell. For a cw signal which fills the cell the spatial distribution is given by equation 6.29. We have

$$d(\rho,t) = A\exp(i\omega_S t)L\,\mathrm{sinc}[(\rho-\rho_S)L/2] \qquad 8.1$$

The spatial distribution is a sinc function with angular half width λ/L.

For a detector, or channel, monitoring the diffraction pattern at a spatial position corresponding to the spatial frequency, ρ, the angular frequencies present are given by equation 6.4.

$$d(\rho,\omega) = \int_{-\infty}^{\infty} d(\rho,t)\exp(-i\omega t)dt \qquad 8.2$$

Following the method given in section 6.2.2, we have

$$d(\rho,\omega) = \int_{0}^{T} A\exp(i\omega_S t)L\,\mathrm{sinc}[(\rho-\rho_S)L/2]\exp(-i\omega t)dt \qquad 8.3$$

Where T is the time the channel is open. This gives

$$d(\rho,\omega) = ALT\,\mathrm{sinc}[(\rho-\rho_S)L/2]\,\mathrm{sinc}[(\omega_S-\omega)(T)/2]\phi \qquad 8.4$$

where ϕ is a phase term.

The temporal profile is a sinc function centred at ω_S with half-width, $\frac{2\pi}{T}$.

8.2.2 Optical-fibre transmitter

The output of the basic multiplexer comprises signal beams and a reference beam. In this system, shown in figure 8.2, the signal beams, 7, are all coupled into a single mode fibre. The reference beam, 8, is coupled into a second single mode fibre. The two fibres are then coupled together, 11, and the signal and reference beams mix. The transmitted signal consists of a radiofrequency modulated monochromatic beam guided in a single mode fibre.

8.2.3 Optical-fibre receiver

The receiver is shown in figure 8.3. After transmission in the fibre, 1, the signal is coupled onto a detector, 2. The detector output is amplified, 3, and used to drive a Bragg-cell, 4. Light from a laser, 5, is expanded and collimated, 6, and used to interrogate the Bragg-cell. The time modulated spatial distribution originally created by the SLM is reconstructed by the lens, 7, on the detector array, 8. Each element of the detector array corresponds to one data channel. The detector output is the demultiplexed signal.

8.2.4 Cross-talk and bandwidth

Cross-talk is produced as a result of non-linear mixing at the detector. Consider a two channel system with Doppler shifts ω_1 and ω_2 and laser optical frequency ω_0. The detector produces a current I given by

$$I = k\ \{A\exp[i\omega_0 t] + B\exp[i(\omega_0+\omega_1)t] + C\exp[i(\omega_0+\omega_2)t]\}\{A\exp[-i\omega_0 t] + B\exp[-i(\omega_0+\omega_1)t] + C\exp[-i(\omega_0+\omega_2)t]\} \qquad 8.5$$

where k is a constant. A, B and C are the light amplitudes of the reference and signal beams, respectively.

$$I = AB\cos[\omega_1 t] + AC\cos[\omega_2 t] + A^2 + B^2 + C^2 + BC\cos(w_1 - w_2)t + BC\cos(w_1+w_2) \qquad 8.6$$

The first two terms are the desired multiplexed signal but there are also undesired DC terms and cross-talk terms at the sum and difference Doppler frequencies.

This limits the cross-talk free useable bandwidth to one-half of the Bragg-cell's maximum operating frequency.

Cross-talk is also produced by diffracted light spreading on to adjacent channels. The normalised value for the cross-talk between two channels due to light diffracting through the wrong modulator channel is given approximately by

$$CT_{1\text{-}2} = \frac{\int_{d-l/2}^{d+l/2} \mathrm{sinc}(Lx/F)\,dx}{\int_{-l/2}^{l/2} \mathrm{sinc}(Lx/F)\,dx} \qquad 8.7$$

where

l is the width of one channel in the transform plane,

d is the separation of the channels in the tranform plane

F is the focal length of the transform lens

L is the Bragg-cell aperture

The larger the separation of the channels, d, the smaller will be the cross-talk, but less of the Bragg-cell's bandwidth will be available. There is therefore a compromise between bandwidth and cross-talk.

8.2.5 Broadband system

The light source may be relatively broadband, e.g. 3nm. Wavelength division multiplexing may then be incorporated to further increase the data-rate. In this case modulation will only be produced when the signal and reference paths are equal to within the coherence length of the source. A diffraction grating may be placed between the source and the SLM and arranged to diffract the light in a direction orthogonal to the Bragg-cell diffraction. This results in a 2-dimensional array with wavelength varying along one axis and Doppler-shift varying along the other. Demodulation at the receiver requires a similar 2-dimensional diffractive process.

8.2.6 Secure transmission

A large path difference, D, may be incorporated in the transmitter between signal and reference arms. If a broad band source is used then the signal and reference beams must be separated by an equal and opposite path difference, -D, at the receiver so that the signal may be recovered. An eavesdropper would need to receive simultaneously the signal and reference beams and also incorporate the appropriate delay. Since the delay can be changed or modulated randomly, foreknowledge of the delay or modulation would be required. The observed signal cannot be stored whilst the correct delay is being sought because once detection has occurred, the phase information is lost. In this way a high degree of security against illicit surveillance is possible.

8.3 EXPERIMENTAL VERIFICATION

8.3.1 Fibre multiplexer with spatial light modulator

8.3.1.1 Experimental lay-out

The multiplexer is constructed as shown in figure 8.4. Light from the Helium-Neon laser, 1, is divided by the beam splitter, 2, into signal and reference beams. The reference beam traverses an adjustable free space path length, 8, before being coupled in to a single mode fibre, 9.

The signal beam is expanded and collimated, 3, before passing through a Bragg-cell, 4. A 1m focal-length lens, 5, creates the Fourier transform of the diffracted light in its focal plane. The Bragg-cell is driven by a chirped radio frequency signal, chirping from 90 to 120 MHz, at a 30kHz repetition rate.

An SLM, 6, - a photographic test card - is placed in the focal plane of the lens 5. A zero order stop is used so that only diffracted light is passed through the SLM.

The light passing through the SLM is coupled, 7, into a single mode fibre using a 1 cm F-1 lens as shown in figure 5. The position of the fibre, 2, is adjusted, 3, so that the coupled power remains fairly constant for all of the diffraction angles, 4, produced by the radiofrequency chirp. The reference and signal fibres are coupled together using a 50/50 fusion spliced coupler, 10. One of the outputs is presented to a photo-diode detector, 12, after passing through a few hundred metres of fibre, 11.

The output from the photodiode is amplified and analysed using an electronic radiofrequency spectrum analyser.

8.3.1.2 Results

The output signal-to-noise ratio is 60 dB +/- 2 dB, the variation across the range being due to the difference in coupling into the fibre over the angular spread.

By adjusting the free-space path lengths in the reference arm the modulated output power can be varied. This is due to the fringe visibility changing. (the laser runs in two longitudinal modes and the visibility curve is approximately a sinusoid).

When a photographic test card consisting of a grid of lines is used as the spatial light modulator, frequency channels are created with cut-off edges consistent with diffraction theory,

$$\delta F = \frac{v_S}{L},$$

where δF is the 3dB cut-off point and v_S is the acoustic velocity within the cell, of aperture width L.

8.3.2 Two channel transmission link

8.3.2.1 Experimental architecture

The multiplexer transmitter and demultiplexer receiver are constructed as shown in figure 8.6. The transmitter and receiver are in different rooms. The multiplexer uses a 10mW He-Ne Laser, 1, whose beam passes through a spatial filter and collimator, 2. This beam is then split by beam splitter, 3, into reference and signal beams. The signal beam passes through a Bragg-cell which is driven by 50ns, 130MHz centre-frequency pulses at a 5 MHz repetition rate. This produces a series of equally spaced diffracted beams, with Doppler shifts varying by 5MHz and with full-width-half-maxima of v_S/L. Two of these diffracted beams are used as the signal channels. The signal and reference beams are directed by mirrors, 5. The signal beams pass through Bragg cells 6 and 7, and the *un-*

diffracted beams are then combined with the reference beam at beam splitters 8 and 9. The Bragg cells 6 and 7 are driven by amplitude modulated 100MHz radio frequency signals and serve as modulators [12] to replace the SLM. A coupling lens, 10, is used to couple the combined beams into a 1000 mm diameter plastic un-clad fibre, 50m long.

At the receiver, a lens, 12, couples light out of the fibre on to a detector, 13. This is connected via an amplifier chain, 14, to a Bragg-cell, 15. Light from a He-Ne Laser, 16, is passed through a spatial filter and collimator, 17, onto the Bragg-cell, 15. Finally, the two diffracted beams are detected by detectors, 18 and 19.

Signals applied to the Bragg cells 6 and 7 are reproduced at the detectors 18 and 19.

8.3.2.2 Experimental results

The output from the multiplexer transmitter has a signal-to-noise ratio of 80dB.

The received signal-to-noise ratio at the detectors 18 and 19 is 30 dB, the difference being mostly due to losses in the transmission fibre.

The channels can be independently modulated at up to 1 MHz, this being the electronic limit of our radiofrequency switches. The modulation depth was limited by the Bragg cells, 6 and 7, to about 50%.

Cross-talk is below the noise floor.

8.4 CONCLUSIONS

We have demonstrated the feasibility of an optical multiplexer-demultiplexer communication link. With Bragg cells commercially available with a 2 GHz bandwidth, similar bandwidths should be available for a communication link. By using wavelength division multiplexing this bandwidth may be further increased.

We are currently developing a new type of Bragg-cell, employing an electroopic interaction as describdd in chapter 7 which will allow much higher bandwidths than are currently available with acoustooptic cells [8.13]. If a device such as this is used to replace the acoustooptic Bragg-cell then bandwidths in excess of 30 GHz should be possible.

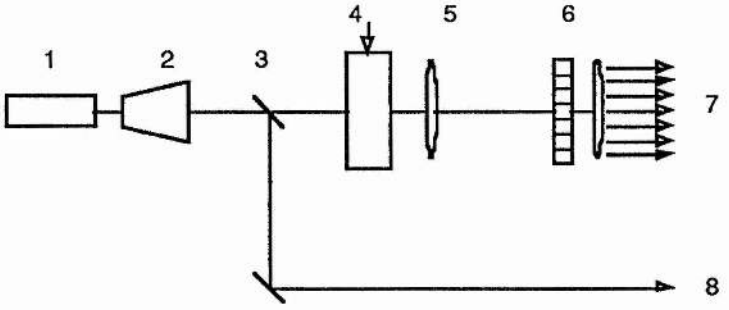

Figure 8.1

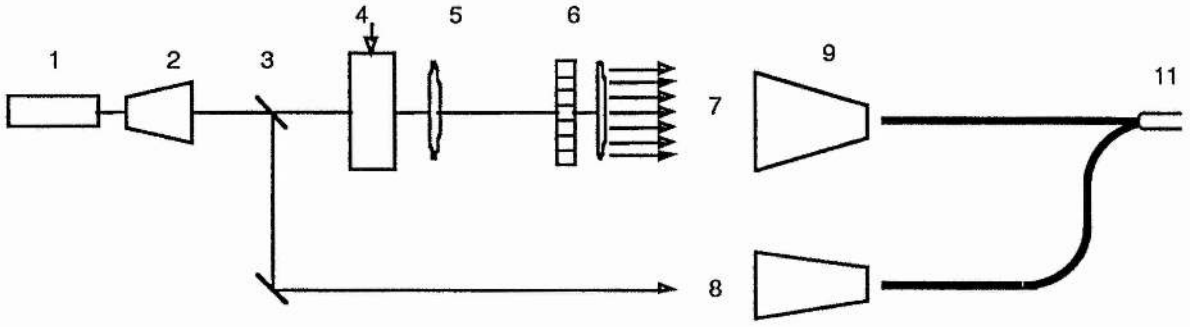

Figure 8.2

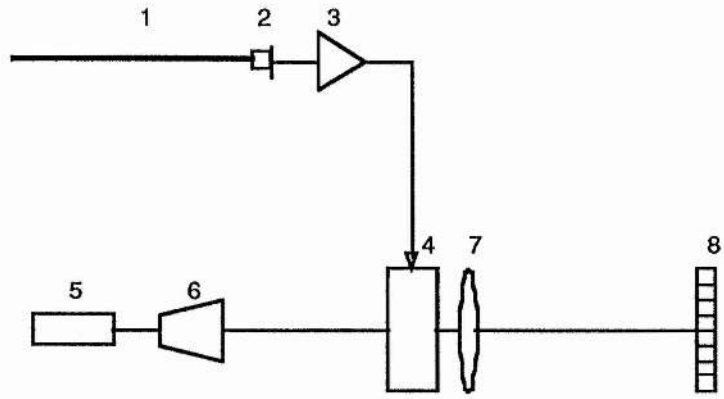

Figure 8.3

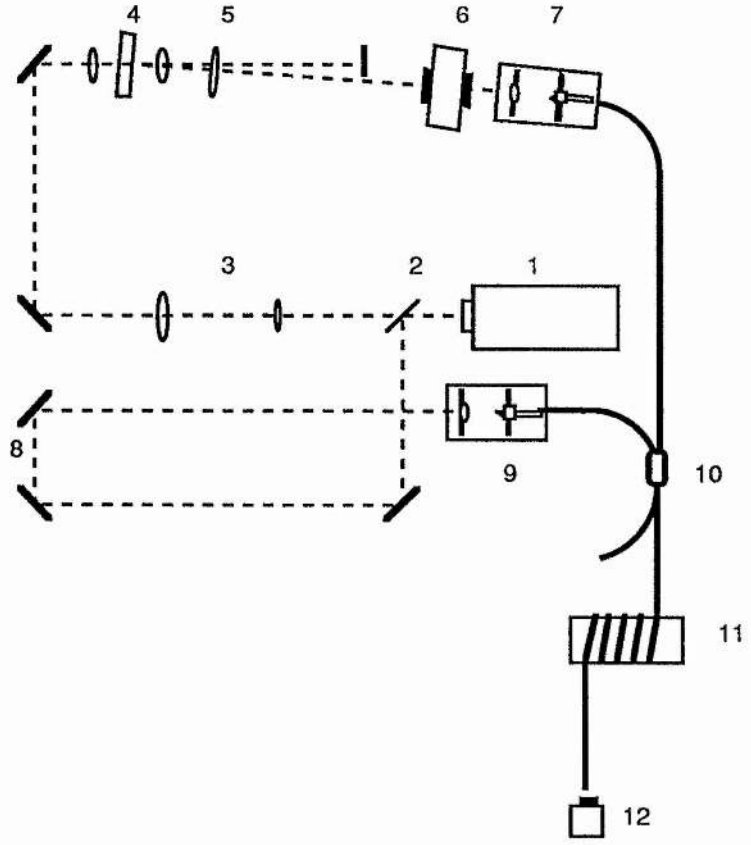

Figure 8.4

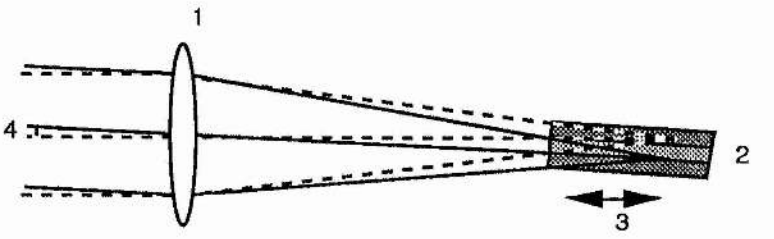

Figure 8.5

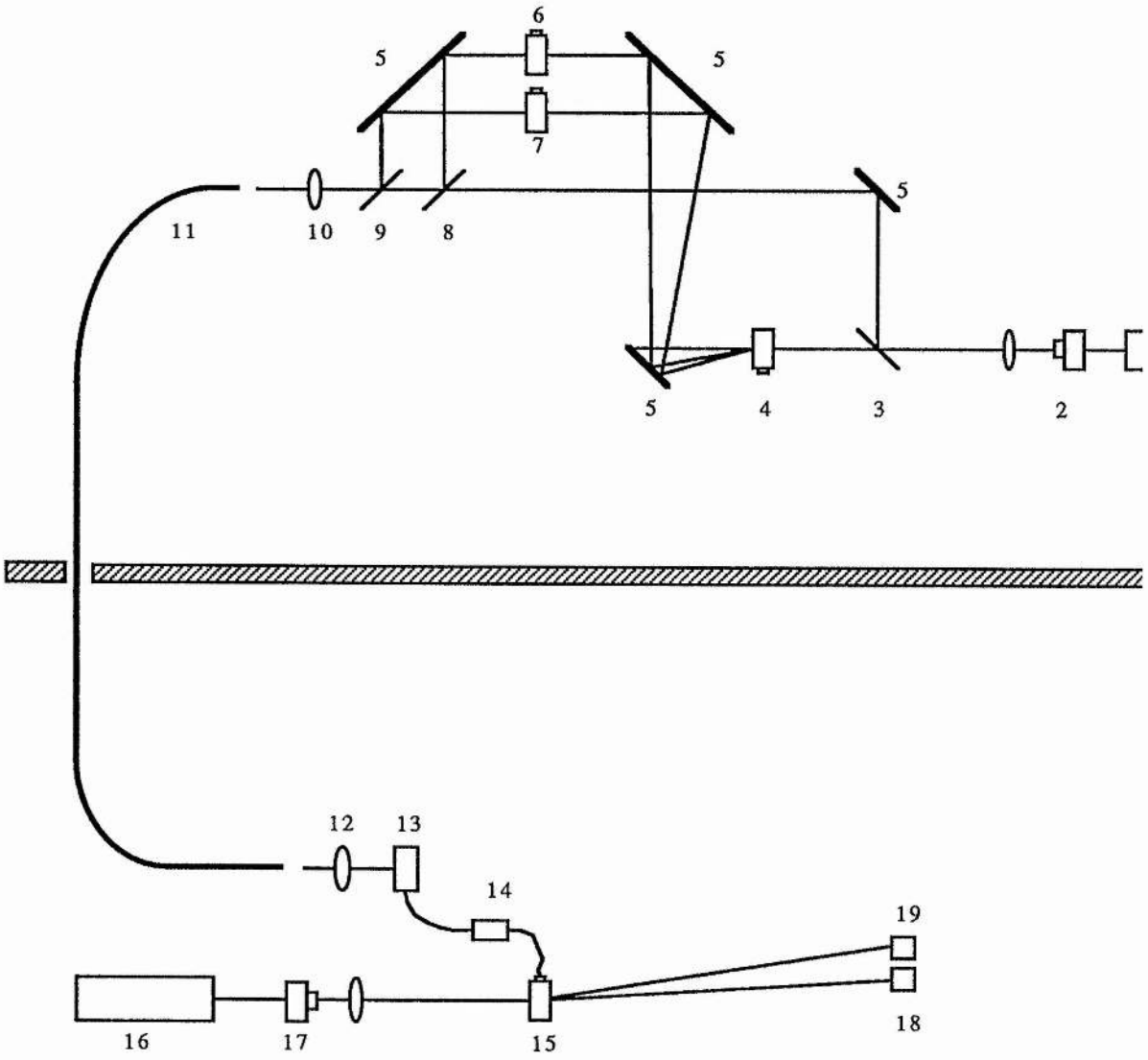

Figure 8.6

8.5 REFERENCES

[8.1] "Acoustooptic Bragg-diffraction with application to ultrahigh data rate communication systems. 1: Theoretical considerations of the standing wave ultrasonic Bragg-cell."

S. Yao, C. Tsai

A.O. Vol. 16, No. 11, 3032-3043, Nov 77

[8.2] "Acoustooptic Bragg-diffraction with application to ultrahigh data rate communication systems. 2: Experimental results of the SUBC and the acoustooptical multiplexer/demultiplexer terminals."

C. Tsai, S. Yao

A.O. Vol. 16, No. 11, 3044-3059, Nov 77

[8.3] "Acoustooptic signal processing"

Berg, Lee

Marcel Dekker inc ISBN 0-8247-1667-12

[8.4] "Acoutooptics"

J. Sapriel

John Wiley and sons ISBN 0-471-99700-5

[8.5] "Ultrasonic signal processing"

A. Alipi

World Scientific ISBN 9971-50-864-8

[8.6] "Interaction of light and microwave sound"

C. F. Quate, C. D. Wilkinson and D. K. Winslow

AO vol. 53 No. 10, Oct 65

[8.7] "Optical spectrum analysis of large space bandwidth signals"

C. Thomas

AO Vol 5, No. 11, 1782-1790, Nov 66

[8.8] "Real time electrooptic signal processors with coherent detection"

M. King, W. Bennet, L. Lambert, M. Arm

AO Vol. 6, No. 8, 1367-1375, Aug. 67

[8.9] "Interferometric spectrum analyser"

A. Vander Lugt, A. Bardos

AO Vol. 23, No. 23, 4269-4278

[8.10] "Spatial and temporal response of an acoustooptic Bragg-cell"

A. Vander Lugt

AO 15 Sept 89 Vol 28, No. 23

[8.11] "Temporal response of short and evolving pulses in interferometric spectrum analysers"

P. Wisseman, A. Vander Lugt

AO Vol. 28, No. 18, 3800-3809, Sep 89

[8.12] "Simple acoustic modulators"

J. Hamer, D. Channin

AO Vol. 11, No. 10, 2203, Oct 72

[8.13] "Light modulating cells"

W. Dawber, P. Hirst, A. Maitland

GB Patent Application No. 9021044.4

Appendix 1

High-Speed Photodiode Circuits

A.1.1 INTRODUCTION

We describe here the photodiode-amplifier circuit used for the experiments involving heterodyne detection. In order to detect an optical beam modulated at hundreds of megahertz, high speed photodiodes must be used. Charge coupled Device (ccd) arrays and photomultiplier tubes are simply not fast enough.

A.1.2 PHOTODIODE CIRCUIT

The "B.P.X. 65" photodiode is a planar silicon PIN photodiode mounted in a modified TO-18 case. Because of its outstanding low junction capacitance and short switching time, coupled with wide bandwidth (spectral response), the BPX 65 is an ideal choice for signal processing applications.

The BPX 65 has a quoted capacitance of 3.5 pF and a cut-off frequency of 500 MHz at a reverse bias of 20 V.

This circuit has a limiting frequency $\omega=1/(RC)$. For operation at 120 MHz (the centre frequency of the Bragg-cell) a resistor of about 200Ω is required.

This gives a (quoted) responsivity of around 0.1 V/mW at 800nm.

In order to shield the diode and bias circuit from noise, the diode was mounted in a diecast aluminium box as shown in figure A.1.3.2. The leads to the chip were kept as short as possible, to reduce losses and cross-talk. A feed-through capacitor was used on the supply rail to stop radiofrequency noise in the power supply entering the box. A BNC-type connector was used for the output and the diode was mounted in a rubber grommet to insulate the case (cathode) from the earth.

A.1.3 AMPLIFIER CIRCUIT

In order to obtain a reasonable output from the photodiode, amplification of the signal from the diode circuit (figure A.1.1) of the order of 60dB is required. The amplifier should have a level response from 40MHz up to around 500MHz.

The OM335 has been found to give good results using the circuit shown in figure A.1.3 Sheet copper is used to provide a continuous connection between the sides of the diecast box and the earth plane of the printed circuit board. Copper tags are also used to connect the lower earth plane to the upper earth plane. This increases the gain from 20 to 27 dB and reduces spurious harmonic levels.

Printed circuit boards for the OM335 are constructed by photo-etching, using a mask. Tapered strips are incorporated to step from 75Ω (the input and output impedance of the

OM335, to 50Ω, the impedance of the BNC connectors). Thetapered strips are calculated by strip-line theory to be about 2mm tapering to 1.5mm, for the board used.

A feed-through capacitor is used for the power rail and all runs to the board are kept to a minimum .

These amplifiers produce around 28dB gain from 100MHz to 1GHz when used singly and 56dB when 2 are used in series, with no harmonics, for an output below -10dBm. With 3 amplifiers in series there is a gain of 78dB but some broad-band noise is produced between 150 and 500 MHz . The gain can be adjusted in all cases by varying the supply voltage, up to 24V.

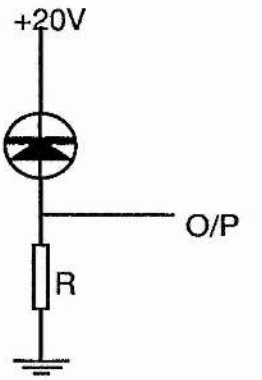

Figure A.1.1

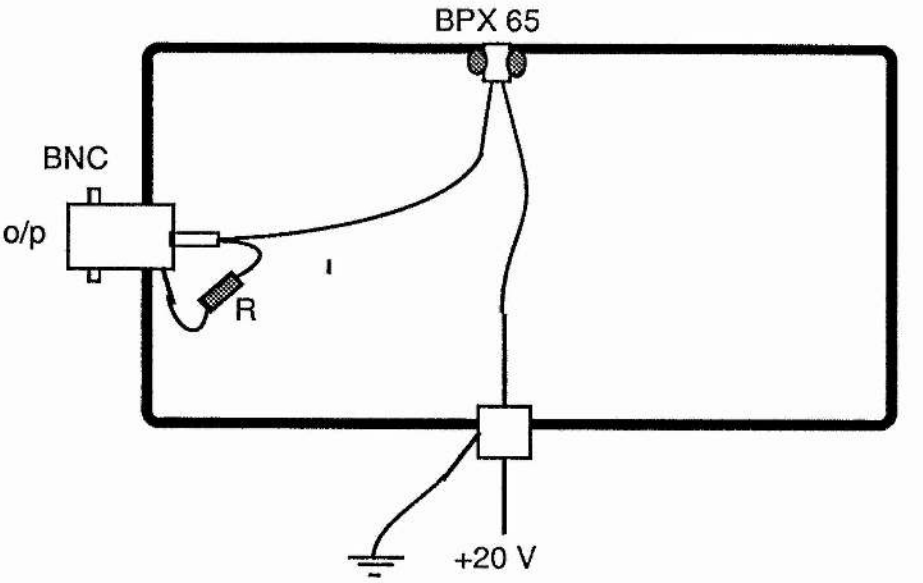

Figure A.1.2

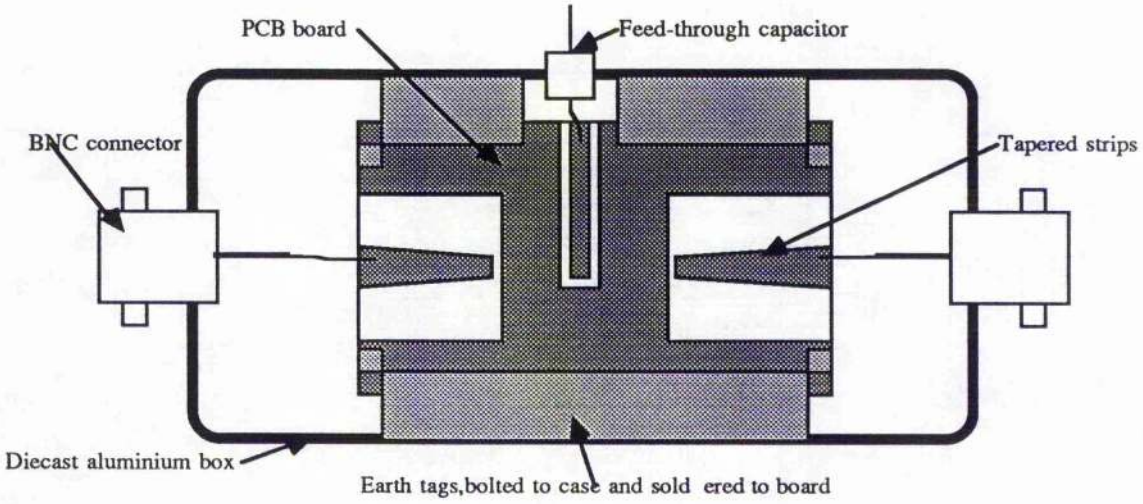
PCB board
Feed-through capacitor
BNC connector
Tapered strips
Diecast aluminium box
Earth tags,bolted to case and sold ered to board

Figure A.1.3

Appendix 2

Temporal Analysis of light Diffracted from Radiofrequency Pulses within an Acoustooptic Bragg-cell

In chapter 6 the full derivations of the Fourier transforms required to obtain the temporal distribution were omitted. The full analysis is given below.

A.2.1 SHORT PULSE CASE

Equation 5 is

$$d_1(\rho,t) = \int_{-L/2}^{-L/2+vt} A\exp[i\omega_s(t-x/v)]\exp(i\rho x)dx \qquad \text{A.2.1}$$

$$= A\exp(i\omega_s t)\int_{-L/2}^{-L/2+vt}\exp[i(\rho-\rho_s)x]dx \qquad \text{A.2.2}$$

$$= Avt\exp(i\omega_s t)\exp[i(\rho_s-\rho)L/2]\exp[i(\rho-\rho_s)vt/2]\mathrm{sinc}[(\rho-\rho_s)vt/2] \qquad \text{A.2.3}$$

$$= Avt\exp[i(\rho+\rho_s)vt/2]\mathrm{sinc}[(\rho-\rho_s)vt/2]\exp[i(\rho_s-\rho)L/2] \qquad \text{A.2.4}$$

and so we have

$$d_1(\rho,t) = A\phi_1 vt\exp[i(\rho+\rho_s)vt/2]\mathrm{sinc}[(\rho-\rho_s)vt/2]\,, \qquad \text{A.2.5}$$

where ϕ_1 is a phase factor.

For $t<\tau$, the diffraction pattern is a sinc function with angular half width λ/vt.

For $\tau<t<T$, the pulse is entirely within the cell and we have

$$d_2(\rho,t) = \int_{-L/2+vt}^{-L/2+vt+v\tau} A\exp[i\omega_s(t-x/v)]\exp(i\rho x)dx \qquad \text{A.2.6}$$

$$= A\exp(i\omega_s t) \int_{-L/2+vt}^{-L/2+vt+v\tau} \exp[i(\rho-\rho_s)x]dx \qquad \text{A.2.7}$$

$$= A\exp(i\omega_s t)\frac{1}{i(\rho-\rho_s)}\exp[i(-L/2+vt)(\rho-\rho_s)]\{\exp[i(\rho-\rho_s)v\tau] - 1\} \qquad \text{A.2.8}$$

$$= Av\tau\exp(i\omega_s t)\exp[i(-L/2+vt)(\rho-\rho_s)]\exp[i(\rho-\rho_s)v\tau/2]\mathrm{sinc}[(\rho-\rho_s)v\tau/2] \qquad \text{A.2.9}$$

$$= Av\tau\exp[i\{(v\tau-L)(\rho-\rho_s)/2+vt\rho\}]\mathrm{sinc}[(\rho-\rho_s)v\tau/2] \; . \qquad \text{A.2.10}$$

But we may write

$$\rho v = \omega_\rho \; , \qquad \text{A.2.11}$$

where ω_ρ is the Doppler-shifted centre-frequency corresponding to the spatial frequency ρ.

Then we have

$$d_2(\rho,t) = Av\tau\exp[i(v\tau-L)(\rho-\rho_s)/2]\exp(i\omega_\rho t)\mathrm{sinc}[(\rho-\rho_s)v\tau/2] \qquad \text{A.2.12}$$

and we obtain

$$d_2(\rho,t) = Av\tau\exp(i\omega_\rho t)\mathrm{sinc}[(\rho-\rho_s)v\tau/2]\phi_2\,, \qquad \text{A.2.13}$$

where ϕ_2 is a phase term.

For $\tau<t<T$, the spatial distribution is a sinc function with angular half width $\lambda/v\tau$.

For $T<t<T+\tau$, the pulse is leaving the cell. By symmetry we see that the diffraction pattern must be the same as that for the pulse entering the system, but with a different phase term, ϕ_3.

$$d_3(\rho,t) = \phi_3 d_1(\rho,t) \qquad \text{A.2.14}$$

$$d_3(\rho,t) = A\phi_4 vt\,\exp[i(\rho+\rho_s)vt/2]\mathrm{sinc}[(\rho-\rho_s)vt/2]\,. \qquad \text{A.2.15}$$

The temporal distribution is given by equation 6.4, where we have

$$d(\rho,\omega) = \int_0^\tau d_1(\rho,t)\exp(-i\omega t)dt + \int_\tau^T d_2(\rho,t)\exp(-i\omega t)dt + \int_T^{T+\tau} d_3(\rho,t)\exp(-i\omega t)dt \qquad \text{(A.2.16)}$$

We may write

$$d(\rho,\omega) = d_1(\rho,\omega) + d_2(\rho,\omega) + d_3(\rho,\omega)\,, \qquad \text{A.2.17}$$

where we have

$$d_1(\rho,\omega) = \int_0^{\tau} d_1(\rho,t)\exp(-i\omega t)dt \qquad \text{A.2.18}$$

$$= \int_0^{\tau} A\phi_1 vt\exp[i(\rho+\rho_s)vt/2]\mathrm{sinc}[(\rho-\rho_s)vt/2]\exp(-i\omega t)dt \qquad \text{A.2.19}$$

$$= A\phi_1 v \int_0^{\tau} \frac{2t\sin[(\rho-\rho_s)vt/2]}{(\rho-\rho_s)vt} \exp\{i[(\rho+\rho_s)v/2-\omega]t\}dt \qquad \text{A.2.20}$$

$$= \frac{2A\phi_1}{\rho-\rho_s} \int_0^{\tau} \sin[(\omega_\rho-\omega_s)t/2]\exp[i(\omega_\rho+\omega_s-2\omega)t/2]dt\,. \qquad \text{A.2.21}$$

We will write equation A.2.21 as

$$d_1(\rho,\omega) = \frac{2A\phi_1}{\rho-\rho_s} I\,, \qquad \text{A.2.22}$$

where

$$I = \int_0^{\tau} \sin[(\omega_\rho-\omega_s)t/2]\exp[i(\omega_\rho+\omega_s-2\omega)t/2]dt \qquad \text{A.2.23}$$

$$= \int_0^{\tau} \sin(\alpha t)\exp(i\beta t)dt \qquad \text{A.2.24}$$

$$= \left[-\frac{1}{\alpha}\cos(\alpha t)\exp(i\beta t) \right]_0^\tau + \frac{i\beta}{\alpha}\int_0^\tau \cos(\alpha t)\exp(i\beta t)dt \qquad \text{A.2.25}$$

$$= \left[-\frac{1}{\alpha}\cos(\alpha t)\exp(i\beta t) \right]_0^\tau + \frac{i\beta}{\alpha^2}\left[\sin(\alpha t)\exp(i\beta t) \right]_0^\tau + \frac{\beta^2}{\alpha^2}\int_0^\tau \sin(\alpha t)\exp(i\beta t)dt \qquad \text{A.2.26}$$

$$I = \left[-\frac{1}{\alpha}\cos(\alpha t)\exp(i\beta t) \right]_0^\tau + \frac{i\beta}{\alpha^2}\left[\sin(\alpha t)\exp(i\beta t) \right]_0^\tau + \frac{\beta^2}{\alpha^2} I \qquad \text{A.2.27}$$

and so we obtain

$$I = \frac{1}{\alpha - \beta^2/\alpha}\{ [\frac{i\beta}{\alpha}\sin(\alpha\tau) - \cos(\alpha\tau)]\exp(i\beta\tau) + 1 \} \qquad \text{A.2.28}$$

$$= \frac{1}{\alpha - \beta^2/\alpha}\{ \left[\frac{i\beta\exp(i\alpha\tau)-\exp(-i\alpha\tau)}{\alpha} \cdot \frac{\exp(i\alpha\tau)+\exp(-i\alpha\tau)}{2i} \right]\exp(i\beta\tau) + 1 \} \qquad \text{A.2.29}$$

$$= \frac{1}{\alpha - \beta^2/\alpha}\{ \frac{\exp[i(\alpha+\beta)\tau]-1}{2}(\frac{\beta}{\alpha} - 1) - \frac{\exp[i(\beta-\alpha)\tau]-1}{2}(\frac{\beta}{\alpha} + 1) \} \qquad \text{A.2.30}$$

$$= \frac{1}{\alpha - \beta^2/\alpha}\{ \exp[-i(\alpha+\beta)\tau/2](\alpha+\beta)\tau/2(\frac{\beta}{\alpha} - 1)\mathrm{sinc}[(\alpha+\beta)\tau/2]$$
$$- \exp[i(\alpha-\beta)\tau/2](\beta-\alpha)\tau/2(\frac{\beta}{\alpha} + 1)\mathrm{sinc}[(\beta-\alpha)\tau/2] \} \qquad \text{A.2.31}$$

$$= -\frac{\tau}{2}\{ \exp[-i(\alpha+\beta)\tau/2]\mathrm{sinc}[(\alpha+\beta)\tau/2] - \exp[i(\alpha-\beta)\tau/2]\mathrm{sinc}[(\beta-\alpha)\tau/2] \} \qquad \text{A.2.32}$$

We write equation A.2.32 as

$$I = -\frac{\tau}{2}\{\ \phi_5\ \mathrm{sinc}[(\omega_\rho-\omega)\tau/2] - \phi_6\mathrm{sinc}[(\omega_s-\omega)\tau/2]\ \} \qquad \text{A.2.33}$$

Therefore from equation A.2.22 we obtain

$$d_1(\rho,\omega) = \frac{A\tau\phi_1}{\rho-\rho_s}\{\phi_6\mathrm{sinc}[(\omega_s-\omega)\tau/2] - \phi_5\ \mathrm{sinc}[(\omega_\rho-\omega)\tau/2]\} \qquad \text{A.2.34}$$

The contribution to the temporal profile for $t < \tau$ consists of two sinc functions, in frequency, centred at ω_ρ and ω_s, respectively, with FWHM of $2\pi/\tau$.

The contribution to the distribution from the period when the pulse is entirely within the cell is given by

$$d_2(\rho,\omega) = \int_\tau^T d_2(\rho,t)\exp(-i\omega t)dt \qquad \text{A.2.35}$$

$$= \int_\tau^T A v\tau\exp(i\omega_\rho t)\mathrm{sinc}[(\rho-\rho_s)v\tau/2]\phi_2\exp(-i\omega t)dt) \qquad \text{A.2.36}$$

$$= A\phi_2 v\tau\mathrm{sinc}[(\rho-\rho_s)v\tau/2]\int_\tau^T \exp[i(\omega_\rho-\omega)t]dt \qquad \text{A.2.37}$$

$$= A\phi_2 v\tau(T-\tau)\mathrm{sinc}[(\rho-\rho_s)v\tau/2]\exp[i(\omega_\rho-\omega)(T+\tau)/2]\mathrm{sinc}[(\omega_\rho-\omega)(T-\tau)/2]$$

A.2.38

We write equation A.2.38 as

$$d_2(\rho,\omega) = A\phi_2\phi_7 v\tau(T-\tau)\mathrm{sinc}[(\rho-\rho_s)v\tau/2]\mathrm{sinc}[(\omega_\rho-\omega)(T-\tau)/2] \qquad \text{A.2.39}$$

Where ϕ_7 is a phase term.

The contribution to the temporal profile for $\tau<t<T$ consists of a sinc function, in frequency space, centred at ω_ρ with a FWHM of $2\pi/(T-\tau)$.

For $t > T$ we have

$$d_3(\rho,\omega) = \int_T^{T+\tau} d_3(\rho,t)\exp(-i\omega t)dt \qquad \text{A.2.40}$$

$$= \int_T^{T+\tau} \phi_3 d_2(\rho,t)\exp(-i\omega t)dt \qquad \text{A.2.41}$$

and we see

$$d_3(\rho,\omega) = \phi_3\, d_1(\rho,\omega) \qquad \text{A.2.42}$$

The contribution to the temporal profile for $t > T$ is the same as that for $t<\tau$ but with a different phase, ϕ_3.

The total temporal distribution of the pulse travelling through the whole cell is given by

$$d(\rho,\omega) = d_1(\rho,\omega) + d_2(\rho,\omega) + d_3(\rho,\omega) \qquad \text{A.2.43}$$

$$d(\rho,\omega) = (1+\phi_3)\frac{A\tau\phi_4}{\rho-\rho_s}\{\phi_6 \text{sinc}[(\omega_s-\omega)\tau/2] - \phi_5 \text{sinc}[(\omega_\rho-\omega)\tau/2]\}$$
$$+ A\phi_2\phi_7 v\tau(T-\tau)\text{sinc}[(\rho-\rho_s)v\tau/2]\text{sinc}[(\omega_\rho-\omega)(T-\tau)/2] \qquad \text{A.2.44}$$

The distribution contains terms centred around ω_ρ with FWHM of $2\pi/\tau$ and $2\pi/(T-\tau)$, the relative magnitudes dependent on the pulse length, τ, compared with the Bragg-cell aperture T. There is also a term centred at ω_s with FWHM $2\pi/\tau$, with magnitude proportional to the pulse length, τ.

A.2.2 LONG-PULSE CASE

For a pulse with duration greater than the Bragg-cell temporal aperture, i.e. $\tau > T$, the contributions from the pulse entering and leaving the cell are similar to those produced by the short pulse.

For $t < T$ (pulse entering the cell), the spatial distribution is given by

$$d_1(\rho,t) = A\phi_1 v t \exp[i(\rho+\rho_s)vt/2]\text{sinc}[(\rho-\rho_s)vt/2] \,. \qquad \text{A.2.45}$$

The contribution to the temporal distribution is

$$d_1(\rho,\omega) = \frac{AT\phi_1}{\rho-\rho_s}\{\phi_6 \text{sinc}[(\omega_s-\omega)T/2] - \phi_5 \text{sinc}[(\omega_\rho-\omega)T/2]\} \,. \qquad \text{A.2.46}$$

There are similar terms for $\tau < t < T+\tau$ (pulse leaving the cell).

For the time the pulse fills the cell, $T<t<\tau$, we have a new term given by

$$d_2(\rho,t) = \int_{-L/2}^{L/2} A\exp[i\omega_s(t-x/v)]\exp(i\rho x)dx \qquad \text{A.2.47}$$

$$d_2(\rho,t) = A\exp(i\omega_s t) \int_{-L/2}^{L/2} \exp[i(\rho-\rho_s)x]dx\ . \qquad \text{A.2.48}$$

Then we have

$$d_2(\rho,t) = A\exp(i\omega_s t)\frac{1}{i(\rho-\rho_s)} \{\exp[i(\rho-\rho_s)L/2] - \exp[-i(\rho-\rho_s)L/2]\ \} \qquad \text{A.2.49}$$

$$d_2(\rho,t) = A\exp(i\omega_s t)L\mathrm{sinc}[(\rho-\rho_s)L/2]\ . \qquad \text{A.2.50}$$

The spatial distribution is a sinc function with angular half width λ/L.

The contribution to the temporal distribution is then given by equation A.2.4 where we have

$$d_2(\rho,\omega) = \int_{T}^{\tau} A\exp(i\omega_s t)L\mathrm{sinc}[(\rho-\rho_s)L/2]\exp(-i\omega t)dt \qquad \text{A.2.51}$$

$$d_2(\rho,\omega) = AL\mathrm{sinc}[(\rho-\rho_s)L/2] \int_{T}^{\tau} \exp[i(\omega_s-\omega)t]dt \qquad \text{A.2.52}$$

$$d_2(\rho,\omega) = AL(\tau-T)\mathrm{sinc}[(\rho-\rho_s)L/2]\exp[i(\omega-\omega_s)(\tau+T)/2]\mathrm{sinc}[(\omega_s-\omega)(\tau-T)/2] \quad 65$$

$$d_2(\rho,\omega) = AL(\tau-T)\text{sinc}[(\rho-\rho_s)L/2]\text{sinc}[(\omega_s-\omega)(\tau-T)/2]\phi_8 , \qquad \text{A.2.53}$$

where ϕ_8 is a phase term.

The contribution to the temporal profile for $T<t<\tau$ is a sinc function centred at ω_s with half-width, $\frac{2\pi}{\tau-T}$.

The full temporal distribution for the long pulse is then

$$d(\rho,\omega) = (1+\phi)\frac{AT\phi_4}{\rho-\rho_s}\{\phi_6\text{sinc}[(\omega_s-\omega)T/2] - \phi_5\,\text{sinc}[(\omega_\rho-\omega)T/2]\}$$
$$+ AL(\tau-T)\text{sinc}[(\rho-\rho_s)L/2]\text{sinc}[(\omega_s-\omega)(\tau-T)/2]\phi_8 \qquad \text{A.2.54}$$

The full temporal distribution contains two terms centred at ω_s with FWHM of $2\pi/T$ and $2\pi/(\tau-T)$. There is a term centred at ω_ρ proportional to T with FWHM of $2\pi/T$.

Appendix 3

Patent Applications

The following pages contain copies of GB Patent Applications which were derived from the research carried out for this thesis.

A Wide Bandwidth Bragg Cell RF Spectrum Analyser

The invention relates to radio-frequency spectrum analysers using acousto-optic or Bragg cells for analysing signals and in particular to spectrum analysers employing Bragg cells in resonant cavities.

One method for spectrum analysis of an FM signal is to apply the signal to a Bragg cell and measure the optical diffraction effects produced by the interaction of laser light and the acoustic waves present in the Bragg cell. The performance of Bragg cells in this application have the following performance limitations:

a) limited frequency bandwidth at high diffraction efficiency;
b) limited dynamic range; and
c) significant material intermodulation effects.

Steir et al, Applied Physics 27, No 8 (15 April 1988), have shown that the diffraction efficiency of a stationary grating may be improved by placing the grating in a resonant cavity. The Bragg cell may be placed in a two-mirror resonant cavity, with one mirror 100% reflecting and the other mirror partially reflecting and this results in enhanced Bragg cell diffraction. This arrangement can be used in a white light RF spectrum analyser. The inventor has shown, however, that a practical spectrum analyser cannot be based on this configuration. Another possible arrangement utilises a four mirror conformal cavity where the round trip path length for a ray of light remains constant for small changes in the Bragg angle. These arrangements have been shown to have limited bandwidth and resolution.

The object of the invention is to provide a wideband resonant cavity Bragg cell spectrum analyser which overcomes problems associated with known arrangements.

The invention provides a broadband electrical signal spectrum analyser comprising:

a Bragg cell;
at least one resonant cavity in which the Bragg cell is located;
a source of light illuminating the cavity; and
means to connect the signal to the Bragg cell;

the arrangement being such that the cavity can be tuned to different wavelengths so as to provide multiple channel, broadband frequency response.

Each tuned cavity provides narrow-band lasing which enhances the Bragg cell efficiency.

In one arrangement a plurality of fixed resonant cavities is formed by providing a fibre optic array. Advantageously the fibres of the array are arranged such that a linear array of input ends is formed on one side of the Bragg cell and the respective other ends of the optical fibres form a linear output array on the opposed side of the Bragg cell.
Advantageously each of the optical fibres is passed around a piezo-electric cylinder to keep the cavities tuned to their respective wavelengths. A fibre optic coupling arrangement may be used to couple light from each resonant optical fibre cavity to an output optical fibre connected to an optical detector. Advantageous photodiodes are used.

In an alternative arrangement a single dynamic cavity is provided by locating the Bragg cell between two mirrors, one mirror being totally reflecting and the other being partially reflecting; the arrangement being that one mirror is oscillated such that the tuned cavity scans a range of wavelengths. Advantageously a slit is provided in the image plane behind the partially transparent mirror and a detector is arranged to detect light passing through the slit.

Advantageously white light is used with a collimating lens being provided on one input side of the Bragg cell and a Fourier transforming lens being provided on the output side of the Bragg cell. Advantageously a high "Q" Bragg cell is used.

The invention will now be described by way of example only with reference to the accompanying Drawings of which:

Figure 1 shows a known laser RF signal spectrum analyser;
Figure 2 shows a white light RF spectrum analyser using cavity enhanced diffraction;
Figure 3 shows a schematic diagram of an alternative RF spectrum analyser

using a fibre optic array; and
Figure 4 shows in greater detail one fibre optic channel of the Figure 3 arrangement.

As shown in Figure 1, in a typical acousto-optic spectrum analyser light from a laser 10 is collimated (11) by an arrangement of lenses 12,13 with a narrow slit (not shown) between to provide a broad beam incident on an acousto-optic Bragg cell 14. A radio frequency (RF) signal to be analysed is coupled to the Bragg cell by a transducer 15, producing propagating acoustic waves within the Bragg cell. The quasi-monochromatic light incident on the Bragg cell 14 interacts with the acoustic field therein to produce a diffraction pattern which is examined in the focal plane of a Fourier transforming lens 16 by an array of detectors 17. A stop 18 is provided to block undiffracted zero-order light. The Bragg cell 14 is positioned such that the angle of incidence of the laser light is fixed. As the frequency of the acoustic wave in the Bragg cell changes, the position of the light focused by lens 16 also changes. Thus the outputs from the array 17 can be used to analyse the RF signal applied to the Bragg cell. When used in this way, there is poor frequency response and the performance is limited by intermodulation effects. Intermodulation effects arise because of two effects:

a) Hecht intermodulation due to light being diffracted more than once by the acoustic signal; and
b) material intermodulation due to the non-linear factors in the interaction equation and the breakdown of the interaction at high acoustic power densities.

In order to improve the bandwidth of the RF spectrum analyser polychromatic white light sources have been tried. In this arrangement collimated light is incident on the Bragg cell. The diffracted light at one output angle of diffraction (equal to the input angle) is monitored with an optical spectrometer. As the radio-frequency in the cell changes, the wavelengths of the light incident on the spectrometer changes. There is always an optical wavelength which satisfies the Bragg condition for diffraction at a given radio-frequency and hence the bandwidth is limited only by the transducer and polychromatic source bandwidths. However, in practice, the resolution of the spectrometer is limited by the degree of collimation of the

incident light we have:

$$\lambda = \theta$$

where λ is the wavelength, θ is the Bragg angle and o θ is the degree of collimation.

When using an arc lamp as the polychromatic source, the beam is collimated by focusing it on to a slit. The angular width subtended by the slit at the lens centre determines the degree of collimation. The resolution is then inversely related to the slit width so we seek a trade-off between resolution and intensity reaching the detectors. In practice, the light intensity reaching the detectors is very low, for resolutions better than 1 part in 100 i.e. 1 MHz resolution at a centre frequency of 100 MHz. Thus, for use in a practical system it has been found that the diffraction efficiency needs to be improved. The inventors have shown that a high "Q" transducer 15 is likely to reduce intermodulation effects but with a penalty of a reduction in frequency bandwidth. Thus, if the bandwidth of the spectrum analyser can be increased, some bandwidth enhancement could be traded for a reduction in intermodulation effects.

Figure 2 shows an RF spectrum analyser according to the invention where a Bragg cell is placed in a tunable resonance cavity. Light from an arc lamp 20 after collimation (21) is incident at angle θ on a Bragg cell 22. The cell 22 is located in a lasing cavity defined by a 100% reflecting mirror 23 and a partially reflecting mirror 24. Light diffracted at an angle θ to the normal is reflected back and forth between the mirrors 23, and 24 and is enhanced by lasing action. Light which is transmitted by the partially reflecting mirror 24 is focused by a lens 25 to a slit in a screen where it is viewed by a detector 27. In this arrangement the wavelength of the diffracted light reaching the slit in the screen 26 is inversely proportional to the frequency applied to the Bragg cell 22. The mirror 23 is oscillated through an amplitude sufficient to change the cavity resonance frequency through the required spectral range. The wavelength which is diffracted to the slit will then be on resonance in the cavity twice during each cycle. The light detected by the detector 27 is a series of pulses whose amplitude is proportional to the amplitude of the RF applied to the cell 22 for low

diffraction efficiencies. It has been found that the cell 22 starts to saturate for cell efficiencies above about 5% and thus the usable dynamic range is limited to input RF powers less than those which give greater than 5% cell efficiencies.

Figure 3 illustrates an arrangement of the invention having a single Bragg cell 30 located within a plurality of fixed resonant cavities formed by a fibre optic array. Fibres 1 to n of a fibre optic array are arranged such that one set of ends forms a linear input array 31 at the optical input side of the Bragg cell 30 while the other ends of the fibres are arranged to form a linear output array 32 on the optical output side of the Bragg cell. Light 33 from a polychromatic source is incident on the Bragg cell 30 after transmission through a collimating lens 34. A Fourier transform lens 35 focuses diffracted light towards the output array of optical fibres 1 to n. After Fourier transformation the spatial position in the image plane of the FT lens 35 corresponds to the frequency of the light emerging from the Bragg cell 30. As in the previous arrangement an electrical signal to be analysed is connected to the Bragg cell such that the acoustic field formed therein interacts with the incident light 33 to produce diffracted light dependent on the amplitude and frequency of the spectral composition of the electrical signal.

Figure 4 shows one monomode fibre optic channel 40 in greater detail. Input light impinges on the Bragg cell 30 at an angle of incidence θ and the linear input and output arrays 31 and 32 are arranged to receive/transmit diffracted light at a range of diffraction angles ϕ. As shown, diffracted light enters the end 41 of the optical fibre 40 in the output array 32. It is then transmitted through the optical fibre via a fibre optic coupling 42 to the opposed end 43 in the input array 31. Diffracted light emerging from the end 43 of the optical fibre is incident on the Bragg cell and the zeroth (undiffracted) order is transmitted linearly through the Bragg cell to enhance the diffracted radiation entering the end 32 of the fibre 40. In this manner diffracted light is circulated repeatedly around the fibre 40 and through the Bragg cell. A proportion of the diffracted light is coupled to an output monomode optical fibre 44 in the coupling 42. The repeated transmission of the diffracted light through the Bragg cell produces lasing action and thereby enhances the signal received by the output fibre 44. A photodiode 45 is provided to measure light in the output fibre 44.

The optical fibre 40 thus forms one fibre ring cavity where the cavity length can be turned by appropriate selection of the length of the optical fibre 40. The optical fibre is passed around a piezo-electric cylinder 46 to enable the length and hence the tuning of the ring to be maintained constant. In like manner each optical fibre in the array is tuned so as to provide n frequency channels with appropriately tuned resonant cavities. The full width of the Bragg cell 30 can be illuminated, so that with this arrangement the resolution and the bandwidth are maintained whilst still retaining the diffraction efficiency of the cavity.

The use of enhanced Bragg cell diffraction should allow large reductions in intermodulation by reducing the acoustic power densities required within the cell. In addition, the invention provides a practical white light system with a very high resolution and large bandwidth without the usual problems associated with extremely low light levels.

FIG.1

TYPICAL ACOUSTO - OPTIC SYSTEM

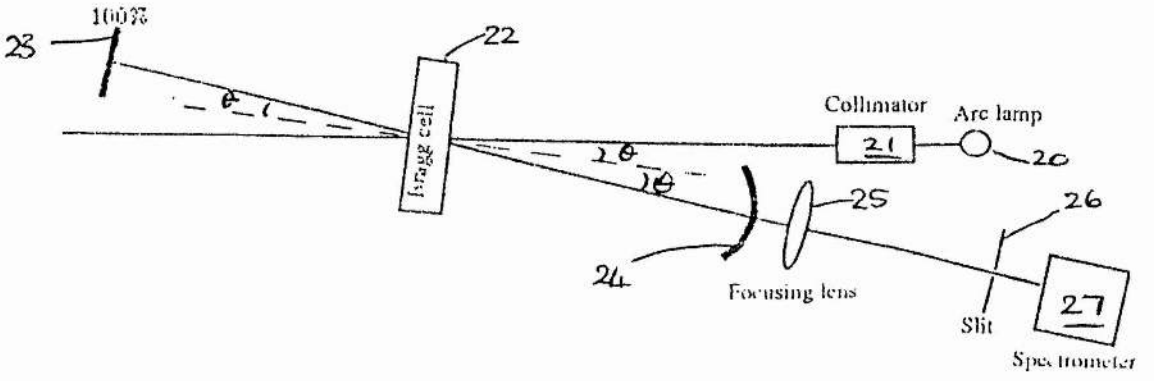

Figure 2: White light RF spectrum analyser using cavity enhanced diffraction

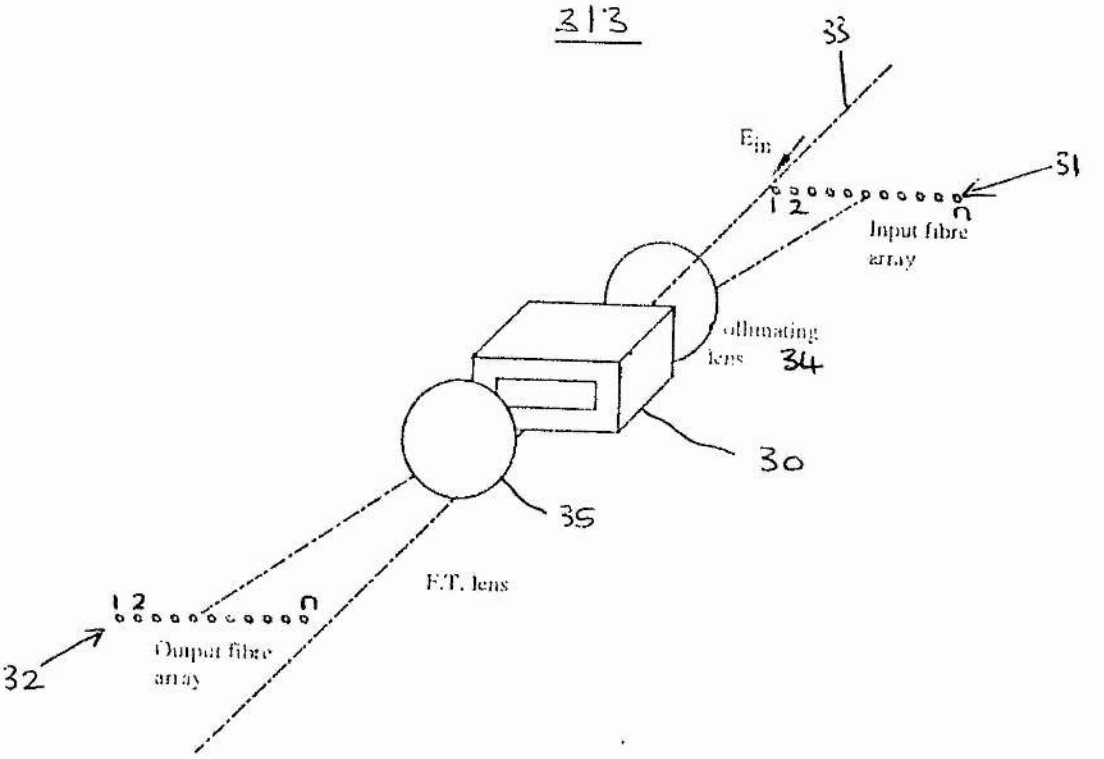

Figure 3 - Multi channel system using fibre optic cavities

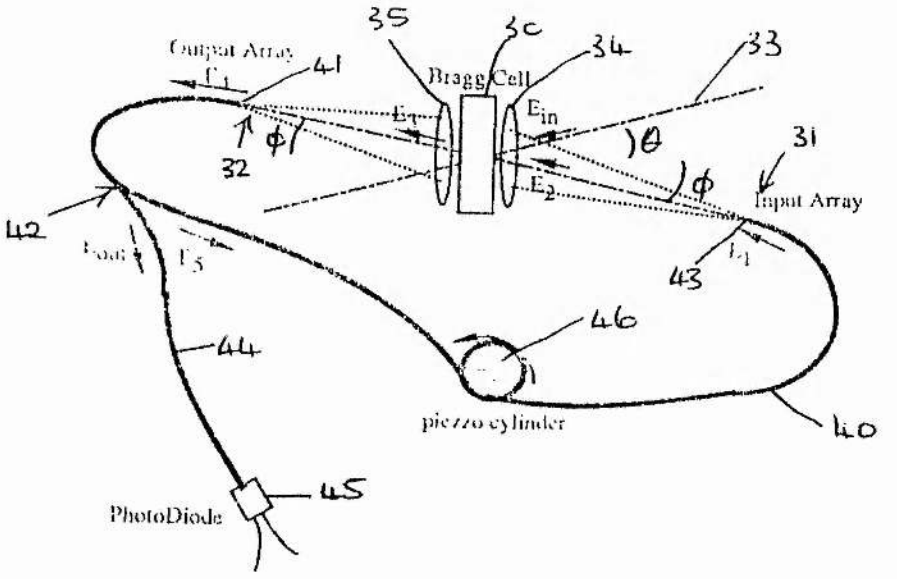

Figure 4 - One channel of multi channel system. Thick lines are mono-mode fibres

Light Modulating Cells

The invention relates to light modulators and in particular to modulation cells, similar to the Bragg cell, wherein a moving phase grating is generated.

In a conventional acousto optic Bragg cell acoustic waves generated in the cell by application of an electrical signal can modulate light transmitted through the acoustic medium. Such cells can be used as described in GB Patent No. 2144847 for rapid spectral analysis of a light source by application of an electrical signal of known spectral content or conversely as described in GB Patent No 2144848 for analysis of an electrical signal by using a known light source. For this purpose the spectral characteristics of the electrical signal applied to the Bragg cell controls a moving phase grating in the acousto optic material of the cell and this in turn controls the wavelength dependence of the diffraction of light passing through the cell. Conventional Bragg cells have bandwidths limited by acoustic losses in the crystals used in these cells and impedance matching of the transducer to the driver and crystal. Commercial cells are available with bandwidths of several Gigahertz.

Many applications, however, require significantly larger bandwidths than those currently available. One such application is the optical multiplexer described in copending GB Patent Application No. 9005647 where the bandwidth of the acousto optic device used is a major factor in determining the multiplexer bandwidth.

The object of the present invention is to provide a light modulation cell with improved bandwidth.

The invention provides a light modulation cell comprising:

an electro- or magneto-optically active medium;
means to create a travelling electromagnetic wave through the medium to thereby generate a moving phase grating in the medium; and
means to detect light transmitted through the medium and modulated by the moving phase grating therein.

In one form an electro-optic medium is located within the electromagnetic field of a transmission line along which a high frequency electrical signal is transmitted. Advantageously the electro-optic medium is a barium titanate crystal located within parallel conducting plates connected to a transmission line.

In an advantageous arrangement the electro-optic material is formed of a layer of crystal material of relatively high dielectric constant sandwiched between layers of crystal material of a relatively low dielectric constant; the optical axis of the middle layer being perpendicular to the optical axis of the outer layers.

In an alternative arrangement the light modulation cell may comprise a cavity for connection to a waveguide; the electro- or magneto-optically active medium being located within the cavity and means being provided to direct light to the medium and means to detect light diffracted by the medium.

The invention will now be described by way of example only with reference to the accompanying Drawings of which:

Figure 1 shows a side elevation of a travelling wave ultrahigh radiofrequency diffraction device according to the invention;

Figure 2 is a perspective diagrammatic view of the device; and

Figure 3 shows an arrangement similar to Figure 1 including sandwiched optically active dielectric material.

As shown in Figures 1 and 2 a radiofrequency electrical signal applied to the parallel plates 10, 11 connected to a transmission line results in a radiofrequency electromagnetic field 12 travelling between the plates. An electrooptically active crystal 13 of barium titanate, Ba Ti O_3, having length D, width L and thickness t is placed between the transmission line plates in the path of the radiofrequency field 12. The radiofrequency field produces changes in the electrooptic material equivalent to a moving phase grating. A beam of light 14 incident on the side 15 of the crystal 13 passes through the crystal, producing a zero order undiffracted light beam 16 and

higher order diffracted beams 17.

The electrooptic material is selected such that the product $r_c n_o^4$ is large, so as to give a high diffraction efficiency. For ferroelectric barium titanate:

r_c, the linear electrooptic coefficient, $\doteq 108 \times 10^{-12}$ m V^{-1} n_o; and
n_o the unperturbed refractive index, = 2.44.

Furthermore, for a large time-bandwidth product for the diffraction cell the radiofrequency dielectric constant, e_3, must be large and the propagation distance, D, should be long.

For barium titanate:

$e_3 = 170$, and

D = 100mm, determined by the length of crystal which can be grown.

In the design of a 50 GHz diffraction cell the thickness, t, is determined to be 0.9mm to provide an impedance of 50 ohms and the maximum interaction length L, based on the permissible limit of phase change of the applied rf wave in the interaction region, was determined to be 0.6mm.

The theoretical characterisation of the travelling wave diffraction cell, as described above, gives the following parameters:

Bandwidth	= 50 GHz	Centre frequency	= 50 GHz
Impedance	= 50 ohms	Diffraction efficiency	= 0.5% per watt
Freespace wavelength	= 6.33 mm	Time-bandwidth product	= 217
Frequency resolution	= 231 MHz	Freespace diffraction angle	= 4.22 mrad
Q	= 6.10^{-4}		

Theory of Operation

The electrooptic effect may be written as:

$$1/n_o^2 = 1/n^2 + rE + RE^2 + \text{higher terms} \quad (1)$$

Where n is the refractive index of a material within an electric field E and n_o is the unperturbed refractive index.

For a birefringent crystal we have:

$$1/n_{ij}^2 + r_{ijk}E_k + R_{ijkl}E_kE_l + \ldots = 1 \quad (2)$$

For a crystal with a predominantly linear electrooptic effect, the induced change in refractive index, Δn, is given by:

$$1/n_o^2 - 1/n^2 = r_cE_3$$

$$2\Delta n\, n_o/n_o^4 = rE$$

$$\Delta n = n_o^3 r_cE_3/2 \quad (3)$$

where r_c is the observed linear electrooptic coefficient. The diffraction intensity ratio of the resulting phase grating is given by:

$$I_d/I_i = J_m(k\Delta nL) \quad (4)$$

where m is the diffraction order, k is the optical wavenumber in the crystal and Jm(x) = m th order Bessel function of first kind.

Assuming we are operating in the Raman-Nath regime, i.e. Q<1, where Q is the parameter,

$$Q = k^*{}^2L/n_ok_o \quad (5)$$

where k_o and k* are respectively the free space optical and microwave wavenumbers in the crystal.

Then for the first diffraction order, operating at low diffraction efficiencies, we have:

$$I_d/I_i = (k\Delta nL/2)^2 \tag{6}$$

From 3 we have:

$$I_d/I_i = 1/16[kr_c n_o^3 E_3 L]^2 \tag{7}$$

and using:

$$k = n_o k_o = 2\pi n_o/\lambda_o$$

$$I_d/I_i = [\pi n_o^4 r_c L E_3/2.\lambda_o]^2 \tag{8}$$

For the parallel plate transmission line shown in Figure 2, the power, P, transmitted along the line is given by:

$$P = V_3^2/Z \tag{9}$$

Where Z is the characteristic impedance. Hence we have:

$$P = V_3^2 \sqrt{C/l} \tag{10}$$

where the capacitance per unit length C, is given by:

$$C = e_3 L/t \tag{11}$$

and the inductance per unit length, l, is given by:

$$l = \mu t/L \tag{12}$$

From 9, 11 and 12, we have:

$$P = V_3^2 L/t \sqrt{e_3/\mu} \tag{13}$$

But

$$E_3 = V_3/t \tag{14}$$

and so

$$P = E_3 2Lt \sqrt{e_3/\mu}; \qquad \therefore E_3 2 = P/Lt \sqrt{N/e_3} \tag{15}$$

From 8 and 15, we obtain the diffraction intensity ratio for the grating,

$$I_d/I_i = [\overline{11} n_o 4 r_c/2\lambda_o]^2 \; LP/t \sqrt{\mu/e_3} \tag{16}$$

The diffraction efficiency per watt, η , is given by:

$$\eta = I_d/I_i(1/P) \tag{17}$$

or

$$= (\overline{11}\; n_o 4 r_c/2\lambda_o)^2 \;\; L/t \sqrt{\mu/e_3} \tag{18}$$

The maximum interaction length, L, is limited by the requirement that the phase of the applied radiofrequency wave must not change significantly (i.e. by not more than a quarter wavelength) as the optical wavefronts pass through the interaction region.

We may write:

$$n_o L/c < 1/(4f) \tag{19}$$

where f is the radio frequency.

The maximum value of L is then given by:

$$L_{max} = c/(4fn_o) \tag{20}$$

The time bandwidth product of the grating, B, is:

$$B = B.D/c \sqrt{e_3} \tag{21}$$

where B is the bandwidth.

The frequency resolution, $\triangle f$, is given by:

$$\triangle f = 1/\tau \tag{22}$$

where τ is the transit time of the radiofrequency wave in the interaction region.

Thus:

$$\triangle f = \frac{c}{D\sqrt{e_3}} \tag{23}$$

The diffraction angle inside the crystal, θ_d, is

$$\theta_d = \frac{\lambda_o f \sqrt{e_3}}{n_o c} \tag{24}$$

and the diffraction angle in free space is:

$$\theta'_d = n_o \theta_d \tag{25}$$

In order to make use of a high dielectric constant e_1 to give a large time-bandwidth (τ_B) product, a sandwich construction could be used as shown in Figure 3. In this arrangement a travelling wave diffraction cell 30 comprises optically active material 31, sandwiched within parallel conducting plates 32, 33 connected to a high frequency rf transmission line. Crystal material of thickness t_3 is located between upper and lower layers 35, 36 which may be of differing thicknesses t_1 and t_3. As shown the crystal layers are cut such that the crystal axis of the centre layer is perpendicular to the common crystal axis of the two outer layers.
This will produce an effective dielectric constant for the transmission line given by:

$$e_{eff} = \frac{e_1 e_3 (2t_1 + t_2)}{e_1 t_2 + 2e_3 t_1} \tag{26}$$

where we have assumed $t_1 = t_3$ and

$$t = 2t_1 + t_2 \tag{27}$$

Equation 14 for the applied field across the middle layer becomes:

$$V_3 = \frac{2e_3t_1 + e_1t_2}{e_1} E_3 \qquad (28)$$

From 9, 10, 11, 12, 26, 27 and 28, we have:

$$P = \left[\frac{2e_3t_1 + e_1t_2}{e_1} E_3\right]^2 \frac{L}{2t_1 + t_2} \sqrt{\frac{e_{eff}}{\mu}} \qquad (29)$$

The diffraction intensity ratio for the grating is, from 8 and 29:

$$\frac{I_d}{I_i} = \left[\frac{\bar{\imath}\bar{\imath} n_o^4 r_c L}{\lambda_o}\right]^2 \left[\frac{e_1}{2e_3t_1 + e_1t_2}\right]^2 \frac{2t_1 + t_2}{L} \sqrt{\frac{\mu}{e_{eff}}} P \qquad (30)$$

From 17 and 30, the diffraction efficiency per watt is:

$$\eta = \left[\frac{\bar{\imath}\bar{\imath} n_o^4 r_c L}{\lambda_o}\right]^2 \left[\frac{e_1}{2e_3t_1 + e_1t_2}\right]^2 \frac{2t_1 + t_2}{L} \sqrt{\frac{\mu}{e_{eff}}} \qquad (31)$$

The theoretical characterisation then gives the following parameters:

L = 0.6mm	D = 100mm
t_1 = 1.9mm	t_2 = 0.01mm
η = 11% per watt	Impedance = 50 ohm
Bandwidth = 50 GHz	Centre frequency = 50 GHz
λ_o = 633nm	τ_B = 892
Δf = 55 MHz	θ'_d = 6 mrad
Q = 0.08	

Although the invention has been described in relation to an electro-optic device for connection to a transmission line, other arrangements of interacting an rf wave with light are possible. For example the magneto-optic effect with suitable materials could be exploited. In addition the electro- or magneto-optic material may be placed within a waveguide provided with suitable arrangements for illuminating the material and for detection of light diffracted thereby.

Further ways of implementing the invention are as follows:

1) Electro-optic effect across a pn-junction;
2) Electro-optic effect in a pin-diode;
3) Electro-optic effect in a laser diode;
4) Electro-optic effect in a heterostructure;
5) Electro-optic effect in epitaxial layers;
6) Use of a microstrip transmission line;
7) Use of slow wave structure;
8) Quantum well structures;
9) Electro- and magneto-optic absorption and polarisation effects.

Claims

1. A light modulation cell comprising:

an electro- or magneto-optically active medium;
means to create a travelling electromagnetic wave through the medium to thereby generate a moving phase grating in the medium; and
means to detect light transmitted through the medium and modulated by the moving phase grating therein.

2. A light modulation cell as claimed in claim 1 wherein arrangement the light modulation cell comprises a cavity for connection to a waveguide; the electro- or magneto-optically active medium being located within the cavity and means being provided to direct light to the medium and means to detect light diffracted by the medium.

3. A light modulation cell as claimed in claim 1 wherein an electro-optic medium is located within the electromagnetic field of a transmission line along which a high frequency electrical signal is transmitted.

4. A light modulation cell as claimed in claim 2 wherein the electro-optic medium is a barium titanate crystal located within parallel conducting plates connected to a transmission line.

5. A light modulation cell as claimed in any one of claims 2 to 4 wherein the material is an electro-optic material formed of a layer of crystal material of relatively high dielectric constant sandwiched between layers of crystal material of a relatively low dielectric constant; the optical axis of the middle layer being perpendicular to the optical axis of the outer layers.

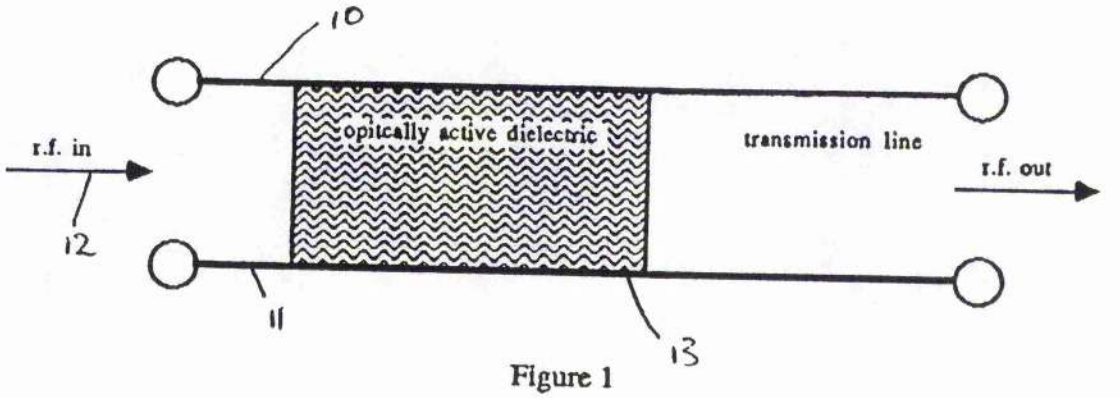

Figure 1

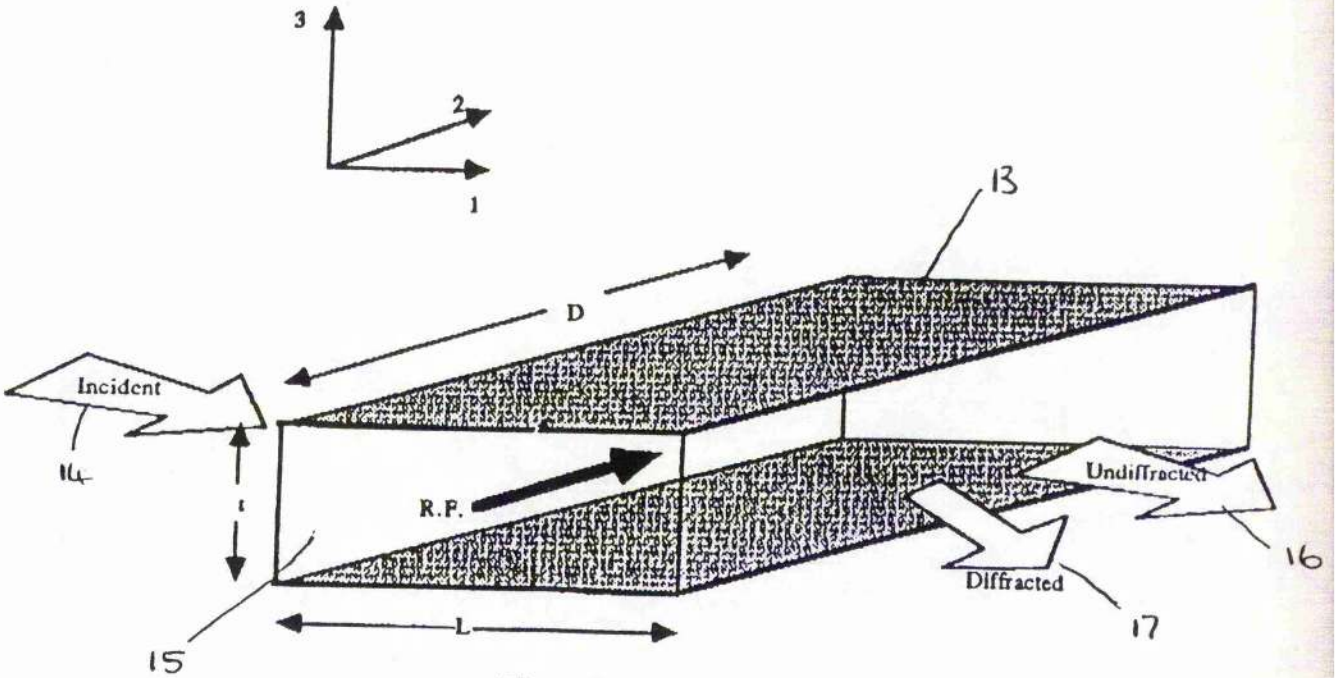

Figure 2

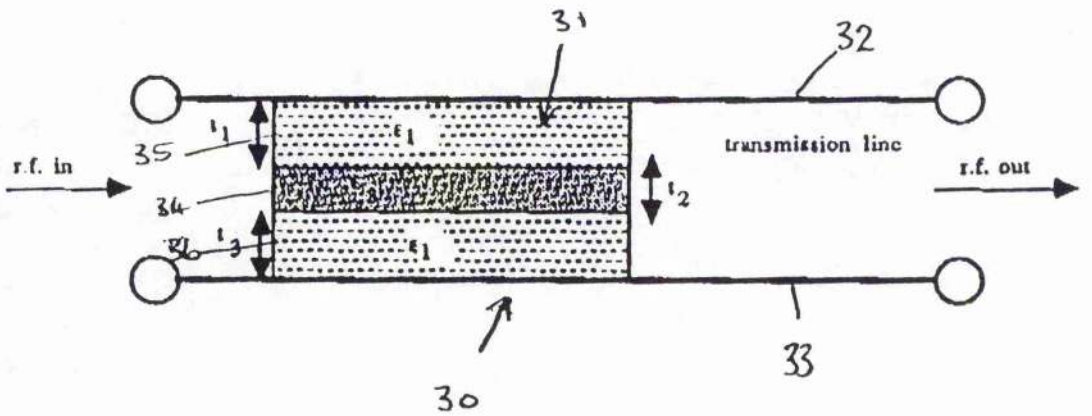
31
32
35
t_1
ε_1
r.f. in
transmission line
r.f. out
34
t_2
t_3
ε_1
30
33

Figure 3

An Optical Multiplexer

The invention relates to communications systems and in particular to such systems employing optical transmission links.

Modern computing and communications systems require ever higher data transmission rates. The speed of transmission is limited by the usable bandwidth of the transmission medium. In the case of transmission along coaxial cables, for example, data rates are limited to around a few hundred megahertz over large distances.
Optical transmission systems offer theoretical bandwidths of peta-hertz. If the transmission is in a dispersive medium, then this data rate is considerably reduced. In commercially available single mode optical fibres, for instance, the theoretical limit is greater than a few hundred gigahertz. This limitation arises from the maximum speeds at which the driving electronics can operate.

The object of the present invention is to provide a communications system capable of operation at high data rates by exploitation of the available bandwidth in optical transmission links.

The invention provides an optical multiplexer for a communications system comprising:
a laser light source;
moving grating means to disperse light from the source to provide a plurality of spatially separated output light beams, each beam having a different non-overlapping optical frequency bandwidth; and
a light modulation means having a plurality of electrical signal input connections corresponding to spatially separated modulation channels, each channel having incident thereon a respective one of the output light beams to form thereby a plurality of parallel signal beams providing orthogonal communications channels.

The principle of operation of the invention relies on the Doppler shift in frequency of optical radiation diffracted by an acousto-optic Bragg cell or other moving grating.

The optical multiplexer thus uses frequency division multiplexing, providing parallel optical channels which can be transmitted through free space or combined in a single optical fibre.

Preferably the light dispersing means comprises an acousto-optic (A-O) device having an input transducer and a source of polychromatic radio frequency signals (RF) connected to the input transducer, and a Fourier Transforming (FT) lens providing an FT of the A-O output in a focal plane in which the light modulation means is located. Advantageously the RF source generates a chirp frequency function. Light transmitted through the A-O device is diffracted such that the angles of diffraction of the light are proportional to the frequency components of the RF signals. This produces a spatial distribution in the focal plane of the lens where the transverse displacement from the optic axis is proportional to the frequency of the RF signal.
In the preferred arrangement a beam expander is provided such that the A-O device, preferably a Bragg cell, is uniformly illuminated by the laser light. Preferably the light modulation means is a 1-dimensional spatial light modulator (SLM) and the output light beams from the A-O cell are focussed by the lens onto the SLM. The SLM is located such that each element thereof defines an independent frequency channel. In one form the laser light may be incident on a plurality of Bragg cells aligned such that the output beams therefrom are directed to respective lines of a 2-dimensional SLM.

In the preferred arrangement an unmodulated reference beam is also provided by the laser source, advantageously by means of a beamsplitter located between the source and the A-O cell. In an optical fibre communications system each signal beam in the communications channels may be heterodyned to the reference beam by coupling the signal beams into a first optical fibre, the reference beam into a second optical fibre, and coupling together the first and second optical fibres into a single transmission optical fibre. In this arrangement a receiver includes a detector whose output is connected to an acousto-optic device, preferably a Bragg cell, arranged to modulate light from a laser light source such that a plurality of beams corresponding to said spatially separated communications channels is produced and a detector array is located such that each beam is incident on a respective detector element of the detector array.

When used in a free space communications system the signal beams are transmitted through collimating optics to produce a free space signal beam. Advantageously the transmitter is arranged such that a delay is introduced between the free space signal beam and the reference beam and the receiver is arranged such that a complementary delay is introduced to thereby bring the signal beams and reference beam into time synchronism. Preferably the delays are introduced by transmitting one of the reference or signal beams via a length of optical fibre in the transmitter and the other of the reference or signal beams via a similar length of optical fibre in the receiver. Conveniently the optical fibre delays are arranged as loops.

A communications system transceiver may comprise a transmitter including an optical multiplexer and a receiver as described above wherein a single Bragg cell is employed; a polychromatic signal generator being provided to drive the Bragg cell during transmission and the received frequency modulated signal being connected to drive the Bragg cell during reception.

The optical multiplexer of the present invention may also be used in a radio frequency (RF) communications system. In an RF system transmitter signal light beams and a reference beam from the optical multiplexer are coupled to an optical fibre connected to an optical detector, the output of which is arranged to modulate an FM carrier signal for connection to an FM aerial. In the FM system the signal is detected by means of an aerial to receive the FM carrier and a local oscillator to demodulate the signal.

In all the above arrangements the optical fibres are preferably single mode.

The invention will now be described with respect to the accompanying Drawings of which:

Figure 1 is a schematic representation of an optical multiplexer according to the invention;

Figure 2 illustrates a coupling arrangement connecting outputs from the Figure 1 multiplexer for transmitting signals to an optical fibre;

Figure 3 is a schematic drawing of a receiver demultiplexer arrangement for connection to the optical fibre of Figure 2;

Figure 4 illustrates a modification of the Figure 1 arrangement for secure

free space transmission;
Figure 5 is a modification of the Figure 3 arrangement for receiving transmissions from the Figure 4 transmitter;
Figure 6 illustrates use of the Figures 1 and 2 arrangements in an RF transmission system;
Figure 7 is a modification of Figure 3 for reception of the Figure 6 RF signals; and
Figure 8 is a schematic diagram of a free space optical transceiver system.

An optical multiplexer is shown in Figure 1. Light from a laser source 10 is transmitted through a beam expander 11 and a beam splitter 12 so as to uniformly illuminate a Bragg cell 13. The beam splitter 12 partially reflects the incident laser light to produce a reference beam 14, shown parallel to the optical axis 15 of the multiplexer after reflection from mirror 16. A frequency chirp or polychromatic RF signal 17, which may be continuous or comprised of a series of pulses, is applied to the input transducer (not shown) of the Bragg cell 13. An acoustic wave having a corresponding frequency spectrum is then produced in the Bragg cell 13. The laser light incident on the Bragg cell 13 is diffracted by the acoustic wave such that the light emerging from the Bragg cell diverges since the angles of diffraction of the light are proportional to the frequency components of the acoustic wave. The diffracted light from the Bragg cell 13 is focused by a lens 18 on to a linear spatial light modulator (SLM) 19 having n elements. The SLM 19 is arranged so that the different diffraction components are spread along its length. The acoustic wave interaction with the laser light in the Bragg cell simultaneously produces a Doppler frequency shift of the output light which is proportional to the frequency of the RF signal applied to the Bragg cell. Thus the Doppler shift varies across the spatial distribution of light output from the Bragg cell by an amount proportional to the transverse displacement from the optic axis 15. This means that for any given transverse position 110 (say) there will be an associated Doppler frequency. Thus each element of the SLM 19 defines a different frequency channel and light transmitted through the SLM 19 and rendered parallel to the optical axis by lens 111 provides n optical output beams or channels 112, each of which can be modulated by application of appropriate signals $S_1 \ldots S_n$ applied to the n elements of the SLM 19. The maximum modulation rate (bandwidth) of each channel is then proportional to the separation of the channels. The total

capacity of the system is the sum of the channel bandwidths and this is determined by the bandwidth of the Bragg cell; currently Bragg cells with bandwidths of 10 gigahertz are available.

The n signal channels 112 and the reference beam 144 may be coupled to a fibre optic communications system as shown in Figure 2. Channels 112 are coupled by coupling optics 21 to a single mode optical fibre 22. The reference beam 14 is coupled to a second single mode optical fibre 23 by further coupling optics 20. The two fibres 22 and 23 are coupled to an output single mode optical fibre 24 via a coupler 25. The signal and reference beams are thus mixed by the coupler 25 and the signal transmitted via the output fibre 24 consists of a radio frequency modulated monochromatic beam.

After transmission the modulated beam is connected via an input single mode optical fibre 31 (which may be identical to the fibre 24) to a detector 32 as shown in Figure 3. The detected signal is connected via an amplifier 33 to the input 34 of a Bragg cell 35. Light from a laser 36 is expanded (37) and collimated to illuminate the Bragg cell 35. Diffracted light from the Bragg cell 35 is focused by a lens 38 on to a linear detector array 39. The spatially distributed frequency channels 112 are thus recreated on the detector array 39. The detector array 39 has n elements with each element 310 corresponding to one of the frequency channels 112. The n output signals 311 from the detector array 39 are the demultiplexed signals.

The optical transmitter/receiver system can be modified as shown in Figures 4 and 5 to provide a secure free space transmission system where like integers are indicated by like reference numerals. The n frequency channels 112 are collimated (41) to produce a free space signal FM signal beam 42. The reference beam in the fibre 23 is delayed relative to the signal by providing a loop delay 43 in the fibre before connection to collimating optics 44 to provide a free space reference beam 45. In the receiver (Figure 5) the signal and reference beams 42 and 45 are connected via respective coupling optics 51 and 52 to single mode optical fibres 53 and 54. A delay loop 55 is provided in the signal fibre 53 to bring the signal and reference beams into time coincidence before mixing in a coupler 56. The output from the coupler 56 is then detected and used to modulate the Bragg cell 35 as in the Figure 3 receiver. In this arrangement the transmitter delay of the reference beam in

loop 43 and the reception delay of the signal beam in loop 55 must be equal within the limit of the coherence length of the source laser otherwise demultiplexing will not occur. Providing this criterion holds, the detected FM signal applied to the Bragg cell 35 reconstructs the transmitted output channels 112 on the detector array 39 and hence the demultiplexed signals S_1 ...S_n appear at the outputs 311 of the elements 1 - n of the detector array 39.

Figures 6 and 7 show a further application of the optical multiplexer of Figure 1 to a radio frequency communications system. Elements of this system in common with the fibre optic system described in relation to Figures 1 - 3 are represented by like reference numerals. The signal and reference beam outputs 112, 114 from a multiplexer as in Figure 1 are coupled in to single mode optical fibres 22, 23 and then coupled together in a further single mode fibre 24. The resulting signal is connected to a detector and after amplification (62) is used to modulate an RF carrier from a local oscillator 63 in mixer 64. The RF signal is then radiated by an aerial 65. In the receiver (Figure 7) signals from an FM aerial 71 are heterodyned in a mixer 72 with the carrier frequency produced by a local FM oscillator 73. The output from the mixer 72 after amplification (33) is used to drive the Bragg cell 35 and demultiplexing occurs as described in relation to Figure 3.

A secure transceiver system for free space optical communications is shown in Figure 8 where elements common to Figures 1-5 are shown with like reference numerals. In this arrangement the free space transmitter of Figure 4 and the receiver of Figure 5 are combined into a single unit using only one Bragg cell 13.

In transmission mode the Bragg cell 13 is driven by a signal connected from chirp generator 81 via adder 82 and amplifier 83 to the input of the Bragg cell 35. The signal beams after transmission through lens 111 are transmitted through a beamsplitter 84 to collimating optics 85 for producing the free space signal beam 86. Alternatively coupling optics could be used as in Figure 2 for connection to an optical fibre. The reference beam 14 after transmission via the optical fibre loop delay 43 is transmitted to a fibre terminous 87 via coupler 88. Light from the terminous 87 passes through collimating optics 89 to provide a free space reference beam 810.

In reception mode received signal and reference beams 86 and 810 are transmitted through the respective optical components 85 and 89. The signal

beam is reflected by the beamsplitter 84 through coupling optics 51 to the delay loop 55 in optical fibre 53. The reference beam is coupled to the optical fibre 54 via coupler 88. The delayed signal beam in fibre 53 is heterodyned to the reference signal from the fibre 54 in the coupler 56. The frequency modulated output from coupler 56 is then detected (32) and connected via amplifier 33, adder 82 and amplifier 83 to drive the Bragg cell 13.

Simultaneous transmission, reception, modulation and demodulation occur in this system. This allows multi-synchronous secure communications. Data may be transmitted in free space or in single mode fibres. A simpler system would allow data to be transmitted at radio frequencies.

A number of applications and advantages result from the implementation of the optical multiplexer which include:

1. High data rates. The data rate is limited by the Bragg cell bandwidth. At present up to 10 gigahertz is possible.
2. A high degree of parallelism is possible. This is limited by the time-bandwidth product of the Bragg cell
3. High data rates/parallelism lead to very low error rates through optical bit-checking.
4. Compatability with existing optical fibre data transmission systems.
5. The elimination of electronic multiplexers in telephony.
6. The transceiver may be reconfigured as an in-line booster for fibre optic communications.
7. The optical multiplexer may be used for the instantaneous (one-shot) transmission of two dimensional images. This is achieved using an array of acousto-optic elements to generate a two-dimensional spatial distribution of Doppler frequencies. A two dimensional SLM is used to transmit the image. Picture resolution may be automatically controlled by the frame rate.
8. The optical multiplexer may be used to enable the various elements of communications and control systems and computers to be separated by some distances. The high degree of parallelism implicit in optical multiplexer-based systems allows each element to communicate independently with every other element down a single fibre. Extremely robust distributed systems are possible without degrading overall system performance.

9. An extremely high degree of security from illicit surveillance is inherent in optical multiplexer-based systems incorporating a delayed reference beam. An eavesdropper would need to receive simultaneously the signal and reference beams and also incorporate the appropriate delay. Since the delay can be changed or modulated randomly, foreknowledge of the delay or modulation would be required. The observed signal cannot be stored whilst the correct delay is being sought because once detection has occurred, the phase information is lost. This process is called "coherence encryption".

10. The signal beam may be less intense than the reference beam. Misdirection is possible by modulation of the reference or signal with dummy information. The performance of the system is unaffected by this misdirection.

11. Multi-synchronous distributed systems may be used, for example, in ships and aircraft to achieve passive covert reception.

12. An integrated optics implementation allows the fabrication of small, robust systems.

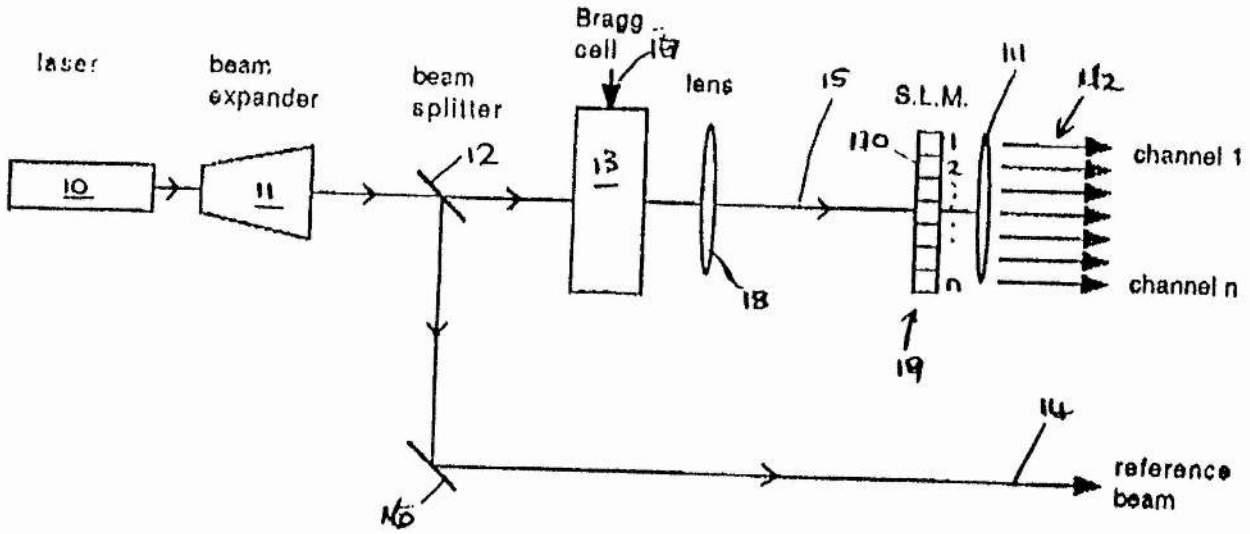

Figure 1 Basic multiplexer

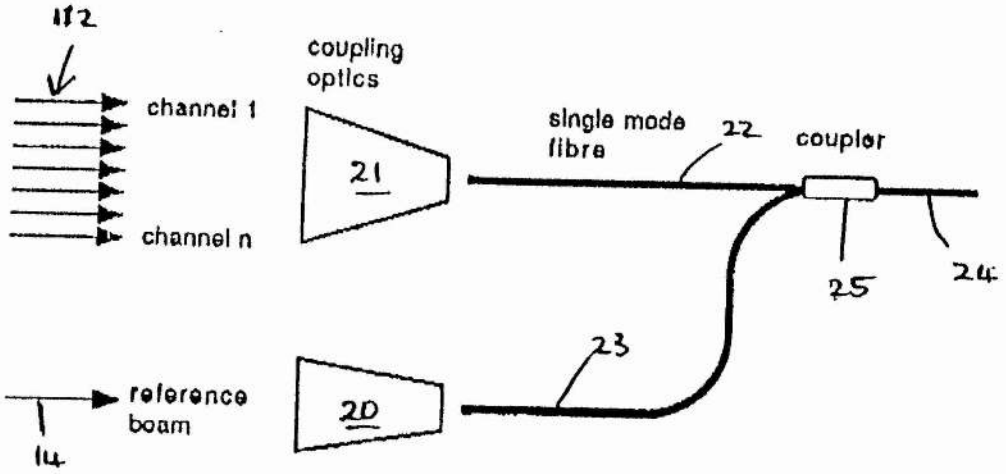

Figure 2 Fibre transmission system

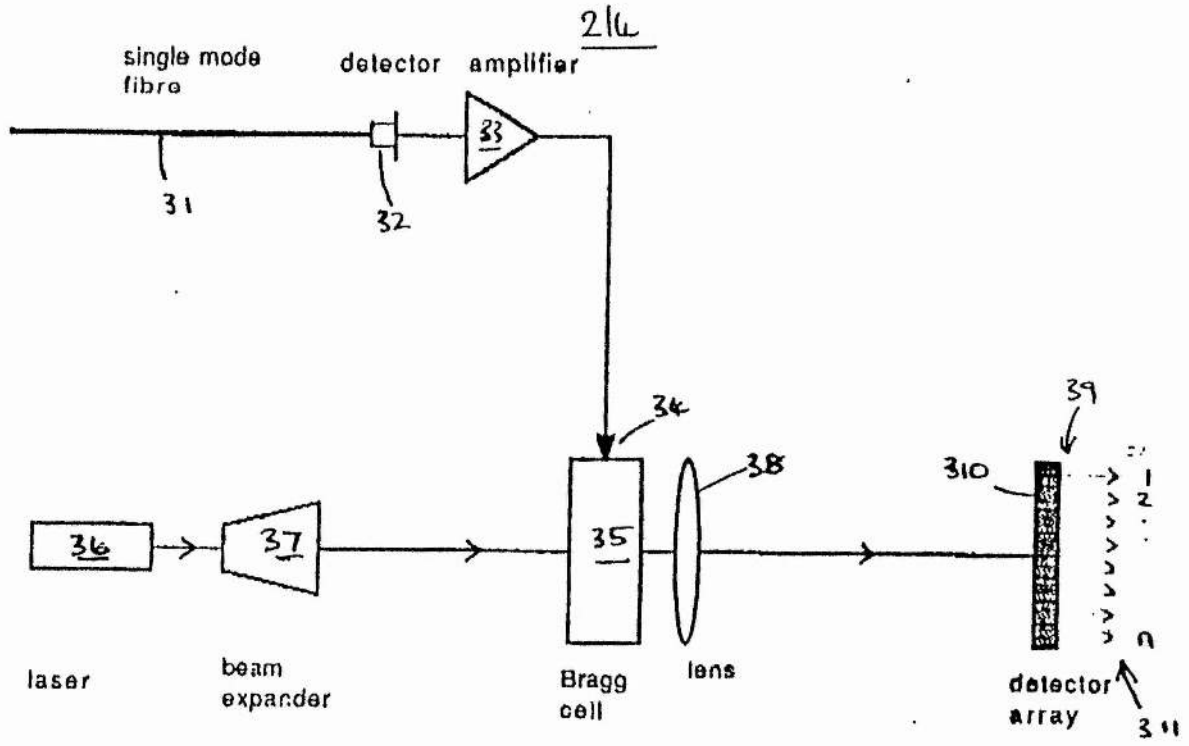

Figure 3 Fibre reception system

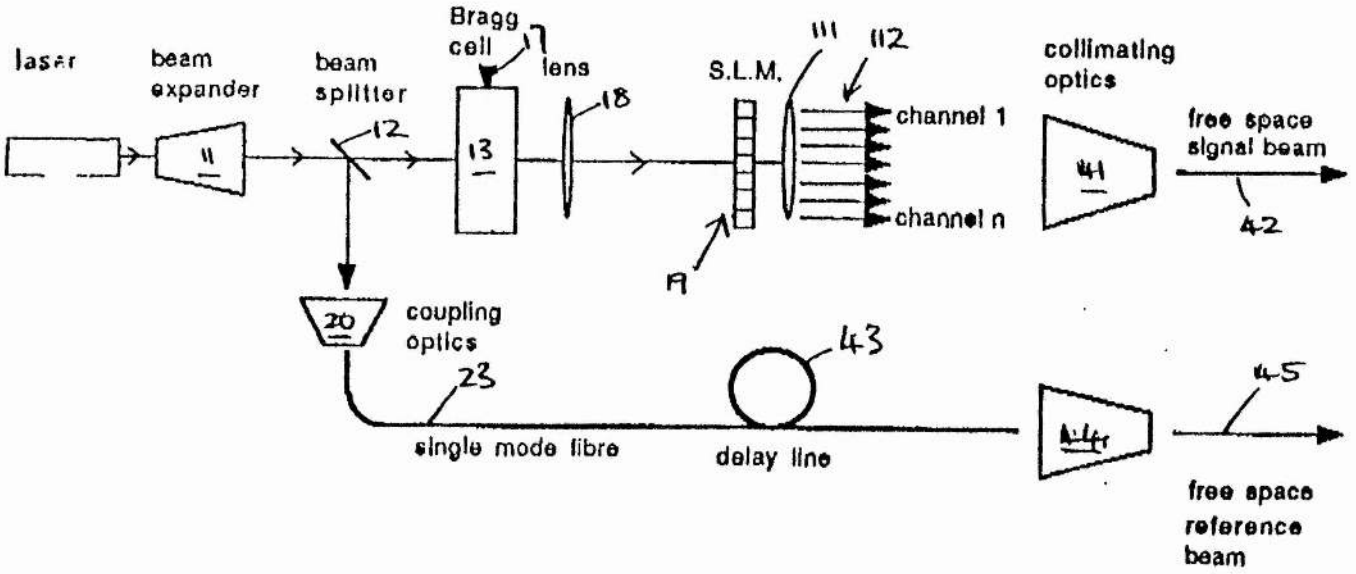

Figure 4 Free space transmission system

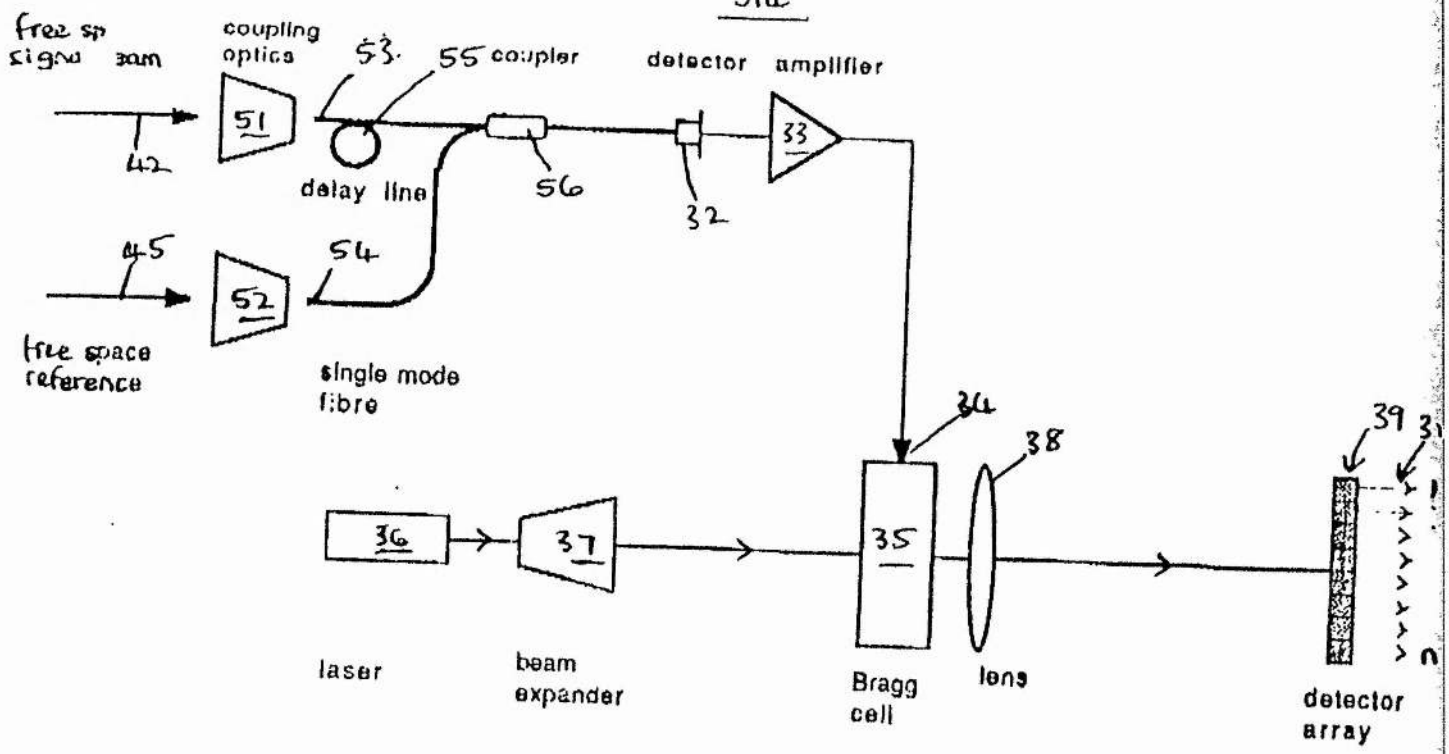

Figure 5 Free space reception system

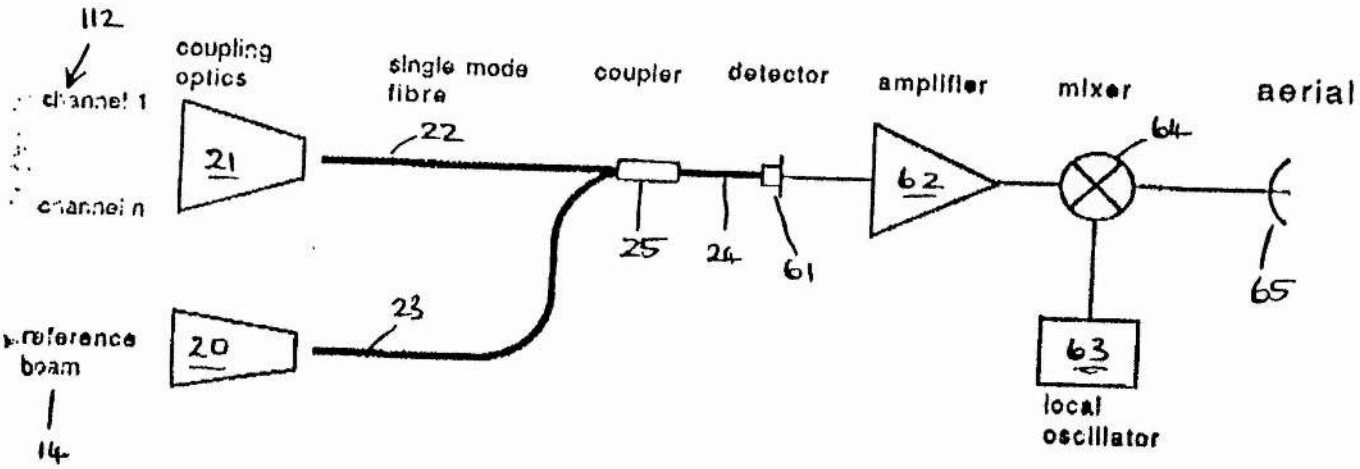

Figure 6 Radio frequency transmission system

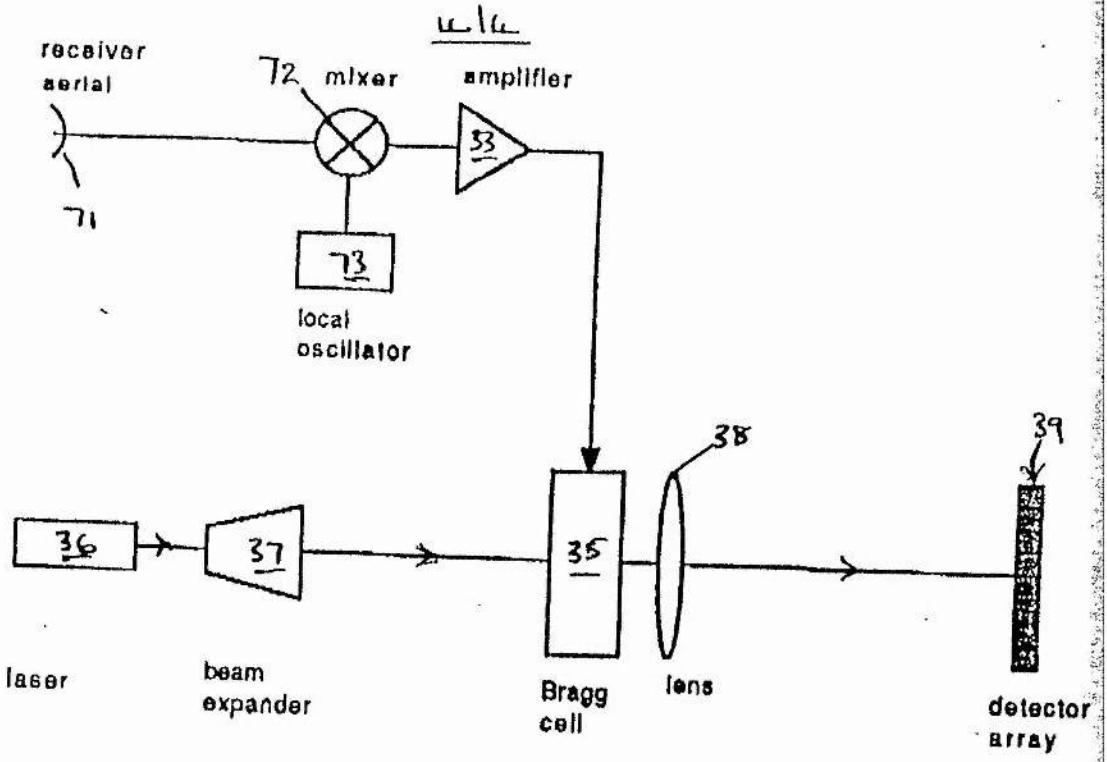

Figure 7 Radio frequency reception system

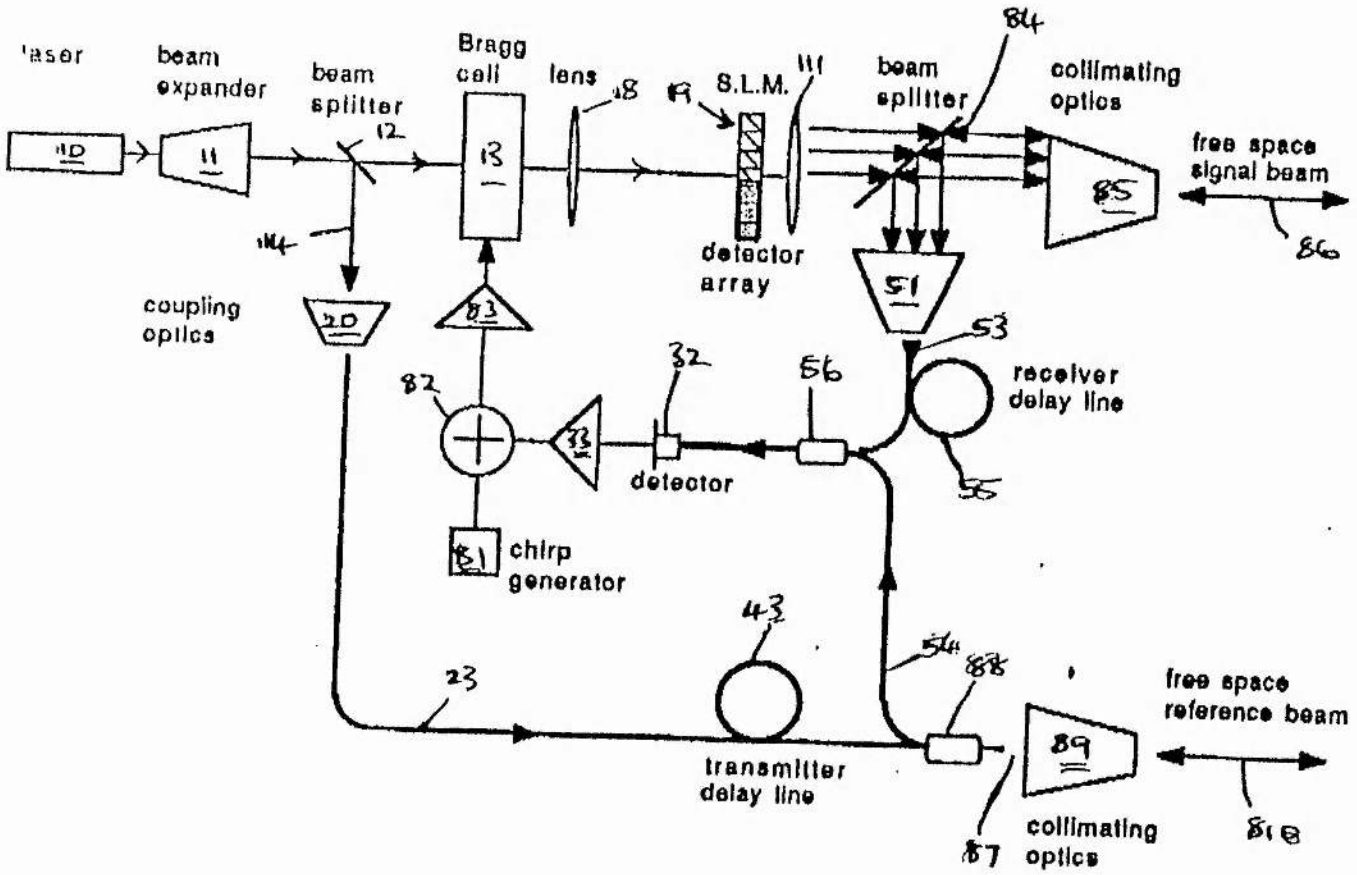

Figure 8 transceiver system